Modeling and analytical computations of burst and interburst dynamics in neuronal networks, applications to neuron-glia interactions and oscillatory brain rhythms

Lou Zonca

▶ To cite this version:

Lou Zonca. Modeling and analytical computations of burst and interburst dynamics in neuronal networks, applications to neuron-glia interactions and oscillatory brain rhythms. Dynamical Systems [math.DS]. Sorbonne Université, 2021. English. NNT : 2021SORUS576 . tel-04257536

HAL Id: tel-04257536
https://theses.hal.science/tel-04257536v1

Submitted on 25 Oct 2023

Ecole Doctorale de Sciences Mathématiques Paris Centre

THESE DE DOCTORAT
Pour obtenir le grade de docteur de Sorbonne Université

Discipline: Mathématiques Appliquées

Présentée par

Lou ZONCA

Modeling and analytical computations of burst and interburst dynamics in neuronal networks, applications to neuron-glia interactions and oscillatory brain rhythms

dirigée par David HOLCMAN

Après avis des rapporteurs

Pr. Igor SOKOLOV	Humboldt-Universität zu Berlin
Pr. Béatrice LAROCHE	INRAE Jouy-en-Josas

Soutenue le 16 juillet 2021 devant le jury composé de

Pr. Igor SOKOLOV	Humboldt-Universität zu Berlin	Rapporteur
Pr. Krasimera TSANEVA	Exeter University	Examinatrice
Pr. Mathieu DESROCHES	INRIA Sofia-Antipolis	Examinateur
Pr. Amandine VEBER	Université Paris Descartes	Examinatrice
Pr. Boris GUTKIN	Ecole Normale Supérieure, PSL	Examinateur
Pr. Emmanuel TRELAT	Sorbonne Université	Examinateur
Pr. Stéphane JAFFARD	Université Paris Est Créteil	Examinateur
Pr. David HOLCMAN	Ecole Normale Supérieure, PSL	Directeur de thèse

Remerciements

Je voudrais commencer par Eric car avec lui tout est mieux.
Je remercie aussi mes collègues du laboratoire : Matteo Dora et Kanishka Basnayake qui ont partagé (et partagent encore) les turpitudes du quotidien de thésard.e avec moi, ainsi que Suney Toste, Annia Abtout, Andrea Papale, et tous les autres... Je m'adresse en particulier à Jérôme Cartailler, Ofir Shukron et Natanaël Hozé pour leur soutien, leurs précieux conseils et leur amitié, sans eux j'aurais eu plus de mal à tenir jusqu'au bout !
J'ai une pensée particulière pour Alexandra Mougin qui m'a partagé sa force et son énergie pour m'accompagner dans cette aventure depuis un peu plus d'un an.
Je remercie également toute ma famille pour leur soutien et leur amour inconditionnel. En particulier ma grand-mère Gilberte qui étudie par procuration avec moi, et mes soeurs Raphaëlle et Giulia qui lisent tout ce que j'écris et ont hâte de ne rien comprendre à ma thèse.
Je tiens également à remercier mes rapporteur.trice.s et membres du jury pour le temps qu'elle.il.s ont accepté de m'accorder pour évaluer mon travail.
Bien entendu, mon directeur de thèse, David Holcman ainsi que Nathalie Rouach et Elena Dossi avec qui j'ai collaboré avec grand plaisir et qui m'ont beaucoup appris.

Enfin et surtout, pour leurs inestimables contributions aux mathématiques et à la science en général ainsi que pour l'exemple qu'elle nous donnent : Ada Lovelace, Maryam Mirzakhani, Emilie du Châtelet, Sophie Germain, Mary Sommerville, Florence Nightingale, Emmy Noether, Karen Uhlenbeck, Grace Hopper, Ingrid Daubechies, Mileva Maric Einstein, Marie Curie, Katherine Johnson, Dorothy Johnson Vaughan, Hanna Neumann, Claire Voisin, Evelyn Boyd Granville, Marie la Juive, Françoise Héritier, Annie Jump Cannon, Stefanie Horovitz, Lise Meitner, Alice Bell, Irène Joliot-Curie, Dorothea Klumpke Roberts, Frances Allen, Madeleine Pelletier, Edmée Chandon, Yvonne Choquet-Bruhat, Marie Meurdrac, Barbara McClintock, Marie-Anne Pierrette Paulze, Andrea Mia Ghez, Maria Goeppert-Mayer, Lisa Gelobter, Mary Tsingou, Donna Theo Strickland, Ida Tacke Noddack, Barbara Liskov Huberman, Marian Croak, Ada Yonath, Chien-Shiung Wu, Vera Rubin, Nicole Reine-Lepaute, Caroline Lucretia Herschel, Sofia Vassilievna Kovalevskaïa, Catherine Vidal, Dorothy Crowfoot Hodgkin, Frances Hamilton Arnold, May Britt Moser, Jennifer Doudna, Emmanuelle Charpentier, Aurélie Jean, Françoise Barré-Sinoussi, Laura Maria Catarina Bassi, Rose Dieng-Kuntz, Nicole El Karoui et toutes celles que j'oublie ou que l'histoire a effacées...

Publications

Published

- ZONCA L. & HOLCMAN D., “Modeling bursting in neuronal networks using facilitation-depression and afterhyperpolarization” *Communications in nonlinear science and numerical simulations*, 94:e105555 (2021) / arXiv:2001.11432
- ZONCA L. & HOLCMAN D., “Escape from an attractor generated by recurrent exit” *Physical Review Research* (2021, in press) / arXiv:2009.06745

Submitted

- ZONCA L. & HOLCMAN D., “Exit versus escape for stochastic dynamical systems and application to neuronal network bursting time computation” *under review in Journal of nonlinear science* / arXiv:2010.06699
- DOSSI E.*, ZONCA L.*, PIVONKOVA H., VARGOVA L., CHEVER O., HOLCMAN D.$^+$ & ROUACH N.$^+$, “Astroglial gap junctions strengthen hippocampal network activity by sustaining afterhyperpolarization via KCNQ channels” *submitted* *,$^+$contributed equally
- ZONCA L. & HOLCMAN D., “Up and Down states occurring in neuronal networks regulate the emergence and fragmentation of the α-band” *under review in PloS Computational Biology*

In preparation

- ZONCA L.*, DOSSI E.$^+$, ROUACH N.$^+$, & HOLCMAN D.* “Statistics of neuronal bursting in electrophysiological and electroencephalogram time series: computational methods and algorithms.” *invited book chapter for a Springer Nature book about Neuromethods* *,$^+$contributed equally
- MILIOR G., VASILE F., EZAN P., ZONCA L., BEMELMANS A., HOLCMAN D. & ROUACH N. “Astroglial IP3R1 mediates calcium signaling in perisynaptic processes and controls hippocampal neuronal excitability”

Résumé

Dans cette thèse de doctorat, je modélise et simule des réseaux de neurones biologiques pour mieux comprendre la genèse et l'évolution des schémas de burst neuronal. Plus précisément, je développe ici un nouveau modèle de champ moyen basé sur la plasticité synaptique à court terme qui tient compte à la fois des bursts et interbursts en ajoutant l'afterhyperpolarisation (AHP), un mécanisme induit par divers canaux de K^+, situés sur la membrane neuronale, avec une dynamique lente qui conduit à une période réfractaire après les bursts.

Le modèle est un système dynamique non linéaire de dimension 3 avec un bruit blanc gaussien additif. Je caractérise les durées des bursts et interbursts en combinant l'étude de l'espace des phases déterministe avec de l'analyse asymptotique pour l'aspect stochastique. La distribution des durées de bursts (définies par de longues trajectoires déterministes en dehors du bassin d'attraction) est déterminée en caractérisant la densité de probabilité des points de sortie sur la séparatrice qui satisfait l'équation de Fokker-Planck. Pour résoudre ce problème, j'utilise l'approximation WKB et la méthode des caractéristiques.

Les interbursts sont définis comme la sortie du bassin d'attraction induite par le bruit. Comme la dynamique autour de l'attracteur est très anisotrope, j'utilise une projection bidimensionnelle du modèle pour étudier ces interbursts. De manière surprenante, la densité de probabilité dans l'espace des phases des trajectoires non sortantes a révélé un maximum qui n'est pas centré sur l'attracteur déterministe et dont la position dépend de l'amplitude du bruit, décrivant ainsi un déplacement de la position de l'attracteur dans le cas stochastique. Enfin, l'analyse des trajectoires sortantes a révélé un nouveau mécanisme de sortie d'un bassin d'attraction (propre aux dimensions ≥ 2) : les trajectoires traversent la séparatrice puis entrent et sortent un grand nombre de fois du bassin d'attraction avant de s'échapper vers l'infini, induisant une différence significative entre le temps mis pour atteindre la séparatrice pour la première fois et celui mis pour s'échapper et ce, quelle que soit l'amplitude du bruit. J'ai caractérisé et quantifié ces deux nouveaux phénomènes dans le cadre général d'un système dynamique bidimensionnel simplifié qui est topologiquement équivalent au modèle d'origine. Ce mécanisme d'entrées / sorties récurrentes explique l'existence de temps de sortie plus longs qu'attendu par la théorie classique de sortie de Kramers.

Dans la deuxième partie de la thèse, je présente deux applications de ce modèle. Tout d'abord, j'étudie les mécanismes sous-jacents à la régulation de la dynamique de bursts-interburst par le réseau astrocytaire, en combinant modélisation mathématique, simulations numériques et analyse de données électrophysiologiques de l'activité neuronale. Dans la seconde application, j'étudie l'existence ou la disparition des oscillations cérébrales et leur connexion avec les états hauts (Up states) et bas (Down states) qui émergent dans les réseaux de neurones connectés. Pour cela, je modélise la dynamique de la boucle thalamo-corticale lors de l'anesthésie générale en reliant entre elles plusieurs populations de neurones, chacune représentée par un modèle de champ moyen avec ou sans AHP.

Abstract

In this PhD thesis I model and simulate biological neural networks to better understand the genesis and maintenance of neuronal bursting patterns. Specifically, I develop a new mean field model based on synaptic short-term plasticity which accounts for both bursts and interbursts by adding afterhyperpolarization (AHP), a mechanism induced by various K^+ channels at the neuronal membrane, with slow dynamics that leads to a refractory period after the bursts.

The model is a nonlinear dynamical system of dimension 3 with an additive Gaussian white noise. I characterize the durations of bursts and interbursts by combining the study of the deterministic phase space with asymptotic analysis for the stochastic aspect. The distribution of burst durations (defined by long deterministic trajectories outside the basin of attraction) is determined by characterizing the probability density of the exit points on the separatrix which satisfies the Fokker-Planck equation. To solve this problem, I use WKB approximation and the method of characteristics.

The interbursts are defined as the exit from the basin of attraction induced by noise. As the dynamics around the attractor is very anisotropic, I use a two-dimensional projection of the model to study the interburst. Surprisingly, the probability density in the phase-space of the non exiting trajectories revealed a maximum which is not centered on the deterministic attractor and whose position depends on the noise amplitude, thus describing a shift in the attractor's position in the stochastic case. Finally, the analysis of the escaping trajectories revealed a new exit mechanism from a basin of attraction (specific to dimensions ≥ 2): the trajectories cross the separatrix then enter and exit the basin of attraction a large number of times before escaping to infinity, inducing a significant difference between the time to reach the separatrix for the first time and the time to escape, regardless of the noise amplitude. I characterized and quantified these two new phenomena in the general framework of a simplified two dimensional dynamical system which is topologically equivalent to the original model. This recurrent input / output mechanism explains the existence of longer escape times than what is expected from the classical Kramers exit theory.

In the second part of the thesis, I present two applications of this model. First, I study the mechanisms underlying the regulation of bursts-interbursts dynamics by the astrocyte network, using a combination of mathematical modeling, numerical simulations and analysis of electrophysiological data of neuronal activity. In the second application, I study the existence or disappearance of brain oscillations and their connexion with the Up and Down states that emerge in connected neural networks. To this end, I model the dynamics of the thalamo-cortical loop during general anesthesia by connecting together several populations of neurons, each represented by a mean-field model with or without AHP.

"Did I pass out?"
"Not exactly. You did go into an altered state of consciousness, though.
For a few seconds. Probably an alpha state."

Philip K. Dick, A Scanner Darkly

Contents

Introduction

In this PhD thesis, I develop and study mathematical models of neuronal bursting with a particular focus on the interburst intervals (IBI), in order to better understand the mechanisms underlying their genesis. I concentrate on the mean behavior of a neuronal population that I model with low dimensional, nonlinear dynamical systems driven by a small noise term. In this introduction section I will briefly present the biological background, then give a short overview of the existing types of bursting models, describe the effects of noise in nonlinear dynamical systems and in particular the question of noise induced escape from an attractor. Finally, I will summarize the main results I obtained during my PhD.

0.1 Biological background: burst and interbursts in neuronal networks

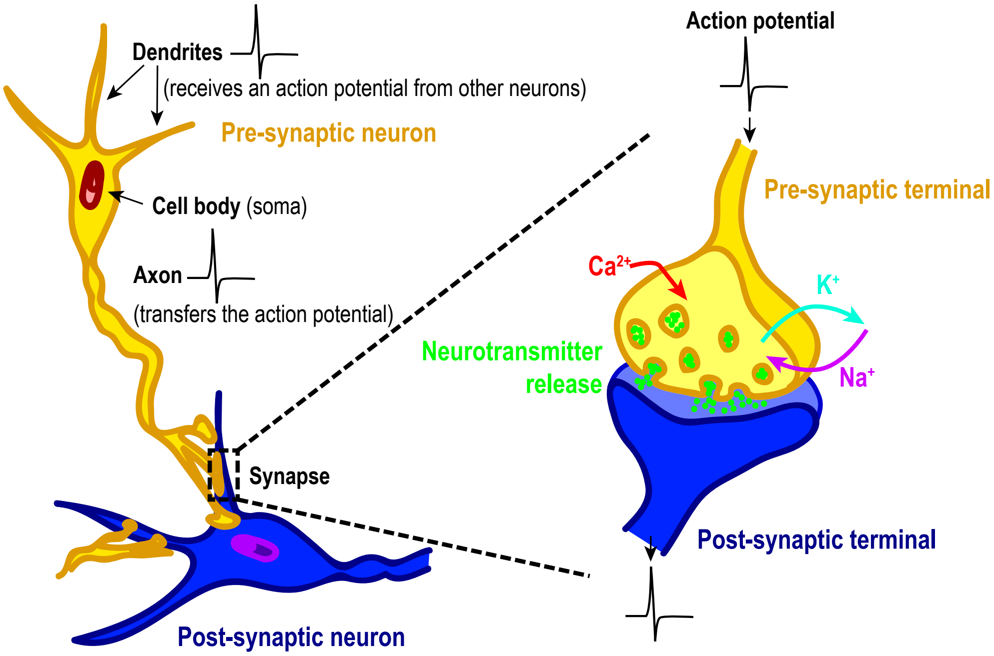

Figure 1: Schematic of two connected neurons (left): the stimulated pre-synaptic neuron (yellow) transfers an action potential to the post-synaptic neuron (blue) through a synapse (inset, right). The action potential (black) triggers the release of neurotransmitters (green) from the pre to the post-synaptic terminals, ions channels on the pre-synaptic membrane allows the release of potassium K^+ (cyan) to the extracellular space while sodium Na^+ (pink) and calcium Ca^{2+} (red) from the extracellular space enter the pre-synaptic terminal.

Neurons are electrically excitable cells. Indeed, the high gradient in the concentrations of extra and intra cellular ions such as potassium (K^+, fig. 1 cyan) and sodium (Na^+, pink) results in a strong difference of potential across their membrane. Neurons communicate together through synapses. Specifically, to transfer a signal, the pre-synaptic neuron (fig. 1 yellow) generates a high intensity electrical pulse called action potential (black). At the synaptic level (fig. 1 inset), this action potential allows ionic channels to open, yielding the release of K^+ in the extracellular space and entrance of Na^+ and Ca^{2+} into the pre-synaptic terminal, which in turn triggers the release of neurotransmitters (fig. 1 green) that are eventually captured by the post-synaptic terminal (blue). I will now describe a specific neuronal activation pattern called bursting and the biological mechanisms involved in its genesis and modulation.

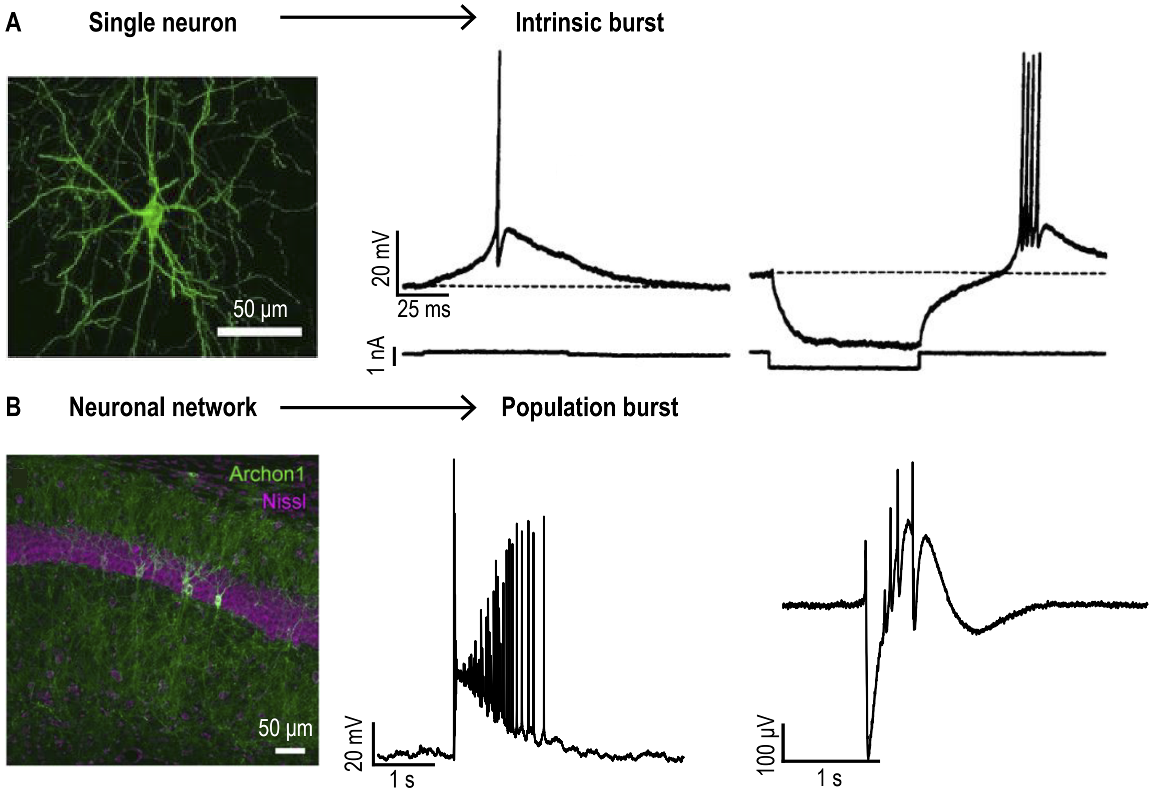

Figure 2: **A.** Intrinsic burst: cortical neuron from confocal fluorescence imaging from [1] (left), intrinsic burst response to a small depolarizing current injection (center) and rebound burst response following hyperpolarizing current injection (right) in thalamic neurons, adapted from [2]. **B.** Network burst: network of hippocampus neurons from confocal fluorescence imaging from [1] (left), network burst from hippocampal pyramidal neurons recorded on a single cell (patch-clamp recording, center) and average response from multi-electrode array (MEA, right).

Bursting Bursting is a neuronal activation pattern where neurons repeatedly fire action potentials at a high frequency (fig. 2), they are followed by, sometimes long, silent phases called interburst intervals (IBI). Bursting plays an important role in neuronal synchronization which is involved in learning and memory [3]. It is also a fundamental feature of Central Pattern Generators such as the respiratory rhythm in the pre-Bötzinger complex [4, 5], mastication, or oscillatory motor neurons [6] which are involved in neuronal rhythm generation. However, bursting can also fall under a pathological behavior such as epilepsy [7].

Two types of bursts can be distinguished, intrinsic bursting occurs at the single cell level (fig. 2A) and combines a depolarizing mechanism with much faster spiking; such cells are called intrinsic bursters and can be found in thalamic [2] or cortical [8] neurons. On the other hand, bursts can also emerge as a network property (fig. 2B) involving excitatory and inhibitory neuronal populations that are not necessarily intrinsic bursters [9, 10]. In this thesis we shall focus on this second type of bursting at the network level. The genesis and maintenance of network bursts relies on synaptic properties [11–13] as well as neuronal membrane depolarization or hyperpolarization, which results from the activation of various ionic channels [2, 14]. Finally, we shall see that astrocytes also play a crucial role in this regulation. We will now briefly define these important biological points.

Synaptic short-term plasticity Short-term synaptic plasticity (STP) is a phenomenon defined by the change over time of the synaptic efficacy as a consequence of the history of the presynaptic activity [15, 16]. The modifications induced by STP are temporary and only last for hundreds to thousands of milliseconds which differentiates it from long term plasticity which is hypothetized as the modification of the neuronal circuitry as a consequence of experience [17]. Two types of complementary STP mechanisms have been observed experimentally:

1. **Short-term depression:** each activation of the pre-synaptic terminal (fig. 3A, yellow) releases a portion of the available vesicles of neurotransmitters (the readily-releasable pool, RRP), when the RRP is depleted faster than it can be refilled, a decreasing post-synaptic (fig. 3A, blue) response over time is observed [18, 19] (fig. 3B, left).
2. **Short-term facilitation:** when a neuron fires an action potential, Ca^{2+} enters in the pre-synaptic terminal increasing the release probability of vesicles of neurotransmitters [20, 21]. In the case of a repetitive stimulation, and thus repetitive firing, the Ca^{2+} accumulates in the pre-synaptic terminal, leading to an increasing response of the post-synaptic terminal over time (fig. 3B center).

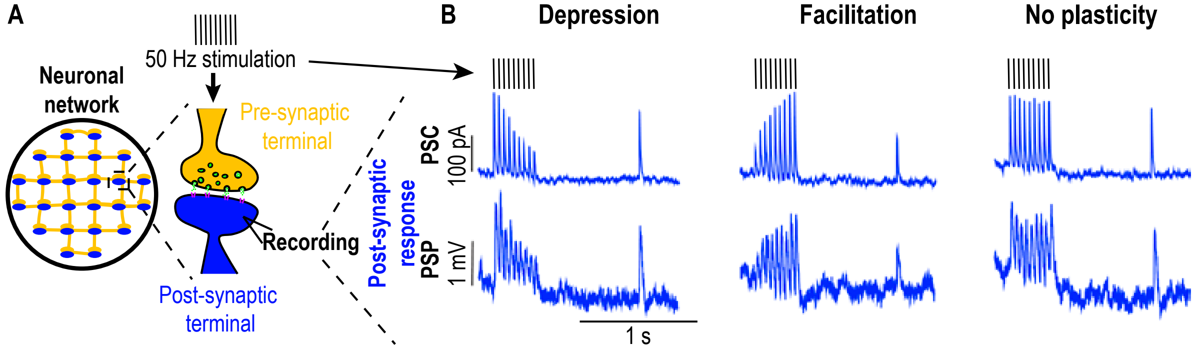

Figure 3: **A.** Schematic representation of a synapse receiving a 50 Hz train of spikes at the presynaptic terminal (yellow) and patch recording of the response at the postsynaptic terminal (blue). **B.** Postsynaptic responses (current PSC, upper and potential PSP, lower) to a 50Hz train of presynaptic spikes for depressing (left), facilitating (center) and without plasticity (right) synapses. Adapted from [22].

Neuronal networks, synchronization and emergence of oscillatory rhythms At the population level ($\approx 100 \mu m$), neurons are connected together through thousands of synapses: 7000 synapses per cortical neuron on average [23]. These connections lead to the emergence of specific network-dependent activation patterns. For instance, several coupled pacemaker neurons receiving an excitatory input from tonic firing neurons can either lead to bursting, tonic spiking or resting depending on the values of the channel conductances and the neuronal coupling level [24–26]. Similarly, the emergence of Up (depolarized with high frequency firing) and Down states (small fluctuations around resting membrane potential) reflects this population level activity [27] and also involves longer connections between different brain regions [28, 29]. These large-scale connections between excitatory and inhibitory populations are thought to be at the origin of neuronal brain waves that can be observed in electroencephalogram (EEG, fig. 4A) such as the α-waves (8-12 Hz, fig. 4B) during general anesthesia [30, 31] which involves interactions between the thalamus and the cortex, or the θ-waves (4-8 Hz) in the hippocampus and cortical regions, which are characteristic of REM sleep [32, 33]. Finally, fast γ-oscillations (20-100Hz, fig. 4B) in the cortex are involved in memory formation and sensory processing [34, 35]. It has been observed that γ-oscillations can be generated without the need for each individual neuron to fire at the γ frequency; this phenomenon is called weak γ and suggests a complex network organization involving clusters of synchronous cells that can be studied using mathematical models [36, 37] highlighting the importance of collaborative network organization in neuronal activation patterns.

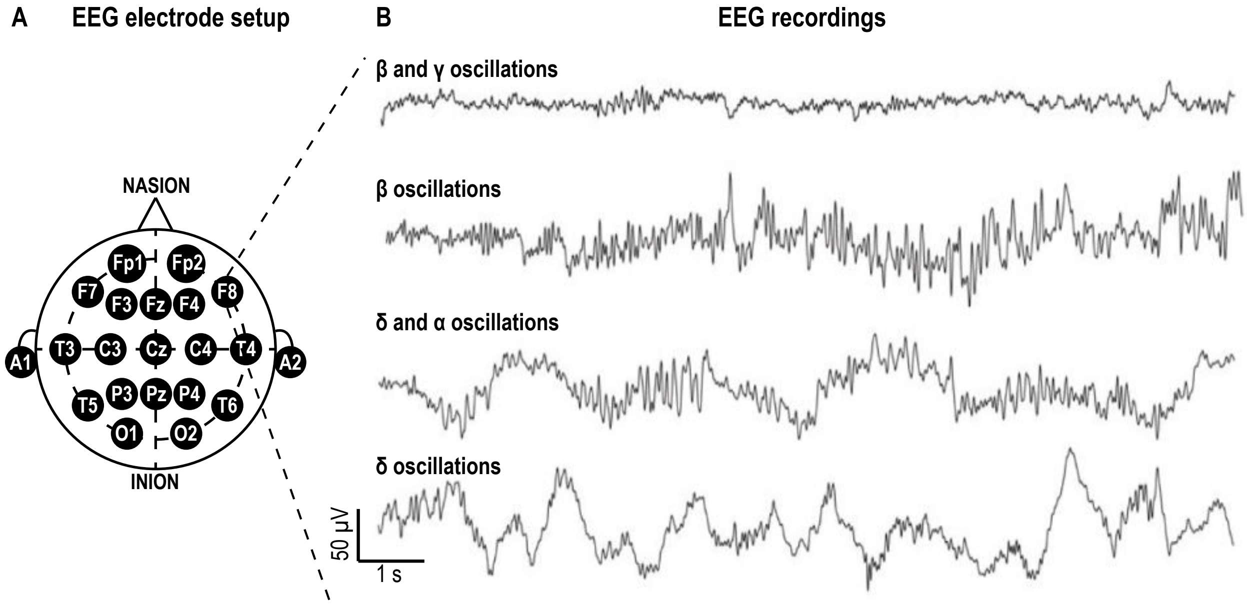

Figure 4: **A.** Schematic of the electrode setup on a patient's head for EEG recording. **B.** Typically observed oscillatory rhythms in EEG during wake (fast γ (20-100Hz) and β (12-20Hz) oscillations, upper traces) and anesthesia (slow δ (0-4Hz) and α (8-12Hz) oscillations, lower traces) adapted from [30].

Afterhyperpolarization In hippocampal pyramidal neurons, the IBI is modulated by the activation of various types of K^+ and Ca^{2+} channels with medium to slow dynamics [14, 38–40]. The activation of these ionic channels, towards the end of a burst leads to medium and slow hyperpolarizing currents taking the cells voltage below their resting membrane potential (fig. 5), a phenomenon known as afterhyperpolarization (AHP). The AHP induces a refractory period during which the cells cannot fire action potentials or initiate a burst. Thus, this mechanism is of fundamental importance in the determination of IBI durations.

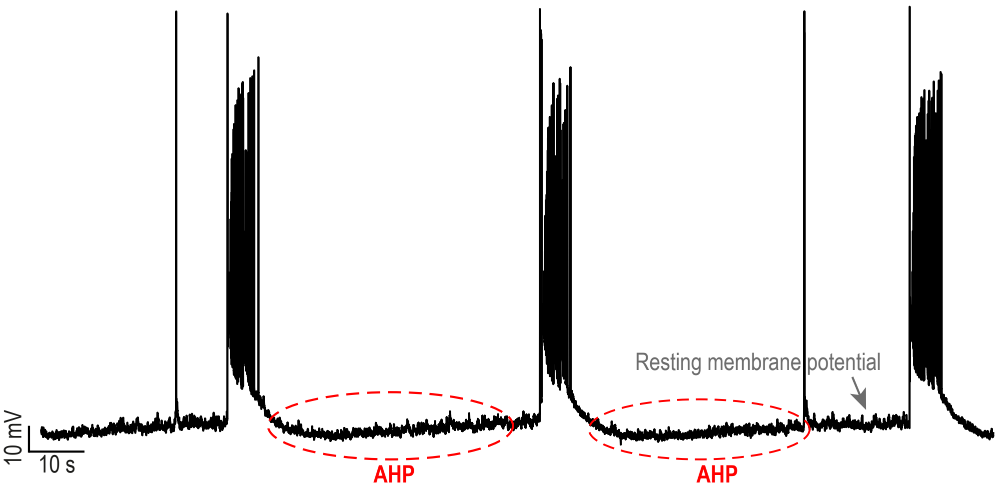

Figure 5: Single cell electrophysiological patch-clamp recording showing afterhyperpolarization (AHP) after the bursts.

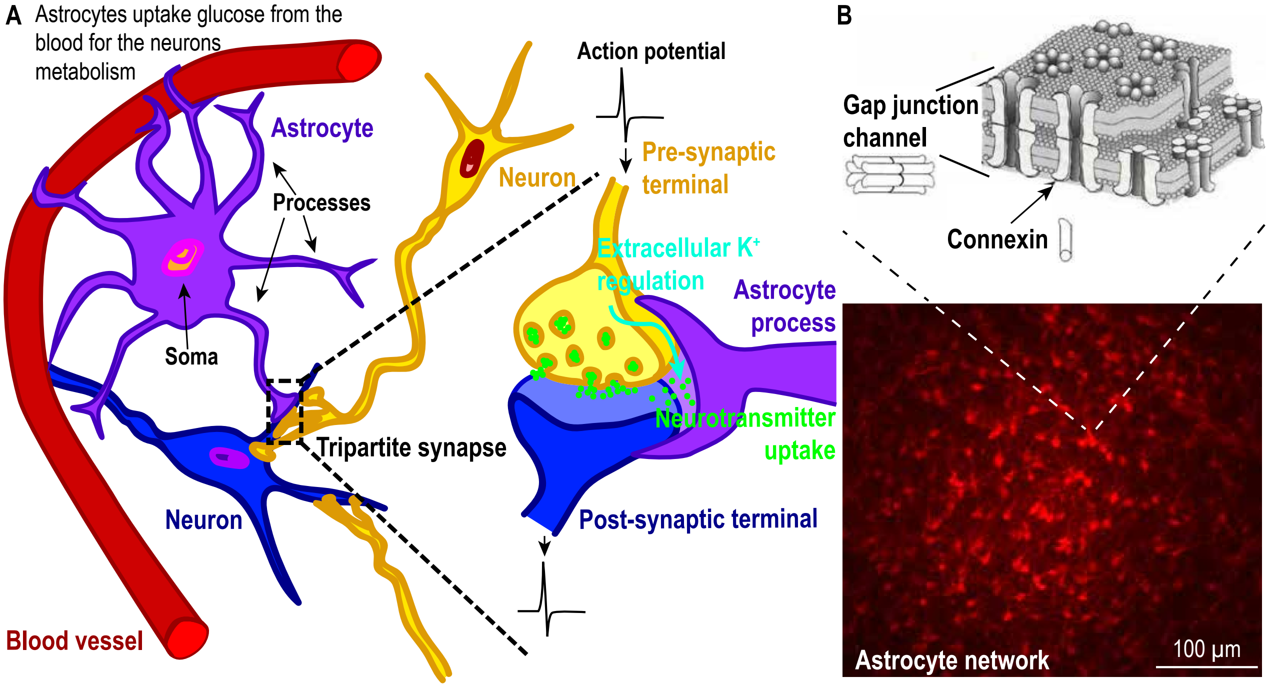

Figure 6: **A.** Astrocytes interact with neurons and the surrounding blood vessels to uptake glucose to "feed" the neurons. Inset: the tripartite synapse, astrocytes buffer neurotransmitters and extracellular K^+ at the synaptic cleft. **B.** Astrocytes are connected in a network (lower) through gap junction channels made of connexins (upper), image courtesy N. Rouach [private communication].

Astrocytes Glial cells gather all the non neuronal cells in the brain and central nervous system. Among them, astrocytes represent 20 to 40 % of all glia [41] and are also the most numerous cell type in the brain [42]. The role of glia and astrocytes has long been underestimated confining them to the simplistic role of glue (hence their name) holding things together in the brain. However, the past decades have marked a major change of perspective regarding the importance and diversity of astrocytes functions in the brain activity [43, 44]. Indeed, it is now known that astrocytes play a key role in brain information processing. At the the single cell level, they can modulate neuronal excitability, synaptic transmission and plasticity via several mechanisms including ions and neurotransmitters uptake, gliotransmitters release and physical coverage of synapses [45, 46], a concept known as the tripartite synapse (fig. 6A). Astrocytes are also organized together in networks via gap junction channels (fig. 6B) which are formed by two main proteins called connexin (Cx43 and Cx30) [47]. This network organization of astrocytes allows long-range exchanges of various ions through their intracellular network [48, 49] thus allowing them to redistribute energy metabolites to neurons (through the so called astrocyte-neuron lactate shuttle), control and buffer the concentration of extracellular ions (such as the K^+ that is released by neuronal firing) and neurotransmitters (mainly Glutamate and GABA). Note that K^+ fluxes are difficult to track experimentally but modeling can provide critical insights on their regulation [50,51]. Through the aforementioned regulation mechanisms (metabolism, extracellular K^+ uptake and neurotransmitter buffering), astrocytic networks modulate neuronal excitability and network synchronization. Specifically, they control population activity by promoting sustained coordinated neuronal bursts [52–54]. In this thesis I will study further the underlying mechanisms involved in the regulation of neuronal bursting by astrocytes using a modeling approach (see chapter 4).

0.2 Modeling population bursting

Models of electrical excitability In 1907 Louis Lapique proposed a first model of neuronal electrical excitability, the integrate and fire (IF) neuron [55], which models the neuronal membrane potential based on its capacitance. The more commonly used leaky integrate and fire (LIF) neuron adds a leak current to account for the membrane permeability to different ions. In this model, when the voltage reaches a certain threshold a spike is generated, but the shape of the spike itself is not modeled; rather this model is used to study the spiking frequency and interspike intervals. Through its mathematical simplicity and small number of parameters it allows analytical computations and extensive study of its parameter space [56]. For example, it is possible to compute the probability distribution of output spikes as a function of the presynaptic inputs and to use these results to study the synchronization of several LIF neurons [57]. Despite its simplicity this model is relevant to study neuronal activation patterns; for example adding hyperpolarizing currents to the voltage equation can modulate the interspike intervals subject to the same presynaptic inputs leading to comparable adaptation patterns as those observed in vivo from pyramidal cells in the cat visual cortex [58]. Network bursting or oscillatory behaviors in neuronal populations can also be obtained by coupling together many LIF neurons [59,60]. The exponential adaptative IF (aEIF) [61], extends the LIF through the addition of an exponential term in the voltage equation to account for the explosion of the voltage value at the moment of the spike (even though the shape of the spike itself is still not modeled) and of a second variable representing the adaptation in the spiking frequency over repetitive stimulation. The advantage of this model is the easy biological interpretation of the parameters which can be estimated using simple patch clamp experiments [61]. Furthermore, a bifurcation analysis of the aEIF model allows to reproduce different spiking dynamics such as tonic, chaotic or phasic spiking and bursting [62]. More recently the aEIF model has been used to reproduce the bistability between Up and Down state firing patterns of cerebellar Purkinje cells [63].

Another pioneering model of neuronal electrical excitability was introduced by Hodgkin and Huxley (HH) in 1952 [67]. By modeling the flow of ionic currents across the neuronal membrane and accounting for the membrane permeability by dynamically modeling the conductance of each ionic channel, the model computes the evolution of the membrane potential. Coupling HH neurons together can be used to model network bursting or induce fast oscillations [68]. More recently, adding noise to a network of

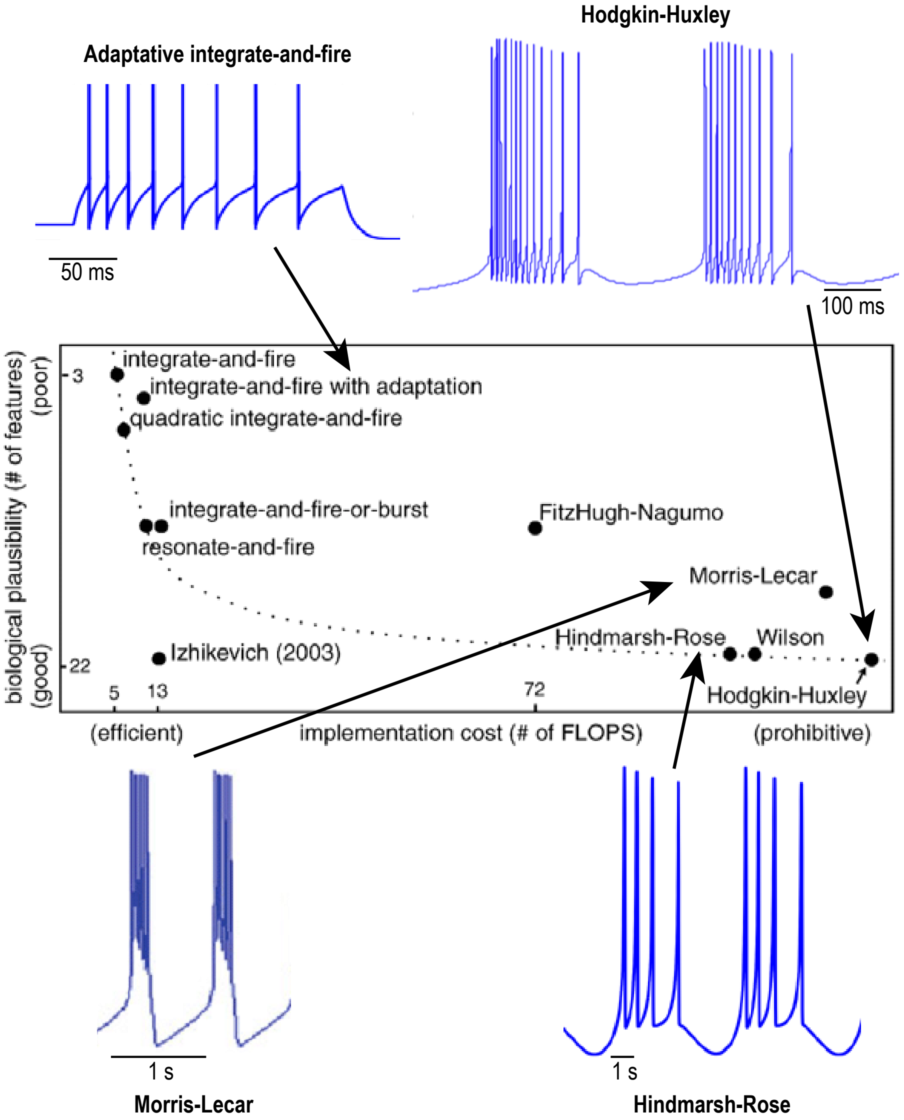

Figure 7: Comparison of the neuronal models (biological plausibility vs computational cost) from [64] with example of simulated burst with the adaptative integrate-and-fire (upper left), Hodgkin-Huxley (upper right, from [65]), Morris-Lecar (lower left from [66]) and Hindmarsh-Rose (lower right) models.

coupled HH models was used to study the effect of desynchronisation [69]. Such models have also been used to study the emergence of spindle oscillations [70, 71] and the addition of synaptic currents such as GABA can lead to the apparition of α-oscillations [72, 73]. However modeling network properties with such models can quickly become computationally expensive due to the high dimensionality and number of parameters (fig. 7).

A lower dimensional neuronal firing model was introduced in 1961 by FitzHugh [74] and the following year by Nagumo [75]. In the FitzHugh-Nagumo model, each time the external input reaches a certain threshold, the dynamics describes a characteristic excursion in the two-dimensional phase-space. This excursion defines the spike before the voltage goes back to resting state. This model is also very commonly used to describe bursting. For example, two coupled FitzHugh-Nagumo systems with different timescales can lead to the generation of mixed-mode oscillations (MMOs) consisting of the combination between local dynamics near a fold bifurcation, defining the small oscillations, and the existence of an attracting limit cycle for the large ones [76]. A piece-wise linear approximation of the FitzHugh-Nagumo system allows to analytically characterize the bistability regime between the stationary and oscillatory solutions [77]. Similarly, Morris and Lecar developed in 1981 a conductance based model initially to represent oscillatory behavior in muscle fibers [78] but which is also considered as a simpler version of the HH model and is widely used in computational neuroscience. For the Morris-Lecar model, a similar piece-wise approximation [77] reveals a transition from stationary state to oscillations with logarithmic dependence which makes it comparable to the LIF model.

Slow-fast systems and canards explosions Bursting can be decomposed into a fast subsystem (the rapid spiking) and a slow subsystem (transient depolarization). Canonical models of slow-fast systems have been developed by Ermentrout and Kopell [79] where the membrane potential is still described as a conductance based model. A classical reduction of these models is the theta model. This framework has been used to study periodic and chaotic bursting patterns [80] as well as burst synchronization in coupled neurons [81].

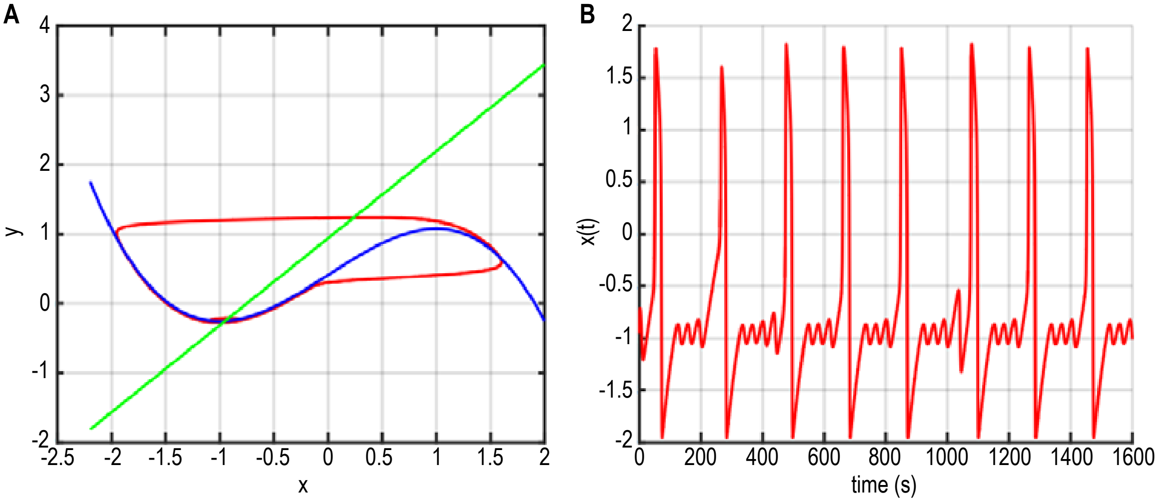

Figure 8: **A.** Phase portrait of a canard solution of a FitzHugh-Nagumo type model with canard trajectory (red) alternatively following the fast and slow parts of the cubic nullcline (blue). **B.** Time-series of the canard solution showing MMOs, from [82].

The Hindmarsh-Rose model [83] implements such strategy with three variables: one for the membrane potential, one for the fast ion channels (fast subsystem) and one for the slow ion channels (slow subsystem). Following this model, different type of bursters have been developed, such as low frequency spiking at the beginning and the end of a burst [84] or parabolic burstsers, which exhibit fast-oscillations frequencies that vary along with the burst slow modulation [79]. The Hindmarsh-Rose model was used to study the importance of delays in synchronization of coupled bursting neurons [85]. A detailed bifurcation analysis coupled with a slow-fast study of the Hindmarsh-Rose model revealed that the routes leading to different bursting patterns depend on the relative location of the fixed points of the system with respect to a homoclinic bifurcation of the fast subsystem [86]. A follow up of this study also showed that tonic spiking and plateau bursting are connected together through branches of the unstable periodic orbits of the Hindmarsh-Rose model [87, 88]. Slow-fast analysis on a conductance based model with K^+ and Ca^{2+} channels with either one fast and two slow variables, or two fast and one slow, revealed a path from pseudo-plateau bursting to MMOs by varying a single model parameter [89]. Finally, such systems are usually treated by considering the slow variables as parameters of the fast subsystem but more recent studies suggest to focus on the slow subsystem and have shown that these two approaches become identical in the limit of both infinitely fast and slow subsystems [90]. In this framework, the classical canard phenomenon describes a very fast transition from a small amplitude limit cycle to a relaxation cycle of larger amplitude (fig. 8A). This phenomenon occurs upon small variations of a control parameter. It was first described in 1981 by the French mathematician Benoit [91]. More recently, the study of synchronization of canard properties revealed synchronization regimes for canards that differ from the classical relaxation cycles [92]. This type of fast transition between different amplitude cycles (ie oscillations in the time domain) can be generalized to describe MMOs (fig. 8B) and even mixed-mode bursting oscillations [93].

Classification of the deterministic burst types according to the corresponding bifurcation All the deterministic bursting patterns cited in the previous paragraphs can be classified according to the type of bifurcation that generates the burst. This involves a bifurcation from a stable point to a limit cycle, that will generate the oscillations, and vice-versa for the burst termination. Specifically, there are four different types of possible bifurcations of co-dimension one for the equilibrium: saddle-node (fold), saddle-node on invariant cycle, supercritical Andronov-Hopf and subcritical Andronov-Hopf; and, in the case of a two-dimensional fast-subsystem, four bifurcations for the limit cycle: saddle-node on invariant cycle, saddle homoclinic orbit, supercritical Andronov-Hopf and fold limit cycle, resulting in 16 possible combinations. This type of classification was first suggested by Rinzel [84] and fully described by Izhikevich [10, 94, 95] (see also Golubitsky [96, 97] for higher co-dimensions). Finally the complexity of the bursts can be evaluated by the co-dimension of their bifurcation (see for example [98] for the case of fold bifurcations inducing pseudo plateau bursting).

Modeling the firing rate probability Bursts can also be modeled by their firing rate probability. This was first introduced by the Wilson-Cowan oscillator [99, 100] which models two reciprocally connected excitatory and inhibitory populations by their respective firing rates. Similar firing rate models have been used to model the visual cortex and reproduce preferred orientation responses [101]. Finally, adding delays into coupled firing rate models has been used to generate a wide range of different activation patterns in neuronal networks [68].

Mean-field models of bursting based on synaptic STP Modeling bursting in mean-field models can be achieved by accounting for the molecular mechanisms at the synaptic level on which bursting depends. A first model based on synaptic short term depression was developed by Tsodyks and Markram in 1997 [102] and was later expanded to account for facilitation [103]. Another example of model based on synaptic short term plasticity was derived at the same period in [104] for the visual cortex and introduced a combination of facilitation and several depressions with different recovery timescales.

The original Tsodyks-Markram model describes the biophysical mechanism of synaptic depression, which results from vesicle depletion. Its equations account for the evolution of the fraction of available resources that are split into three states: E for the effective resources, I for the inactive ones and R for the recovered. The equations read

$$\begin{aligned} \frac{dR}{dt} &= \frac{I}{\tau_{rec}} - U_{SE} R \delta(t - t_{AP}) \\ \frac{dE}{dt} &= \frac{E}{\tau_{inact}} + U_{SE} R \delta(t - t_{AP}) \\ I &= 1 - R - E, \end{aligned} \tag{1}$$

where τ_{rec} and τ_{inact} are the time rates for recovery and inactivation respectively and U_{SE} reflects the fraction of used resources at each action potential occurring at time t_{AP}. This model was later simplified to represent the mean-field firing rate and synaptic depression to which noise was added to replicate Up and Down states in cortical neurons [105]. The equations become

$$\begin{aligned} \tau \dot{V} &= -V + \mu U w_T \alpha (V-T)^+ + \sqrt{\tau}\sigma\dot{\omega} \\ \dot{\mu} &= \frac{1-\mu}{t_r} - U\mu\alpha(V-T)^+, \end{aligned} \tag{2}$$

where V is the average synaptic input (in mV), $(V-T)^+ = max(V-T, 0)$ the mean firing rate, $\alpha = 1Hz/mV$ a conversion factor, w_T the average synaptic strength, U the vesicle utilization parameter and t_r the recovery time constant of the synaptic depression. Finally, $\dot{\omega}$ is a Gaussian white noise and σ its amplitude. Using this model, the authors could reproduce for the first time Up and Down states dynamics as a consequence of STP driven by noise.

The phase-space associated with the two-dimensional dynamical system (2) consists of two attractor points, one of which is inside an unstable limit cycle. The distribution of exit times of the stochastic trajectories starting at the attractor and exiting the basin of attraction is solution of the Fokker-Planck equation (FPE) and can be expanded in eigenfunctions, solution of the adjoint operator. An asymptotic solution is obtained using WKB analysis. This analysis reveals that, at least, the first two eigenvalues are necessary to describe the multiple peaks in the distribution of exit times present both in simulations and experimental data. Interestingly, the spectrum is obtained by solving a Riccati equation in a boundary layer of the limit cycle [106–108]. However, the method used to derive these results fundamentally depends on dimension two and thus, cannot be extended to the case of the three-dimensional model [109]. We introduce now the three dimensional model composed of three variables: the mean voltage h, the facilitation x and the depression y

$$\begin{aligned} \tau \dot{h} &= -h + Jxyh^+ + \sqrt{\tau}\sigma\dot{\omega} \\ \dot{x} &= \frac{X-x}{t_f} + K(1-x)h^+ \\ \dot{y} &= \frac{1-y}{t_r} - Lxyh^+, \end{aligned} \tag{3}$$

where $h^+ = max(h, 0)$ is a linear threshold function of the synaptic current which defines the firing rate. The combined effect of synaptic short-term facilitation and depression on the mean voltage is described by the term Jxy where the parameter J represents the network connectivity (mean number of synapses per neuron) [110]. The second equation describes facilitation, and the third one, depression. The parameters K and L describe how the firing rate is transformed into molecular events modulating the duration and probability of vesicular release respectively. The time scales t_f and t_r define the recovery of a synapse from the network activity. Finally, $\dot{\omega}$ is an additive Gaussian noise and σ its amplitude, it represents fluctuations in the synaptic current (synaptic noise).

Recently, the emergence of Up and Down states in the Tsodyks-Markram facilitation-depression model was associated to a chaotic behavior, called Shilnikov chaos, near an unstable manifold that modifies the shape of trajectories inducing a high sensitivity to the initial condition [111]. We shall see in chapter 5 of this thesis that the bifurcation induced by increasing the network connectivity parameter J in model (3) can also lead to the emergence of Up and Down states due to bistability without the need for a chaotic behavior.

Finally, a double depression model, decomposing the vesicles into ready and recovering pools was also proposed to account for long recovery periods of the synapses [112].

Noisy dynamical systems Noisy nonlinear dynamical systems can exhibit peculiar behaviors where the presence of noise leads to more than fluctuations around the expected deterministic dynamics. For example, noise can induce large fluctuations away from a stable attractor [113–115] or enhance the response to periodic external stimuli, a phenomenon known as stochastic resonance [116]. An opposite behavior, called inverse stochastic resonance consists in inhibiting an otherwise active system (e.g. silencing spontaneously spiking neurons) by the addition of noise of a specific variance [63]. Noise can also sustain oscillations that would be damped in the deterministic case [117], induce a shift in bifurcation values [118] or stabilize an otherwise unstable equilibrium [119–121].

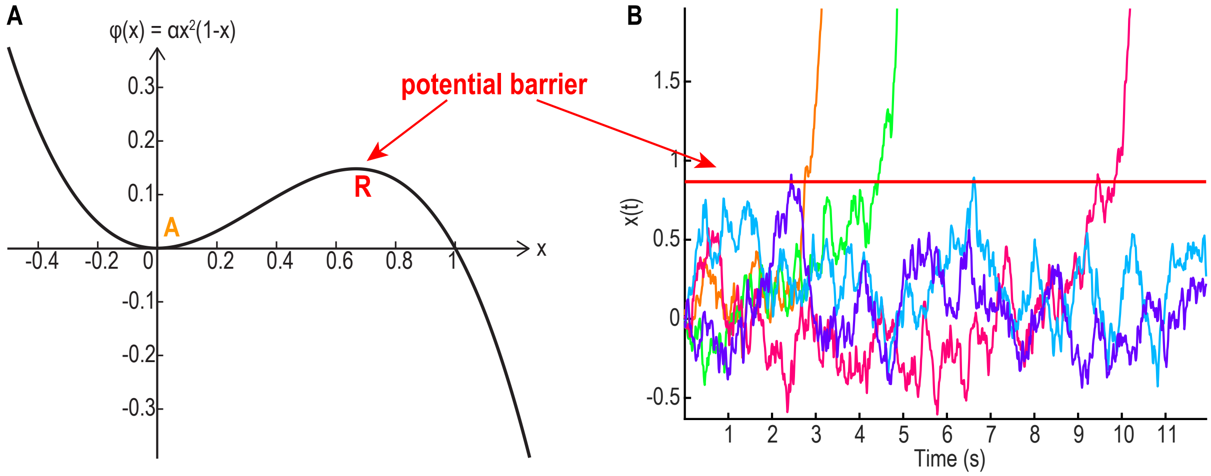

Figure 9: **A.** Potential well defined by the function $\psi(x) = \alpha x^2(1-x)$ with one stable attractor A (yellow) and a repulsive equilibrium R (red) which defines the barrier of potential to cross to escape. **B.** Trajectories $x(t)$ satisfying $\dot{x} = -\dfrac{d\psi(x)}{dx} + \sigma\dot{\omega}$ where $\dot{\omega}$ is a Gaussian white noise and σ its amplitude. The presence of noise can induce escape from the basin of attraction of A when the trajectories reach the boundary of the basin of attraction (red line).

Noise activated escape from an attractor (fig. 9A-B) as described in Kramers theory [122–125] is a problem that has driven considerable attention over the years. Indeed, this problem has applications in domains as diverse as chemistry, for example to accelerate chemical reaction simulations [126] or provide insight on the backward binding rate [114,127], communication theory for the loss-of-lock of phase controllers [128], finance, to compute future derivatives in the financial market [129] polymer physics [130] or even better characterizing the search for a small target in a complex environment [131, 132]. Although it had long been thought to depend only on the topology of the noiseless dynamics [133], in some cases, the stochastic dynamics deviate from the deterministic theory. For instance, in dimensions ≥ 2, the distribution of exit points peaks at a distance $O(\sqrt{\sigma})$ from the saddle-point (where σ is the noise amplitude), whereas, in the deterministic theory it is expected to be centered at the point that minimizes the vector field, ie the saddle-point itself [123, 134]. Similarly, when a focus attractor falls into the boundary layer of the basin of attraction, escaping trajectories exhibit periodic oscillations leading to an escape time distribution which is not exponential [106, 108, 135–138], indeed in this case several eigenvalues are necessary to describe the distribution. In the limit of small noise, the escape rate and the distribution of exit points can be computed by solving the Fokker-Planck equation (FPE) satisfied by the stochastic process. This can be achieved using WKB approximation and the method of characteristics [123, 125, 128, 139] or using spectral decomposition [140, 141].

0.3 Main results of the thesis

Part I: Modeling and computation of burst and interburst durations

Result *section 1.1* Development of a facilitation-depression model accounting for AHP Bursting models usually pay little attention to the IBI although it plays a crucial role in the definition of oscillatory brain rhythms or switches between Up and Down sates. In this thesis, I extended the facilitation-depression model (3) [109] to account for AHP by introducing two features: 1) a new equilibrium state representing hyperpolarization and 2) two timescales (medium and slow) to describe the slow recovery to the steady state due to the effect of the slow K^+ channels that take over the dynamics after the burst phase. The new model equations are

$$\begin{aligned}
\tau_0 \dot{h} &= -(h - T_0) + Jxy(h - T_0)^+ + \sqrt{\tau_0}\sigma\dot{\omega} \\
\dot{x} &= \frac{X - x}{\tau_f} + K(1 - x)(h - T_0)^+ \\
\dot{y} &= \frac{1 - y}{\tau_r} - Lxy(h - T_0)^+.
\end{aligned} \tag{4}$$

Where the parameters τ_0 and T_0 are defined piece-wise, according to our decomposition of the burst into four phases (fig. 10A):

- **step 1: Burst (fig. 10A, blue).** It is defined for $\{y > Y_{AHP}$ and $h \geq H_{AHP}$ or $\dot{y} \leq 0\}$ (fig. 10B, above the purple and orange surfaces). During this phase, the time constant τ_0 of h is fixed to $\tau_0 = \tau$ and the resting value of h is $T_0 = T$ (see Table 1.1 page 44 for the parameters values).
- **Step 2: Hyperpolarization (fig. 10A, orange).** This phase is initiated when the depression variable y starts to increase after the burst $\left(\dot{y} > 0 \iff y < \dfrac{1}{1 + Lx(h - T_0)}\right)$, and lasts as long as $y < Y_h$ (fig. 10B, below the orange surface). During this phase the parameters are $\tau_0 = \tau_{mAHP}$ and $T_0 = T_{AHP} < T$ thus forcing the voltage to hyperpolarize.
- **Step 3: Slow recovery period (fig. 10A-B, purple).** During this phase, the depression y is still increasing ($\dot{y} > 0$), with the condition that $\{Y_{AHP} < y$ or $h < H_{AHP}\}$, the time constant is $\tau_0 = \tau_{sAHP}$ and the resting value of h is set to its initial value $T_0 = T$ thus accounting for the slow recovery to the resting membrane potential.
- **Step 4: Quiescent phase (QP, fig. 10A-B, green).** This phase models the fluctuations of the voltage around the steady state due to the synaptic noise. The conditions and parameters are the same as for step 1 ($\{y > Y_{AHP}$ and $h \geq H_{AHP}$ or $\dot{y} \leq 0\}$, $\tau_0 = \tau$ and $T_0 = T$).

This new model, driven by noise reproduces spontaneous bursts followed by long AHP refractory periods (fig. 10C).

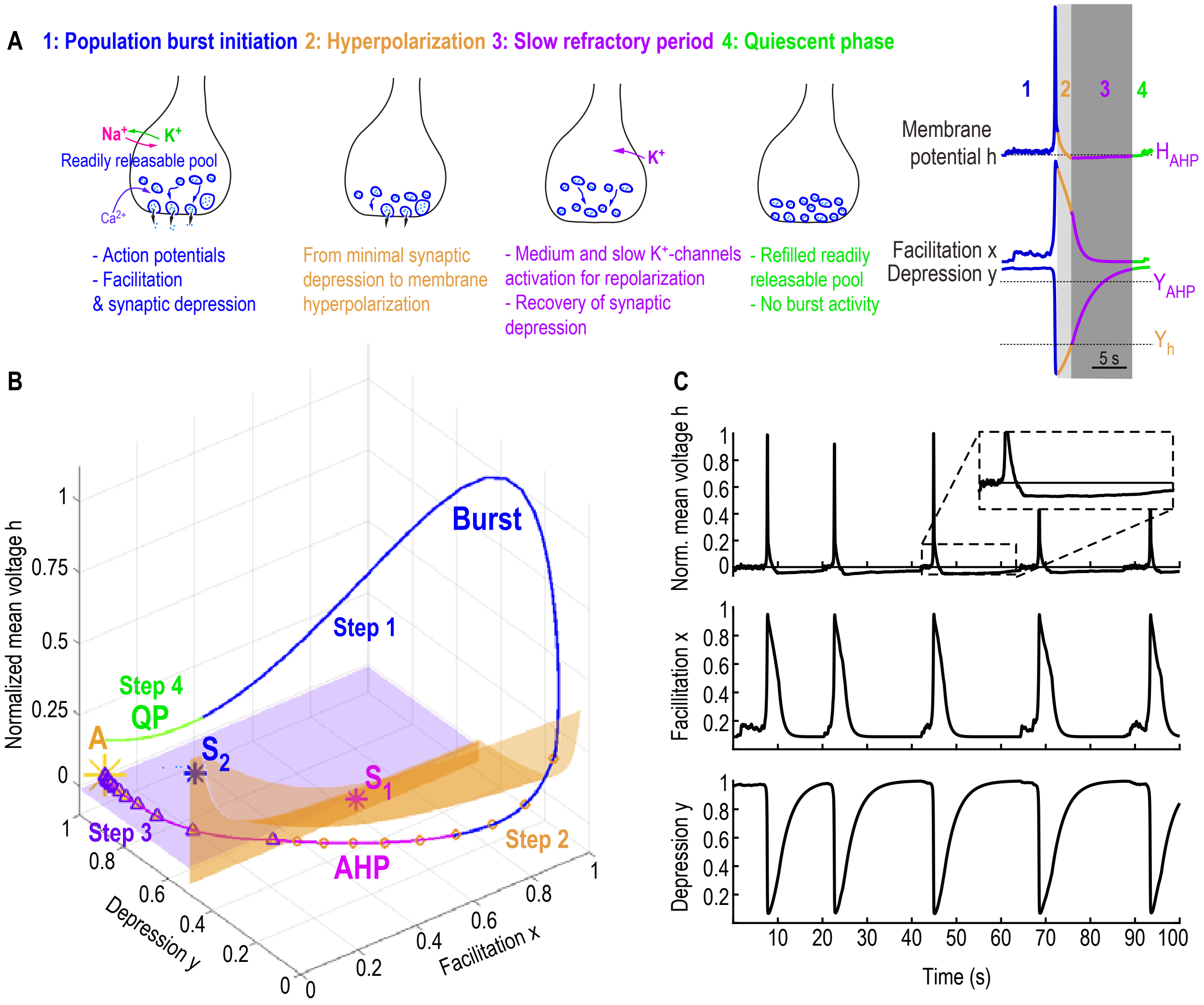

Figure 10: **A.** Schematic of the four phases of a burst as stated in the decomposition of model (4) with the h, x and y time-series of a complete burst (right). **B.** Phase-space of model (4) with a complete deterministic burst trajectory decomposed according to the four phases described in **A**. **C.** Stochastic time-series of h, x and y exhibiting spontaneous bursts followed by AHP periods (inset).

Mathematical description of the phase-space of the facilitation-depression model accounting for AHP In this paragraph I briefly describe the deterministic phase-space of system (4) (see section 1.1.2 page 44 for the detailed description). It has three critical points: one attractor A (stable-node) with three real negative eigenvalues (fig. 11 yellow), and two saddle-points. The first saddle-point S_1 (fig. 11 magenta) is a saddle with repulsive focus, ie it has one real negative eigenvalue and two complex-conjugate eigenvalues with positive real part. The second saddle S_2 (fig. 11 blue), closer to A is a saddle-node with an unstable manifold of dimension 1 and a stable manifold Γ (fig. 11 cyan) of dimension 2 which defines the boundary of the basin of attraction of A. Note that since there is only one attractor in the phase-space, all deterministic trajectories will finally return to A, however I separated the trajectories going directly back to A thus defining the "basin of attraction" of A (below Γ) from the trajectories doing a long excursion in the phase-space (trajectories starting above Γ, fig. 11 the long red trajectory is the unstable manifold of S_2, see also the trajectory in fig. 10B) which defines the burst.

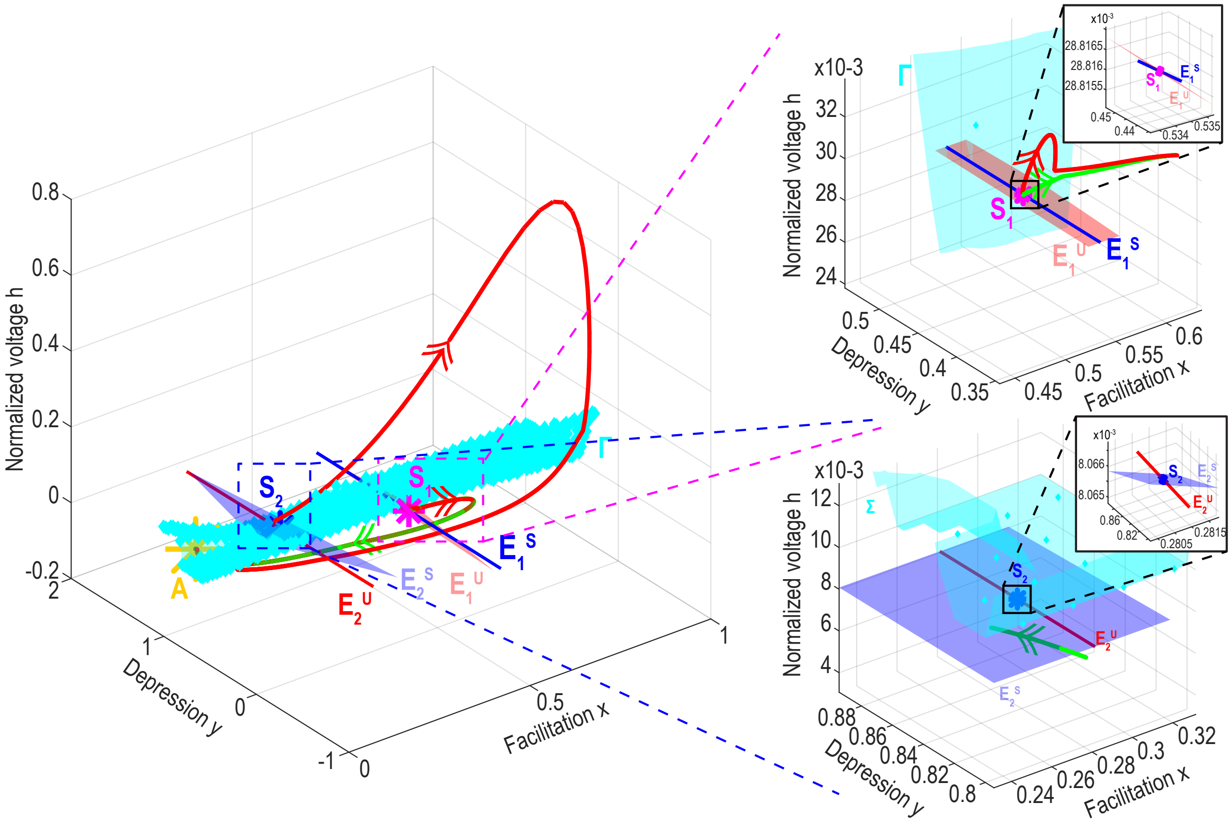

Figure 11: 3D deterministic phase-space of model (4) with insets around the two saddle-points S_1 (magenta) and S_2 (blue). The separatrix Γ (cyan surface) delimiting the basin of attraction of A (yellow) is the 2D stable manifold of S_2.

Result *(section 1.2)* A slow-fast approximation allows to obtain analytical formulas for the deterministic burst and AHP durations In this section I summarize the slow-fast decomposition of the deterministic (ie with $\sigma = 0$) model (4) that I used to compute analytical formulas for the burst and AHP durations (see section 1.2 page 56 for the detailed calculations). The goal is to understand the parameter dependency of the deterministic component of the burst and AHP phases.

Since, in the first phases of the burst, the voltage variable h is much faster than the facilitation x and depression y variables ($\tau = 0.05 \ll \tau_f = 0.9 \ll \tau_r = 2.9$s), and then, during the AHP phase it is much slower ($\tau = 10.5 \gg \tau_r = 2.9 \gg \tau_f = 0.9$s) I could decompose the system into a slow subsystem and a fast subsystem in order to linearize and integrate it. To do so, I approximated the voltage variable by a step function (fig. 12) that I injected into the x and y equations:

$$H(t) = \begin{cases} H_1, & \text{for } t \in [0, t_1] \\ H_2, & \text{for } t \in]t_1, t_2] \\ 0 & \text{for } t > t_2, \end{cases} \tag{5}$$

yielding the simplified system

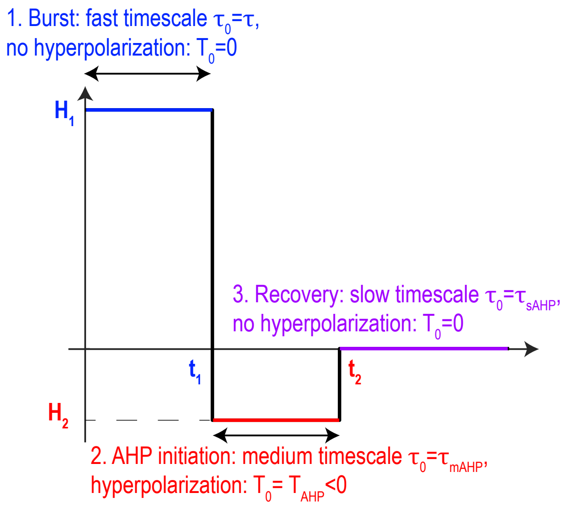

Figure 12: Step function $H(t)$

$$\begin{aligned} \tau_0\dot{h} &= -(h-T_0(t)) + Jxy(h-T_0(t))^+ \\ \dot{x} &= \frac{X-x}{\tau_f} + K(1-x)H(t) \\ \dot{y} &= \frac{1-y}{\tau_r} - LxyH(t), \end{aligned} \tag{6}$$

where I account for AHP by changing T_0 and τ_0 as follows

$$T_0(t) = \begin{cases} 0 & \text{for } t \in [0,t_1] \\ T_{AHP} & \text{for } t \in]t_1,t_2] \\ 0 & \text{for } t > t_2 \end{cases} \quad \text{and} \quad \tau_0(t) = \begin{cases} \tau & \text{for } t \in [0,t_1] \\ \tau_{mAHP} & \text{for } t \in]t_1,t_2] \\ \tau_{sAHP} & \text{for } t > t_2. \end{cases} \tag{7}$$

I then integrated system (6) piece-wise on the three time segments $[0,t_1]$, $]t_1,t_2]$ and $]t_2,\infty[$ and obtained analytical formulas for the x and y variables. Then, to integrate the h variable, the present method differs from the classical slow-fast analysis in the sense that instead of now approximating the slow variables x and y by constant values in the differential equation of h, I injected the integrated formulas obtained from the first piece-wise integration. Finally, I used the analytical formulas of the three variables h, x and y, to find the following analytical formulas for the burst and AHP durations, entailing the following proposition:

Proposition 1.1 Analytical formulas for the burst t_i and AHP durations $\Delta_{AHP} = t_e - t_i$. *For the three-dimensional dynamical system defined by equation* (6)*, if the parameters* $\tau_0 \ll \tau_f, \tau_0 \ll \tau_r$ *or* $\tau_f \gg \tau_0, \tau_0 \gg \tau_r$ *then:*

(i) System (6) *can be integrated piece-wise yielding analytical formulas for the three variables* h *(equations 1.58-1.65-1.68),* x *(equations 1.51-1.59-1.66) and* y *(equations 1.55-1.61-1.67),*

(ii) The burst duration t_i *is defined by the equation* $h(t_i) = 0$*, which can be inverted analytically, yielding the expression*

$$t_i \approx t_1(J) + \frac{-\Lambda - \sqrt{\Lambda^2 + 4\tilde{\Lambda}\frac{\tau_{mAHP}}{J}\ln\left(\frac{-T_{AHP}}{h_0 - T_{AHP}}\right)}}{2\tilde{\Lambda}}, \tag{8}$$

where $t_1(J)$, $\Lambda = \Lambda(J, K, L, H_2, t_1(J))$ *and* $\tilde{\Lambda} = \tilde{\Lambda}(K, L, H_2, t_1(J))$ *are smooth explicit functions of the parameters* J, K, L *and* H_2 *of system* (6) *calculated in section 1.2 pages 63 and 65.*

(iii) *The AHP duration* $\Delta_{AHP} = t_e - t_i$ *is solution of equation* $h(t_e) = \epsilon$ *which can be explicitly inverted and is given by*

$$t_e \approx t_2(J) + \left(\frac{\tau_{sAHP}}{J} \ln \left(\frac{h(t_2)}{\epsilon} \right) + f(X, \tau_f, \tau_r) \right) \frac{J}{JX - 1}, \tag{9}$$

where f *is a rational function of parameters* X, τ_f *and* τ_r *explicited page 66.*

The proof is given in section 1.2, pages 59-66.

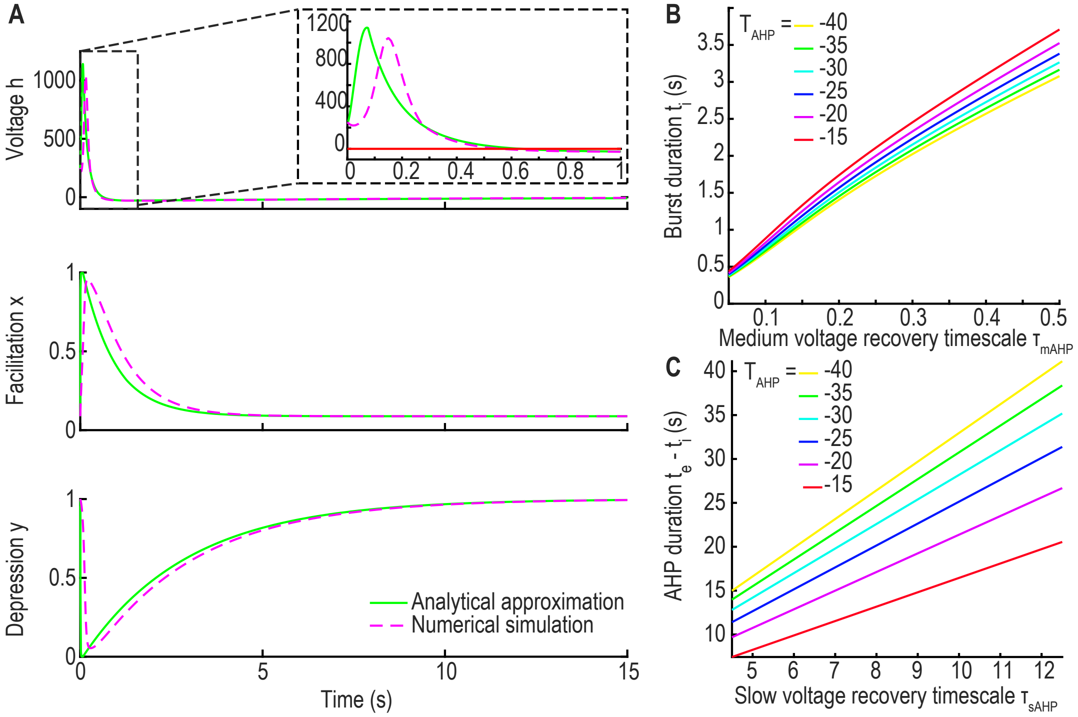

Figure 13: **A.** Analytical results (green) vs numerical integration (dotted magenta) for h (upper), x (center) and y (lower) over the three phases. **B.** Analytical burst duration t_i as a function of the medium AHP timescale τ_{mAHP} for several values of T_{AHP}. **C.** Analytical AHP duration $\Delta_{AHP} = t_e - t_i$ as a function of the slow AHP recovery timescale τ_{sAHP} for several values of T_{AHP}.

Remark: Numerical applications for burst and AHP durations. The numerical application (see Table 1.1 page 44 and 1.3 page 74 for the parameter values) gives $t_i \approx 0.6$ s, which is comparable to the bursting times observed in experimental data [52], and from the numerical integration in the noiseless case (fig. 13A). For the AHP duration, we obtain $\Delta_{AHP} = t_e - t_i \approx 14.3$ s, which is also coherent with the durations obtained from the numerical integration (fig. 13A), as well as classical AHP durations found in the literature [38].

To conclude, formulas (8) and (9) allow us to understand how the deterministic component of the burst and AHP durations are modulated by the different parameters of the model (fig. 13B-C, see also section 1.2).

Result *(section 1.1.3)* The distribution of burst durations is defined by the probability density of exit points on the separatrix During the long excursions outside the basin of attraction defining the burst in model (4), the deterministic vector field is strongly dominant compared to the noise term, thus the length and duration of the trajectories only depend on their initial point: the exit point on the separatrix Γ (fig. 14). The goal here is thus to determine this distribution of exit points on Γ for trajectories starting in the neighborhood of the attractor A.

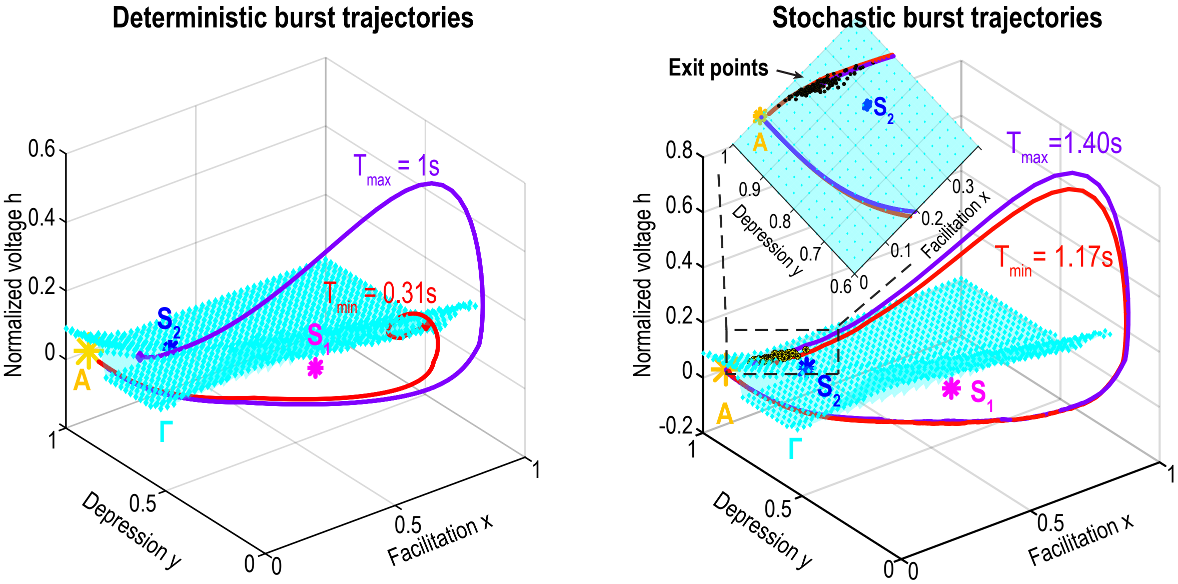

Figure 14: Extreme burst trajectories in the deterministic case (left) and in the stochastic case (right) where the possible burst trajectories depend on the exit point (yellow dots) on the separatrix Γ (cyan surface).

Theorem 1.1 *For stochastic trajectories of system* (4) *starting in the neighborhood of the attractor* A*, the distribution* p_Γ *of exit points located on the separatrix* Γ *is given per unit surface* $d\boldsymbol{s}$ *by*

$$p_\Gamma(\tilde{s}|\boldsymbol{s}_0) = \frac{J(\tilde{s}|\boldsymbol{s}_0)\cdot\nu(\tilde{s})d\tilde{s}}{\oint_\Sigma J(\tilde{s}|\boldsymbol{s}_0)\cdot\nu(\tilde{s})d\tilde{s}} \text{ for } \tilde{s}\in\Gamma, \tag{10}$$

where the probability flux is

$$J(\tilde{s}|\boldsymbol{s}_0) = \begin{pmatrix} \dfrac{Jxy-1}{\tau}hq(\tilde{s}) - \dfrac{\Gamma}{2\tau}\dfrac{\partial q(\tilde{s})}{\partial h} \\ \left(\dfrac{X-x}{\tau_f} + K(1-x)h\right)q(\tilde{s}) \\ \left(\dfrac{1-y}{\tau_r} - Lxyh\right)q(\tilde{s}) \end{pmatrix}, \tag{11}$$

$\nu(\tilde{s})$ *is the unit normal vector at the point* $\tilde{s}$ *and* q *is the solution of the steady-state renewal degenerated Fokker-Planck equation*

$$-\frac{\partial}{\partial h}\left[\frac{(Jxy-1)h}{\tau}q\right] - \frac{\partial}{\partial x}\left[\left(\frac{X-x}{\tau_f} + K(1-x)h\right)q\right] - \frac{\partial}{\partial y}\left[\left(\frac{1-y}{\tau_r} - Lxyh\right)q\right] + \frac{\sigma}{2\tau}\frac{\partial^2}{\partial h^2}q = \delta(\boldsymbol{s}-A) \tag{12}$$

with the absorbing boundary condition

$$q(\boldsymbol{s}|A) = 0 \textit{ for } \boldsymbol{s} \in \Gamma. \tag{13}$$

The solution q can be approximated by WKB and has the formal expression

$$q(\tilde{s}|\boldsymbol{s}_0) = q_\sigma(\tilde{s})Q_0(\tilde{s})e^{-\dfrac{\psi(\tilde{s})}{\sigma}}, \tag{14}$$

where $q_\sigma(\tilde{s})$ is the boundary layer solution.
Finally, the probability flux can be expressed as

$$J(\tilde{s}|\boldsymbol{s}_0)\cdot\nu(\tilde{s})d\tilde{s} = K_0\tilde{s}^{-\dfrac{\nabla\cdot\boldsymbol{B}_{|S_2}}{\lambda_2}}e^{-\dfrac{\psi(\tilde{s})}{\sigma}}d\tilde{s}, \tag{15}$$

where $\nabla\cdot\boldsymbol{B}_{|S_2}$ is the divergence of the field B at the saddle-point S_2, λ_2 is the dominant stable eigenvalue of the Jacobian of B at S_2 and ψ is solution of the degenerated eikonal equation

$$\frac{(Jxy-1)h}{\tau}\frac{\partial\psi}{\partial h} + \left(\frac{X-x}{\tau_f} + K(1-x)h\right)\frac{\partial\psi}{\partial x} + \left(\frac{1-y}{\tau_r} - Lxyh\right)\frac{\partial\psi}{\partial y} + \frac{1}{2\tau}\left(\frac{\partial\psi}{\partial h}\right)^2 = 0. \tag{16}$$

The proof is given in section 1.1.3 pages 51-56.

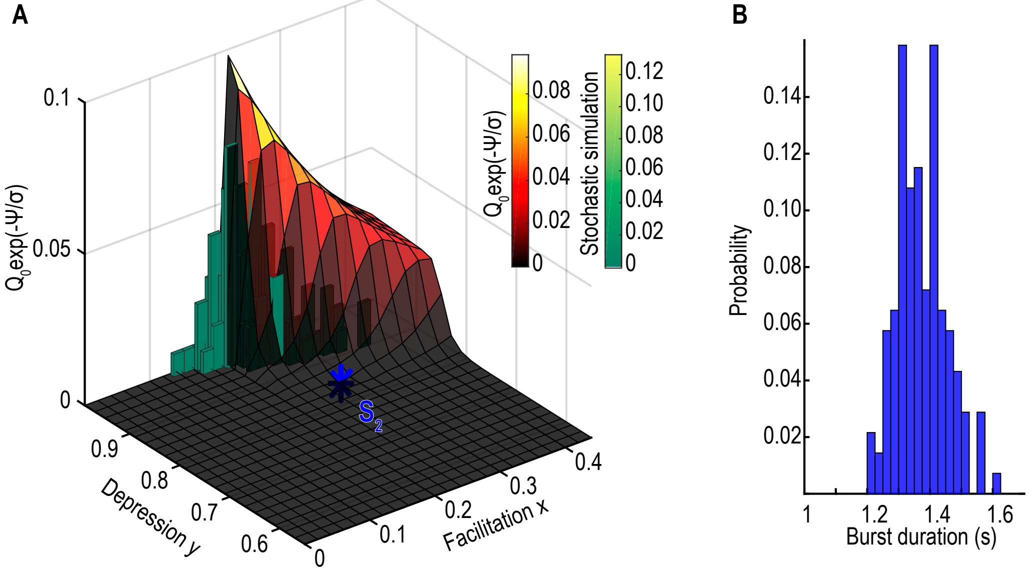

Figure 15: **A.** Probability density function (pdf) of the exit points on Γ obtained from numerical simulations (green histogram) and by solving the FPE (dark surface). **B.** Distribution of burst durations from 10^4 s simulations.

Remark: The distribution of exit points explains the peaked distribution of burst durations. The analytical distribution of exit points p_Γ is peaked close to the saddle-point S_2 (fig. 15A dark surface). This result was confirmed by numerical simulations where I recorded the exit point on Γ for successive bursts (fig. 15A green histogram, see also fig. 14 yellow dots). This peaked distribution of exit points forces the bursting trajectories to stay confined in a tubular shape following an almost deterministic path. This new result explains the small variance in the distribution of bursts durations (fig. 15B).

Result *(chapters 2 & 3)* Numerical simulations reveal two new stochastic features: a shifted attractor and a novel escape pattern From a mathematical point of view the QP corresponds to the escape from the basin of attraction of A. Because the dynamics close to A is very anisotropic: $|\lambda_1| = \dfrac{1-JX}{\tau} \approx 12.6 \gg |\lambda_2| = \dfrac{1}{\tau_f} \approx 1.1 \gg |\lambda_3| \approx \dfrac{1}{\tau_r} = 0.34$, (using the parameters in table 1.1) I projected it in the 2D plan $y = constant \iff \dot{y} = 0$ yielding the simplified 2D dynamics

$$\begin{aligned} \dot{h} &= \frac{h\,(Jx - 1 - \tau_r L x h^+)}{\tau(1+\tau_r L x h^+)} + \sqrt{\tau}\sigma\dot{\omega} \\ \dot{x} &= \frac{X - x}{\tau_f} + K(1-x)h^+. \end{aligned} \tag{17}$$

Numerical simulations of this simplified 2D model revealed two surprising behaviors:

1. The stochastic trajectories are not centered around the deterministic attractor A but rather accumulate around a shifted attractor, the position of which depends on the noise amplitude (fig. 16A).
2. The exiting trajectories do not escape directly once they reach the separatrix but they can reenter multiple times in the basin of attraction before actually escaping to infinity (fig. 16B).

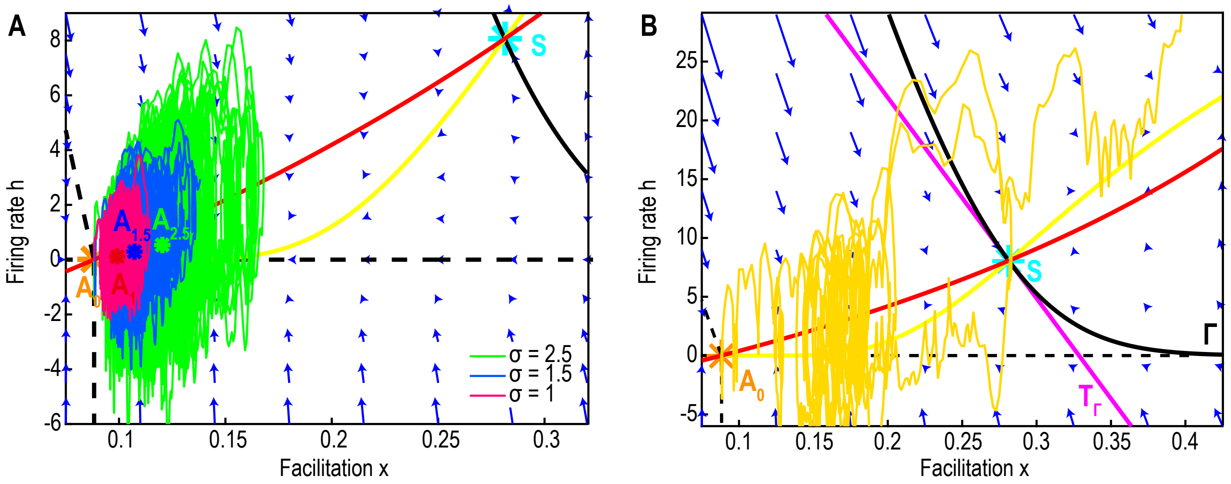

Figure 16: **A.** 2D phase-space of model (17) with non escaping stochastic trajectories for $\sigma = 1$ (pink) 1.5 (blue) and 2.5 (green) oscillating around a shifted attractor A_σ approximated by the center of mass of the trajectories (red, blue and green stars). **B.** Trajectory reentering the basin of attraction before escaping to infinity.

Description of the shifted attractor and recurrent exit pattern in a generalized framework To characterize the phenomena mentioned in the previous paragraph in a general framework, I introduced the simple 2D dynamical system

$$\begin{aligned} \dot{h} &= -\alpha h + x^2 + \sigma\dot{\omega} \\ \dot{x} &= F(h, x), \end{aligned} \tag{18}$$

where

$$F(h,x) = \begin{cases} h - \gamma x & \text{for} \quad h \geq 0 \\ -\gamma x & \text{for} \quad h \leq 0, \end{cases} \tag{19}$$

$\alpha \in]0,1]$, $\gamma \in]0,\alpha[$, $\dot{\omega}$ is a Gaussian white noise and σ its amplitude. This system has two critical points, one attractor $A = (0,0)$ (fig. 17A, yellow) which is a stable node with only real negative eigenvalues and $S = (\gamma^2\alpha, \gamma\alpha)$ (fig. 17A, cyan) which is a saddle-node with one positive and one negative real eigenvalues. The stable manifold of S (fig. 17A, black curve Γ) is the separatrix which delimits the basin of attraction of A. System (18) is topologically equivalent to system (17) restricted to $\{x \leq 0.5 \text{ and } h \leq 30\}$ (see section 3.2.2 page 88 for the description of the phase-space of system (17) and section 3.3 page 89 for system (18)).

Result *(section 3.3)* An analytical formula for the shift in the attractor's position To compute the position of the shifted attractor in the stochastic case, I considered the probability density function (pdf) in the basin of attraction of A, of the non exiting trajectories. The stochastic process $\boldsymbol{s} = (x,h)^T$ satisfies the stochastic differential equation

$$d\boldsymbol{s} = \boldsymbol{B}(\boldsymbol{s})dt + \Xi dW, \tag{20}$$

where

$$\boldsymbol{B}(\boldsymbol{s}) = \begin{pmatrix} b_1(\boldsymbol{s}) \\ b_2(\boldsymbol{s}) \end{pmatrix} \text{ and } \Xi = \begin{pmatrix} \sqrt{\sigma} & 0 \\ 0 & 0 \end{pmatrix}. \tag{21}$$

The steady-state PDF p satisfies the stationary FPE

$$\frac{\sigma}{2}\frac{\partial^2 p}{\partial h^2} - (\nabla \cdot \boldsymbol{B})p - \boldsymbol{B} \cdot \nabla p = -\delta_A, \tag{22}$$

where δ_A is the δ-Dirac function at point A. Due to the discontinuity of the field at $h = 0$, I computed $\nabla \cdot \boldsymbol{B}$ on the two half spaces $(h \geq 0)$ and $(h \leq 0)$ separately. I could compute p using the same method as in section 1.1.3 based on WKB approximation and the method of characteristics, yielding:

Theorem 3.1. *For stochastic processes* $d\boldsymbol{s} = \boldsymbol{B}(\boldsymbol{s})dt + \Xi dW$, *where the drift* $B = (b_1, b_2)^T$ *is*

$$\begin{aligned} b_1(\boldsymbol{s}) &= -\alpha h + x^2 \\ b_2(\boldsymbol{s}) &= \begin{cases} h - \gamma x & \textit{for} \quad h \geq 0 \\ -\gamma x & \textit{for} \quad h \leq 0, \end{cases} \end{aligned}, \tag{23}$$

and

$$\Xi = \begin{pmatrix} \sqrt{\sigma} & 0 \\ 0 & 0 \end{pmatrix}, \tag{24}$$

where $\alpha \in]0,1]$, $\gamma \in]0,\alpha[$, dW *is a two dimensional Gaussian white noise and* $\sigma \geq 0$. *We denote by* Ω *the basin of attraction of the attractor* $A = (0,0)$. *We consider trajectories starting at* A *and staying inside* Ω. *The pdf* p *associated to equation* (18) *is solution of the stationary FPE*

$$\frac{\sigma}{2}\frac{\partial^2 p}{\partial h^2} - (\nabla \cdot \boldsymbol{B})p - \boldsymbol{B} \cdot \nabla p = -\delta_A, \tag{25}$$

and the solution can be found explicitly in the two following sub domains:

(i) For $\boldsymbol{s} = \{(h,x) \in \Omega | h \geq 0\}$,

$$p(\boldsymbol{s}) = \mathcal{N} \frac{x_0}{x_0 + \gamma x} e^{-\dfrac{\psi(\boldsymbol{s})}{\sigma}}. \tag{26}$$

(ii) For $\boldsymbol{s} = \{(h,x) \in \Omega | h \leq 0\}$,

$$p(\boldsymbol{s}) = \mathcal{N} \left(\frac{x_0}{x_0 + \gamma x} \right)^{\dfrac{\alpha+\gamma}{\gamma} - \dfrac{1}{(\alpha-\gamma)^2}} e^{-\dfrac{\psi(\boldsymbol{s})}{\sigma}}, \tag{27}$$

where ψ *is the solution of the eikonal equation associated to* (25) *and* $\mathcal{N}$ *is a normalization constant such that* $\int_\Omega p(\boldsymbol{s}) d\boldsymbol{s} = 1$.

The next proposition allows us to determine an explicit expression for the solution of the eikonal equation.

Proposition 3.1. *Under the assumptions of theorem 3.1, the solution of the eikonal equation*

$$\boldsymbol{B} \cdot \nabla \psi + \frac{1}{2} \left(\frac{\partial \psi}{\partial h} \right)^2 = 0 \tag{28}$$

is

(i) For $\boldsymbol{s} = \{(h,x) \in \Omega | h \geq 0\}$,

$$\psi(h,x) = \alpha \left(h - \left(h_0 - \frac{x_0^2}{\alpha - 2\gamma} - \frac{q_{1,0}}{2\alpha} \right) \left(\frac{x}{x_0} \right)^{\dfrac{\alpha}{\gamma}} - \frac{x^2}{\alpha - 2\gamma} \right)^2, \tag{29}$$

where the initial conditions are $h(0) = h_0, x(0) = x_0, q_1(0) = q_{1,0}$ *and* $q_2(0) = q_{2,0} > 0$.

(ii) For $\boldsymbol{s} = \{(h,x) \in \Omega | h \leq 0\}$,

$$\psi(h,x) \approx \frac{Q_0^2}{4\alpha} \left(\frac{2\gamma(h+x)}{q_{2,0}} \right)^{\dfrac{2\alpha}{\gamma}} + \frac{\gamma(h+x)^2}{(\gamma-\alpha)^2} + \frac{Q_0 q_{2,0}}{\gamma^2 - \alpha^2} \left(\frac{2\gamma(h+x)}{q_{2,0}} \right)^{\dfrac{\alpha+\gamma}{\gamma}}, \tag{30}$$

where

$$\begin{aligned} Q_0 &= q_{1,0} + \frac{q_{2,0}}{\gamma - \alpha} \\ H_0 &= h_0 - \frac{Q_0}{2\alpha} + \frac{q_{2,0}}{\gamma^2 - \alpha^2} \\ X_0 &= x_0 - \frac{H_0}{\gamma - \alpha} - \frac{Q_0}{2\alpha(\gamma+\alpha)} + \frac{q_{2,0}}{2\gamma(\gamma^2 - \alpha^2)} \end{aligned} \tag{31}$$

and the initial conditions are $h(0) = h_0, x(0) = x_0, q_1(0) = q_{1,0}$ *and* $q_2(0) = q_{2,0} > 0$.

The proofs are given in section 3.3 pages 95-99.

The pdf in the domain $\{(h,x) \in \Omega | h \geq 0\}$ shows a maximum along the $h = 0^+$ axis and its position depends on the value of σ (fig. 17B). The position of the maximum corresponds to the shifted attractor. I could thus compute it as a function of the noise amplitude yielding the following corrollary:

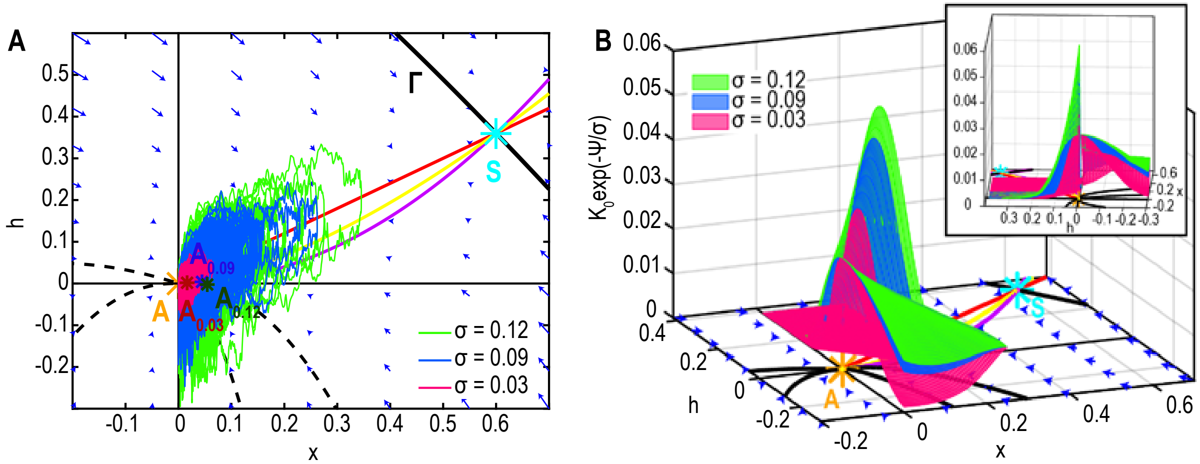

Figure 17: **A.** 2D phase-space of model (18) with non escaping stochastic trajectories for $\sigma = 0.03$ (pink) 0.09 (blue) and 0.12 (green) oscillating around a shifted attractor A_σ approximated by the center of mass of the trajectories (red, blue and green stars). **B.** Analytical pdf p (equations 26 and 27) for the three values of σ.

Corollary 3.2 Position of the shifted stochastic attractor *The pdf p of stochastic trajectories solution of equation* (18) *that did not escape the basin of attraction Ω peaks at a shifted position compared to the attractor A, and the shift depends on the noise amplitude σ. The maximum of the pdf p is located on the line $h = 0^+$ and is given by the implicit equation*

$$-\frac{A1}{1+\frac{\gamma}{x_0}x} - \frac{1}{\sigma}\left(A_2 x^{\frac{2\alpha}{\gamma}-1} + A_3 x^{\frac{\alpha}{\gamma}} + A_4 x\right) = 0, \tag{32}$$

where

$$A_1 = \left(\frac{\alpha+\gamma}{\gamma} - \frac{1}{(\alpha-\gamma)^2}\right)\frac{\gamma}{x_0}, A_2 = \frac{Q_0^2}{q_{2,0}}\left(\frac{2\gamma}{q_{2,0}}\right)^{\frac{2\alpha}{\gamma}-1}, A_3 = \frac{2Q_0}{\gamma-\alpha}\left(\frac{2\gamma}{q_{2,0}}\right)^{\frac{\alpha}{\gamma}}, A_4 = \frac{2\gamma}{(\alpha-\gamma)^2}. \tag{33}$$

The proof is page 101. This equation cannot be solved analytically, however, I shall describe here a case where equation (32) can be approximated by a polynomial equation.

Corollary 3.3 Approximation of the distance $|A_\sigma - A|$ in the parameter range $0.5 < \frac{\gamma}{\alpha} < 0.645$: *the solution of equation* (32) *is*

$$x_M(\sigma) = |A_\sigma - A| = \left(\frac{-q(\sigma) - \sqrt{\Delta(\sigma)}}{2}\right)^{1/3} + \left(\frac{-q(\sigma) + \sqrt{\Delta(\sigma)}}{2}\right)^{1/3} - \frac{c_2}{3c_1}, \tag{34}$$

where

$$\begin{aligned} c_1 &= A_2 + A_3 + \frac{A_4\gamma}{x_0} > 0 \\ c_2 &= A_2 + A_3 \\ q(\sigma) &= \frac{2c_2^3 - 9c_1c_2A_4}{27c_1^3} + \frac{A_1}{c_1}\sigma \\ \Delta(\sigma) &= q(\sigma)^2 + \frac{4}{27}\left(\frac{3c_1A_4 - c_2^2}{3c_1^2}\right)^3 \end{aligned} \tag{35}$$

(expression (34) *is valid as long as* $\Delta(\sigma) \geq 0$*, that is* $\sigma > 0.0114$*).*

The proof is given page 102.

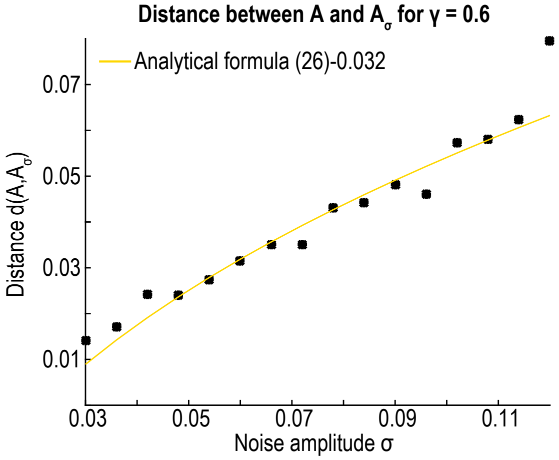

Figure 18: Analytical approximation (34) (yellow) minus the corrective constant $\hat{c} = 0.032$ for $\gamma = 0.6$ compared to numerical simulations (black dots).

Remark 1: Comparison with the numerical simulations. I ran numerical simulations to obtain the position of the shifted attractor for values of $\sigma \in [0, 0.2]$ and compared it to the analytical result (34) showing a good match (fig. 18 yellow curve compared to the result of numerical simulations, black dots where I subtracted a corrective constant $\hat{c} = 0.032$ obtained by minimizing the difference between analytical formula (34) and simulations).

Similarly, I obtained an analytical formula in the range $0.885 \leq \frac{\gamma}{\alpha} < 1$ (see corollary 3.4 page 102).

Remark 2: Approximation ranges validity. To obtain the aforementioned approximation ranges, we computed the absolute difference $d(\sigma) = |x_{M,num}(\sigma) - x_M(\sigma)|$ between the numerical result $x_{M,num}(\sigma)$ and the solution $x_M(\sigma)$ defined by corollary 3.3 (respectively 3.4), for $\sigma \in [0, 0.2]$, and we used the criteria $d_{max} = \max_{\sigma \in [0,0.2]} (d(\sigma)) < 0.02$ (see page 101 for details).

Description of the recurrent exit mechanism The escape from the attractor takes three steps: 1) from the deterministic attractor A, the trajectories fall into the basin of the shifted attractor A_σ, 2) the trajectories reach the separatrix Γ (fig. 19 black) and 3) the trajectories can exit and reenter the basin of attraction several times (green, cyan) before escaping to infinity (pink). In the previous paragraph I have described the position of the shifted attractor. However, step 1 is almost immediate and can be neglected with respect to steps 2 and 3 when it comes to computing the escape time. I shall now describe the recurrent exit pattern and quantify the mean and distribution of escape times in this scenario.

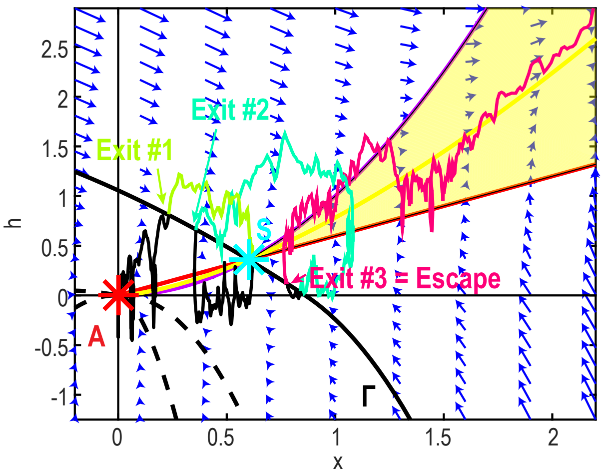

Figure 19: Trajectory escaping from the basin of attraction of A (red star) after 1) reaching the separatrix Γ (black curve) for the first time (black) 2) exiting and reentering in the basin (green, cyan) and 3) escaping to infinity (pink).

Result *(sections 2.2 and 3.4.3)* The mean escape time is multiplied by a factor 2.3 compared to the first exit time Since the trajectories can reenter several times in the basin, I need to take into account the time spent doing these round trips (RT) around the separatrix Γ: they are defined as the portion of trajectory from the time t_n at which a trajectory exits the basin of attraction, then reenters until it exits again at time t_{n+1}. The mean escape time is thus summarized in the following lemma:

Lemma 3.1 *We consider a phase-space composed of a single bounded basin of attraction. Outside the basin of attraction the trajectories converge to infinity. Then, the mean escape time to infinity from the basin of attraction is given by the sum*

$$\langle \tau_{esc} \rangle = \langle \tau_0 \rangle + \frac{\langle \tau_{ext} \rangle + \langle \tau_{int} \rangle}{\tilde{p}}, \tag{36}$$

where $\tilde{p}$ is the probability that a trajectory crossing the separatrix Γ does not return inside the basin of attraction, $\langle \tau_0 \rangle$ is the mean time to reach the separatrix for the first time and $\langle \tau_{ext} \rangle$ (resp. $\langle \tau_{int} \rangle$) is the mean time spent outside (resp. inside) the basin of attraction during one RT.

The proof is given page 106.

Remark: Numerical simulations of (18) **shows a factor 2.3 in the escape time.** Computing the times $\langle \tau_0 \rangle$, $\langle \tau_{ext} \rangle$ and $\langle \tau_{int} \rangle$ numerically lead to the conclusion that, for system (18), the mean escape time $\langle \tau_{esc} \rangle$ is increased by a factor 2.3 compared to the time $\langle \tau_0 \rangle$ to reach the separatrix for the first time (see section 2.2 page 80 and section 3.4.3 page 105 for details) thus confirming the importance of accounting for this recurrent exit mechanism in the computation of the escape time.

Result *(sections 2.2 and 3.4.4)* The distribution of escape times can be decomposed according to the number of RT before escape Similarly, the distribution of escape times is given by

Lemma 3.2 *Under the assumptions of lemma 3.1, the distribution of escape times is*

$$P(\tau_{esc} < t) = \sum_{k=0}^{\infty} f_0(t) * f_1(t)^{*k} \tilde{p}(1-\tilde{p})^k. \tag{37}$$

where $f(t)^{*k} = f(t) * f(t) * ... * f(t)$, k times, f_0 is the distribution of escape times for trajectories escaping without any RT and f_1 of a single RT.

The proof is page 108.

Remark: Comparison to numerical simulations. I found f_0 and f_1 for both dynamical systems (17) and (18) by fitting the distributions obtained with numerical simulations. I could then compute all the terms of the distribution (37) and found that they match the distributions obtained from numerical simulations (see fig. 3.7 page 107). These results apply to the facilitation-depression model (17) and explain why the IBI are longer than what is expected from the classical theory of noise activated escape.

To conclude this part, I propose that this recurrent exit mechanism can be generalized for stochastic dynamical systems of dimensions ≥ 2 under the following assumptions:

Conjecture 3.1 Recurrent exit mechanism *For stochastic dynamical systems of dimension ≥ 2 perturbed by a small Gaussian noise, if the following conditions are satisfied:*

1. *The distribution of exit points peaks at a distance $O(\sqrt{\sigma})$ from the saddle-point [134].*
2. *The shallow field near the separatrix allows the trajectories to reenter the basin of attraction with a probability p close to 1.*
3. *The peaks P_k of the successive exit points distributions converge to the saddle-point S.*
4. *When the stochastic trajectories enter the region where the field B satisfies the condition $B = (b_1 \geq 0, ..., b_n \geq 0)$, they eventually escape to infinity.*

Then the trajectories present multiple reentries into the basin of attraction and the escape time τ_{esc} is not given by the classical Kramer's exit theory and can be much higher due to the additive term in equation (36).

Part II: Applications to data analysis and computational neuroscience

Time-series segmentation and numerical simulations to study how astrocytes regulate neuronal bursting dynamics *(chapter 4)*

Result *(section 4.5.2)* Segmentation of experimental time-series recordings shows AHP is the main determinant of IBI duration I developed a segmentation method based on low-pass filtering and a combination of thresholding steps (see section 4.5.2 page 134 for the details of the

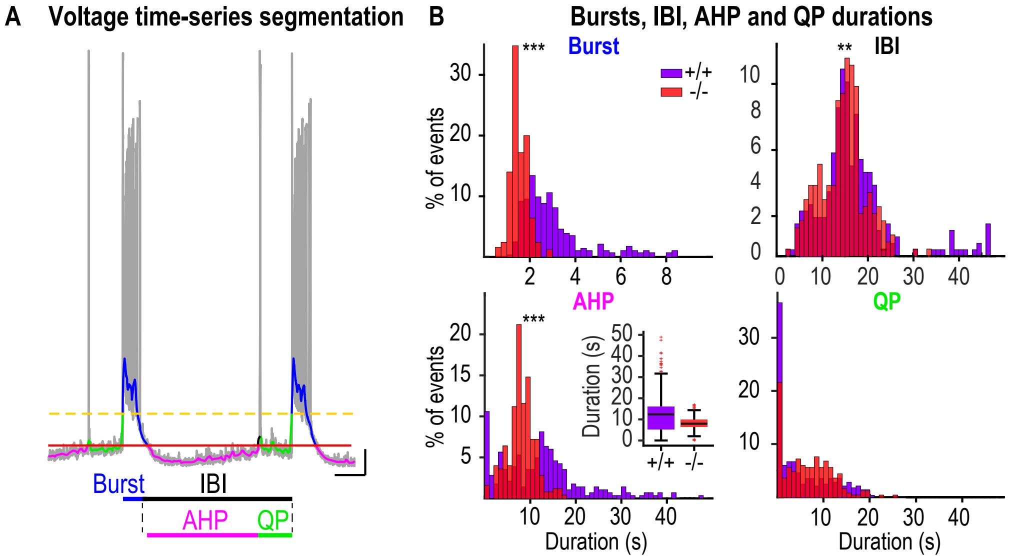

Figure 20: **A.** Segmentation of the traces into burst (blue), AHP (pink) and QP (green), scalebar: 10 s, 10 mV. **B.** Distributions of bursts (upper left), IBI=AHP+QP (upper right), AHP (lower left) and QP (lower right) durations for the WT (purple) and KO (red) datasets.

segmentation algorithm) to segment electrophysiological recordings of neuronal activity into: burst (fig. 20A blue), AHP (pink) and a quiescent phase QP (green). The IBI (black) is defined by IBI=AHP+QP and I obtained the distributions of burst, AHP and QP durations for wild type (WT) mice (fig. 20B purple) and mice with a disrupted astrocyte network (knockout (KO) of the gap junctions, fig. 20B red, see sections 4.4.1 and 4.4.2 page 129 for a description of the experiments). This segmentation showed that the main component determining the IBI duration was the AHP, while the QP was almost not affected by the disruption of the astrocyte network (fig. 20B).

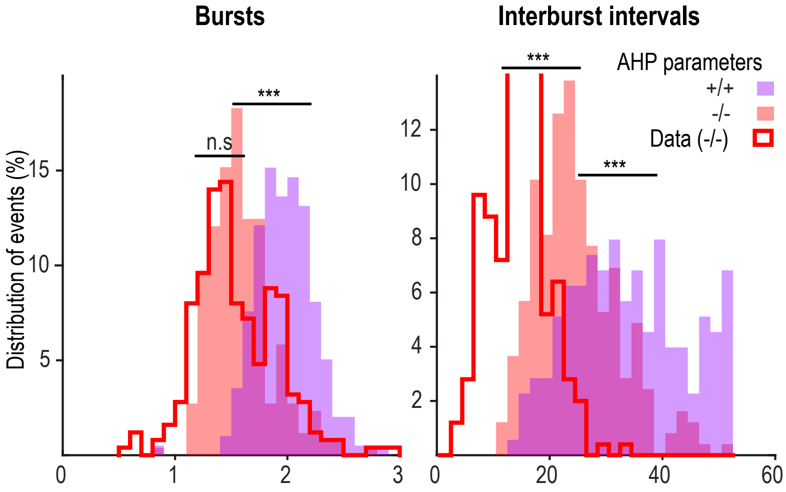

Figure 21: Distributions of burst (left) and IBI (right) durations, for simulations of the WT case (light purple) and simulations with modified AHP parameters (light red) compared to the KO data (red curve).

Result *(section 4.2.2)* Numerical simulations reveal the contribution of each parameter I calibrated the model (4) to reproduce the distributions of both burst and AHP durations in the WT and KO cases (section 4.2.1 page 120) and then used the calibrated model to decipher the respective influence on neuronal bursting activity of AHP, synaptic noise and membrane depolarization, which are all affected by the disruption of the astrocyte network. Specifically, I ran simulations of the model with all the parameters obtained in the case of the WT fit (fig. 21 light purple) and then changed to the KO values only the parameters corresponding to one phenomenon. I then compared the distribution of the simulated burst and IBI durations (fig. 21 light red) to the KO data distributions (red curve). I found that the AHP was sufficient to explain the change in burst and IBI durations observed in the KO data, while the increase of synaptic noise had some effect on burst durations but not much on IBI and the membrane depolarization had no effect on either duration (see section 4.2.2 and fig. 4.4 page 121 for the full simulation results and section 4.2.3 for the experimental validation). To conclude, these results help decipher the physiological mechanisms underlying the regulation of neuronal bursting by the astrocyte network in a way that would not have been possible experimentally.

Application to a computational study of the α-band *(chapter 5)*

EEG is used to monitor the brain activity and to reveal and quantify the presence of multiple frequency oscillations [142] over time [143]. During general anesthesia, the dominant oscillation is the α-band (8-12Hz) [30, 31]. Since Up and Down states reflect the neuronal activity at the population level [27, 28], I modeled the emergence and fragmentation of the α-band using the mean field model of synaptic facilitation-depression accounting for AHP (4) in a case were it could reproduce Up and Down states.

Result *(Section 5.1.2)* A model bifurcation leads to the emergence of Up and Down states First, I investigated how the model (4) with and without AHP (fig. 22A) could exhibit Up and Down states. To do so, I increased the network connectivity parameter J until the model reached a bifurcation where the saddle-focus S_1 becomes an attractor. In this case, the model (with and without AHP) exhibits bistability with one attractor representing the Down state (fig. 22B-C right, purple) and the second one representing the Up state (fig. 22B-C right, red). I will now briefly summarize the results obtained in the two cases of a single population with and without AHP.

Result *(Section 5.1.2)* A single population without AHP exhibits a dominant oscillation frequency due to the Up state focus attractor In the case without AHP, the Up state attractor is a saddle-focus (see section 5.4.2 page 166 for a detailed analysis of the phase-space) and the dominant oscillation frequency is determined by the imaginary part of the complex conjugate eigenvalues (fig. 22B left). This result shows that the α-band dynamics depend on the properties of the Up state attractor (fig. 22B right, red star). I found that the peak value of the oscillation frequency is an increasing function of the network connectivity J: a higher connectivity leads to faster oscillations (fig. 5.2C page 145). However, in this case the system stays locked in the Up state due to the multiple reentries in the Up state basin of attraction of the stochastic trajectories.

Result *(Section 5.1.2)* The AHP allows to switch dynamically between Up and Down states For the model with AHP, the synaptic noise is sufficient to generate spontaneous switching between the Up and Down states (fig. 22C left), however there is no dominant oscillation in the Up state because in this case the Up state attractor is a stable node with only real eigenvalues (fig. 22C right and see section 5.4.2 for the detailed analysis of the phase-space). This result suggests that although the dynamics at the Up state shape the oscillatory behavior, the dynamic switch between Up and Down states results from ionic membrane properties such as the ones responsible for AHP.

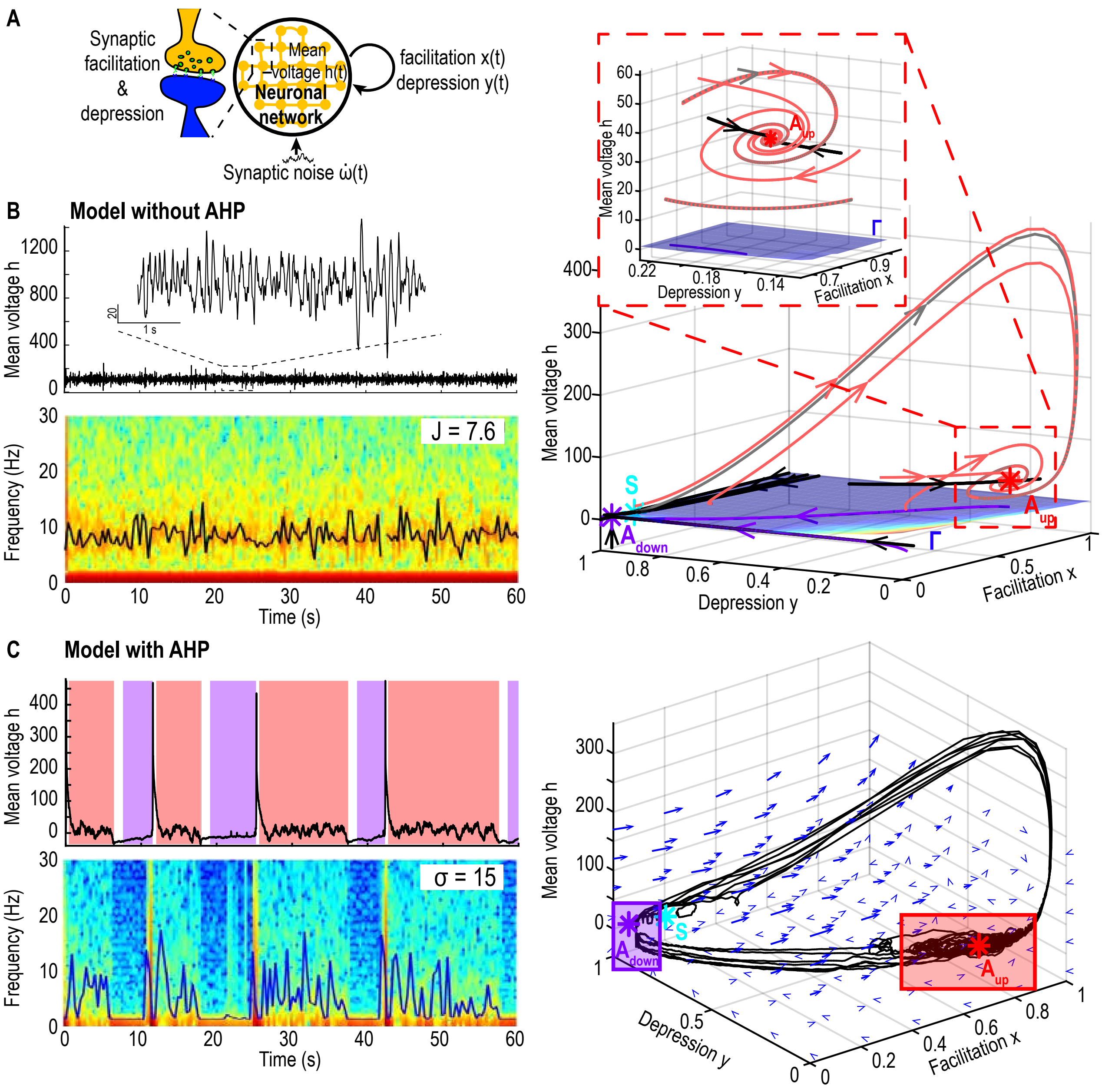

Figure 22: **A.** Schematic of the model for one single population. **B.** Model (4) for $J = 7.6$ without AHP. Left: h time-series (upper) and spectrogram (lower, 1 min simulation) with tracking of the peak value of the α-band (black curve). Right: 3D phase-space with an inset around the focus attractor A_{Up}. **C.** Model (4) for $J = 7.6$ with AHP. Left: h time-series (upper) and spectrogram (lower, 1 min simulation) with the spectral edge frequency at 95% (SEF95 blue curve). Right: 3D phase-space with a stochastic trajectory oscillating between the two stable attractors A_{Down} (purple) and A_{Up} (red).

Multiscale model of the thalamo-cortical loop Finally, to reproduce a more physiological behavior where the Up and Down states coexist with a dominant α-band in the Up state I coupled two excitatory components with one inhibitory component (fig. 23). This model represents the large scale interactions between the cortical and thalamic neurons, which are known to be involved in the genesis and maintenance of the oscillatory brain rhythms observed in EEG during general anesthesia [30].

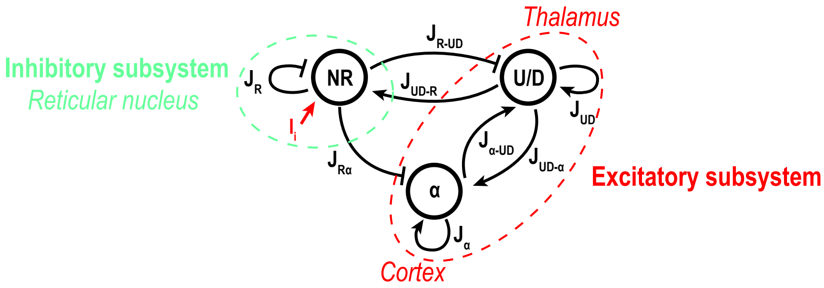

Figure 23: Schematic of the thalamo-cortical loop model.

Result *(Section 5.1.4)* Two excitatory and one inhibitory coupled populations can reproduce the coexistence of α-band and Up and Down states The multi-scale model (fig. 23) of the thalamo cortical loop revealed that the α-band spontaneously emerges with the suppression of all external stimuli (fig. 5.5 page 149). I found that coupling two excitatory components with one inhibitory is the minimal configuration allowing to reproduce switches between Up and Down states combined with a dominant α-oscillation in the Up state. Indeed, one excitatory population (the one without AHP) induces the oscillation in the Up state while the other one (with AHP) triggers the switches between Up and Down states driven by the synaptic noise. I could then use this model to study the fragmentation and disappearance of the α-band when the inhibitory pathway is stimulated. The stimulation of the inhibitory neuronal population models the injection of a hypnotic drug such as propofol. I found that increasing the stimulation on inhibition modulates the proportion of time spent in Up vs Down states (fig. 5.6E page 150). This result suggest that the fragmentation of the α-band, which precedes the appearance of iso-electric suppression [144] is in fact associated to an increase in the proportion of Down states. Finally, this model could be used to investigate further the activation pathways of anesthetic drugs and it could also be applied to study different oscillatory rhythms such as the θ-band which is characteristic of REM sleep [32, 33].

Organisation of the manuscript

Part I: Modeling and computation of bursts and interbursts durations in neuronal networks

Chapter 1 In this chapter I introduce the new facilitation-depression model with AHP and describe its deterministic 3D phase-space. I explain the peaked distribution of burst durations obtained from stochastic simulations by expliciting the distribution of exit points on the separatrix Γ. This distribution is obtained by solving the steady-state renewal FPE for trajectories starting at the attractor and with an absorbing boundary condition on the separatrix. Finally, I use a slow-fast decomposition to compute analytical formulas for the burst and AHP durations in the deterministic case.

Chapters 2 & 3 In chapter 2 I briefly describe the recurrent escape mechanism in the generic case of a simple 2D system and its application to the 2D projection of the facilitation-depression model close to the attractor to explain longer than expected IBI. In chapter 3 I describe numerically and analytically the shift in the attractor's position induced by the presence of an additive noise and I give algebraic formulas for the dependency between the shift and the noise amplitude. Then I further detail the recurrent exit mechanism introduced in chapter 2 in the general case and its application to the long IBI in the facilitation-depression model.

Part II: Applications to data analysis and computational neuroscience

Chapter 4 In this chapter I study the mechanisms underlying the regulation of burst and IBI by the astrocyte network. The experiments from our collaborators in Collège de France are explicited. I detail the data analysis, in particular the segmentation algorithms I developed. I explain how the model is used to further understand the data: I calibrate the facilitation-depression model to reproduce the distributions of both burst and AHP durations obtained from the segmentation of the experimental data. I then use numerical simulations to decipher the respective influence on the neuronal bursting dynamics of various parameters that are affected by the disruption of the astrocyte network. Finally, the model predictions are verified experimentally.

Chapter 5 In the final chapter of this thesis, I describe how a bifurcation of the facilitation-depression model (with and without AHP) can lead to the existence of Up and Down states. I use numerical simulations to investigate the relation between Up and Down states and the emergence of dominant oscillatory bands in the spectrogram of the simulated voltage time series. I then build multi-scale models of the thalamo-cortical loop by coupling several excitatory and inhibitory neuronal populations and I use these models to investigate the emergence and transient disappearance of the α-band through the effect of external stimulations. Finally I show that the stability of the α-band depends on the balance of time spent in Up vs Down states.

Part I

Modeling and computation of bursts and interbursts durations in neuronal networks

Chapter 1

Modeling bursting in neuronal networks using facilitation-depression and afterhyperpolarization

Published in ZONCA L. & HOLCMAN D., "Modeling bursting in neuronal networks using facilitation-depression and afterhyperpolarization" Communications in nonlinear science and numerical simulations, 94:e105555 (2021) / arXiv:2001.11432

Abstract

In the absence of inhibition, excitatory neuronal networks can alternate between bursts and interburst intervals (IBI), with heterogeneous length distributions. As this dynamic remains unclear, especially the durations of each epoch, we develop here a bursting model based on synaptic depression and facilitation that also accounts for afterhyperpolarization (AHP), which is a key component of IBI. The framework is a novel stochastic three dimensional dynamical system perturbed by noise: numerical simulations can reproduce a succession of bursts and interbursts. Each phase corresponds to an exploration of a fraction of the phase-space, which contains three critical points (one attractor and two saddles) separated by a two-dimensional stable manifold Σ. We show here that bursting is defined by long deterministic excursions away from the attractor, while IBI corresponds to escape induced by random fluctuations. We show that the variability in the burst durations, depends on the distribution of exit points located on Σ that we compute using WKB and the method of characteristics. Finally, to better characterize the role of several parameters such as the network connectivity or the AHP time scale, we compute analytically the mean burst and AHP durations in a linear approximation. To conclude the distribution of bursting and IBI could result from synaptic dynamics modulated by AHP.

Introduction

Neuronal networks can exhibit periods of synchronous high-frequency activity called bursts separated by interburst intervals (IBI), corresponding to low amplitude time periods. Bursting can either be due to intrinsic channel activities driven by calcium and voltage-gated channels or by collective synchronization of large ensemble of neuronal cells [10]. Yet the large distributions observed in electrophysiological recordings of bursting and IBI remains unclear.

Bursting is a fundamental feature of Central Pattern Generators such as the respiratory rhythm in the pre-Bötzinger complex [4, 5], mastication or oscillatory motor neurons [6] which are involved in the genesis and maintenance of rhythmic patterns. Interestingly, several coupled pacemaker neurons receiving an excitatory input from tonic firing neurons can either lead to bursting, tonic spiking or resting depending on the values of the channel conductances and the neuronal coupling level [24–26].
Bursts that emerge as a network property have been studied using different modeling approaches such as coupled integrate and fire neurons [59, 60], improved recently by adding noise to connected Hodgkin-Huxley type neurons, to allow desynchronisation [69]. Bursting can also depend on the balance between excitatory and inhibitory neurons: coupling excitatory neurons results in in-phase bursting within the network, whereas inhibitory coupling leads to anti-phase dynamics [81]. Furthermore, time-delays [68] play a crucial role in synchronisation, by generating coherent bursting, specifically when the time-delays are inversely proportional to the coupling strength [85].
Rhythm generation based on network bursting also depends on the bursting frequency and the interburst intervals. Synaptic properties shape the genesis and maintenance of bursts [11–13]. Synaptic short-term plasticity modeled in the mean-field approximation, is based on facilitation, depression and network firing rate [102]. Long interburst intervals have been generated by introducing a two state synaptic depression [112]. Interestingly, different levels of facilitation and depression lead to various network dynamics [145] such as resting, bursting, spiking and, when noise is added, to Up and Down state transitions [105]. Such models were used to interpret bursting in small hippocampal neuronal islands [109] to show that the correlation between successive bursts could result from synchronous depressing-facilitating synapses.
However in all these models, the distribution of Bursting and IBI durations remains unclear. In particular, the IBI in hippocampal pyramidal neurons is shaped by various type of potassium and calcium ionic channels [14, 38–40], leading to medium and slow hyperpolarizing currents in the cells, a phenomenon known as afterhyperpolarization (AHP). AHP results from the activation of these slow and fast potassium channels, but their exact biophysical properties and distributions are not fully known. Thus, we decided here to model the consequences of these channels by using a phenomenological approach to reproduce the shape of the AHP. We analyse this model using WKB methods to determine how the distribution of bursts durations depends on some properties of exit points in the phase-space. Furthermore, we wish to better understand how the IBI durations depend on various parameters such as the network connectivity, the AHP time scales and the facilitation-depression dynamics. We do so by deriving analytical formulas for the burst and AHP durations using a linear approximation of our model.
The manuscript is organized in two main sections: in the first one, we introduce a phenomenological three-dimensional dynamical system, where we have added the effect of AHP to the facilitation-depression model by modifying the dynamics in certain portions of the phase-space. Noise perturbation on the voltage variable can produce bursting periods followed by IBI. We describe the phase-space that contains three critical points (one attractor and two saddles). Moreover, we relate the distribution of burst durations to the one of the exit points on the stable manifold, delimiting the region of non bursting trajectories of the stable equilibrium. In the second section, we use a linear approximation of the phenomenological system we introduced in section 1, to obtain a closed relation between the burst and AHP durations and key parameters. Finally, we study how the network connectivity, facilitation and depression parameters influence the burst and IBIs.

1.1 A facilitation-depression model with AHP

1.1.1 Model description

Since AHP involves the combination of several types of slow and fast potassium channels, to avoid entering into a difficult choice of channels, we decided instead to use a coarse-grained representation. We thus rather model the consequences of channel activity by modifying the facilitation-depression short-term synaptic plasticity model. This is well accounted for by a mean-field system of equations for a sufficiently well connected ensemble of neurons. The stochastic dynamical system consists of three equations [102, 109] for the mean voltage h, the depression y, and the synaptic facilitation x:

$$\begin{aligned}
\tau\dot{h} &= -h + Jxyh^+ + \sqrt{\tau}\sigma\dot{\omega} \\
\dot{x} &= \frac{X-x}{t_f} + K(1-x)h^+ \\
\dot{y} &= \frac{1-y}{t_r} - Lxyh^+,
\end{aligned} \tag{1.1}$$

The population average firing rate is given by $h^+ = max(h, 0)$, which is a linear threshold function of the synaptic current [105]. The term Jxy reflects the combined effect of synaptic short-term dynamics on the network activity. The second equation describes facilitation, while the third one describes depression. The mean number of connections (synapses) per neurons is accounted for by the parameter J [110]. We previously distinguished [109] the parameters K and L which describe how the firing rate is transformed into molecular events that are changing the duration and the probability of vesicular release respectively. The time scales t_f and t_r define the recovery of a synapse from the network activity. Finally, $\dot{\omega}$ is an additive Gaussian noise and σ its amplitude, it represents fluctuations in the firing rate. The model (1.1) does not account for long AHP periods, where the voltage is hyperpolarized and then slowly depolarized due to potassium channels [38], leading to a refractory period. To account for AHP, we thus incorporated changes in the facilitation-depression model by introducing two features: 1) a new equilibrium state representing hyperpolarization, after the peak response 2) a slow recovery with two timescales (medium and slow) to describe the slow transient to the steady state. The new equations are

$$\begin{aligned}
\tau_0\dot{h} &= -(h-T_0) + Jxy(h-T_0)^+ + \sqrt{\tau_0}\sigma\dot{\omega} \\
\dot{x} &= \frac{X-x}{\tau_f} + K(1-x)(h-T_0)^+ \\
\dot{y} &= \frac{1-y}{\tau_r} - Lxy(h-T_0)^+.
\end{aligned} \tag{1.2}$$

These changes lead to a piece-wise system that decomposes into four steps:

- **step 1: burst phase.** It is defined when the dynamics fall into the subspace $\{y > Y_{AHP}$ and $h \geq H_{AHP}$ (fig. 1.1B purple surface)$\}$. During this phase the time constant τ_0 of h is fixed to $\tau_0 = \tau$ and the resting value of h is $T_0 = T$ (see Table 1.1).
- **Step 2: depression phase.** In this phase, the depression parameter y increases ($\dot{y} > 0 \iff y < \dfrac{1}{1 + Lx(h-T_0)}$, fig. 1.1B curved orange surface), and it lasts until y reaches the threshold Y_h

	Parameters	Values
τ	Fast time constant for h	0.05s [105]
τ_{mAHP}	Medium time constants for h	0.15s
τ_{sAHP}	Slow time constants for h	5s
J	Synaptic connectivity	4.21 (*modified: 3-5 in* [145])
K	Facilitation rate	0.037Hz (*modified: 0.04Hz in* [109])
X	Facilitation resting value	0.08825 (*modified: 0.5-0.1 in* [145])
L	Depression rate	0.028Hz (*modified: 0.037Hz in* [109])
τ_r	Depression time rate	2.9s (*modified: 2-20s in* [109])
τ_f	Facilitation time rate	0.9s (*modified: 1.3s in* [109])
T	Depolarization parameter	0
σ	Noise amplitude	3
T_{AHP}	Undershoot threshold	-30

Table 1.1: Model parameters

(i.e. $y < Y_h$, fig. 1.1B vertical orange surface). During this phase the parameters are $\tau_0 = \tau_{mAHP}$ and $T_0 = T_{AHP} < T$. These parameter values forces the voltage to hyperpolarize.

- **Step 3: return to steady state.** In that phase, the depression y is still increasing ($\dot{y} > 0$), with the condition that $Y_{AHP} < y$ or $h < H_{AHP}$. During this phase, we change the time constant to $\tau_0 = \tau_{sAHP}$ and the resting value of h is set to its initial value $T_0 = T$. These modifications account for the slow recovery from hyperpolarization to the resting state, this phase ends when y reaches the second threshold Y_{AHP} and h reaches its threshold H_{AHP}.

- **Step 4: resting state.** This phase models the fluctuations of the voltage around the steady state due to noise. The conditions and parameters are the ones of step 1 ($\{y > Y_{AHP}$ and $h \geq H_{AHP}\}$, $\tau_0 = \tau$ and $T_0 = T$).

The values of the parameters for the classical facilitati,on-depression part are chosen in agreement with [102,105,109,145], while the AHP parameters (T_{AHP}, τ_{mAHP} and τ_{sAHP}, Table 1.1) are consistent with the biological observations [38].
Numerical simulations of equations (1.2) with a sufficient level of noise exhibit spontaneous bursts in the voltage variable followed by AHP periods (fig. 1.1A-B).
We segmented the simulated time series into two phases: bursting (fig. 1.1C, blue) and IBI, which is further decomposed into an AHP period (pink) and a quiescent phase (QP, green). The quiescent phase is a period where the voltage fluctuates around its equilibrium value $h = 0$. This segmentation allows us to obtain the distributions of burst, AHP and QP durations (fig. 1.1D).

1.1.2 Phase-space analysis

Studying the phase-space of the deterministic system (1.2) is a key step to analyze the stochastic dynamics.

Equilibrium points

We first search for the equilibrium points. There are three of them:

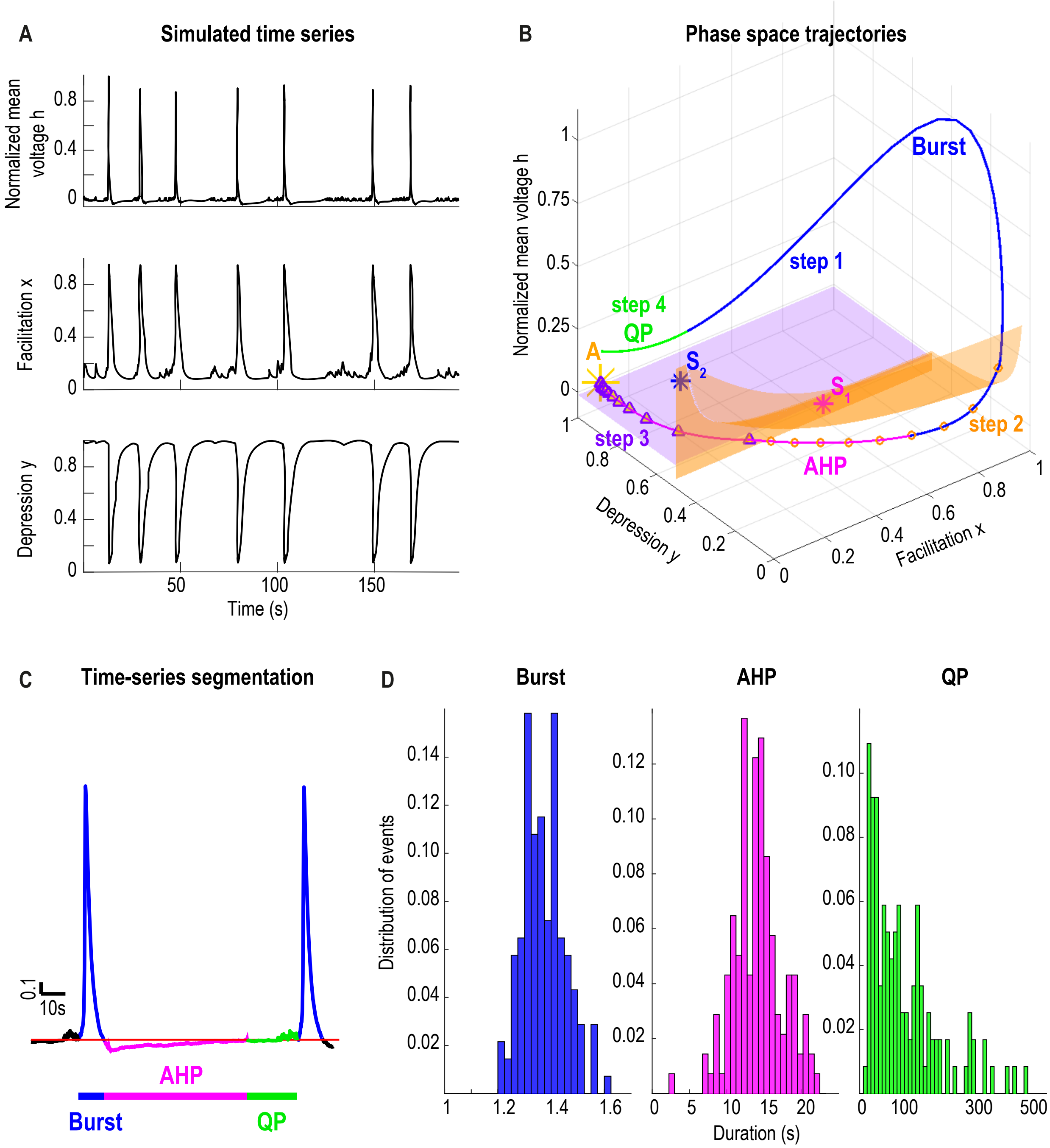

Figure 1.1: **Depression-facilition-AHP model**. **A**. Voltage time series (parameter h) normalized, the facilitation x and the depression y (lower) simulated from eq. (1.2). **B**. Three dimensional phase-space showing a trajectory, decomposed into a QP (green), a burst (blue) and an AHP (pink) phase. The phase-space is divided into 3 regions: 1) the medium dynamics (step 2) of hyperpolarization where $\tau_0 = \tau_{mAHP}$, & $T_0 = T_{AHP}$ under and right of the orange surface. In this region the trajectory is highlighted with orange circles. 2) The slow recovery dynamics (step 3, $\tau_0 = \tau_{sAHP}$ & $T_0 = 0$, region under the purple plan), where the trajectory is highlighted with purple triangles. 3) The fast dynamics (steps 1 and 4, $\tau_0 = \tau$ & $T_0 = 0$). Here $Y_{AHP} = 0.85$, $Y_h = 0.5$ and $H_{AHP} = -7.5$. **C**. Segmentation of the time series in burst (blue) and IBI: AHP (pink) and QP (green). **D**. Distribution of bursts (left, blue), AHP (center, pink) and QP (right, green) durations from numerical simulations lasting $10^4 s$.

Attractor. The first equilibrium point A is given by $h = 0, x = X, y = 1$ (fig.1.1B and 1.2A, yellow star) and the Jacobian at this point is given by

$$J_A = \begin{pmatrix} \dfrac{-1 + JX}{\tau} & 0 & 0 \\ K(1 - X) & -\dfrac{1}{\tau_f} & 0 \\ LX & 0 & -\dfrac{1}{\tau_r} \end{pmatrix}. \tag{1.3}$$

The eigenvalues $(\lambda_1, \lambda_2, \lambda_3) = \left(\dfrac{-1 + JX}{\tau}, -\dfrac{1}{\tau_f}, -\dfrac{1}{\tau_r} \right)$ are real strictly negative. With the parameters of Table 1.1, we obtain three orders of magnitude $|\lambda_1| = 12.6 \gg |\lambda_2| = 1.1 \gg |\lambda_3| = 0.34$. The dynamics near the attractor is thus very anisotropic, restricted to the plan perpendicular to the eigenvector associated to the highest eigenvalue $|\lambda_1|$.

Saddle-points S_1 and S_2. The other steady-state solutions are given by $Jxy = 1$ thus,

$$\frac{X - x}{\tau_f} + K(1 - x)(h - T - T_0) = 0 \Leftrightarrow h = T + T_0 + \frac{x - X}{\tau_f K(1 - x)},$$

leading to

$$\frac{1 - \dfrac{1}{Jx}}{\tau_r} - \frac{L}{J} \frac{X - x}{\tau_f K(1 - x)} = 0 \Leftrightarrow (J\tau_f K + L\tau_r)x^2 - (\tau_f K(J + 1) + LX\tau_r)x + \tau_f K = 0.$$

The discriminant is

$$\Delta = (\tau_f K(J + 1) + LX\tau_r)^2 - 4(J\tau_f K + L\tau_r)\tau_f K > 0, \tag{1.4}$$

leading to

$$\begin{aligned} x_{1,2} &= \frac{\tau_f K(J + 1) + LX\tau_r \pm \sqrt{\Delta}}{2(J\tau_f K + L\tau_r)} \\ y_{1,2} &= \frac{1}{Jx_{1,2}} \\ h_{1,2} &= T + T_0 + \frac{x_{1,2} - X}{\tau_f K(1 - x_{1,2})}. \end{aligned} \tag{1.5}$$

The Jacobians at these points are

$$J_{S_{1,2}} = \begin{pmatrix} 0 & \dfrac{Jy_{1,2}(h_{1,2} - T - T_0)^+}{\tau_0} & \dfrac{Jx_{1,2}(h_{1,2} - T - T_0)^+}{\tau_0} \\ K(1 - x_{1,2}) & -\dfrac{1}{\tau_f} - K(h_{1,2} - T - T_0)^+ & 0 \\ -\dfrac{L}{J} & -Ly_{1,2}(h_{1,2} - T - T_0)^+ & -\dfrac{1}{\tau_r} - Lx_{1,2}(h_{1,2} - T - T_0)^+. \end{pmatrix} \tag{1.6}$$

With the parameter values of Table 1.1, $y_{1,2} > Y_h$ and thus $T_0 = 0$. Moreover, $\dot{y}_{|y_{1,2}} < 0$ so $\tau_0 = \tau$. We computed numerically the eigenvalues of the matrices $J_{S_{1,2}}$. The first saddle point S_1 has one real strictly negative eigenvalue and two complex-conjugate eigenvalues with positive real-parts $(\lambda_1, \lambda_2, \lambda_3) = (-5.06, 1.05 + 1.16i, 1.05 - 1.16i)$: S_1 is a saddle-focus (with a repulsive focus and a stable manifold of dimension 1, fig. 1.2B). The second saddle point S_2 has two real negative eigenvalues and one positive one $(\lambda_1, \lambda_2, \lambda_3) = (-4.58, -0.25, 3.01)$, it is a saddle-point with a stable manifold of dimension two and unstable of dimension one (fig. 1.2C).

Two dimensional separatrix Σ: boundary of long excursions away from the stable equilibrium A

The deterministic trajectories can be compartmentalized in two categories: 1) bursting trajectories, doing long excursions away from the attractor A before going back and 2) trajectories going straightforwardly back to A. We determine the *bursting boundary* as the separatrix surface Σ (fig. 1.2, cyan surface) passing through S_2 (the stable manifold of S_2) and splitting the phase-space in 2 regions: B_+ situated "above" Σ where deterministic trajectories define bursts and B_-, "below" Σ where trajectories go straight back to A.

To determine Σ, we sampled the (h,x,y)-space with various initial conditions to determine the location where trajectories are confined to B_- and other characterized by a long trajectory away from the attractor in B_+, which describes the bursting phase. Finally, we note that the shape of Σ can become very complex away from the saddle-point S_2, however here our trajectories are confined within the square prism defined by $\{x \in [0, 1] \ \& \ y \in [0, 1]\}$ and our numerical simulations show that in this domain the surface Σ is still simple enough for our approximation and that it does split the phase-space in the two subdomains described (fig. 1.2 and 1.3 cyan surface).

We constructed the separatrix Σ with a precision $\Delta h = 0.01$ for a normalized amplitude of h to 1, which is smaller than the spatial scale of the stochastic component of the simulation $\sigma\sqrt{\tau\Delta t} \approx 0.07$.

To characterize the range of bursting durations, we further determined numerically the durations of the shortest (fig. 1.2D and 1.3 red) and longest (purple) trajectories, starting in the upper neighborhood of the separatrix Σ and ending below $h = 0$ (fig. 1.2D): we found that the fastest and shortest durations are 1s and 0.31s respectively. Note that these durations are measured after departure from Σ (no return, which could be possible in the stochastic case), that could explain the difference with the burst duration histogram (Fig. 1.1D). The extreme trajectories are determined when we sampled the initial condition in the discretized approximation of Σ by a grid $(x_k, y_q) = (k\Delta x, q\Delta y) \in [0, 1]^2$, where we used the resolution $\Delta x = \Delta y = 0.025$.

1.1.3 Distribution of exit points

To characterize the distribution of bursting durations, we decided first to focus on the distribution of exit points from the region B_- located on the surface Σ. Our rational was the dominant dynamics above Σ is deterministic. Thus any fluctuation should come from the statistics of the exit points distribution.

Distribution of exit points obtained from stochastic simulations

We first ran stochastic simulations of system (1.2) with the attractor $A = (0, X, 1)$ as initial point for a fixed noise amplitude. For each burst, we recorded the intersection point (exit point) of the trajectory

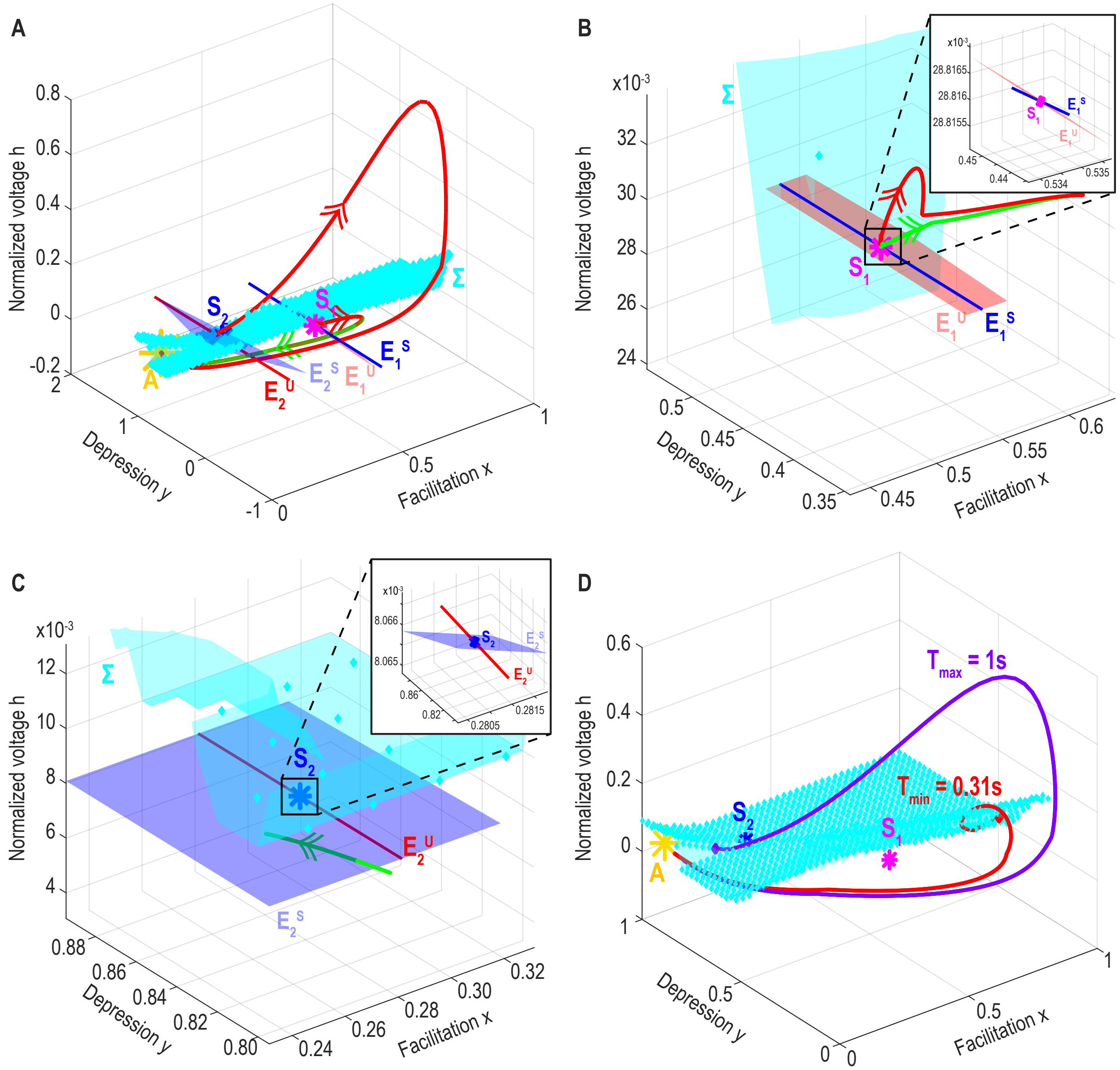

Figure 1.2: **Phase-space dynamics starting from saddle points. A**. Repulsive trajectories starting near S_1 (pink) and S_2 (blue) with corresponding stable and unstable eigenspaces E^U and E^S. **B**. Inset around S_1. Linear 2D-unstable eigenspace E_1^U (light red plane) and linear 1D-stable eigenspace E_1^S (blue line). **C**. Magnification around S_2: linear 1D-unstable eigenspace E_2^U (red line) and linear 2D-stable eigenspace E_1^S (blue plane). **D**. Plot of the longest (purple) and shortest (red) trajectories starting just above Σ.

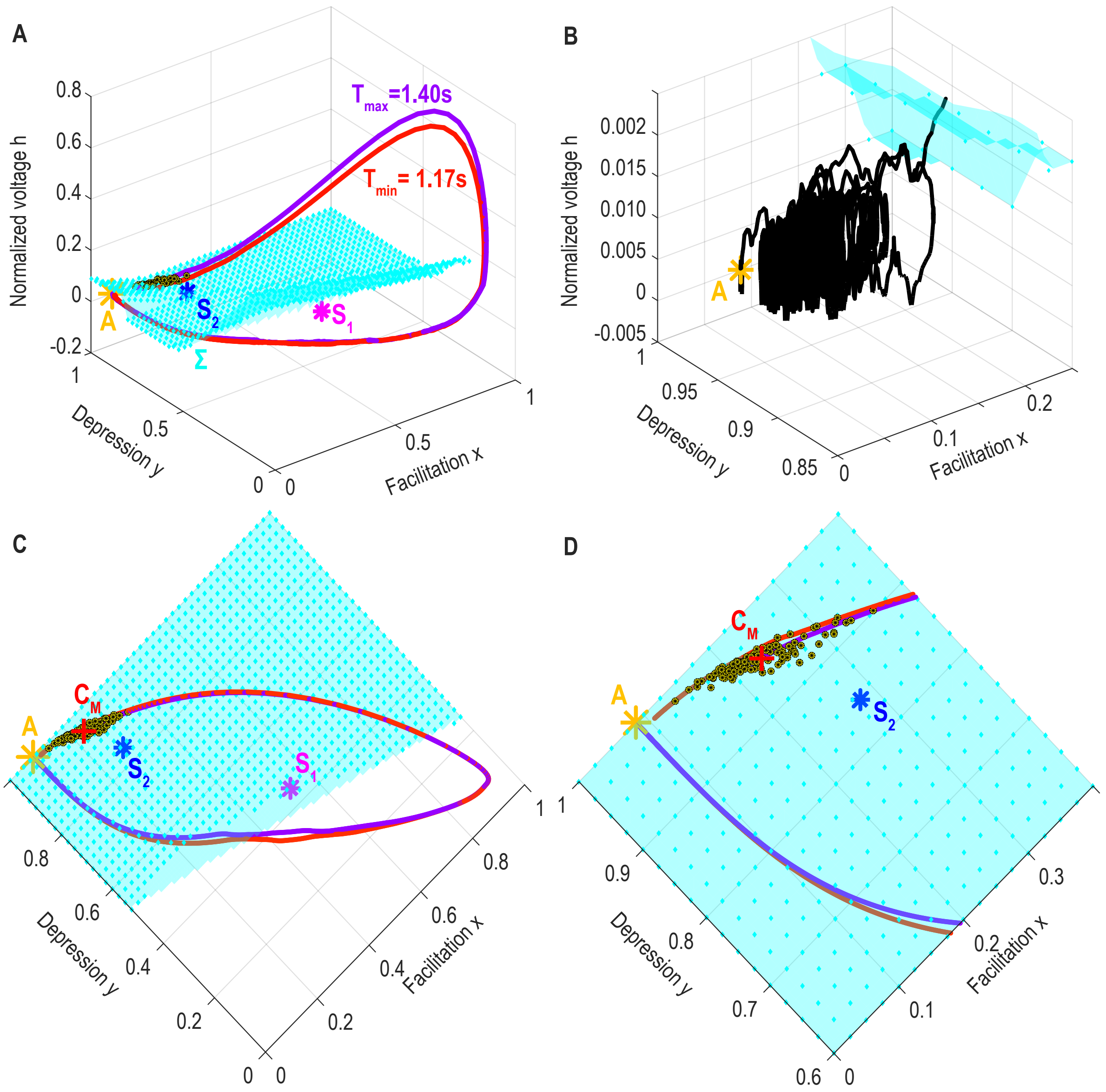

Figure 1.3: **Stochastic dynamics in the phase-space of model (1.2).** **A**. Distribution of exit points (black dots on Σ) of system (1.2) starting from A (5000s runs with variance $\sigma = 3$) with the longest (purple) and shortest (red) trajectories. **B**. Example of an escaping trajectory (black) starting from A (yellow star), making multiple short loops before exit. **C**. Top view of **A** and center of mass C_M of the exit points (red cross). **D**. Magnification of **C**.

and Σ (fig. 1.3). In this region of the phase-space, the dynamics simplifies to the system (1.1) without AHP, which can be written in the matrix form

$$\dot{\boldsymbol{s}} = \boldsymbol{B}(\boldsymbol{s}) + \sqrt{\boldsymbol{\sigma}}\dot{W} \tag{1.7}$$

where $\boldsymbol{s} = (h, x, y)^T$ and

$$\boldsymbol{B}(\boldsymbol{s}) = \begin{pmatrix} b_1(\boldsymbol{s}) = -\dfrac{h}{\tau} + \dfrac{Jxyh^+}{\tau} \\ b_2(\boldsymbol{s}) = \dfrac{X - x}{\tau_f} + K(1-x)h^+ \\ b_3(\boldsymbol{s}) = \dfrac{1-y}{\tau_r} - Lxyh^+ \end{pmatrix} \tag{1.8}$$

and $\sqrt{\boldsymbol{\sigma}} = diag\left(\sqrt{\dfrac{\sigma}{\tau}}, 0, 0\right)$.

Distribution of exit points obtained from solving the Fokker-Planck equation

At this stage, we decided to compare the empirical distribution with the probability density function (pdf) $q(\boldsymbol{s})$ obtained form the steady-state renewal Fokker-Planck equation (FPE) [125, 128], when the initial point is A. We obtained the following result:

Theorem 1.1 *For stochastic trajectories of system* (1.2) *starting in the neighborhood of the attractor A, the distribution p_Γ of exit points located on the separatrix Γ is given per unit surface $d\boldsymbol{s}$ by*

$$p_\Gamma(\tilde{s}|\boldsymbol{s}_0) = \frac{J(\tilde{s}|\boldsymbol{s}_0) \cdot \nu(\tilde{s}) d\tilde{s}}{\oint_\Sigma J(\tilde{s}|\boldsymbol{s}_0) \cdot \nu(\tilde{s}) d\tilde{s}} \; for \; \tilde{s} \in \Sigma \tag{1.9}$$

where the probability flux is

$$J(\tilde{s}|\boldsymbol{s}_0) = \begin{pmatrix} \dfrac{Jxy - 1}{\tau} h q(\tilde{s}) - \dfrac{\sigma}{2\tau}\dfrac{\partial q(\tilde{s})}{\partial h} \\ \left(\dfrac{X - x}{\tau_f} + K(1-x)h\right) q(\tilde{s}) \\ \left(\dfrac{1-y}{\tau_r} - Lxyh\right) q(\tilde{s}) \end{pmatrix}, \tag{1.10}$$

$\nu(\tilde{s})$ is the unit normal vector at the point $\tilde{s}$ and q is the solution of the steady-state renewal degenerated Fokker-Planck equation

$$-\frac{\partial}{\partial h}\left[\frac{(Jxy-1)h}{\tau} q\right] - \frac{\partial}{\partial x}\left[\left(\frac{X-x}{\tau_f} + K(1-x)h\right) q\right] - \frac{\partial}{\partial y}\left[\left(\frac{1-y}{\tau_r} - Lxyh\right) q\right] + \frac{\sigma}{2\tau}\frac{\partial^2}{\partial h^2} q = \delta(\boldsymbol{s} - A)$$

with the absorbing boundary condition

$$q(\boldsymbol{s}|A) = 0 \; for \; \boldsymbol{s} \in \Gamma. \tag{1.11}$$

The solution q can be approximated by WKB and has the formal expression

$$q(\tilde{s}|\boldsymbol{s}_0) = q_\sigma(\tilde{s})Q_0(\tilde{s})e^{-\dfrac{\psi(\tilde{s})}{\sigma}}, \tag{1.12}$$

where $q_\sigma(\tilde{s})$ is the boundary layer solution.
Finally, the probability flux can be expressed as

$$J(\tilde{s}|\boldsymbol{s}_0)\cdot\nu(\tilde{s})d\tilde{s} = K_0\tilde{s}^{-\dfrac{\nabla\cdot\boldsymbol{B}_{|S_2}}{\lambda_2}}e^{-\dfrac{\psi(\tilde{s})}{\sigma}}d\tilde{s}, \tag{1.13}$$

where $\nabla\cdot\boldsymbol{B}_{|S_2}$ is the divergence of the field B at the saddle-point S_2, λ_2 is the dominant stable eigenvalue of the Jacobian of B at S_2 and ψ is the solution of the degenerated eikonal equation

$$\frac{(Jxy-1)h}{\tau}\frac{\partial\psi}{\partial h} + \left(\frac{X-x}{\tau_f} + K(1-x)h\right)\frac{\partial\psi}{\partial x} + \left(\frac{1-y}{\tau_r} - Lxyh\right)\frac{\partial\psi}{\partial y} + \frac{1}{2\tau}\left(\frac{\partial\psi}{\partial h}\right)^2 = 0. \tag{1.14}$$

Proof: This density is obtained by conditioning on trajectories of the process (1.7) that are absorbed on Σ. It is solution of

$$-\frac{\partial}{\partial h}\left[\frac{(Jxy-1)h}{\tau}q\right] - \frac{\partial}{\partial x}\left[\left(\frac{X-x}{\tau_f} + K(1-x)h\right)q\right] - \frac{\partial}{\partial y}\left[\left(\frac{1-y}{\tau_r} - Lxyh\right)q\right] + \frac{\sigma}{2\tau}\frac{\partial^2}{\partial h^2}q = \delta(\boldsymbol{s}-A) \tag{1.15}$$

where

$$q(\boldsymbol{s}|A) = 0 \text{ for } \boldsymbol{s}\in\Sigma. \tag{1.16}$$

To solve equation (1.15), we search for a WKB approximation of the solution in the form

$$q(\boldsymbol{s}|A) = Q_\sigma(\boldsymbol{s})e^{-\dfrac{\psi(\boldsymbol{s})}{\sigma}}, \tag{1.17}$$

where Q_σ is a regular function with the formal expansion

$$Q_\sigma(\boldsymbol{s}) = \sum_{i=0}^{\infty} Q_i(\boldsymbol{s})\sigma^i. \tag{1.18}$$

The function ψ satisfies the eikonal equation [125, 128]

$$\frac{(Jxy-1)h}{\tau}\frac{\partial\psi}{\partial h} + \left(\frac{X-x}{\tau_f} + K(1-x)h\right)\frac{\partial\psi}{\partial x} + \left(\frac{1-y}{\tau_r} - Lxyh\right)\frac{\partial\psi}{\partial y} + \frac{1}{2\tau}\left(\frac{\partial\psi}{\partial h}\right)^2 = 0. \tag{1.19}$$

We use the method of characteristics to solve the eikonal equation. Setting

$$p = \nabla\psi = \begin{pmatrix} p_1 \\ p_2 \\ p_3 \end{pmatrix}, \tag{1.20}$$

and

$$F(\boldsymbol{s},\psi,p) = b_1(\boldsymbol{s})p_1 + b_2(\boldsymbol{s})p_2 + b_3(\boldsymbol{s})p_3 + \frac{1}{2\tau}p_1^2, \tag{1.21}$$

the characteristics are given by

$$\begin{aligned} \frac{dh}{dt} &= F_{p_1} = b_1 + \frac{1}{\tau}p_1 \\ \frac{dx}{dt} &= F_{p_2} = b_2 \\ \frac{dy}{dt} &= F_{p_3} = b_3, \end{aligned} \tag{1.22}$$

$$\begin{aligned} \frac{dp_1}{dt} &= -F_h = -\frac{Jxy-1}{\tau}p_1 - K(1-x)p_2 + Lxyp_3 \\ \frac{dp_2}{dt} &= -F_x = -\frac{Jyh}{\tau}p_1 + \left(\frac{1}{\tau_f} + Kh\right)p_2 + Lyhp_3 \\ \frac{dp_3}{dt} &= -F_y = -\frac{Jxh}{\tau}p_1 + \left(\frac{1}{\tau_r} + Lxh\right)p_3 \end{aligned} \tag{1.23}$$

and

$$\frac{d\psi}{dt} = \frac{1}{2\tau}p_1^2. \tag{1.24}$$

We solve (1.22)-(1.24) starting at the attractor A, however, this characteristic will be trapped at A. To avoid this difficulty, we follow the method proposed in [125] p.165-170, and we start from points located in a neighborhood V_A of A. In V_A, the solution of the eikonal equation has a quadratic approximation

$$\psi(\boldsymbol{s}) = \frac{1}{2}\boldsymbol{s}^T R\boldsymbol{s} + o(|\boldsymbol{s}|^2). \tag{1.25}$$

To find the matrix R, we linearized the eikonal equation around the attractor A

$$(J_A\boldsymbol{s})^T \cdot \nabla\psi + \frac{1}{2\tau}p_1^2 = 0, \tag{1.26}$$

where J_A is the Jacobian defined in (1.3). Due to the noise present in only one coordinate, this matrix equation (1.26) does not have a unique solution. We shall use the one given by

$$\psi(\boldsymbol{s}) \approx (1-JX)h^2. \tag{1.27}$$

We now follow the method of reconstruction [125] by choosing the initial points on the contours $\psi(\boldsymbol{s}) = \delta = 0.05$, that is

$$h = \pm\sqrt{\frac{\delta}{1-JX}} \approx 0.28. \tag{1.28}$$

We then computed the characteristics numerically (fig. 1.4A-B).
The final step to determine the exit points distribution is to solve the transport equation (3.29)

$$\begin{aligned}\frac{1-Jxy}{\tau}\left(h\frac{\partial Q_0}{\partial h}+Q_0\right)+\left(\frac{1}{\tau_f}+Kh\right)Q_0-\left(\frac{X-x}{\tau_f}+K(1-x)h\right)\frac{\partial Q_0}{\partial x}+\left(\frac{1}{\tau_r}+Lxh\right)Q_0\\ -\left(\frac{1-y}{\tau_r}-Lxyh\right)\frac{\partial Q_0}{\partial y}-\frac{1}{\tau}\frac{\partial Q_0}{\partial h}\frac{\partial \psi}{\partial h}-\frac{Q_0}{2\tau}\frac{\partial^2\psi}{\partial h^2}=0.\end{aligned} \tag{1.29}$$

To find Q_0, we follow the method from [125] p.172-175: we rewrite equation (1.29)

$$\boldsymbol{B}\cdot\nabla Q_0+\frac{1}{\tau}\frac{\partial Q_0}{\partial h}\frac{\partial\psi}{\partial h}=-\left(\nabla\cdot\boldsymbol{B}+\frac{1}{2\tau}\frac{\partial^2\psi}{\partial h^2}\right)Q_0 \tag{1.30}$$

where $\boldsymbol{B}$ is defined in (1.8). Along the characteristics, (1.30) becomes

$$\frac{dQ_0(s(t))}{dt}=\nabla Q_0(s(t))\cdot\frac{d\boldsymbol{s}(t)}{dt}=-\left(\nabla\cdot\boldsymbol{B}(s(t))+\frac{1}{2\tau}\frac{\partial^2\psi(s(t))}{\partial h^2}\right)Q_0(s(t)). \tag{1.31}$$

Our goal is to compute Q_0 on the separatrix and for that purpose, we need to evaluate $\frac{\partial^2\psi(s(t))}{\partial h^2}$ by differentiating the characteristics equations (1.22)-(1.24) with respect to the initial point $\boldsymbol{s}_0=\boldsymbol{s}(0)$. Setting

$$\boldsymbol{s}_j(t)=\frac{\partial\boldsymbol{s}(t)}{\partial\boldsymbol{s}_0^j},\qquad p_j(t)=\frac{\partial p(t)}{\partial\boldsymbol{s}_0^j},\qquad \frac{\partial^2\psi(\boldsymbol{s}(t))}{\partial s^i\partial s^j}=R^{i,j}(t), \tag{1.32}$$

we have $R(t)=P(t)S(t)^{-1}$, where $P(t)$ (resp. $S(t)$) is the matrix with columns $p_j(t)$ (resp. $\boldsymbol{s}_j(t)$). The initial conditions are

$$s_j^i(0)=\delta_{i,j},\qquad p_j^i(0)=\frac{\partial^2\psi(0)}{\partial s^i\partial s^j}=R^{i,j}. \tag{1.33}$$

The dynamics has the form

$$\begin{aligned}
\frac{d\boldsymbol{s}_1^1}{dt} &= \frac{dh_1}{dt} = \left(\frac{\partial b_1}{\partial h} + \frac{1}{\tau}\frac{\partial p^1}{\partial h}\right) h_1\\
\frac{d\boldsymbol{s}_2^1}{dt} &= \frac{dh_2}{dt} = \left(\frac{\partial b_1}{\partial h} + \frac{1}{\tau}\frac{\partial p^1}{\partial h}\right) h_2\\
\frac{d\boldsymbol{s}_3^1}{dt} &= \frac{dh_3}{dt} = \left(\frac{\partial b_1}{\partial h} + \frac{1}{\tau}\frac{\partial p^1}{\partial h}\right) h_3\\
\frac{d\boldsymbol{s}_1^2}{dt} &= \frac{dx_1}{dt} = \qquad \frac{\partial b_2}{\partial x} x_1\\
\frac{d\boldsymbol{s}_2^2}{dt} &= \frac{dx_2}{dt} = \qquad \frac{\partial b_2}{\partial x} x_2\\
\frac{d\boldsymbol{s}_3^2}{dt} &= \frac{dx_3}{dt} = \qquad \frac{\partial b_2}{\partial x} x_3\\
\frac{d\boldsymbol{s}_1^3}{dt} &= \frac{dy_1}{dt} = \qquad \frac{\partial b_3}{\partial y} y_1\\
\frac{d\boldsymbol{s}_2^3}{dt} &= \frac{dy_2}{dt} = \qquad \frac{\partial b_3}{\partial y} y_2\\
\frac{d\boldsymbol{s}_3^3}{dt} &= \frac{dy_3}{dt} = \qquad \frac{\partial b_3}{\partial y} y_3
\end{aligned} \tag{1.34}$$

and because we are only interested in $R^{1,1}$ we only need to compute the first row of $P(t)$, thus

$$\begin{aligned}
\frac{dp_1^1(t)}{dt} &= \left(-\frac{Jxy-1}{\tau}\frac{\partial p^1}{\partial h} - K(1-x)\frac{\partial p^2}{\partial h} + Lxy\frac{\partial p^3}{\partial h}\right) h_1\\
\frac{dp_2^1(t)}{dt} &= \left(-\frac{Jxy-1}{\tau}\frac{\partial p^1}{\partial h} - K(1-x)\frac{\partial p^2}{\partial h} + Lxy\frac{\partial p^3}{\partial h}\right) h_2\\
\frac{dp_3^1(t)}{dt} &= \left(-\frac{Jxy-1}{\tau}\frac{\partial p^1}{\partial h} - K(1-x)\frac{\partial p^2}{\partial h} + Lxy\frac{\partial p^3}{\partial h}\right) h_3.
\end{aligned} \tag{1.35}$$

In the limit $t \to \infty$ the characteristic that hits the saddle point S_2 is tangent to the separatrix and $-\left(\nabla \cdot \boldsymbol{B} + \frac{1}{2\tau}\frac{\partial^2 \psi}{\partial h^2}\right) Q_0 \to -\nabla \cdot \boldsymbol{B}_{|S_2} \approx 1.82$. Indeed, $\frac{\partial^2 \psi}{\partial h^2}$ tends to 0 near the saddle point S_2 as shown in fig. 1.4C. Thus, near the saddle point, we have

$$\frac{dQ_0(s(t))}{dt} = -(\nabla \cdot \boldsymbol{B}_{|S_2} + o(1))Q_0(s(t)). \tag{1.36}$$

The solution is approximated by

$$Q_0(s(t)) = Q_0(s(0))e^{-\nabla \cdot \boldsymbol{B}_{|S_2} t(1+o(1))}. \tag{1.37}$$

Finally, the characteristic $s(t)$ near the saddle point S_2 can be expressed with respect to the arc length $\tilde{s}$:

$$\tilde{s}(t) \approx \int_0^t \sqrt{\dot{s_2}(u)^2}du, \tag{1.38}$$

where s_2 is the dominant coordinate of $s \in \Sigma$ in the eigenvectors basis of the jacobian J_{S_2} of system (1.2) at S_2, ($\lambda_1 \approx -4.58$ and $\lambda_2 \approx -0.25$), thus locally

$$\tilde{s}(t) \approx \int_0^t \sqrt{s_2(0)e^{2\lambda_2 u}}du, \tag{1.39}$$

and

$$\tilde{s}(t) \approx \int_0^t \sqrt{s_2(0)e^{2\lambda_2 u}}du = s_2(0)\frac{e^{\lambda_2 t}-1}{\lambda_2}. \tag{1.40}$$

Finally, using (1.37) and (1.40), we obtain locally

$$Q_0(\tilde{s}) = Q_0(0)\tilde{s}^{-\frac{\nabla \cdot \boldsymbol{B}_{|S_2}}{\lambda_2}}, \tag{1.41}$$

where $-\frac{\nabla \cdot \boldsymbol{B}_{|S_2}}{\lambda_2} \approx -7.23$.
The distribution of exit points is constructed from the solution q of the FPE (1.15) by accounting for the boundary layer function q_σ that has to be added to the transport solution in the form $Q_0 q_\sigma$, such that this product now satisfies the absorbing boundary condition (1.16). We do not compute here q_σ as the computation follows the one of [125] p. 182-183 near the separatrix. It is a regular function of the form $-\sqrt{\frac{2}{\pi}}\int_0^{\rho\gamma(s_1,s_2)/\sqrt{\sigma}} e^{-\eta^2/2}d\eta$, where ρ is the distance to the separatrix Σ in a neighborhood of S_2 and $\gamma(s_1, s_2)$ is a regular function.
Finally, the exit point distribution per unit surface $d\boldsymbol{s}$ is given by

$$p_\Sigma(\tilde{s}|\boldsymbol{s}_0) = \frac{J(\tilde{s}|\boldsymbol{s}_0)\cdot \nu(\tilde{s})d\tilde{s}}{\oint_\Sigma J(\tilde{s}|\boldsymbol{s}_0)\cdot \nu(\tilde{s})d\tilde{s}} \text{ for } \tilde{s} \in \Sigma \tag{1.42}$$

where the probability flux is

$$J(\tilde{s}|\boldsymbol{s}_0) = \begin{pmatrix} \frac{Jxy-1}{\tau}hq(\tilde{s}) - \frac{\sigma}{2\tau}\frac{\partial q(\tilde{s})}{\partial h} \\ \left(\frac{X-x}{\tau_f} + K(1-x)h\right)q(\tilde{s}) \\ \left(\frac{1-y}{\tau_r} - Lxyh\right)q(\tilde{s}) \end{pmatrix}, \tag{1.43}$$

and $\nu(\tilde{s})$ is the unit normal vector at the point $\tilde{s}$. The flux is computed by differentiating expression (1.17) on the boundary

$$q(\tilde{s}|\boldsymbol{s}_0) = q_\sigma(\tilde{s})Q_0(\tilde{s})e^{-\frac{\psi(\tilde{s})}{\sigma}}. \tag{1.44}$$

We obtain

$$\begin{aligned} J(\tilde{s}|\boldsymbol{s}_0)\cdot \nu(\tilde{s})d\tilde{s} &= -\sqrt{\frac{2\sigma}{\pi}}q(\tilde{s}|\boldsymbol{s}_0)\gamma(s_1, s_2)d\tilde{s} \\ &= K_0\tilde{s}^{-\frac{\nabla \cdot \boldsymbol{B}_{|S_2}}{\lambda_2}}e^{-\frac{\psi(\tilde{s})}{\sigma}}d\tilde{s}, \end{aligned} \tag{1.45}$$

where $\gamma(s_1, s_2)$ has been approximated by its value at $\tilde{s} = 0$. Furthermore, in the limit $\tilde{s} \to 0$, $\tilde{s}^{-\frac{\nabla \cdot \boldsymbol{B}_{|S_2}}{\lambda_2}}$ tends to infinity, however it is compensated by $e^{-\frac{\psi(\tilde{s})}{\sigma}}$ which is small enough, as we observe numerically. We plotted the distribution of exit points in fig. 1.4D-E for $K_0 = 1$. Finally, we compare the distribution p_Σ with the one obtained from the stochastic simulations of system (1.2) with the same level of noise ($\sigma = 3$). Both distributions are peaked, showing that the exit points are constrained in a small area of the separatrix. $\square$

To conclude this part, our two different methods confirm that the exit point distribution is peaked, thus the trajectories associated to the bursting periods are confined in a tubular neighborhood of a generic trajectory and thus the distribution of the bursting times is peaked, as observed in fig. 1.1D. Finally, the distribution of bursting durations should be quite concentrated near a deterministic value.

1.2 Computing the burst and AHP durations

How the burst duration depends on specific parameters such as the neuronal connectivity, the characteristic time of depression, facilitation or AHP durations is usually very difficult to address from a computational point of view. Indeed, it requires integrating a nonlinear dynamical system. Most of the time, the sensitivity analysis to parameters is explored numerically by sampling a certain fraction of the phase space. However, we shall show here that it is possible to get some expressions for the bursting and IBI durations.

1.2.1 Deriving explicit expressions for the bursting and the AHP durations

In this section we develop an approximation procedure to compute the mean bursting and afterhyperpolarization durations from the AHP facilitation-depression model (1.2).

The approximation procedure is based on the following considerations: because in the first phases of burst and AHP, the voltage h evolves much faster than the facilitation x and depression y, to compute the duration of the bursting phase, we will replace the dynamics of h in the depression and facilitation equations by a piecewise constant function $H(t)$ (fig.1.5). This approximation decouples the system (1.2), thus x and y can be computed. Indeed, h increases quickly from 0 to a high value in less than 100 ms and then decays. Since we are interested in the decay phase, we will freeze the value of h in equation (1.47) for x and y in the time interval $[0, t_1]$ (the time t_1 will be estimated in section 1.2.3) to a high value H_1 (to be determined). Moreover, in the interval $[t_1, t_2]$, we will fix the value of h to a constant H_2 (to be determined) to account for the AHP phase. Then we will re-compute h using the approximated equations for x and y. We will then examine numerically how the unperturbed and perturbed solutions differs. Note that we are interested in the longer time phase (thus the different behavior of the solutions in the short-time will not matter much) so that we will able to use the analytical formulas to compute the burst and the AHP durations.

We shall now specify the function $H(t)$. In the bursting phase, it is constant equal to H_1 for $t \in [0; t_1]$. In the hyperpolarization phase, $H(t) = H_2$ for $t \in [0; t_2]$. For $t > t_2$ (that will also be specified in

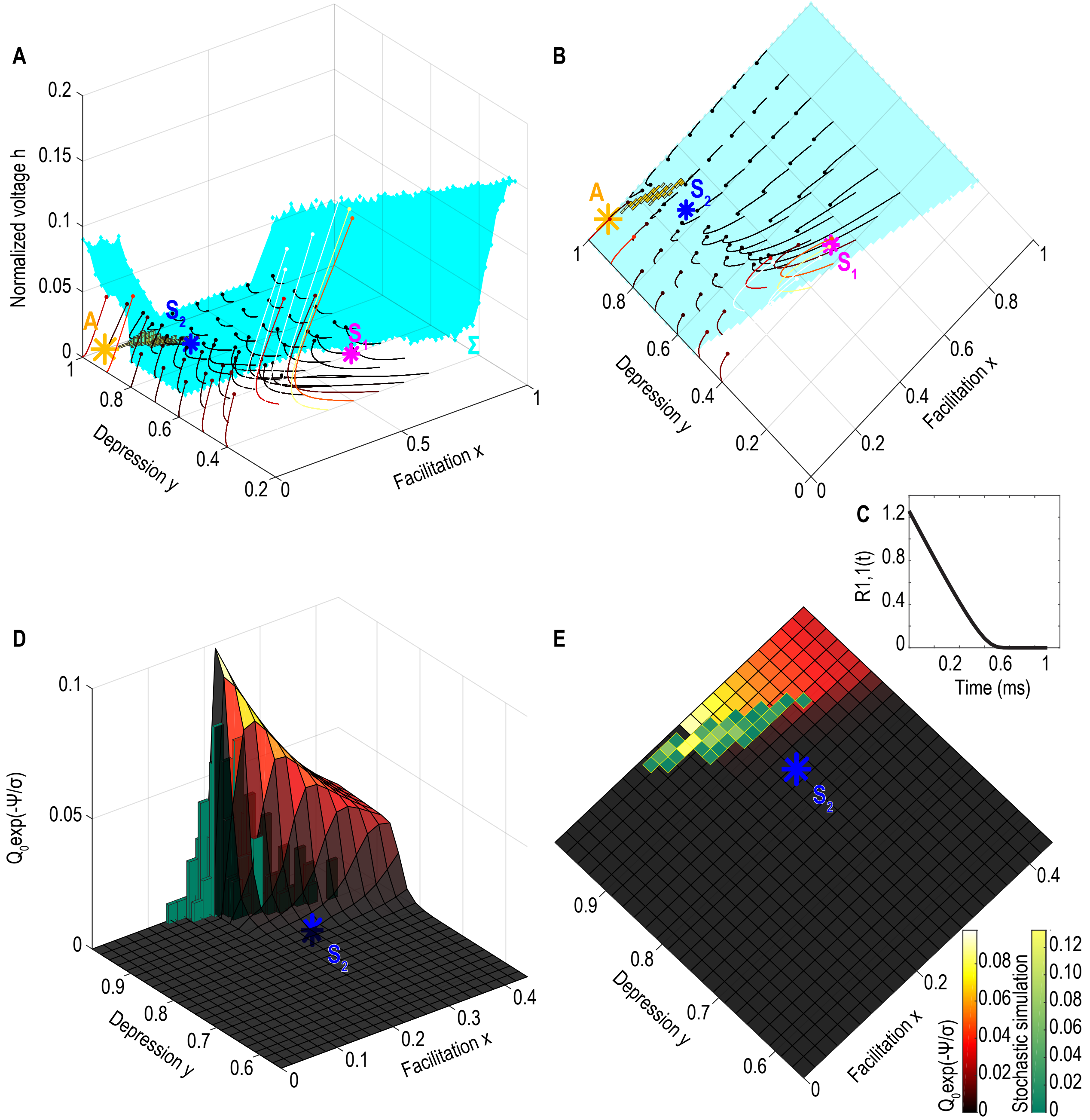

Figure 1.4: **Exit point distributions: characteristics vs stochastic realizations. A-B**. Characteristics crossing the separatrix Σ (the darker the line color is, the lower the value of ψ on Σ is) and distribution of exit points obtained from numerical simulations (yellow); visualized with two different angles. **C**. Element $R^{1,1}(t) = \dfrac{\partial^2 \psi}{\partial h^2}$ of the matrix 1.32 vs time along the characteristics computed numerically. **D-E**. pdf of the exit points $p_\Sigma = Q_0 e^{-\dfrac{\psi}{\sigma}}$ on the separatrix Σ compared to the distribution obtained from the stochastic simulations (green histogram), visualized with two different angles.

section 1.2.3), we choose $H(t) = 0$ to account for the recovery phase.

$$H(t) = \begin{cases} H_1, & \text{for } t \in [0, t_1] \\ H_2, & \text{for } t \in]t_1, t_2] \\ 0 & \text{for } t > t_2. \end{cases} \tag{1.46}$$

The approximated system of equations becomes:

$$\begin{aligned} \tau_0 \dot{h} &= -(h - T_0(t)) + Jxy(h - T_0(t))^+ \\ \dot{x} &= \frac{X - x}{\tau_f} + K(1 - x)H(t) \\ \dot{y} &= \frac{1 - y}{\tau_r} - LxyH(t) \end{aligned} \tag{1.47}$$

where the AHP is accounted for by changing the threshold and timescales as follows

$$T_0(t) = \begin{cases} 0 & \text{for } t \in [0, t_1] \\ T_{AHP} & \text{for } t \in]t_1, t_2] \\ 0 & \text{for } t > t_2 \end{cases} \quad \text{and} \quad \tau_0(t) = \begin{cases} \tau & \text{for } t \in [0, t_1] \\ \tau_{mAHP} & \text{for } t \in]t_1, t_2] \\ \tau_{sAHP} & \text{for } t > t_2. \end{cases} \tag{1.48}$$

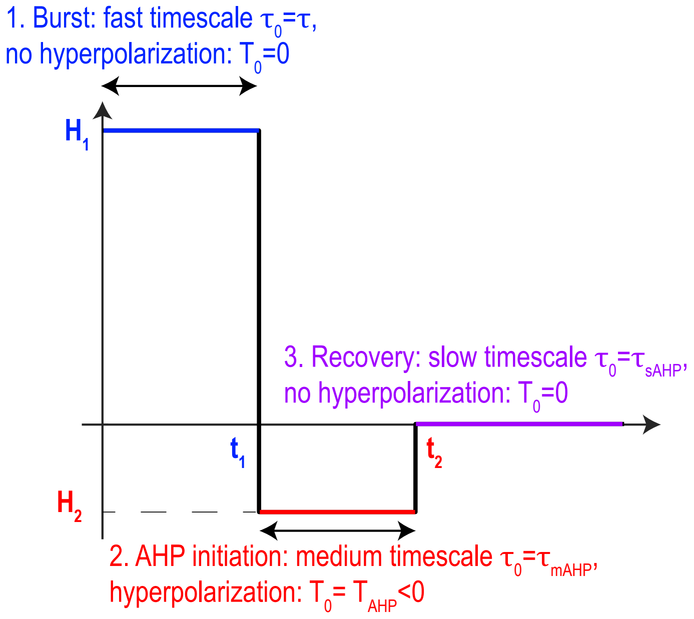

Figure 1.5: Approximated voltage step function $H(t)$.

Proposition 1.1 Analytical formulas for the burst t_i and AHP durations $\Delta_{AHP} = t_e - t_i$. *For the three-dimensional dynamical system defined by equation* (6)*, if the parameters* $\tau_0 \ll \tau_f, \tau_0 \ll \tau_r$ *or* $\tau_f \gg \tau_0, \tau_0 \gg \tau_r$ *then:*

(i) System (1.47) *can be integrated piece-wise yielding analytical formulas for the three variables* h *(equations 1.58-1.65-1.68),* x *(equations 1.51-1.59-1.66) and* y *(equations 1.55-1.61-1.67),*

(ii) *The burst duration* t_i *is defined by the equation* $h(t_i) = 0$*, which can be inverted analytically, yielding the expression*

$$t_i \approx t_1(J) + \frac{-\Lambda - \sqrt{\Lambda^2 + 4\tilde{\Lambda}\frac{\tau_{mAHP}}{J}\ln\left(\frac{-T_{AHP}}{h_0 - T_{AHP}}\right)}}{2\tilde{\Lambda}}, \tag{1.49}$$

where $t_1(J)$*,* $\Lambda = \Lambda(J, K, L, H_2, t_1(J))$ *and* $\tilde{\Lambda} = \tilde{\Lambda}(K, L, H_2, t_1(J))$ *are smooth explicit functions of the parameters* J, K, L *and* H_2 *of system* (6) *calculated in section 1.2 pages 63 and 65.*

(iii) *The AHP duration* $\Delta_{AHP} = t_e - t_i$ *is solution of equation* $h(t_e) = \epsilon$ *which can be explicitly inverted and is given by*

$$t_e \approx t_2(J) + \left(\frac{\tau_{sAHP}}{J}\ln\left(\frac{h(t_2)}{\epsilon}\right) + f(X, \tau_f, \tau_r)\right)\frac{J}{JX - 1}, \tag{1.50}$$

where f *is a rational function of parameters* X*,* τ_f *and* τ_r *explicited page 66.*

Proof: The proof of proposition 1.1 is divided into three subsections, first in subsection 1.2.2 we prove (i) and calculate the analytical expressions of h, x and y. Then, in subsection 1.2.3 we identify the times t_1 and t_2 for the piece-wise decomposition and finally, in subsection 1.2.4 we derive the explicit formulas (1.49) and (1.50).

1.2.2 Explicit representation of the facilitation, depression and voltage variables in three phases

Phase 1 $[0, t_1]$

To integrate the facilitation and depression equations in (1.47), we note that during the bursting phase (fig. 1.5, phase 1, blue) $H(t) = H_1$ with the initial conditions: $x(0) = X$ and $y(0) = 1$ (resting values). We obtain

$$x(t) = A_1 e^{-\alpha_1 t} + B_1, \tag{1.51}$$

where

$$\alpha_1 = \frac{1}{\tau_f} + KH_1, \qquad A_1 = \frac{KH_1(X-1)}{\alpha_1}, \qquad B_1 = \frac{\frac{X}{\tau_f} + KH_1}{\alpha_1}. \tag{1.52}$$

Injecting expression (1.51) in the third equation of system (1.47), we obtain

$$\dot{y} = \frac{1-y}{\tau_r} - L(A_1 e^{-\alpha_1 t} + B_1)H_1 y$$

The solution is

$$y(t) = \left(C_1 + \frac{1}{\tau_r}\int_0^t \exp(f_1(s))ds\right)\exp(-f_1(t)), \tag{1.53}$$

where the function

$$f_1(t) = \beta_1 t - \frac{LA_1H_1}{\alpha_1} e^{-\alpha_1 t}.$$

To approximate the integral $\int_0^t \exp(f_1(s))ds$, we use that f_1 is monotonic on the interval $[0;t_1]$, thus using a Taylor's expansion at order 1, we get

$$\int_0^t \exp(f_1(s))ds \approx \exp(f_1(t)) \int_0^t \exp(f_1'(t)(s-t))ds = \frac{\exp(f_1(t))}{f_1'(t)}(1-\exp(-tf_1'(t))). \tag{1.54}$$

Using expression (1.53), we obtain for $t \in [0, t_1]$

$$y(t) \approx \left(\frac{1}{\tau_r} \frac{(1-\exp(-tf_1'(t)))}{f_1'(t)} \right) + C_1 \exp(-f_1(t)), \tag{1.55}$$

where

$$\beta_1 = \frac{1}{\tau_r} + B_1 LH_1 \text{ and } C_1 = \exp\left(-\frac{LH_1A_1}{\alpha_1} \right). \tag{1.56}$$

We now compute the firing rate h: the first equation in system (1.47) is

$$\tau \dot{h} = -h + Jxyh^+ \tag{1.57}$$

where the initial condition is $h(0) = \tilde{H}_1$. We note that for numerical computations, the value of $\tilde{H}_1$ has to be much smaller than H_1 in order to guarantee that the facilitation and depression are immediately in the bursting state (Table 1.3).
A direct integration leads to

$$h(t) = \tilde{H}_1 \exp\left(-\frac{t}{\tau} + \frac{J}{\tau} \int_0^t x(s)y(s)ds \right). \tag{1.58}$$

We derive an explicit expression (appendix 1.3.1) for the solution h using (1.51) and (1.55) for x and y respectively.

Phase 2 $[t_1, t_2]$

The second phase starts at t_1 where $H(t) = H_2$, the equations and the approximation are similar to the paragraph above. However we use the following initial conditions: $x(t_1^-) = x(t_1^+)$ and $y(t_1^-) = y(t_1^+)$. This yields for $t \in [t_1; t_2]$,

$$x(t) = A_2 e^{-\alpha_2 t} + B_2, \tag{1.59}$$

where

$$\alpha_2 = \frac{1}{\tau_f} + KH_2, \qquad A_2 = (x(t_1^-) - B_2)e^{\alpha_2 t_1}, \qquad B_2 = \frac{\frac{X}{\tau_f} + KH_2}{\alpha_2}. \tag{1.60}$$

$$y(t) \approx \left(\frac{1}{\tau_r} \frac{(1 - \exp(-(t - t_1) f_2'(t)))}{f_2'(t)} \right) + C_2 \exp(-f_2(t)), \tag{1.61}$$

where

$$f_2(t) = \beta_2 t - \frac{L A_2 H_2}{\alpha_2} e^{-\alpha_2 t}, \tag{1.62}$$

$$\beta_2 = \frac{1}{\tau_r} + B_2 L H_2 \text{ and } C_2 = y(t_1^-) \exp(f_2(t_1)). \tag{1.63}$$

Finally, we use equation (1.48) for $T_0 = T_{AHP}$ and $\tau_0 = \tau_{mAHP}$ so that the voltage equation reduces to

$$\tau_{mAHP} \dot{h} = -(h - T_{AHP}) + Jxy(h - T_{AHP})^+ \tag{1.64}$$

with the initial condition $h(t_1^+) = h(t_1^-)$. We obtain by a direct integration

$$h(t) = (h(t_1^-) - T_{AHP}) \exp\left(-\frac{t - t_1}{\tau_{mAHP}} + \frac{J}{\tau_{mAHP}} \int_{t_1}^{t} x(s) y(s) ds \right) + T_{AHP}, \tag{1.65}$$

as detailed in appendix 1.3.2.

Phase 3 $[t_2, \infty[$

The recovery phase starts at time t_2 where $H(t) = 0$. We use the following initial conditions: $x(t_2^-) = x(t_2^+)$ and $y(t_2^-) = y(t_2^+)$, leading for $t \geq t_2$ to the representation

$$x(t) = X + (x(t_2^-) - X) \exp\left(-\frac{t - t_2}{\tau_f} \right) \tag{1.66}$$

$$y(t) = 1 + (y(t_2^-) - 1) \exp\left(-\frac{t - t_2}{\tau_r} \right). \tag{1.67}$$

Finally, when $t > t_2$, h enters into a slow relaxation phase, (see relation (1.48)), where $T_0 = 0$ and $\tau_0 = \tau_{sAHP}$, and the initial condition is $h(t_2^-) = h(t_2^+)$. A direct integration of equation (1.47) leads to (see appendix 1.3.3 for the detailed solution)

$$h(t) = h(t_2^-) \exp\left(-\frac{t - t_2}{\tau_{sAHP}} + \frac{J}{\tau_{sAHP}} \int_{t_2}^{t} x(s) y(s) ds \right). \tag{1.68}$$

1.2.3 Identification of the termination times t_1 and t_2

End of phase 1

Following burst activation, medium and slow K^+ channels start to be activated forcing the voltage to hyperpolarize. To account for the overall changes in the voltage dynamics due to this K^+ channels activation, we change the recovery timescale τ_0 to τ_{mAHP} (equation (1.48)) and $H(t)$ to H_2 in (1.46) at

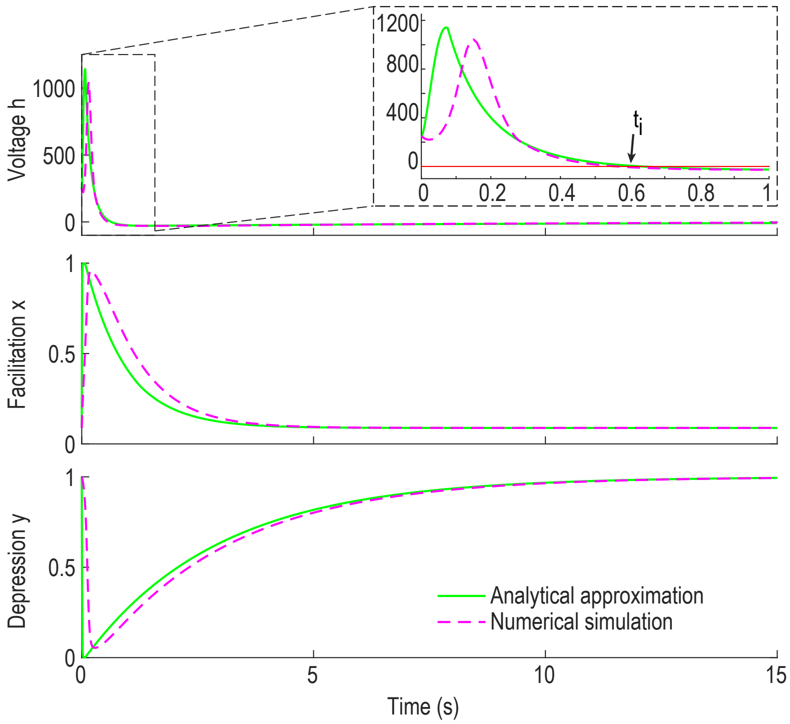

Figure 1.6: Analytical approximation (green) from formulas (1.58, 1.65 and 1.68) for the three phases for h (upper), formulas (1.51, 1.59 and 1.66) for x (center) and (1.55, 1.61 and 1.67) for y (lower) vs exact solutions (dashed magenta) obtained numerically. With an inset of h for $t \in [0, 1]$, showing the burst duration t_i such that $h(t_i) = 0$ (red line: $h = 0$).

time t_1. In practice the hyperpolarization initiation is defined in the region where h is decreasing after reaching its maximum, as the first time t_1 such that $h(t_1) = h_0$ (expression (1.58)), leading to equation

$$\begin{aligned} &t_1 \frac{B_1 J - \tau_r \beta_1}{\tau_r \beta_1 J} - \frac{1}{\tau_r L H_1 \alpha_1} \ln \left(\frac{1 + \frac{L A_1 H_1}{\beta_1} e^{-\alpha_1 t_1}}{1 + \frac{L A_1 H_1}{\beta_1}} \right) + \frac{e^{-\alpha_1 t_1} - 1}{\alpha_1} \frac{L A_1 H_1 B_1}{\tau_r \beta_1^2} - \frac{e^{-2\alpha_1 t_1} - 1}{2\alpha_1} \frac{(L A_1 H_1)^2 B_1}{\tau_r \beta_1^3} + \\ &\frac{e^{-(\beta_1 + L A_1 H_1) t_1} - 1}{\beta_1 + L A_1 H_1} \frac{B_1 (1 - \tau_r \beta_1)}{\tau_r \beta_1} + \frac{e^{-(\alpha_1 + \beta_1 + L A_1 H_1) t_1} - 1}{\alpha_1 + \beta_1 + L A_1 H_1} \frac{A_1 (-\tau_r \beta_1^2 + \beta_1 - L H_1 B_1)}{\tau_r \beta_1^2} \\ &+ \frac{e^{-(2\alpha_1 + \beta_1 + L A_1 H_1) t_1} - 1}{2\alpha_1 + \beta_1 + L A_1 H_1} \left(-\frac{L A_1^2 H_1}{\tau_r \beta_1^2} + \frac{(L A_1 H_1)^2 B_1}{\tau_r \beta_1^3} \right) + \frac{e^{-(3\alpha_1 + \beta_1 + L A_1 H_1) t_1} - 1}{3\alpha_1 + \beta_1 + L A_1 H_1} \frac{L^2 A_1^3 H_1^2}{\tau_r^2 \beta_1^3} = \frac{\tau}{J} \ln \left(\frac{h_0}{H_1} \right). \end{aligned} \tag{1.69}$$

Equation (1.69) is transcendental and cannot be solved explicitly. However, we will search for an approximated solution by neglecting the exponential terms as shown by the range of our parameters (Tables 1.1 and 1.3), leading to

$$\begin{aligned} t_1 \approx \frac{1}{\Gamma_1} \Bigg(&-\Gamma_2 \ln \left(\frac{1}{1 + \Gamma_3} \right) + \frac{\Gamma_4}{\alpha_1} + \frac{\Gamma_5}{\beta_1 + L A_1 H_1} + \frac{\Gamma_6}{\alpha_1 + \beta_1 + L A_1 H_1} + \frac{\Gamma_7}{2\alpha_1 + \beta_1 + L A_1 H_1} \\ &+ \frac{\Gamma_8}{3\alpha_1 + \beta_1 + L A_1 H_1} + \frac{\Gamma_9}{2\alpha_1} + \frac{\tau}{J} \ln \left(\frac{h_0}{\tilde{H}_1} \right) \Bigg), \end{aligned} \tag{1.70}$$

where

$$\begin{aligned}
&\Gamma_1 = \frac{B_1 J - \tau_r \beta_1}{\tau_r \beta_1 J},\ \Gamma_2 = -\frac{1}{\tau_r L H_1 \alpha_1},\ \Gamma_3 = \frac{L A_1 H_1}{\beta_1},\ \Gamma_4 = \frac{L A_1 H_1 B_1}{\tau_r \beta_1^2},\ \Gamma_5 = \frac{B_1(1 - \tau_r \beta_1 e^{\frac{L A_1 H_1}{\alpha_1}})}{\tau_r \beta_1},\\
&\Gamma_6 = \frac{A_1(-\tau_r \beta_1^2 e^{\frac{L A_1 H_1}{\alpha_1}} + \beta_1 - L H_1 B_1)}{\tau_r \beta_1^2},\ \Gamma_7 = \frac{L A_1^2 H_1}{\tau_r \beta_1^2}\left(\frac{L H_1 B_1}{\beta_1} - 1\right),\ \Gamma_8 = \frac{L^2 A_1^3 H_1^2}{\tau_r^2 \beta_1^3} \text{ and}\\
&\Gamma_9 = -\frac{(L A_1 H_1)^2 B_1}{\tau_r \beta_1^3}.
\end{aligned} \tag{1.71}$$

In order to grasp the respective influence of the network parameters J, K and L on t_1, we rewrite formula (1.70) by using the numerical values of all the other parameters (Table 1.1), yielding (see appendix 1.3.5 relation (1.84) for the intermediate formulas)

$$t_1(J) \approx \frac{29J}{2.9 L H_1 - J}\left(F(K,L) + \frac{\tau}{J}\ln\left(\frac{h_0}{\tilde{H}_1}\right)\right), \tag{1.72}$$

where $J \in [3,6]$ and

$$F(K,L) = \exp\left(-0.9\frac{L}{K}\right)\frac{0.01L + K}{0.1L + K}. \tag{1.73}$$

With parameters of Table 1.1, $t_1 \approx 100$ ms, suggesting that the medium and slow K^+ channels start to be activated quite early following burst initiation.

End of phase 2

The second phase is dominated by hyperpolarization and ends when the voltage reaches asymptotically its minimum. In practice we introduce a threshold h_{AHP} so that when the condition $h(t_2) = h_{AHP}$ is satisfied (expression (1.65)), we switch into the third phase (see (1.46) and (1.48)). This leads to equation

$$\begin{aligned}
&(t_2 - t_1)\frac{B_2 J - \tau_r \beta_2}{\tau_r \beta_2 J} - \frac{1}{\tau_r L H_2 \alpha_2}\ln\left(\frac{1 + \frac{L A_2 H_2}{\beta_2} e^{-\alpha_2 t_1} e^{-\alpha_2 (t_2 - t_1)}}{1 + \frac{L A_2 H_2}{\beta_2} e^{-\alpha_2 t_1}}\right) + \frac{e^{-\alpha_2 (t_2 - t_1)} - 1}{\alpha_2} e^{-\alpha_2 t_1}\frac{L A_2 H_2 B_2}{\tau_r \beta_2^2}\\
&-\frac{e^{-2\alpha_2 (t_2 - t_1)} - 1}{2\alpha_2} e^{-2\alpha_2 t_1}\frac{(L A_2 H_2)^2 B_2}{\tau_r \beta_2^3} + \frac{e^{-(\beta_2 + L A_2 H_2)(t_2 - t_1)} - 1}{\beta_2 + L A_2 H_2} e^{-(\beta_2 + L A_2 H_2) t_1}\frac{B_2(1 - C_2 e^{\frac{L A_2 H_2}{\alpha_2}} \tau_r \beta_2)}{\tau_r \beta_2}\\
&\frac{e^{-(\alpha_2 + \beta_2 + L A_2 H_2)(t_2 - t_1)} - 1}{\alpha_2 + \beta_2 + L A_2 H_2} e^{-(\alpha_2 + \beta_2 + L A_2 H_2) t_1}\frac{A_2(-C_2 e^{\frac{L A_2 H_2}{\alpha_2}} \tau_r \beta_2^2 + \beta_2 - L H_2 B_2)}{\tau_r \beta_2^2}\\
&+\frac{e^{-(2\alpha_2 + \beta_2 + L A_2 H_2)(t_2 - t_1)} - 1}{2\alpha_2 + \beta_2 + L A_2 H_2} e^{-(2\alpha_2 + \beta_2 + L A_2 H_2) t_1}\left(-\frac{L A_2^2 H_2}{\tau_r \beta_2^2} + \frac{(L A_2 H_2)^2 B_2}{\tau_r \beta_2^3}\right)\\
&+\frac{e^{-(3\alpha_2 + \beta_2 + L A_2 H_2)(t_2 - t_1)} - 1}{3\alpha_2 + \beta_2 + L A_2 H_2} e^{-(3\alpha_2 + \beta_2 + L A_2 H_2) t_1}\frac{L^2 A_2^3 H_2^2}{\tau_r^2 \beta_2^3} = \frac{\tau_{mAHP}}{J}\ln\left(\frac{h_{AHP} - T_{AHP}}{h_0 - T_{AHP}}\right).
\end{aligned}$$

Contrary to the equivalent expression (1.69), all terms are of the same order and thus we cannot neglect any of them. To estimate the value of t_2, we solve now numerically the transcendental equation

$$\begin{aligned}
&\Lambda_1(t_2-t_1)+\Lambda_2\ln\left(\frac{1+\Lambda_3 e^{-\alpha_2(t_2-t_1)}}{1+\Lambda_3}\right)+\Lambda_4\frac{e^{-\alpha_2(t_2-t_1)}-1}{\alpha_2}+\Lambda_5\frac{e^{-(\beta_2+LA_2H_2)(t_2-t_1)}-1}{\beta_2+LA_2H_2}\\
&+\Lambda_6\frac{e^{-(\alpha_2+\beta_2+LA_2H_2)(t_2-t_1)}-1}{\alpha_2+\beta_2+LA_2H_2}+\Lambda_7\frac{e^{-(2\alpha_2+\beta_2+LA_2H_2)(t_2-t_1)}-1}{2\alpha_2+\beta_2+LA_2H_2}\\
&+\Lambda_8\frac{e^{-(3\alpha_2+\beta_2+LA_2H_2)(t_2-t_1)}-1}{3\alpha_2+\beta_2+LA_2H_2}+\Lambda_9\frac{e^{-2\alpha_2(t_2-t_1)}-1}{2\alpha_2}-\frac{\tau_{mAHP}}{J}\ln\left(\frac{h_{AHP}-T_{AHP}}{h_0-T_{AHP}}\right)=0,
\end{aligned}\tag{1.74}$$

where

$$\begin{aligned}
\Lambda_1&=\frac{B_2J-\tau_r\beta_2}{\tau_r\beta_2J},\ \Lambda_2=-\frac{1}{\tau_rLH_2\alpha_2},\ \Lambda_3=\frac{LA_2H_2}{\beta_2}e^{-\alpha_2t_1},\ \Lambda_4=\frac{LA_2H_2B_2}{\tau_r\beta_2^2}e^{-\alpha_2t_1},\\
\Lambda_5&=\frac{B_2(1-\tau_r\beta_2C_2e^{\frac{LA_2H_2}{\alpha_2}})}{\tau_r\beta_2}e^{-(\beta_2+LA_2H_2)t_1},\\
\Lambda_6&=\frac{A_2(-C_2e^{\frac{LA_2H_2}{\alpha_2}}\tau_r\beta_2^2+\beta_2-LH_2B_2)}{\tau_r\beta_2^2}e^{-(\alpha_2+\beta_2+LA_2H_2)t_1},\\
\Lambda_7&=\frac{LA_2^2H_2}{\tau_r\beta_2^2}\left(\frac{LH_2B_2}{\beta_2}-1\right)e^{-(2\alpha_2+\beta_2+LA_2H_2)t_1},\\
\Lambda_8&=\frac{L^2A_2^3H_2^2}{\tau_r^2\beta_2^3}e^{-(3\alpha_2+\beta_2+LA_2H_2)t_1}\ \text{and}\ \Lambda_9=-\frac{(LA_2H_2)^2B_2}{\tau_r\beta_2^3}e^{-2\alpha_2t_1}.
\end{aligned}\tag{1.75}$$

The time t_2 depends on J and we obtain a numerical approximation for $J \in [2.95, 5.25]$ by fitting a rational function of the same form as the one we obtained for t_1 (appendix fig. 1.9):

$$t_2(J) \approx \frac{43.96J+42.29}{-4.28J+130.4}. \tag{1.76}$$

With our parameters we obtain $t_2 \approx 2$ s (appendix 1.3.6). Finally, we compare the analytical approximation for h, x and y (dashed magenta) with the exact solution obtained using numerical simulations (green) in fig. 1.6. In these computations, we have chosen $H_1 = 8000$ and $H_2 = -1$ such that the analytical approximations for x and y fit well their numerical solutions. Even though the burst peak is slightly before, with a shift of $\approx$ 100ms for the approximated system compared to the unperturbed solution (fig. 1.6 inset), the decreasing phase is similar for both. We use this numerical agreement to justify that we use the approximated system to compute the burst duration, by finding the time t_i such as $h(t_i) = 0$ and in this time range the analytical approximation fits well the numerical solution.

1.2.4 Bursting and AHP durations

Bursting duration

The burst duration is defined from the voltage jump at time $t = 0$ to $h(t) = H_1$ and ends when $h(t_i) = 0$ for the first time. In practice, we use expression (1.65) as in section 1.2.3 for the end of phase

2 however, here $t_i - t_1$ is small enough to allow us to use Taylor expansions to second order leading to the quadratic equation

$$\tilde{\Lambda}(t_i - t_1)^2 + \Lambda(t_i - t_1) - \frac{\tau_{mAHP}}{J} \ln\left(\frac{-T_{AHP}}{h_0 - T_{AHP}}\right) = 0, \tag{1.77}$$

where

$$\tilde{\Lambda} = \left(\frac{\Lambda_2\Lambda_3\alpha_2^2}{2(1+\Lambda_3)^2} + \frac{1}{2}\big(\alpha_2\Lambda_4 + (\beta_2 + LA_2H_2)\Lambda_5 + (\alpha_2 + \beta_2 + LA_2H_2)\Lambda_6 + (2\alpha_2 + \beta_2 + LA_2H_2)\Lambda_7 \right.$$
$$\left. + (3\alpha_2 + \beta_2 + LA_2H_2)\Lambda_8 + 2\alpha_2\Lambda_9\big)\right),$$

and

$$\Lambda = \left(-\frac{\Lambda_2\Lambda_3\alpha_2}{1+\Lambda_3} + \Lambda_1 - \Lambda_4 - \Lambda_5 - \Lambda_6 - \Lambda_7 - \Lambda_8 - \Lambda_9\right)$$

We keep the positive root

$$t_i \approx t_1(J) + \frac{-\Lambda - \sqrt{\Lambda^2 + 4\tilde{\Lambda}\frac{\tau_{mAHP}}{J}\ln\left(\frac{-T_{AHP}}{h_0 - T_{AHP}}\right)}}{2\tilde{\Lambda}}. \tag{1.78}$$

Similarly as for t_1, we give simplified formulas for $\Lambda = \Lambda(J, K, L, H_2, t_1(J))$ and $\tilde{\Lambda} = \tilde{\Lambda}(K, L, H_2, t_1(J))$ depending only on the parameters J, K, L and the threshold H_2 such as

$$\tilde{\Lambda}(K, L, H_2, t_1(J)) = \frac{-0.08 - 0.49KH_2 - 0.66LH_2 + 0.06t_1(J) + 0.54KH_2t_1(J) + 0.1LH_2t_1(J)}{0.27 + 2.26KH_2 + 1.9LH_2} \tag{1.79}$$

and

$$\Lambda(J, K, L, H_2, t_1(J)) = \frac{A(K, L, H_2) + (B(K, L, H_2) + C(K, L, H_2)t_1(J))\,J}{J(\tilde{A} + \tilde{B}J)}, \tag{1.80}$$

where

$$\begin{aligned} A(K, L, H_2) &= 33.3 - 246KH_2 - 143LH_2 \\ B(K, L, H_2) &= 27.2 - 122KH_2 - 106LH_2 \\ C(K, L, H_2) &= 11.6 + 86.3KH_2 + 49.8LH_2 \\ \tilde{A} &= 33.3 \\ \tilde{B}(K, L, H_2) &= 246KH_2 + 143LH_2 \end{aligned} \tag{1.81}$$

The simplified formulas for the intermediary parameters $\Lambda_1 - \Lambda_9$ are given in appendix 1.3.5 formula (1.86) and approximated values are given in Table 1.2.
Using parameters from Table 1.1 and Table 1.3, we obtain $t_i \approx 0.6$ s, which is comparable to the bursting times observed in experimental data [52], and from our numerical simulations in the noiseless case (fig. 1.2D).

AHP duration

The AHP starts at time t_i computed above, however using expression (1.68) the termination time to reach $h(t_e) = 0$ would be infinite. Thus, we introduce a threshold ϵ and define the end of AHP t_e such as $h(t_e) = \epsilon$. In practice, the value ϵ can be estimated from the amplitude of the voltage fluctuations at equilibrium. We obtain from expression (1.68)

$$\left(-\frac{1}{J}+X\right)(t_e-t_2)-\tau_r X(y(t_2)-1)\left(e^{-\frac{t_e-t_2}{\tau_r}}-1\right)-\tau_f(x(t_2)-X)\left(e^{-\frac{t_e-t_2}{\tau_f}}-1\right)$$

$$-\frac{(y(t_2)-1)(x(t_2)-X)\tau_f\tau_r}{\tau_f+\tau_r}\left(e^{-(t-t_2)\frac{\tau_f+\tau_r}{\tau_f\tau_r}}-1\right)=\frac{\tau_{sAHP}}{J}\ln\left(\frac{\epsilon}{h(t_2)}\right)$$

because $t_e - t_2$ is large enough, we neglect the exponential terms so that

$$(t_e-t_2)\left(X-\frac{1}{J}\right)+\tau_r X(y(t_2)-1)+\tau_f(x(t_2)-X)+\frac{(x(t_2)-X)(y(t_2)-1)\tau_f\tau_r}{\tau_f+\tau_r}=\frac{\tau_{sAHP}}{J}\ln\left(\frac{\epsilon}{h(t_2)}\right),$$

leading to

$$t_e=t_2+\left(\frac{\tau_{sAHP}}{J}\ln\left(\frac{\epsilon}{h(t_2)}\right)-\tau_r X(y(t_2)-1)-\tau_f(x(t_2)-X)-\frac{(x(t_2)-X)(y(t_2)-1)\tau_f\tau_r}{\tau_f+\tau_r}\right)\frac{J}{JX-1},$$

This simplifies to

$$t_e \approx t_2(J)+\left(\frac{\tau_{sAHP}}{J}\ln\left(\frac{h(t_2)}{\epsilon}\right)+0.26\right)\frac{J}{1-JX}, \tag{1.82}$$

using the approximated value of t_2 we obtain

$$t_e \approx \frac{43.96J+42.29}{-4.28J+130.4}+\left(\frac{\tau_{sAHP}}{J}\ln\left(\frac{h(t_2)}{\epsilon}\right)+0.26\right)\frac{J}{1-JX}.$$

Using the parameter values from Table 1.1 and Table 1.3 we obtain $t_e \approx 15.4$ s and $\Delta_{AHP} = t_e - t_i \approx 14.3$ s, which is coherent with the durations obtained from the numerical simulations (fig. 1.1D), as well as classical AHP durations found in the literature [38]. □

Study of parameter influence on burst and AHP durations

To evaluate the influence of the main parameters on the bursting and AHP durations we plotted these times vs the recovery timescales τ_{mAHP} and τ_{sAHP}, the hyperpolarization level T_{AHP} and the arbitrary thresholds h_0, $\tilde{H}_1$, h_{AHP} and ϵ. First, the burst duration that varies between 0.5 and 3s, is an increasing function of τ_{mAHP} and does not depend much on T_{AHP} in the range $[-15; -40]$ (fig. 1.7A). In addition, the AHP duration increases with τ_{sAHP}, but in a larger range from 9 to 35s. However, the hyperpolarization level T_{AHP} has a larger influence on this duration (fig. 1.7B). To verify that the arbitrary thresholds that we use do not influence much the burst and AHP durations, we plotted them in fig. 1.7C-F with respect to the phase 1 termination threshold h_0, the phase 2 termination threshold h_{AHP}, the duration of phase 1 t_1 and the AHP termination threshold ϵ, respectively. These figures show that there is almost no dependency with respect to $\tilde{H}_1$ and T_{AHP}, as well as h_0 and h_{AHP} due to the effect of the logarithmic term.

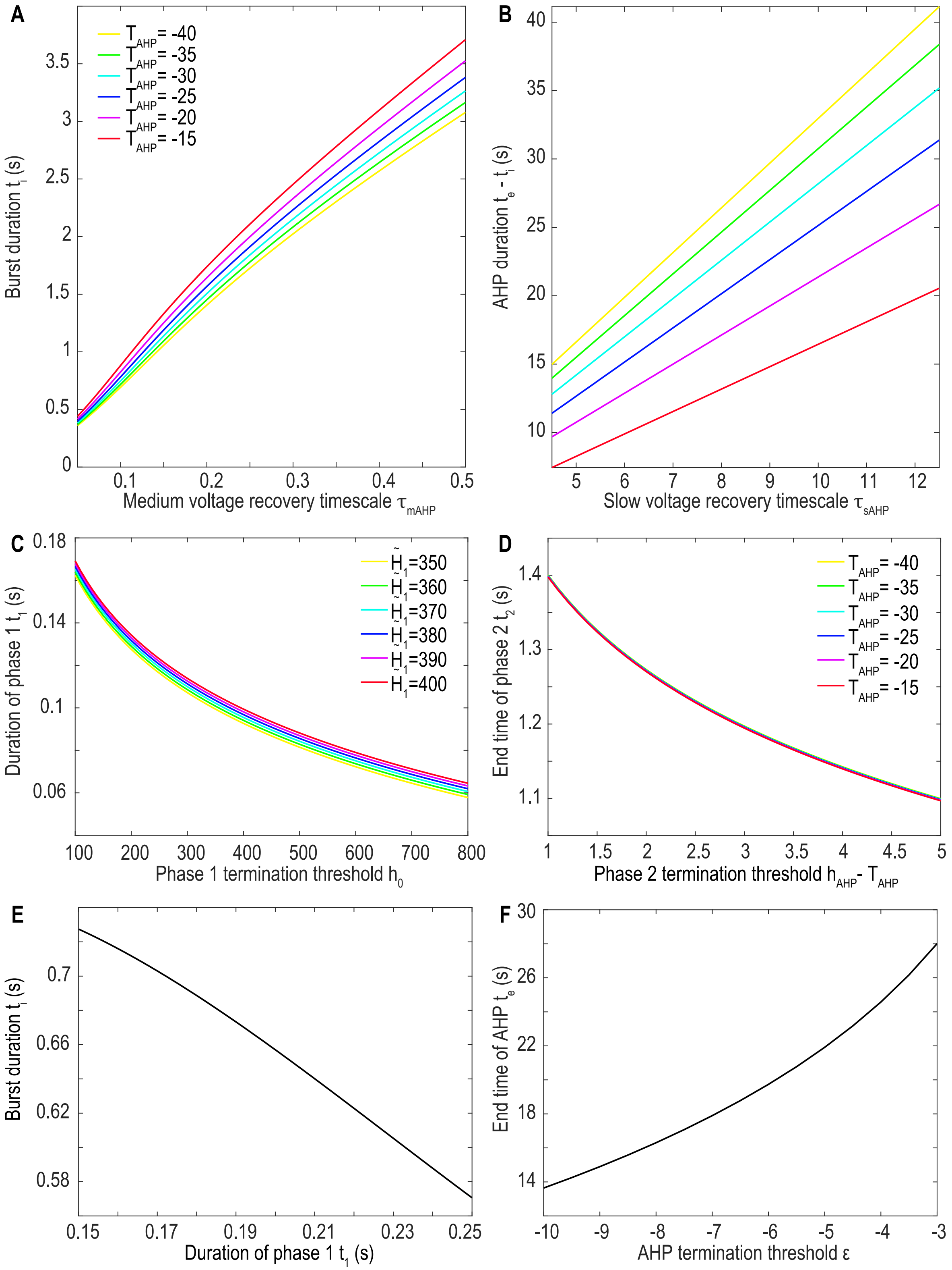

Figure 1.7: **Parameter influence on burst and AHP durations.** **A**. Evolution of the burst duration t_i as a function of the medium timescale τ_{mAHP} for multiple values of the hyperpolarization level T_{AHP}. **B**. Evolution of the AHP duration $t_e - t_i$ as a function of the slow timescale τ_{sAHP} for multiple values of the hyperpolarization level T_{AHP}. **C**. Duration of phase 1 t_1 as a function of its termination threshold h_0 for multiple values of the initial voltage value $h(0) = \tilde{H}_1$. **D**. End time of phase 2 t_2 as a function of its termination threshold h_{AHP} (relatively to T_{AHP}) for multiple values of the hyperpolarization level T_{AHP}. **E**. Bursting duration as a function of t_1 for $\tau_{mAHP} = 0.1s$. **F**. AHP duration as a function of the threshold ϵ for $\tau_{sAHP} = 7.5s$ and $T_{AHP} = -30$.

1.2.5 Burst and IBI durations vs J, K, L parameters

To study the influence of the network connectivity J on burst, AHP and QP durations, we ran numerical simulations of the stochastic system (1.2), where we varied J, as well as the facilitation and depression parameters K and L. To determine the time distributions of burst and IBI, we segmented the traces obtained for 5000 seconds simulations with a noise amplitude $\sigma = 6$ and computed the mean value of the bursts (fig. 1.8A), AHP (fig. 1.8B) and QP durations (fig. 1.8C). Interestingly, we observe two different regimes depending on the values of the parameters: no bursts ($J < 3.05$ for $K = 0.047, L = 0.028$; $J < 3.2$ for $K = 0.037, L = 0.028$; $J < 3.5$ for $K = 0.027, L = 0.028$; fig. 1.8 left column, or $J < 3.7$ for $K = 0.037, L = 0.038$ and $J < 4.1$ for $K = 0.037, L = 0.048$, right column) and bursts followed by AHP (for higher values of J).

Interestingly, in the bursting regime, changing J does not influence much the mean burst duration. However, AHP durations decreases as J increases. Finally, QP durations reach a peak at the transition value of J between the two regimes and then quickly decrease around QP $\approx 25s$. The mean burst durations obtained here are longer than the ones observed in fig. 1.1D, because in these simulations, we used $\sigma = 6$ (vs $\sigma = 3$ for fig. 1.1D). Indeed, the mean burst duration increases with the noise because, at the beginning of the burst, the deterministic part of the trajectory is still perturbed by the noise component, leading to a longer trajectory when the noise level is higher.

We also compared these mean durations to the ones obtained with the analytical formulas (1.78) and (1.82) (fig. 1.8A, B dashed lines) with $K = 0.037$ and $L = 0.028$. To account for the difference in burst durations induced by the noise, we added a constant $c = 0.8s$ to the burst durations obtained from our analytical formula. The burst duration increases slowly with the network connectivity J, which is comparable to the numerical observations (for $J \geq 3.25$, black dashed line). We also compared the analytical AHP duration to the one observed with the numerical results: we obtain a good fit for a small range of J (between $J \in [3.25, 4]$, black dashed lines) but then the AHP value keeps increasing with our analytical result, whereas it is decreasing in the numerical simulations. This difference might be due to the effect of noise that modifies the deterministic behavior of the system.

To conclude, a sufficient connectivity level is necessary to generate bursting, however inside this regime, increasing the level of neuronal connectivity does not change much the bursting times.

Conclusion and discussion

We presented here a novel mean-field model of synaptic short-term plasticity for the voltage, depression and facilitation variables that now accounts for long AHP periods. This model generalizes the facilitation-depression model introduced in [102] and developed in [105,109,146,147]. The AHP significantly increases the interburst duration by introducing a recovery phase after network bursting. When a Gaussian noise of small amplitude is added to the dynamics, it exhibits spontaneous bursts followed by AHP periods. We have studied here the distribution of bursts and of interbursts, decomposed in AHP and QP durations. Interestingly, we found that the distribution of bursts durations is quite concentrated (subsection 1.1.1). To explain this property, we studied the three-dimensional phase-space of the dynamical system (1.2), that contains one attractor and two saddle points. By computing numerically the two-dimensional stable manifold at one of the saddles, we found the distribution of exit points (on this manifold) when the initial point of the stochastic dynamics is located at the attractor. To compute this distribution we used two methods: 1) stochastic simulations, and 2) the method of characteristics to solve the FPE (1.15) in the limit of small noise. In both cases, we found a peaked distribution of exit points close to the saddle point, as predicted for two-dimensional stochastic sys-

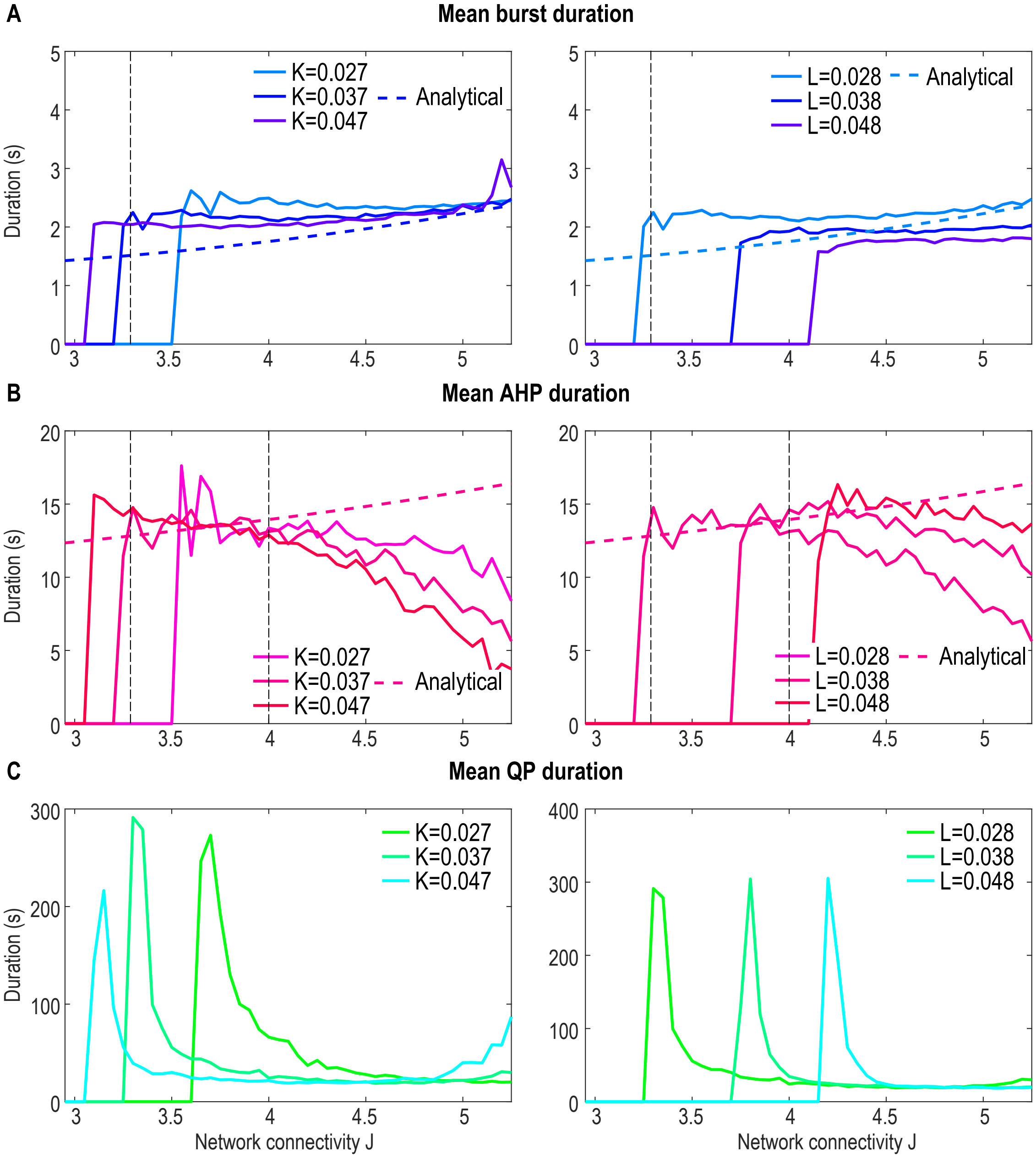

Figure 1.8: **Influence of the network connectivity J on bursting dynamics.** **A**. (resp.**B**, **C**) Mean burst (resp. AHP, QP) duration in seconds from 5000s simulations for J varying from 2.95 to 5.25 and three values of K (left) and L (right) with a fixed noise level ($\sigma = 6$) compared to the analytical result (dashed) obtained for t_1 (1.78) (resp. $\Delta_{AHP} = t_e - t_i$ (1.82)) for $(K, L) = (0.037, 0.028)$. The vertical black dashed lines show the range of validity for J.

tems [125, 148, 149], summarized by expression (1.45). After the stochastic trajectories have crossed the separatrix, they follow an almost deterministic behavior, confirming that the distribution of exit points on the separatrix defines the spread of the distribution of burst durations.

We also derived here analytical formulas (subsection 1.2.4) that reveal the influence of the parameters on burst and AHP durations. These computations can be used to calibrate the AHP parameters with respect to the expected values of burst and AHP durations, that could be measured experimentally. This model could thus be used to decipher the main mechanisms leading to changes in bursting and interburst dynamics, for example when the neuronal network is disrupted, during epilepsy or in the case of a glial network alteration [52].

Classical bursting models describe accurately the burst phase [69, 79, 95, 150], but interburst is often considered as the continuation in the phase-space of the deterministic trajectories. Here the interburst phase is composed of a deterministic refractory period, the AHP, followed by the escape from an attractor due to noise (subsection 1.1.1). During successive bursts, trajectories are not reset at the attractor, but explore the region B_- of non bursting trajectories. This exploration depends on the previous bursting trajectory. Thus, we expect a correlation between successive burst and interburst durations. This correlation may also depend on the amplitude of the voltage fluctuations. Finally, we predict that modifying the AHP duration could affect bursting, because it corresponds to a change in the attractor's position and dominates the effect of synaptic depression.

1.3 Appendix: detailed computations of burst and AHP durations

1.3.1 Integral term of h in phase 1

To compute the integral in expression (1.58), we split it into two parts:

$$\int_0^t x(s)y(s)ds = \underbrace{C_1\int_0^t (A_1e^{-\alpha_1 s}+B_1)e^{-f_1(s)}\,ds}_{I} + \underbrace{\int_0^t (A_1e^{-\alpha_1 s}+B_1)\left(\frac{1-e^{-sf_1'(s)}}{\tau_r f_1'(s)}\right)ds}_{II}\,.$$

We start by I:

$$I = \underbrace{C_1A_1\int_0^t e^{-(\alpha_1+\beta_1)s+\frac{LA_1H_1}{\alpha_1}e^{-\alpha_1 s}}\,ds}_{I_A} + \underbrace{C_1B_1\int_0^t e^{-\beta_1 s+\frac{LA_1H_1}{\alpha_1}e^{-\alpha_1 s}}\,ds}_{I_B}\,.$$

Using a Taylor expansion at first order, $e^{-\alpha_1 s}\approx 1-\alpha_1 s$, we obtain

$$I_A(t)\approx A_1C_1\int_0^t e^{\frac{LA_1H_1}{\alpha_1}-\left(\alpha_1+\beta_1+LA_1H1\right)s}\,ds \approx -\frac{A_1\left(e^{-(\alpha_1+\beta_1+LA_1H1)t}-1\right)}{\alpha_1+\beta_1+LA_1H1}$$

and

$$I_B(t)\approx -\frac{B_1\left(e^{-(\beta_1+LA_1H1)t}-1\right)}{\beta_1+LA_1H1}.$$

Similarly, we write $II = II_A + II_B$, where

$$II_A(t) = \frac{A_1}{\tau_r}\int_0^t \frac{e^{-\alpha_1 s}\left(1-e^{-\beta_1 s - LA_1H_1se^{-\alpha_1 s}}\right)}{\beta_1+LA_1H_1e^{-\alpha_1 s}}ds$$

$$\approx \frac{A_1}{\tau_r\beta_1}\left(\underbrace{\int_0^t \frac{e^{-\alpha_1 s}}{1+\frac{LA_1H_1}{\beta_1}e^{-\alpha_1 s}}ds}_{(i)} - \underbrace{\int_0^t \frac{e^{-(\alpha_1+\beta_1+LA_1H_1)s}}{1+\frac{LA_1H_1}{\beta_1}e^{-\alpha_1 s}}ds}_{(ii)}\right).$$

For (i), using the change of variable $u=e^{-\alpha_1 s}$, we obtain

$$(i) = -\frac{1}{\alpha_1}\int_1^{e^{-\alpha_1 t}} \frac{du}{1+\frac{LA_1H_1}{\beta_1 1}u} = -\frac{\beta_1}{\alpha_1 LA_1H_1}\ln\left(\frac{1+\frac{LA_1H_1}{\beta_1}e^{-\alpha_1 t}}{1+\frac{LA_1H_1}{\beta_1}}\right)$$

For small s, $se^{\alpha_1 s} \approx s$ and using the condition $\left|\dfrac{LA_1H_1}{\beta_1}\right| < 1$, we expand the denominator to second order to obtain

$$\begin{aligned}(ii) &\approx \int_0^t e^{-(\alpha_1+\beta_1+LA_1H_1)s}\left(1-\frac{LA_1H_1}{\beta_1}e^{-\alpha_1 s}+\left(\frac{LA_1H_1}{\beta_1}\right)^2 e^{-2\alpha_1 s}\right)ds\\ &\approx -\frac{e^{-(\alpha_1+\beta_1+LA_1H_1)t}-1}{\alpha_1+\beta_1+LA_1H_1}+\frac{LA_1H_1}{\beta_1}\frac{e^{-(2\alpha_1+\beta_1+LA_1H_1)t}-1}{2\alpha_1+\beta_1+LA_1H_1}\\ &\quad -\left(\frac{LA_1H_1}{\beta_1}\right)^2\frac{e^{-(3\alpha_1+\beta_1+LA_1H_1)t}-1}{3\alpha_1+\beta_1+LA_1H_1}.\end{aligned}$$

Finally,

$$\begin{aligned}II_A(t) \approx& -\frac{1}{\tau_r LH_1\alpha_1}\ln\left(\frac{1+\dfrac{LA_1H_1}{\beta_1}e^{-\alpha_1 t}}{1+\dfrac{LA_1H_1}{\beta_1}}\right)+\frac{A_1}{\tau_r\beta_1}\frac{e^{-(\alpha_1+\beta_1+LA_1H_1)t}-1}{\alpha_1+\beta_1+LA_1H_1}\\ &-\frac{LA_1^2H_1}{\tau_r\beta_1^2}\frac{e^{-(2\alpha_1+\beta_1+LA_1H_1)t}-1}{2\alpha_1+\beta_1+LA_1H_1}+\frac{L^2A_1^3H_1^2}{\tau_r^2\beta_1^3}\frac{e^{-(3\alpha_1+\beta_1+LA_1H_1)t}-1}{3\alpha_1+\beta_1+LA_1H_1}.\end{aligned}$$

Similarly, we obtain the following expression for

$$\begin{aligned}II_B(t) \approx \frac{B_1}{\tau_r\beta_1}\int_0^t &\left(1-\frac{LA_1H_1}{\beta_1}e^{-\alpha_1 s}+\left(\frac{LA_1H_1}{\beta_1}\right)^2 e^{-2\alpha_1 s}-e^{-(\beta_1+LA_1H_1)s}\right.\\ &\left.+\frac{LA_1H_1}{\beta_1}e^{-(\alpha_1+\beta_1+LA_1H_1)s}-\left(\frac{LA_1H_1}{\beta_1}\right)^2 e^{-(2\alpha_1+\beta_1+LA_1H_1)s}\right)ds\end{aligned}$$

$$\begin{aligned}II_B \approx \frac{B_1}{\tau_r\beta_1}&\left(t+\frac{LA_1H_1}{\beta_1}\frac{e^{-\alpha_1 t}-1}{\alpha_1}-\left(\frac{LA_1H_1}{\beta_1}\right)^2\frac{e^{-2\alpha_1 t}-1}{2\alpha_1}+\frac{e^{-(\beta_1+LA_1H_1)t}-1}{\beta_1+LA_1H_1}\right.\\ &\left.-\frac{LA_1H_1}{\beta_1}\frac{e^{-(\alpha_1+\beta_1+LA_1H_1)t}-1}{\alpha_1+\beta_1+LA_1H_1}+\left(\frac{LA_1H_1}{\beta_1}\right)^2\frac{e^{-(2\alpha_1+\beta_1+LA_1H_1)t}-1}{2\alpha_1+\beta_1+LA_1H_1}\right).\end{aligned}$$

1.3.2 Integral term of h in phase 2

Our goal is now to compute expression (1.65). We decompose it into four parts:

$$\int_{t_1}^{t} x(s)y(s)ds = I_A + I_B + II_A + II_B.$$

All computations and approximations are similar except that we integrate between t_1 and t. We obtain

$$I_A(t) \approx -\frac{A_2 C_2 e^{\frac{LA_2H_2}{\alpha_2}} \left(e^{-(\alpha_2 + \beta_2 + LA_2H_2)t} - e^{-(\alpha_2 + \beta_2 + LA_2H_2)t_1} \right)}{\alpha_2 + \beta_2 + LA_2H_2}$$

$$I_B(t) \approx -\frac{B_2 C_2 e^{\dfrac{LA_2H_2}{\alpha_2}} \left(e^{-(\beta_2 + LA_2H2)t} - e^{-(\beta_2 + LA_2H_2)t_1} \right)}{\beta_2 + LA_2H_2}$$

$$\begin{aligned} II_A(t) \approx & -\frac{1}{\tau_r L H_2 \alpha_2} \ln \left(\frac{1 + \dfrac{LA_2H_2}{\beta_2} e^{-\alpha_2 t}}{1 + \dfrac{LA_2H_2}{\beta_2} e^{-\alpha_2 t_1}} \right) \\ & + \frac{A_2}{\tau_r \beta_2} \frac{e^{-(\alpha_2 + \beta_2 + LA_2H_2)t} - e^{-(\alpha_2 + \beta_2 + LA_2H_2)t_1}}{\alpha_2 + \beta_2 + LA_2H_2} \\ & - \frac{LA_2^2H_2}{\tau_r \beta_2^2} \frac{e^{-(2\alpha_2 + \beta_2 + LA_2H_2)t} - e^{-(2\alpha_2 + \beta_2 + LA_2H_2)t_1}}{2\alpha_2 + \beta_2 + LA_1H_2} \\ & + \frac{L^2 A_2^3 H_2^2}{\tau_r^2 \beta_2^3} \frac{e^{-(3\alpha_2 + \beta_2 + LA_2H_2)t} - e^{-(3\alpha_2 + \beta_2 + LA_2H_2)t_1}}{3\alpha_2 + \beta_2 + LA_1H_2} \end{aligned}$$

$$\begin{aligned} II_B(t) \approx \frac{B_2}{\tau_r \beta_2} \Bigg(& t - t_1 + \frac{LA_2H_2}{\beta_2} \frac{e^{-\alpha_2 t} - e^{-\alpha_2 t_1}}{\alpha_2} - \left(\frac{LA_2H_2}{\beta_2} \right)^2 \frac{e^{-2\alpha_2 t} - e^{-2\alpha_2 t_1}}{2\alpha_2} \\ & + \frac{e^{-(\beta_2 + LA_2H_2)t} - e^{-(\beta_2 + LA_2H_2)t_1}}{\beta_2 + LA_2H_2} - \frac{LA_2H_2}{\beta_2} \frac{e^{-(\alpha_2 + \beta_2 + LA_2H_2)t} - e^{-(\alpha_2 + \beta_2 + LA_2H_2)t_1}}{\alpha_2 + \beta_2 + LA_2H_2} \\ & + \left(\frac{LA_2H_2}{\beta_2} \right)^2 \frac{e^{-(2\alpha_2 + \beta_2 + LA_2H_2)t} - e^{-(2\alpha_2 + \beta_2 + LA_2H_2)t_1}}{2\alpha_2 + \beta_2 + LA_2H_2} \Bigg). \end{aligned}$$

1.3.3 Integral term of h in phase 3

Similarly as in phases 1 and 2 we compute the integral in expression (1.68) and obtain

$$\begin{aligned} \int_{t_2}^{t} x(s)y(s)ds = \int_{t_2}^{t} & (X + X(y(t2^-) - 1)e^{\dfrac{t_2 - s}{\tau_r}} + (x(t2^-) - X)e^{\dfrac{t_2 - s}{\tau_f}} \\ & + (y(t2^-) - 1)(x(t2^-) - X)e^{(t_2 - s)(\dfrac{1}{\tau_f} + \dfrac{1}{\tau_r})} ds \end{aligned}$$

$$
\begin{aligned}
&= X(t-t_2) - \tau_r X(y(t2^-)-1)(e^{-\dfrac{t-t_2}{\tau_r}} - 1) - \tau_f(x(t2^-)-X)\left(e^{-\dfrac{t-t_2}{\tau_f}} - 1\right)\\
&\quad - \frac{(y(t2^-)-1)(x(t2^-)-X)\tau_f\tau_r}{\tau_f+\tau_r}\left(e^{-(t-t_2)\dfrac{\tau_f+\tau_r}{\tau_f\tau_f}} - 1\right).
\end{aligned}
$$

1.3.4 Numerical values of intermediate and approximation parameters

	Parameters	Values	
Γ_1	-0.24	Λ_1	-0.18
Γ_2	$5.2.10^{-6}$	Λ_2	11.47
Γ_3	-0.91	Λ_3	-0.077
Γ_4	$1.4.10^{-3}$	Λ_4	$4.4.10^{-3}$
Γ_5	-0.50	Λ_5	0.054
Γ_6	0.46	Λ_6	0.89
Γ_7	$1.9.10^{-6}$	Λ_7	0.07
Γ_8	$4.0.10^{-4}$	Λ_8	$1.8.10^{-3}$
Γ_9	$1.3.10^{-3}$	Λ_9	$2.8.10^{-3}$

Table 1.2: Intermediate parameters

	Parameters	Values
H_1	Approximation of h for x and y during phase 1	8000
$\tilde{H}_1$	Initial value of h	250
H_2	Approximation of h for x and y during phase 2	-1
h_0	End of phase 1 threshold	400
h_{AHP}	End of phase 2 threshold	-29
ϵ	End of AHP threshold	-5
t_1	End of phase 1 time	200ms
t_2	End of phase 2 time	1.37s
A_1	Approximation of x on phase 1 parameter	-0.91
B_1	Approximation of x on phase 1 parameter	0.99
C_1	Approximation of y on phase 1 parameter	1.98
α_1	Approximation of x on phase 1 parameter	297Hz
β_1	Approximation of y on phase 1 parameter	224Hz
A_2	Approximation of x on phase 2 parameter	1.16
B_2	Approximation of x on phase 2 parameter	0.06
C_2	Approximation of y on phase 2 parameter	0.0017
α_2	Approximation of x on phase 2 parameter	1.07Hz
β_2	Approximation of y on phase 2 parameter	0.34Hz

Table 1.3: Approximation parameters

1.3.5 Simplified formulas (1.72) and (1.79)

We give here the simplified formulas of the intermediary parameters used to obtain (1.72) and (1.79).

Phase 1 parameters In this phase $H_1 \gg 1$, yielding

$$\begin{array}{rcl} \alpha_1 & \approx & 1.1 + KH_1 \approx KH_1, \\ A_1 & \approx & -0.9, B_1 \approx 1, \beta_1 \approx LH_1 \text{ and } C_1 \approx \exp\left(0.9\dfrac{L}{K}\right). \end{array} \tag{1.83}$$

Using these values we can compute $\Gamma_1 - \Gamma_9$:

$$\begin{array}{rcll} \Gamma_1 & \approx & \dfrac{J - 2.9LH_1}{2.9JLH_1} & \sim \; 0.24 \textit{ (with our parameters)} \\ \Gamma_2 \ln\left(\dfrac{1}{1+\Gamma_3}\right) & \approx & \dfrac{1}{2.9LKH_1^2}\ln\left(\dfrac{1}{1-0.9\dfrac{L}{K}}\right) & \sim \; 10^{-5} \\ \Gamma_4 & \approx & -\dfrac{0.9}{2.9LH_1} & \sim \; 10^{-3} \\ \Gamma_5 & \approx & -\exp\left(-0.9\dfrac{L}{K}\right) & \sim \; 0.5 \\ \Gamma_6 & \approx & 0.9\exp\left(-0.9\dfrac{L}{K}\right) & \sim \; 0.46 \\ \Gamma_7 & \approx & \dfrac{0.81}{2.9LH_1}\left(\dfrac{LH_1}{LH_1} - 1\right) & \sim \; 10^{-6} \\ \Gamma_8 & \approx & \dfrac{0.81}{8.41LH_1} & \sim \; 10^{-4} \\ \Gamma_9 & -\approx & \dfrac{0.81}{8.41LH_1} & \sim \; 10^{-4} \end{array} \tag{1.84}$$

In our parameter range, we neglect the terms $\Gamma_2 \ln\left(\dfrac{1}{1+\Gamma_3}\right)$, Γ_4, Γ_7, Γ_8 and Γ_9 in formula (1.70).

Phase 2 parameters In this phase, $|H_2| = O(1)$ and thus we can neglect the second order terms in K and L, that are small in our parameter range. It yields

$$\begin{array}{rcl} \alpha_2 & \approx & 1.1 + KH_2,\; x(t_1) \approx 1 \text{ thus } A_2 \approx \dfrac{1}{1.1+KH_2}\exp\left((1.1+KH_2)t_1\right) \\ B_2 & \approx & \dfrac{0.1+KH_2}{1.1+KH_2},\; \beta_2 \approx \dfrac{0.37+0.34KH_2+0.1LH_2}{1.1+KH_2} \text{ and } y(t_1) \approx 0 \text{ thus } C_2 \approx 0. \end{array} \tag{1.85}$$

We can use these formulas to simplify the formulas for $\Lambda_1 - \Lambda_9$:

$$
\begin{aligned}
\Lambda_1 &\approx \frac{J(0.1+KH_2) - 1.1 - KH_2 - 0.29LH_2}{(1.1+KH_2+0.29LH_2)J},\\
\Lambda_2 &\approx -\frac{1}{3.19LH_2},\\
\Lambda_3 &\approx \frac{LH_2}{0.1LH_2+0.34KH_2+0.37}\\
\Lambda_4 &\approx \frac{LH_2}{29(0.37+0.34KH_2+0.1LH_2)}\\
\Lambda_5 &\approx \frac{1.1+1.2KH_2-0.037t_1-0.4KH_2t_1-0.11LH_2t_1}{1.18+2.26KH_2+0.32LH_2}\\
\Lambda_6 &\approx \frac{0.4+0.74KH_2-0.14t_1-0.26KH_2t_1-0.4LH_2t_1}{0.44+1.2KH_2+0.23LH_2}\\
\Lambda_7 &\approx \frac{-1.1LH_2+0.37LH_2t_1}{0.44+1.2KH_2+0.23LH_2}\\
\Lambda_8 &\approx \Lambda_9 \approx o(KH).
\end{aligned}
\tag{1.86}
$$

1.3.6 Termination time t_2 vs network connectivity J

We fitted Equation (1.74) defined with respect to the network connectivity parameter J by a rational function

$$
t_2(J) = \frac{AJ+B}{CJ+D}\left(1+\frac{\tau_{mAHP}}{J}\ln\left(\frac{h_{AHP}-T_{AHP}}{h(t_1)-T_{AHP}}\right)\right). \tag{1.87}
$$

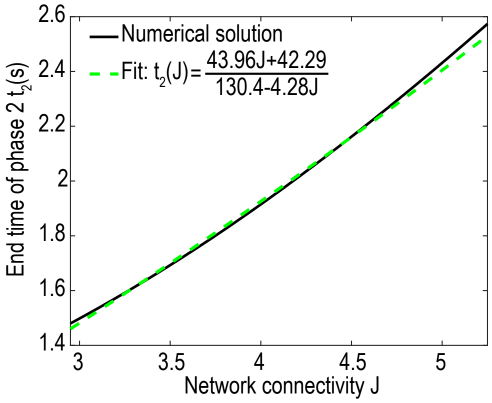

Figure 1.9: **Phase 2 termination time vs network connectivity J:** numerical solution (1.74) (solid black) fitted by a rational function of J (dashed green).

Chapter 2

Escape from an attractor generated by recurrent exit

Published in ZONCA L. & HOLCMAN D., "Escape from an attractor generated by recurrent exit" Physical Review Research (2021, in press) / arXiv:2009.06745

Abstract

Kramer's theory of activation over a potential barrier consists in computing the mean exit time from the boundary of a basin of attraction of a randomly perturbed dynamical system. Here we report that for some systems, crossing the boundary is not enough, because stochastic trajectories return inside the basin with a high probability a certain number of times before escaping far away. This situation is due to a shallow potential. We compute the mean and distribution of escape times and show how this result explains the large distribution of interburst durations in neuronal networks.

In Kramer's theory [122–125], the escape time over a potential barrier consists in computing the mean first passage time (MFPT) of a dynamical system perturbed by a small noise to the boundary of a basin of attraction. The MFPT measures the stability and provides great insight of the backward binding rate in chemistry [114, 127], loss-of-lock for phase controllers in communication theory [128], escape of receptors from the post-synaptic density at neuronal synapses and is also used to evaluate future derivatives in the financial market [129]. The full distribution of exit times can be used to characterize both short and intermediate time asymptotics relevant in polymer physics [130], accelerating chemical reaction simulations [126], or better characterizing the search for a small target in a complex environment [131, 132].

In the limit of small noise, a trajectory escapes a basin of attraction with probability one [151], but the escape time is exponentially long depending on the topology of the noiseless dynamics [133, 152] and its behavior at the boundary. In addition, the distribution of exit points peaks at a distance $O(\sqrt{\sigma})$ from a saddle-point, where σ is the noise intensity [123, 128, 134]. Interestingly, when a focus attractor is located near the boundary of the basin of attraction, the escape time deviates from an exponential distribution because trajectories oscillate inside the attractor before escape [108, 136–138, 153].

In these previous examples, the escape ends at the first time a trajectory crosses the separatrix that delimits the basin of attraction. Recurrent returns inside a basin of attraction can be quantified by the Green's function of the inner domain used in the additive properties of the MFPT [154]. In their specific case, where the escape time consists in the first crossing of the boundary of the basin of attraction

and a second separatrix, their results show a factor two between the escape time and the exit from the basin of attraction. In dimension one, a recurrent return can be quantified using a relaxation time computed from the survival probability when it does not converge to zero in the long times regime [155]. We show here that for some shallow two-dimensional dynamical systems, trajectories can first exit the basin of attraction, then make excursions outside before coming back inside the domain, a behavior that occurs several times before eventually escaping far away. This situation is peculiar and specific to dimensions greater than two and these recurrent entries need to be taken into account in computing the final escape time.
This letter reports such phenomenon. We present formulas for the mean and distribution of escape times and we show that these recurrent re-entries inside the basin of attraction can increase the escape time by a factor between two and three. Finally, we apply these results to explain the origin of long interburst durations found in neuronal network models [150].

2.1 Recurrent escape patterns

We start with a generic two-dimensional system

$$\begin{aligned} \dot{h} &= -\alpha h + x^2 + \sigma\dot{\omega} \\ \dot{x} &= \begin{cases} h - \gamma x & \text{for} \quad h \geq 0 \\ -\gamma x & \text{for} \quad h \leq 0, \end{cases} \end{aligned} \tag{2.1}$$

where $\alpha \in]0,1]$, $\gamma \in]0,\alpha[$, $\dot{\omega}$ is a Gaussian white noise and σ its intensity. The determinist part of this system has two critical points: one attractor $A = (0,0)$ (fig. 2.1A red star) and one saddle-point $S = (\gamma^2\alpha, \gamma\alpha)$ (fig. 2.1A cyan star) and the separatrix Γ delimits the basin of attraction of A (fig. 2.1A solid black).

The escape of the basin of attraction occurs in two steps. 1) A trajectory starting at A reaches Γ for the first time (fig. 2.1A black trajectory between A and the first exit point Exit n^{o}1, light green). 2) The trajectory exits and crosses Γ several times, that we count by using a round-trip (RT) number (fig. 2.1A, light green and cyan loops) before eventually escaping far away (fig. 2.1A, pink). To characterize the final escape times and the distribution of crossing points on Γ, we ran stochastic simulations of system (2.1) (500 runs, fig. 2.1B trajectories exhibit one (yellow) and two (orange) RT before escape). To further characterize the recurrent crossing points, we plotted their distributions (fig. 2.1C) and found that they were peaked near the saddle-point. These recurrent excursions are not due to a focus, since the saddle point S has only real eigenvalues $\lambda_{\pm} = -\frac{1}{2}\left(-(\alpha+\gamma) \pm \sqrt{(\alpha+\gamma)^2 + 4\alpha\gamma}\right)$, $\lambda_+ \approx 0.314, \lambda_- \approx -1.914$ (with $\alpha = 1$ and $\gamma = 0.6$). A possible explanation for this phenomenon is the very shallow field tangent to the separatrix: only near the unstable manifold (fig. 2.1A yellow curve) trajectories can depart to infinity when they are located inside the ensemble of points where the two drift components are positive $\dot{x} > 0$ and $\dot{h} > 0$, thus $C_\infty = \left\{ h > \gamma x \text{ and } h < \frac{x^2}{\alpha} \right\}$ (fig. 2.1A, B yellow area, situated between the x-nullcline (red) and the h-nullcline (purple)). Before reaching C_∞, the noise pushes the trajectories back and forth into the basin of attraction.
To conclude this part we shall summarize the escape dynamics:

1. The distribution of exit points peaks at a distance $O(\sqrt{\sigma})$ from the saddle-point (generically

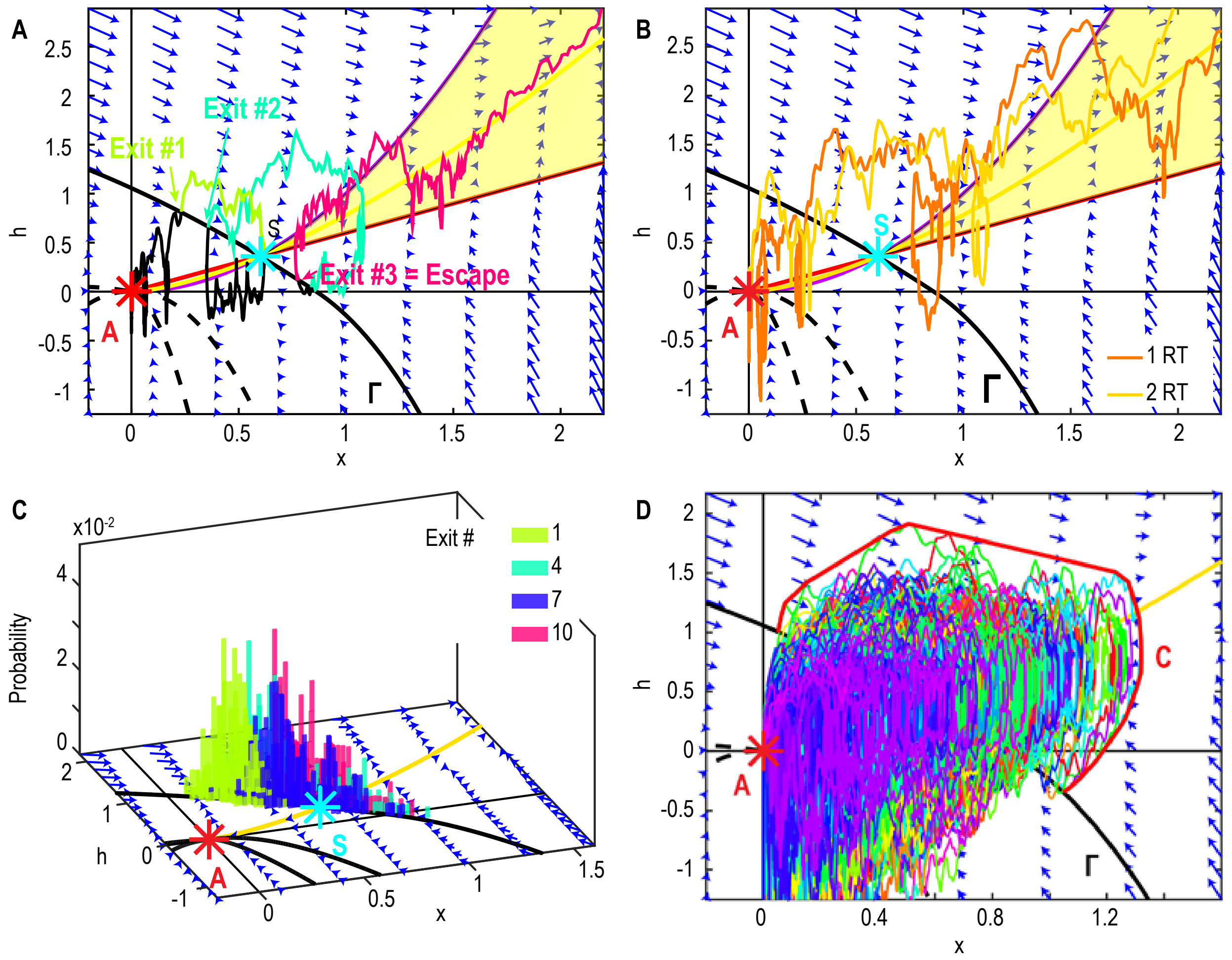

Figure 2.1: **Recurrent escape patterns A.** Escaping trajectories reach the separatrix Γ for the first time (step 1, black) and re-cross it several times going back and forth inside and outside of the basin of attraction (step 2, green, cyan) before eventually escaping far away (pink). **B.** Stochastic trajectories with one (yellow) and two (orange) round-trips (RT) before escape. **C.** Distributions of exit points on Γ (500 runs) for successive RT. **D.** Outer boundary layer C computed as the convex hull of all trajectories reentering the basin of attraction (red).

satisfied [134]).

2. The shallow field near the separatrix allows the trajectories to reenter with high probability.

3. The peaks of the successive exit points distributions drift towards the saddle-point S (fig. 2.1C).

4. When the trajectories enter the escape cone C_∞ (yellow surface in fig. 2.1A-B) where the field increases, they eventually escape to infinity.

Finally, this escape pattern could not occur in dimension one since conditions 1 and 3 cannot be satisfied.

2.2 Characterizing the escape time

We compute here the total escape time. To this end, we decomposed it into the time to reach the separatrix Γ for the first time plus the time spent to go back and forth around Γ before the final escape. Using Baye's law and conditioning on the RT numbers, the mean escape time can be written as

$$\langle \tau_{esc} \rangle = \sum_{k=0}^{\infty} \langle \tau | k \rangle P_{RT}(k), \tag{2.2}$$

where $\langle \tau | k \rangle$ (resp. $P_{RT}(k)$) is the mean time (resp. probability) to return k times inside the basin of attraction. To estimate the escape probability $\tilde{p}$ for a trajectory that has crossed Γ to escape to infinity, we ran $N = 500$ trajectories starting from A and lasting $T = 300s$. We first counted the proportion of trajectories reentering the basin of attraction at least once and obtained 88%. We then reiterated this process and counted the proportion of trajectories reentering the basin of attraction one more time after each RT. We found that this proportion was stable equal to 88%, leading to $\tilde{p} = 0.12$. We applied this process for values of the noise $\sigma \in [0.21, 1.05]$ and found that $\tilde{p}$ did not depend on σ. After $T = 300s$ all trajectories had escaped to infinity (for all the values of σ), thus choosing a higher value for T would not change the value of $\tilde{p}$. This escape phenomenon could be interpreted as follows: a trajectory has escaped when it reaches a distance far away from the separatrix and to better characterize such a distance outside the basin of attraction, we generated empirical trajectories that will return (have not yet escaped) and estimated their convex hull C (fig. 2.1D red, 500 runs). Formally, this is equivalent to looking at trajectories starting at A conditioned to a return to the basin of attraction, thus defining a sort of Brownian bridge. This procedure leads to a bounded domain: any point inside C has a high probability of reentering the basin of attraction while points further away will escape to infinity.

Due to the strong Markovian properties, each RT can be considered independent of the previous ones, thus the probability to escape after exactly $k-$RT is given by

$$P_{RT}(k) = \tilde{p}(1-\tilde{p})^{k-1}, \tag{2.3}$$

and thus the mean escape time is

$$\begin{aligned} \langle \tau_{esc} \rangle &= \langle \tau_0 \rangle + (\langle \tau_{ext} \rangle + \langle \tau_{int} \rangle)\tilde{p} \textstyle\sum_{k=1}^{\infty} k(1-\tilde{p})^{k-1} \\ &= \langle \tau_0 \rangle + \frac{\langle \tau_{ext} \rangle + \langle \tau_{int} \rangle}{\tilde{p}}, \end{aligned} \tag{2.4}$$

where $\langle \tau_0 \rangle$ is the mean time to reach the separatrix for the first time and $\langle \tau_{ext} \rangle$ (resp. $\langle \tau_{int} \rangle$) is the time spent on the outside (resp. inside) the basin of attraction of A for each RT (fig. 2.2A). When the escape probability $\tilde{p}$ tends to zero, the escape time tends to infinity, corresponding to trajectories that would be trapped in C. In our case, the mean escape time is $\langle \tau_{esc} \rangle \approx \langle \tau_0 \rangle + 8.33(\langle \tau_{ext} \rangle + \langle \tau_{int} \rangle)$. With the present parameters $\langle \tau_0 \rangle \approx 5.1s$ and $\langle \tau_{ext} \rangle + \langle \tau_{int} \rangle \approx 1s$ showing that the escape time is increased by a factor 2.6. Interestingly, the noise intensity does not influence the number of RT before escape (fig. 2.2B). For the parameter value $\gamma = 0.6$, we found that a trajectory performs 8 RT on average (fig. 2.2B, inset). These results indicate that the noise intensity does not directly influence the probability to escape to infinity.

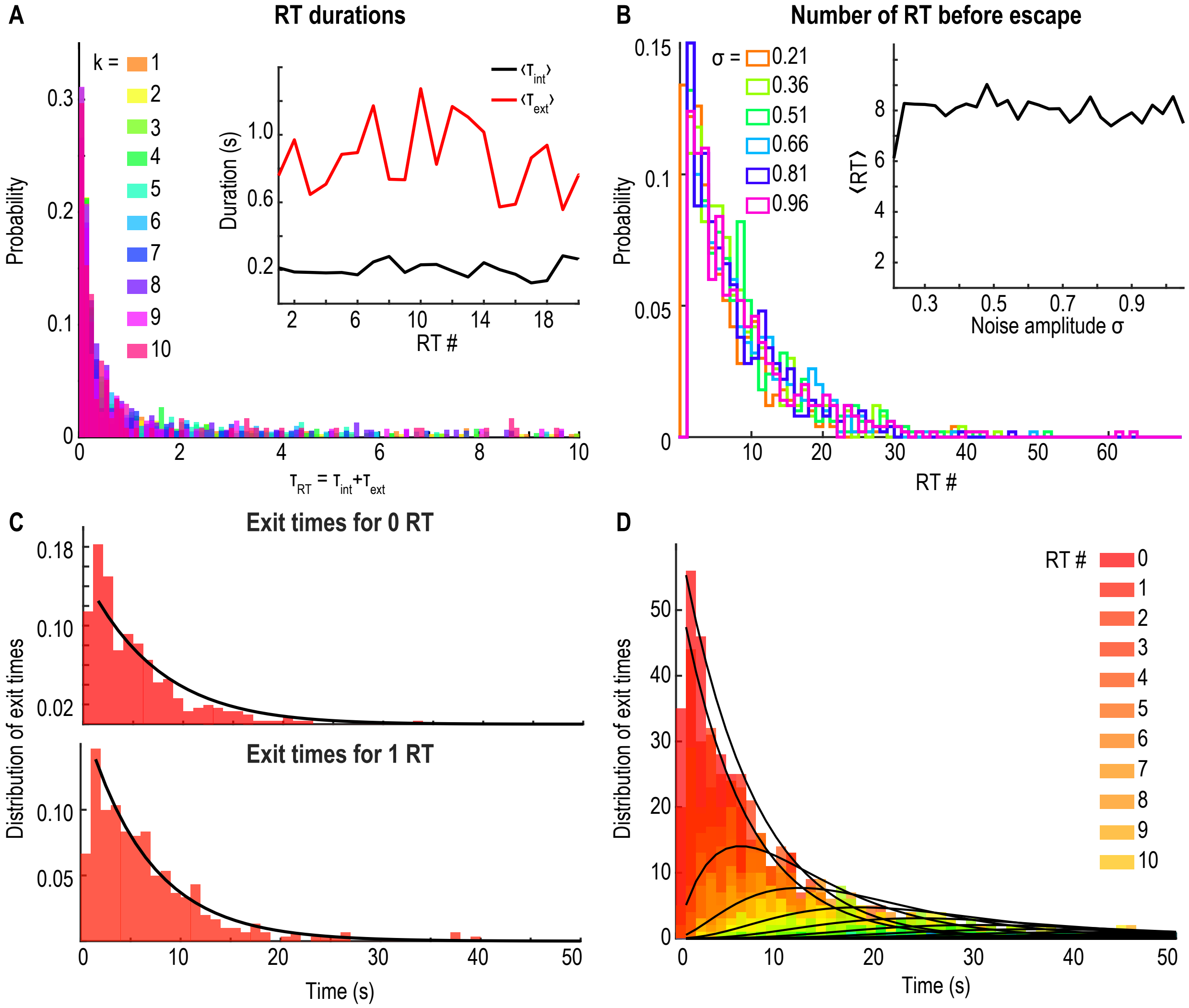

Figure 2.2: **Distribution of RT and escape times. A.** Distributions of a RT duration $\tau_{RT,k} = \tau_{ext,k} + \tau_{int,k}$ for $k \in [1, 10]$. Inset: mean time spent outside (resp. inside) the basin of attraction $\langle\tau_{ext,k}\rangle$ (resp. $\langle\tau_{int,k}\rangle$) vs the RT number k. **B.** Distributions of the RT number around the separatrix before a trajectory eventually escapes for various values of σ (with $\gamma = 0.6$ and $\alpha = 1$). 500 runs for each value of σ. Inset: mean RT number with respect to the noise intensity σ. **C.** Distributions f_0 (upper), resp. f_1 (lower), of escape times for trajectories with zero and one RT. The fit uses eq. (2.8). **D.** Distribution of exit times with the contribution of each RT number compared to the analytical distribution (eq. 2.7).

We now determine the distribution of escape times

$$P(\tau_{esc} < t) = \sum_{k=0}^{\infty} P(\tau^k < t|k) P_{RT}(k), \tag{2.5}$$

where $P(\tau^k < t|k)$ is the conditional probability distribution to escape after k RT. Because RT are i.i.d, this probability is the k-th convolution of the distribution of times of a single RT $f_1(t)$ with the distribution of escape times without RT $f_0(t)$

$$P(\tau^k < t|k) = f_0(t) * f_1(t)^{*k}, \tag{2.6}$$

where $f(t)^{*k} = f(t) * f(t) * ... * f(t)$, k times. Thus the pdf of exit times is given by

$$f(t) = \sum_{k=0}^{\infty} f_0(t) * f_1(t)^{*k} \tilde{p}(1-\tilde{p})^{k-1}. \tag{2.7}$$

To compare this formula to the results of our numerical simulations, we approximate the distributions f_0 and f_1 by

$$f_i(t) = c_i \left(1 + erf\left(\frac{t-a_i}{b_i}\right)\right) e^{-\lambda_i t}, \text{ for } i = 0, 1, \tag{2.8}$$

where $erf(x) = \dfrac{2}{\sqrt{\pi}} \displaystyle\int_0^x e^{-u^2} du$ is the error function. We fitted the distributions obtained from the numerical simulations of trajectories that escaped without doing any RT (f_0 fig. 2.2C, upper) and after one single RT (f_1 fig. 2.2C, lower) with the condition that $\lambda_1 \geq \lambda_0$. We obtained $c_0 = 1.09$, $c_1 = 1.63$, $\lambda_0 = 0.06$ $\lambda_1 = 0.13$, $a_0 = -38.28$, $a_1 = -138.64$, $b_0 = -36.72$, $b_1 = -121.69$. We then computed each term of the sum (2.7) and we could compare it to the corresponding parts of the distribution of escape times obtained from stochastic simulations (fig. 2.2D).

2.3 Interburst durations in a firing excitatory neuronal network

Burst and interburst are fundamental network events occurring during dominant imbalance dominated by excitatory neuronal activity. Network burst generation could rely on specific spiking frequencies in connected neurons [156] despite a high variability in interspike intervals [157]. Neuronal population bursts separated by long interbursts have been modeled using a two-state synaptic depression [112], or by using the refractory period induced by afterhyperpolarization (AHP), a mechanism leading to a long voltage hyperpolarisation transient and generated by various potassium channels [158]. Here we show that the recurrent escape mechanism described above can be used as one explanation of the origin of long interburst intervals without the need of any other mechanism. However, we note that this mechanism does not have to be exclusive and that long interburst intervals could also be explained in some cases by a combination of mechanisms such as the recurrent escape pattern presented here and AHP. Indeed, we start from the depression-facilitation short-term synaptic plasticity mean-field model of network neuronal bursting [102, 105, 109], which consists of three equations (2.9) for the mean voltage h, the depression y, and the facilitation x. The depression mechanism describes the depletion of the vesicular pool necessary for neurotransmission following successive action potentials, while the facilitation mechanism corresponds to a transient increase of the release probability mediated by a local calcium accumulation at synapses.

$$\begin{aligned} \tau\dot{h} &= -h + Jxyh^+ + \sqrt{\tau}\sigma\dot{\omega} \\ \dot{x} &= \frac{X-x}{t_f} + K(1-x)h^+ \\ \dot{y} &= \frac{1-y}{t_r} - Lxyh^+, \end{aligned} \tag{2.9}$$

where $h^+ = max(h, 0)$ is a linear threshold function of the synaptic current that gives the average population firing rate [102, 105, 145]. The mean number of connections (synapses) per neuron is accounted

for by the parameter J and the term Jxy represents the combined effect of the short-term synaptic plasticity (facilitation and depression mechanisms) on the network activity. The parameters K and L describe how the firing rate is transformed into molecular events that are changing the duration (depression) and probability (facilitation) of vesicular release. The time scales t_f and t_r define the recovery of an averaged synapse from the network activity. Finally, $\dot{\omega}$ is an additive Gaussian noise and σ its intensity, this additive noise term represents the fluctuations of the mean voltage generated by the average of independent vesicular release events and/or closings and openings of voltage gated channels.
This system has 3 critical points, one attractor and two saddles. Interestingly, near the attractor $A = (0, X, 1)$, the dynamic is anisotropic ($|\lambda_1| = 12.6 \gg |\lambda_2| = 1.11 \gg |\lambda_3| = 0.34$, with the parameters from Table 2.1) and thus we project the system on the two-dimensional plan $y = constant$

$$\dot{y} = 0 = \frac{1-y}{\tau_r} - Lxyh^+ = 0 \iff y = \frac{1}{1+\tau_r Lxh^+} \tag{2.10}$$

leading to the simplified system

$$\begin{aligned} \dot{h} &= \frac{h\left(Jx - 1 - \tau_r Lxh^+\right)}{\tau(1+\tau_r Lxh^+)} + \sqrt{\tau}\sigma\dot{\omega} \\ \dot{x} &= \frac{X-x}{\tau_f} + K(1-x)h^+ \end{aligned} \tag{2.11}$$

The deterministic component of this system has 3 critical points, two attractors and one saddle-point .

Attractor A_0 A first equilibrium point is given by $h = 0$ and $x = X$. The Jacobian at this point is

$$J_A = \begin{pmatrix} \dfrac{-1+JX}{\tau} & 0 \\ K(1-X) & -\dfrac{1}{\tau_f} \end{pmatrix}. \tag{2.12}$$

With our parameters (Table 2.1) the eigenvalues $\lambda_1 = \dfrac{JX-1}{\tau} \approx -12.6$ and $\lambda_2 = -\dfrac{1}{\tau_f} \approx -1.11$ are both negative confirming A is an attractor.

Saddle-point S The second critical-point is $S_1(h_1 \approx 8.07; x_1 \approx 0.28)$. Its eigenvalues are $\lambda_1 \approx -5.73$ and $\lambda_2 \approx 1.43$. It is a saddle-point.

Attractor A_2 The third critical-point is $A_2(h_2 \approx 28.8; x_2 \approx 0.53)$. Its eigenvalues are $\lambda_1 \approx -11.9$ and $\lambda_2 \approx -1.33$. It is another attractor. The two attractors are separated by the 1D stable manifold of the saddle-point S_1 (fig. 2.3A, solid black curve).
The phase-space of system (2.11), restricted to the region $\{x \leq 0.5$ and $h \leq 30\}$ has the same topological properties than system (2.1): one attractor and one saddle-point, the separatrix delimiting the basin of attraction is the stable manifold of S_1 (fig. 2.3A). The escaping trajectories exits and re-enters the basin of attraction several times before eventually escaping (fig. 2.3A, orange).
Thus, we can now understand that the interburst intervals correspond to the exit times of trajectories

from the basin of attraction. Using formula (2.7) to fit the distribution of exit times, we obtain that $\tilde{p} \approx 0.13$ (fig. 2.3B) and

$$f_0(t) = 0.23 \exp(-0.25t) \left(1 + erf\left(\frac{t - 2.45}{0.43}\right)\right) \tag{2.13}$$

and

$$f_1(t) = 0.19 \exp(-0.25t) \left(1 + erf\left(\frac{t + 15.97}{0.58}\right)\right). \tag{2.14}$$

Finally, similar to the generic system (2.1), the RT number before escape does not depend on the noise intensity (fig. 2.3C). Trajectories are making on average 8 RT before escape (inset). To determine the mean escape time, we use formula (2.4) and obtain $\langle\tau_{esc}\rangle \approx \langle\tau_0\rangle + 7.7(\langle\tau_{ext}\rangle + \langle\tau_{int}\rangle)$ where $\langle\tau_0\rangle \approx 4.35s$ and $\langle\tau_{ext}\rangle + \langle\tau_{int}\rangle \approx 0.7s$ (fig. 2.3D) thus leading to a factor 2.2 in the increase of the escape time $\langle\tau_{esc}\rangle$ compared to the first exit time $\langle\tau_0\rangle$. At this stage we conclude that long interburst durations, generated by excitatory neuronal networks [52], can be explained by the recurrent escape mechanism introduced here.

Concluding remarks

We presented an escape mechanism for which reaching the boundary of the deterministic basin of attraction induced by noise is not sufficient to escape. After crossing the separatrix, the noise tends to bring trajectories back inside the basin of attraction until they reach a region (escape cone-like domain C_∞), narrow near S and that widens with the distance. The size of the characteristic distance from S (boundary layer) after which trajectories escape is $\sqrt{\frac{\lambda_+}{\sigma}}$ [139]. We derived formulas for the mean escape time and the distribution of escape times taking into account the excursions inside and outside of the basin of attraction before the final escape.

Numerical methods

All simulations were run in Matlab using the Runge-Kutta 4 scheme with a time-step $\delta_t = 0.01s$ (we also tried $\delta_t = 0.001s$ and obtained the same results thus ensuring stability). The same results were also obtained using the Euler method.

Acknowledgments

LZ received funding from French Research Ministry (ED386 Ecole doctorale de Sciences Mathématiques Paris centre) and Fondation pour la Recherche Médicale (FRM - FDT202012010690). This project has received funding from the European Research Council (ERC) under the European Union's Horizon 2020 research and innovation program (grant agreement No 882673)

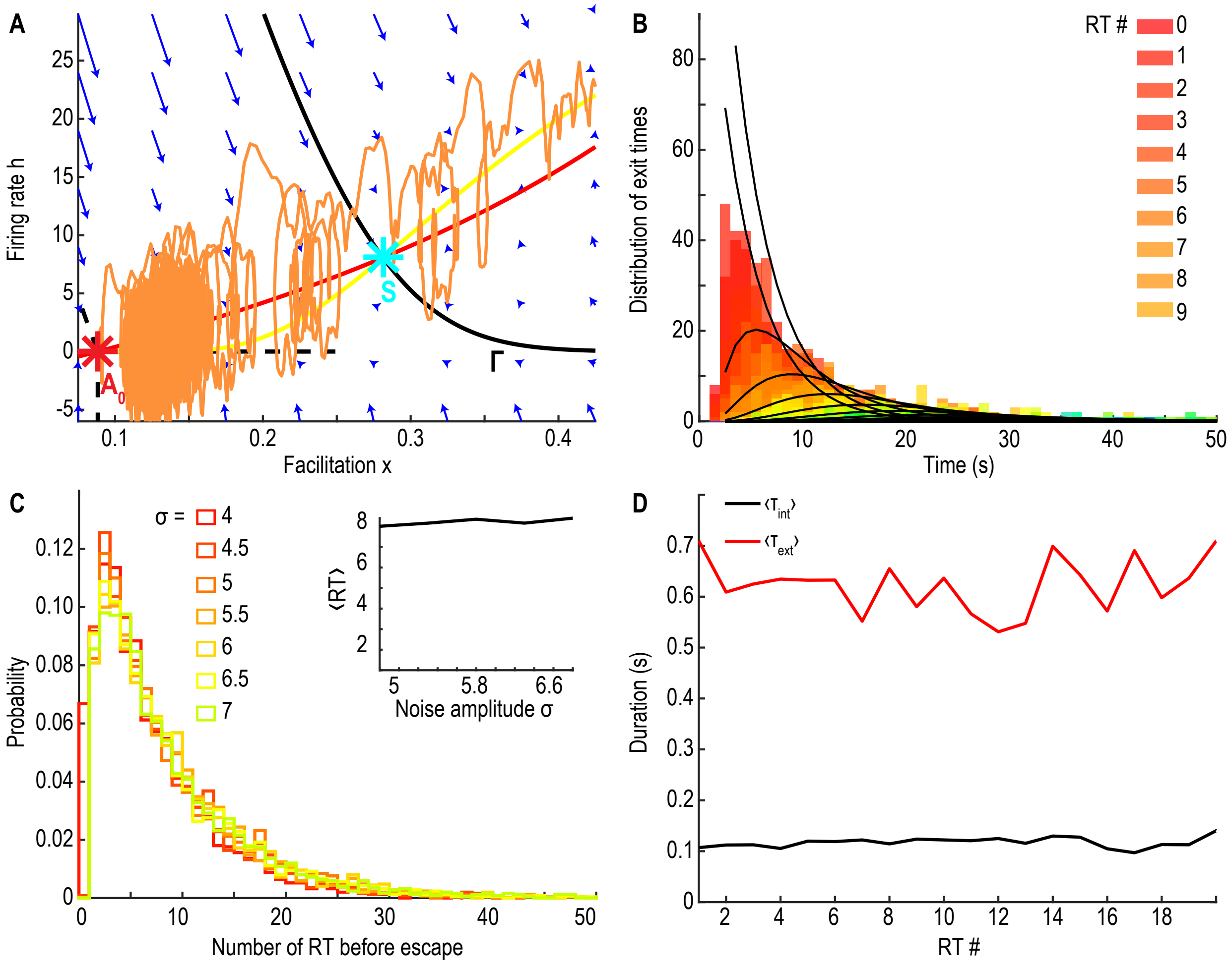

Figure 2.3: **Application to the dynamical system** (2.11). **A.** 2D phase-space restricted to $\{x \leq 0.5 \text{ and } h \leq 30\}$. The basin of attraction of A_0 (red star) is delimited by the stable manifold of S (solid black curve Γ) with an exiting trajectory doing 1 RT (orange) around the separatrix before escape . **B.** Distribution of exit times with the contribution of the trajectories per RT number before escape with the analytical fit (equations 2.7, 2.13 and 2.14). **C.** Distribution of the RT number for $\sigma \in [4, 7]$ and mean RT number with respect to noise (inset). **D.** Values of $\langle \tau_{ext} \rangle$ (red) and $\langle \tau_{int} \rangle$ (black) with respect to the RT number.

	Parameters	Values
τ	Time constant for h	0.05s [158]
J	Synaptic connectivity	4.21 [158]
K	Facilitation rate	0.037Hz [158]
X	Facilitation resting value	0.08825 [158]
L	Depression rate	0.028Hz [158]
τ_r	Depression time rate	2.9s [158]
τ_f	Facilitation time rate	0.9s [158]
T	Depolarization parameter	0

Table 2.1: Model (2.9) parameters

Chapter 3

Exit versus escape for stochastic dynamical systems and application to neuronal network bursting time computation

Under review in Journal of nonlinear science: ZONCA L. & HOLCMAN D., "Exit versus escape for stochastic dynamical systems and application to neuronal network bursting time computation" arXiv:2010.06699

Abstract

We study the exit time of two-dimensional dynamical systems perturbed by small noise that exhibit two peculiar behaviors: 1) the maximum of the probability density function of the position is not located at the point attractor, which came as a surprise. The distance between the maximum and the attractor increases with the noise amplitude σ, as shown by using WKB approximation and numerical simulations. 2) For such systems, exiting from the basin of attraction is not sufficient to guarantee a full escape, due to trajectories that can return several times inside the basin of attraction after crossing the boundary, before eventually escaping far away. We apply these results to neuronal networks that can generate burst events. To analyse interburst periods and their statistics, we study the phase-space of a mean-field model, based on synaptic short-term changes, that exhibit burst and interburst dynamics and we identify that interburst corresponds to an escape with multiple re-entries inside the basin of attraction. To conclude, escaping far away from a basin of attraction is not equivalent to reaching the boundary, thus explaining long-interburst durations present in neuronal dynamics.

3.1 Introduction

Trajectories of a dynamical system perturbed by small noise can escape from a basin of attraction and present large fluctuations away from a stable attractor [113–115]. These perturbations can even induce switching in multi-stable systems. Noise can also enhance the response to periodic external stimuli, a phenomenon known as stochastic resonance [116]. In the case of interaction between noise and a dynamics presenting a Hopf bifurcation, oscillations that would disappear in the deterministic case can be maintained. Finally, noise can induce a shift in bifurcation values [118] or stabilize an unstable equilibrium [119–121].

In the context of modeling biological neuronal networks, noise also plays a critical role in defining collective rhythms or large synchronization. To reduce the complexity and difficulty inherent in analyzing large neuronal ensembles, mean-field models are used to study averaged behavior, which corresponds to projecting a high dimensional system into a low dimension, as it is the case for modeling fast synaptic adaptations [102]. Such models are used to study bursting activity, synchronization and oscillations in excitatory neuronal networks [59, 60, 105, 109, 145]. However, in such models the distribution of interburst durations remains unclear, although these durations have recently been shown to control to the overall neuronal networks dynamics [52] and can even influence the bursting activity during epilepsy.

Stuyding the escape rate from a basin of attraction for a noisy dynamical system usually consists in collecting trajectories that terminate when they hit for the first time the boundary of the basin of attraction, which occurs with probability one [139, 151]. The escape rate and the distribution of exit points can be computed in the small noise limit using WKB approximation. Another interesting property is that the exit point distribution peaks at a distance $O(\sqrt{\sigma})$ from the saddle-point (where σ is the noise amplitude) [123, 134]. Metrics relations can also play a role in shaping the dynamics, so that when a focus attractor falls into the boundary layer of the basin of attraction, escaping trajectories exhibit periodic oscillations leading to an escape time distribution which is not exponential, because several eigenvalues are necessary to describe the distribution [106, 108, 135–138].

In the case of periodically-driven systems, the escape rate scales by the field intensity [152, 159]. In all these examples, escape ends when a trajectory hits the separatrix for the first time which will not be the case for the systems we wish to study here. We consider here a class of dynamical systems perturbed by a white noise of small amplitude for which trajectories exiting the basin of attraction can reenter multiple times before eventually escaping to infinity. This effect requires to clarify the difference between exiting versus escaping that we explain below.

The manuscript is organized as follows: in the first part, we introduce a reduced stochastic dynamical system for bursting, based on modeling synaptic depression-facilitation for an excitatory neuronal network [102, 109]. The distribution of interburst intervals corresponds to the escape from an attractor and numerical simulations reveal a shift in the distribution of exit points and multiple returns inside the attractor. In the second part, we describe a generic two-dimensional dynamical system, containing an attractor and one saddle-point. We analyze the stochastic perturbation, and show that the maximum of the probability density function of trajectories before escape is not centered at the attractor, but at a shifted location that depends on the noise amplitude σ. Finally, we focus on the escape from the basin of attraction. After exiting, trajectories can return inside the basin of attraction multiple times before eventually escaping to infinity. To conclude, the excursions outside and inside the basin of attraction increase the total escape time by a factor between 2 to 3 compared to the first exit time, providing a novel explanation for the large tail distribution of interbust intervals in experimental time series [52].

3.2 Modeling the interburst durations in neuronal networks

3.2.1 Noisy depression-facilitation model

Biological neuronal networks exhibit complex patterns of activity as revealed by time series of a single neuron [160, 161], a population or an entire Brain area [162]. To analyse neuronal networks, mean-field models are used to formulate the dynamics as stochastic differential equations.

Bursting dynamics is a transient period of time where an ensemble of neurons discharge and these events can be accounted for by using short-term plasticity properties of synapses, such as the classical depression and facilitation [102, 109, 145]. Bursting is followed by an interburst period, where the network is almost silent. Neuronal population bursts separated by long interbursts can result from two-state synaptic depression [112]. However, the refractory period could also be the result of other mechanisms such as afterhyperpolarization (AHP), mediated by leading long-lasting voltage hyperpolarisation transient and generated by potassium channels [158].
We focus here on a depression-facilitation short-term synaptic plasticity model of network neuronal bursting [102,105,147], which consists of three equations (3.1) for the mean voltage h, the depression y, and the facilitation x. We recall that synaptic depression describes the possible depletion of vesicular pools, necessary for neurotransmission following an action potential. In this phenomenology, facilitation is a synaptic mechanism that reflects a transient increase of the vesicular release probability, possibly mediated by an increase of the local calcium concentration in the pre-synaptic terminal. The associated equation is driven by two opposite forces: one is the return to an equilibrium X with a time constant t_f and the other is an increase induced by a mean firing rate $h^+ = max(h, 0)$. Similarly, the depression variable y returns exponentially to steady state with a time constant t_r. It can also decrease following a firing rate h^+, proportional to the available fraction y of vesicles and the facilitation x. The three coupled equations for the mean voltage h, the depression y, and the synaptic facilitation x are

$$\begin{aligned} \tau\dot{h} &= -h + Jxyh^+ + \sqrt{\tau}\sigma\dot{\omega} \\ \dot{x} &= \frac{X-x}{t_f} + K(1-x)h^+ \\ \dot{y} &= \frac{1-y}{t_r} - Lxyh^+, \end{aligned} \tag{3.1}$$

where the population average firing rate $h^+ = \max(h, 0)$ is a linear threshold function of the synaptic current. The mean number of connections (synapses) per neuron is accounted for by the parameter J and the term Jxy reflects the combined effect of the short-term synaptic plasticity on the network activity. We previously distinguished [109] the parameters K and L which describe how the firing rate is transformed into molecular events that are changing the duration and probability of vesicular release. The time scales t_f and t_r define the recovery of a synapse from the network activity. Finally, $\dot{\omega}$ is an additive Gaussian noise and σ its amplitude. We shall focus now on a reduced version of this system to study the distribution of interburst intervals which are interpreted as escape from a basin of attraction that we will define below, with similar properties as the ones we will present in equation (3.5).

3.2.2 Reduction to a two-dimensional system and phase-space analysis

System (3.1) has 3 critical points: one attractor and two saddle-points. At the attractor $A = (0, X, 1)$, the dynamics is very anisotropic $\left(|\lambda_1| = \frac{1-JX}{\tau} \approx 12.6 \gg |\lambda_2| = \frac{1}{\tau_f} \approx 1.1 \gg |\lambda_3| \approx \frac{1}{\tau_r} = 0.34, \text{using parameters in table 3.1}\right)$ and thus can be reduced to a 2D-plan $y = constant$ so that

$$\dot{y} = 0 = \frac{1-y}{\tau_r} - Lxyh^+ = 0 \iff y = \frac{1}{1+\tau_r Lxh^+}, \tag{3.2}$$

and we obtain the simplified system:

$$\begin{aligned} \dot{h} &= \frac{h\,(Jx - 1 - \tau_r Lxh^{+})}{\tau(1+\tau_r Lxh^{+})} + \sqrt{\tau}\sigma\dot{\omega} \\ \dot{x} &= \frac{X-x}{\tau_f} + K(1-x)h^{+}. \end{aligned} \tag{3.3}$$

The deterministic system (3.3) for $\sigma = 0$ has 3 critical points, two attractors and one saddle-point:

Attractor A_0 is given by $h = 0$ and $x = X$. The Jacobian is

$$J_{A_0} = \begin{pmatrix} \dfrac{-1+JX}{\tau} & 0 \\ K(1-X) & -\dfrac{1}{\tau_f} \end{pmatrix}. \tag{3.4}$$

With the parameters defined in table 3.1, the eigenvalues are $(\lambda_1, \lambda_2) = \left(\dfrac{JX-1}{\tau}, \dfrac{1}{\tau_f}\right) \approx (-12.6, -1.11)$.

Saddle-point S has coordinates $S_1(h_1 \approx 8.07; x_1 \approx 0.28)$. Its eigenvalues are $(\lambda_1, \lambda_2) \approx (-5.73, 1.43)$.

Attractor A_2 is given by $A_2(h_2 \approx 28.8; x_2 \approx 0.53)$. Its eigenvalues are $(\lambda_1, \lambda_2) \approx (-11.9, -1.33)$. The two attractors are separated by a 1D stable manifold Γ passing through the saddle-point S (fig. 3.1A, solid black). To study the dynamics around the attractor A_0, where we approximate $\dot{y} = 0$, we first generated stochastic trajectories and observed two novel phenomena: 1) in the basin of attraction before exiting, trajectories fluctuate around a point not centered at the attractor A_0, but rather around a shifted point A_σ the position of which depends on the noise amplitude (fig. 3.1B.2-B.3); 2) trajectories that exit the basin of attraction through the separatrix Γ can reenter multiple times before finally escaping. In the reduced system (3.3), escape is characterized by falling to the second attractor A_2. The most interesting unexplain phenomena revealed by figs. 3.1C.1-C.2 is the single exponential decay rate with a decay $\lambda = 0.09$ (or $\bar{\tau}_e = 11s$). This is in contrast with the mean escape time $\langle \tau_0 \rangle = 4.35$ (estimated numerically) from the attractor for a trajectory starting at the attractor A and reaching the separatrix Γ. The rest of the manuscript is dedicated to the resolution of this discrepancy and also to the study of properties 1) and 2) that we identified numerically. For that purpose, we study below a generic dynamical system that serves as a model and obtain specific computational criteria and finally, we resolve the present enigma.

3.3 When a perturbation of a two-dimensional system by a Gaussian noise induces a shift of the density function peak with respect to the attractor's position

We consider a class of two-dimensional stochastic dynamical system described by

$$\begin{aligned} \dot{h} &= -\alpha h + x^2 + \sigma\dot{\omega} = b_1(\boldsymbol{s}) + \sigma\dot{\omega} \\ \dot{x} &= F(h,x) = b_2(\boldsymbol{s}), \end{aligned} \tag{3.5}$$

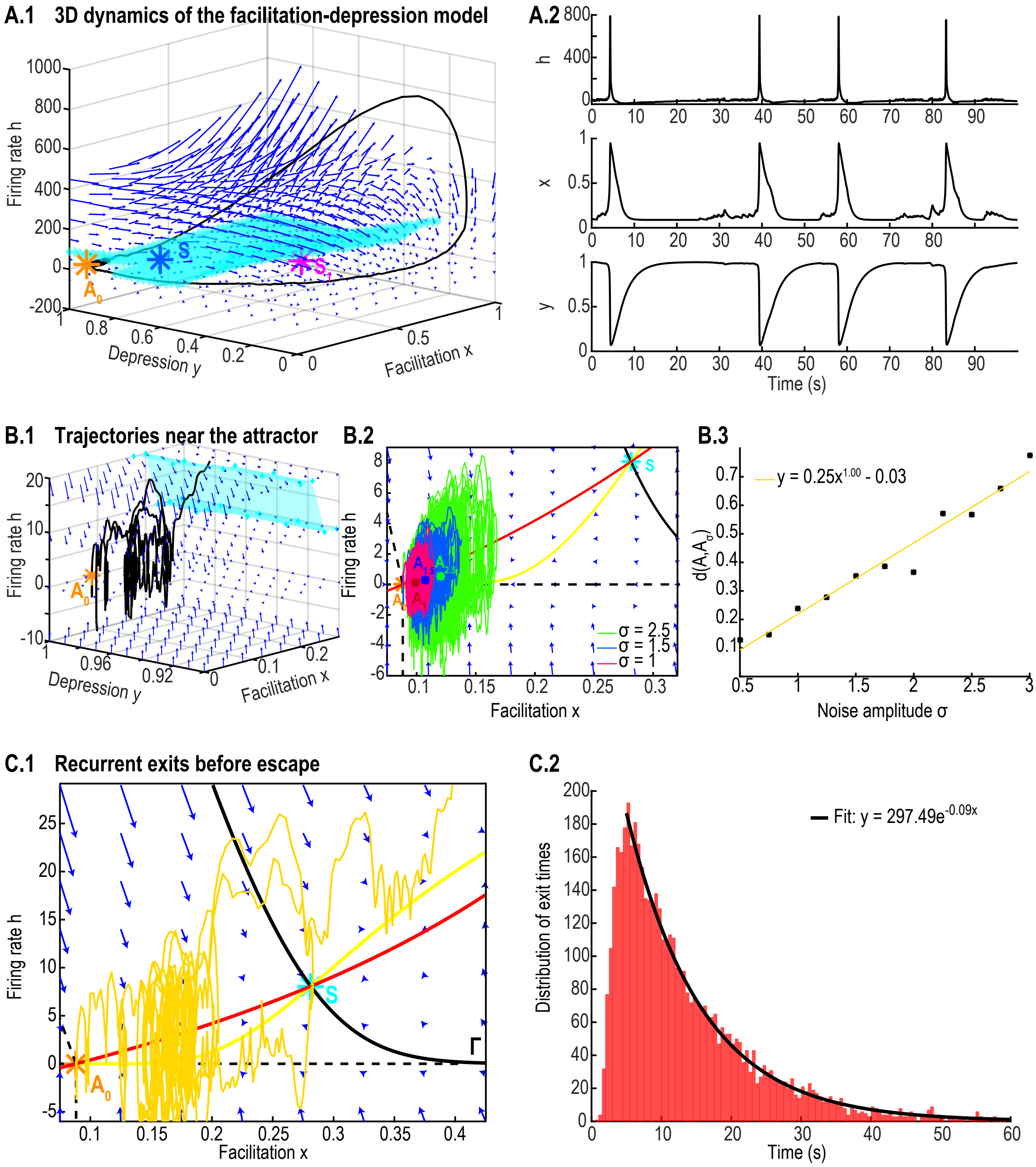

Figure 3.1: **Modeling Bursting and interbursting using a facilitation-depression model A. Dynamics generated by system** (3.1). **A.1** a bursting trajectory (black) in the phase-space, characterized by an attractor A_0 (yellow), two saddle-points S (blue) and S_1 (pink) with a separatrix delimiting the basin of attraction of A_0 (cyan surface). **A.2** Simulated time-series of system (3.1) with a noise amplitude $\sigma = 5$, mean voltage h (upper), facilitation x (center) and depression y (lower) for $T = 100s$. **B. Dynamics in the basin of attraction of** A_0. **B.1** Inset near A_0 showing an escaping trajectory (black). **B.2** Phase-space of the 2D projected dynamics (3.3) for several trajectories ($T = 500s$) associated with three noise levels $\sigma = 1$ (pink),1.5 (blue) and 2.5 (green) rotating around shifted attractors A_σ (centers of mass of the trajectories). **B.3** Distance d(A_0,A_σ) for $\sigma \in [0.5, 3]$ compared to a numerical fit (yellow). **C. Escape dynamics with several returns inside the basin of attraction. C.1** Trajectory exiting the basin of attraction. **C.2** Distribution of exit times where the tail is well approximated by a single exponential with $\lambda_e = 0.09$ (or $\bar{\tau}_e$ 11s).

where

$$F(h,x) = \begin{cases} h - \gamma x & \text{for} \quad h \geq 0 \\ -\gamma x & \text{for} \quad h \leq 0, \end{cases} \tag{3.6}$$

We rewrite this process with $\boldsymbol{s} = (x,h)^T$

$$d\boldsymbol{s} = \boldsymbol{B}(\boldsymbol{s})dt + \Xi dW, \tag{3.7}$$

where

$$\boldsymbol{B}(\boldsymbol{s}) = \begin{pmatrix} b_1(\boldsymbol{s}) \\ b_2(\boldsymbol{s}) \end{pmatrix} \text{ and } \Xi = \begin{pmatrix} \sqrt{\sigma} & 0 \\ 0 & 0 \end{pmatrix}. \tag{3.8}$$

In the following, $\alpha \in]0,1]$, $\gamma \in]0,\alpha[$, $\dot{\omega}$ is a Gaussian white noise and σ its amplitude. Our goal here is to study some properties of such systems. This system has two critical points, $A = (0,0)$ (fig. 3.2A yellow star) and $S = (\gamma^2\alpha, \gamma\alpha)$ (fig. 3.2A cyan star). The jacobian of the system at point A can be computed either for $h \geq 0$ or for $h \leq 0$ and in both cases, we have

$$J_A = \begin{pmatrix} -\alpha & 0 \\ 1 & -\gamma \end{pmatrix}. \tag{3.9}$$

The attractor A has real eigenvalues $\lambda_1 = -\alpha$ and $\lambda_2 = -\gamma$ (its stable manifolds are shown in fig. 3.2A, dotted black lines). The first coordinate of the point S is $h_S = \gamma^2\alpha > 0$ and the jacobian is

$$J_S = \begin{pmatrix} -\alpha & 2\alpha\gamma \\ 1 & -\gamma \end{pmatrix}. \tag{3.10}$$

Both eigenvalues are real, $\lambda_\pm = -\frac{1}{2}\left(-(\alpha+\gamma) \pm \sqrt{(\alpha+\gamma)^2 + 4\alpha\gamma}\right)$ and thus S is a saddle point (with $\alpha = 1$ and $\gamma = 0.6$ we have $\lambda_+ \approx 0.314$ and $\lambda_- \approx -1.914$).

The separatrix that delimits the basin of attraction of A is the stable manifold of S (fig. 3.2A solid black curve). As we shall describe below the unstable manifold defines the escaping direction (fig. 3.2A yellow curve). It is located between the x (respectively h) nullcline $\Phi_x = \{(x,h) | h = \gamma x\}$, 3.2A red (respectively $\tilde{\Phi}_h = \{(x,h) | h = x^2/\alpha\}$, purple).

Numerical simulations reveal that the stochastic trajectories are not centered around the deterministic attractor A (fig. 3.2B, green trajectory). Indeed, we computed the shifted attractor as the expectation of the center of mass for each trajectory, before escaping at time τ_ω,

$$A_\sigma = \mathbb{E}_\omega \left[\frac{1}{\tau_\omega} \int_0^{\tau_\omega} \boldsymbol{s}_\omega(t) dt \right]. \tag{3.11}$$

The empirical distribution peaks at the point A_σ, which we found to be shifted towards the right of the attractor A (fig. 3.2B, green star). Our next goal is to study how this shift depends on σ.

3.3.1 Numerical study of a shifted maximum density at A_σ

To better characterize the shifted peak A_σ induced by the noise for the maximum of the density position, before trajectories escape the attractor, we ran simulations of model eq. (3.5) (fig. 3.2B $\sigma = 0.09$), where trajectories are simulated for 500s. We observed that trajectories are looping around

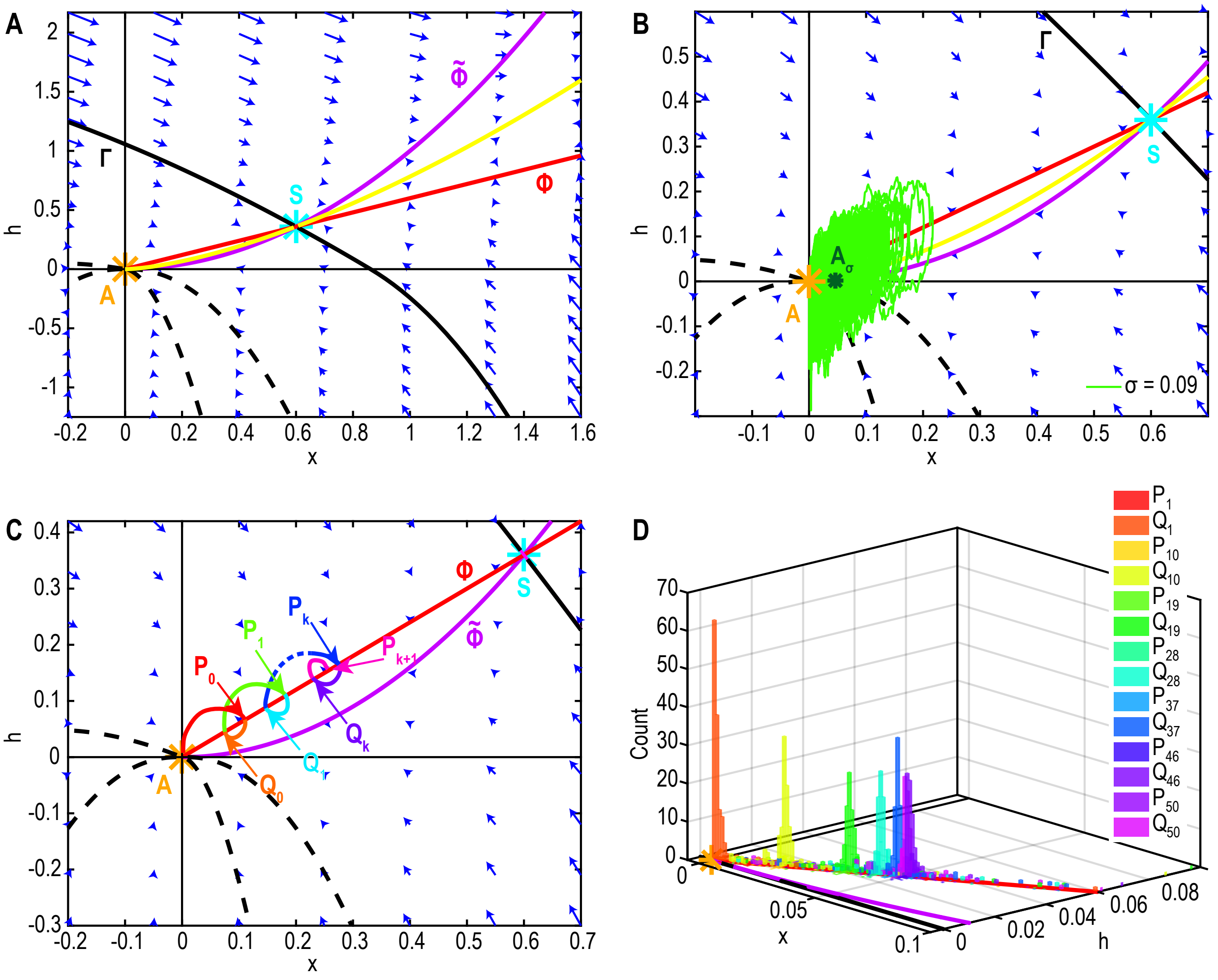

Figure 3.2: **Emergence of a shift in the attractor's position for the noisy dynamical system** (3.5). **A.** Phase-space of system (3.5). The basin of attraction associated to the attractor A (yellow) has two stable manifolds (dashed lines) and is delimited by the stable manifold Γ (solid black) passing through the saddle-point S (cyan). **B.** Stochastic trajectory (green) for a noise amplitude $\sigma = 0.09$. The center of mass A_σ is shifted towards the right with $x_{A_\sigma} \approx 0.05$. **C.** Successive intersection points P_k and Q_k of trajectories with Φ (red). **D.** Distributions ρ_{P_k} and ρ_{Q_k} (500 runs, $\sigma = 0.09$) for $1 \leq k \leq 50$. The peak of the converging distributions $\rho_{P_{46}}$ to $\rho_{P_{50}}$ (purple) indicates the x-coordinate of the shifted attractor $x_{A_\sigma} \approx 0.05$.

the x-nullcline Φ (red). To characterize the shift in the distribution, we study the distribution of points P_0

$$\rho_{P_0} = P(\boldsymbol{s}(t) \in \Phi | \boldsymbol{s}(0) = A) \tag{3.12}$$

where a trajectory starting at A hits Φ for the first time (fig. 3.2C, red). We generated the empirical distribution ρ_{P_0} by simulating 150 trajectories (fig. 3.2D, red) and we found that this distribution is peaked at P_0 close to A. To further understand the dynamics we then investigated the distribution of points Q_0

$$\rho_{Q_0} = P(\boldsymbol{s}(t) \in \Phi | \boldsymbol{s}(0) = P_0) \tag{3.13}$$

where a trajectory starting at P_0 hits Φ for the first time (fig. 3.2C, orange). This distribution is also peaked and located nearby ρ_{P_0} (fig. 3.2D, orange). We then iterated this process to obtain the successive distributions P_k

$$\rho_{P_k} = P(\boldsymbol{s}(t) \in \Phi | \boldsymbol{s}(0) = Q_{k-1}), \tag{3.14}$$

of points where a trajectory starting initially at Q_{k-1} hits Φ. Similarly, we define the distributions of the points

$$\rho_{Q_k} = P(\boldsymbol{s}(t) \in \Phi | \boldsymbol{s}(0) = P_k) \tag{3.15}$$

where a trajectory starting at the peak of ρ_{P_k} hits Φ for the first time (fig. 3.2D). Interestingly, we observed that the distributions are peaked and progress along Φ towards the separatrix Γ. However, after a few iterations, the successive distributions ρ_{P_k} and ρ_{Q_k}, seems to accumulate toward a shifted equilibrium (fig. 3.2D, pink and purple distributions).

3.3.2 Computing the steady-state distribution and the distance of its maximum to the attractor A using WKB approximation

In this section we study analytically the existence and position of the shifted attractor in the stochastic case. This is summarized by the following theorem.

Theorem 3.1 *For stochastic processes* $d\boldsymbol{s} = \boldsymbol{B}(\boldsymbol{s})dt + \Xi dW$, *where the drift* $B = (b_1, b_2)^T$ *is*

$$\begin{aligned} b_1(\boldsymbol{s}) &= -\alpha h + x^2 \\ b_2(\boldsymbol{s}) &= \begin{cases} h - \gamma x & for \quad h \geq 0 \\ -\gamma x & for \quad h \leq 0, \end{cases}, \end{aligned} \tag{3.16}$$

and

$$\Xi = \begin{pmatrix} \sqrt{\sigma} & 0 \\ 0 & 0 \end{pmatrix}, \tag{3.17}$$

where $\alpha \in]0, 1]$, $\gamma \in]0, \alpha[$, dW *is a two dimensional Gaussian white noise and* $\sigma \geq 0$. *We denote by* Ω *the basin of attraction of the attractor* $A = (0, 0)$. *We consider trajectories starting at* A *and staying inside* Ω. *The pdf* p *associated to equation* (3.5) *is solution of the stationary FPE*

$$\frac{\sigma}{2}\frac{\partial^2 p}{\partial h^2} - (\nabla \cdot \boldsymbol{B})p - \boldsymbol{B} \cdot \nabla p = -\delta_A, \tag{3.18}$$

and the solution can be found explicitly in the two following sub domains:

(i) For $\boldsymbol{s} = \{(h, x) \in \Omega | h \geq 0\}$,

$$p(\boldsymbol{s}) = \mathcal{N} \frac{x_0}{x_0 + \gamma x} e^{-\dfrac{\psi(\boldsymbol{s})}{\sigma}}. \tag{3.19}$$

(ii) For $\boldsymbol{s} = \{(h, x) \in \Omega | h \leq 0\}$,

$$p(\boldsymbol{s}) = \mathcal{N} \left(\frac{x_0}{x_0 + \gamma x} \right)^{\dfrac{\alpha + \gamma}{\gamma} - \dfrac{1}{(\alpha - \gamma)^2}} e^{-\dfrac{\psi(\boldsymbol{s})}{\sigma}}, \tag{3.20}$$

where ψ *is the solution of the eikonal equation associated to* (3.18) *and* $\mathcal{N}$ *is a normalization constant such that* $\int_\Omega p(\boldsymbol{s}) d\boldsymbol{s} = 1$.

The next proposition allows us to determine an explicit expression for the solution of the eikonal equation.

Proposition 3.1 *Under the assumptions of theorem 3.1, the solution of the eikonal equation*

$$\boldsymbol{B} \cdot \nabla \psi + \frac{1}{2} \left(\frac{\partial \psi}{\partial h} \right)^2 = 0 \tag{3.21}$$

is

(i) For $\boldsymbol{s} = \{(h, x) \in \Omega | h \geq 0\}$,

$$\psi(h, x) = \alpha \left(h - \left(h_0 - \frac{x_0^2}{\alpha - 2\gamma} - \frac{q_{1,0}}{2\alpha} \right) \left(\frac{x}{x_0} \right)^{\dfrac{\alpha}{\gamma}} - \frac{x^2}{\alpha - 2\gamma} \right)^2, \tag{3.22}$$

where the initial conditions are $h(0) = h_0, x(0) = x_0, q_1(0) = q_{1,0}$ *and* $q_2(0) = q_{2,0} > 0$.

(ii) For $\boldsymbol{s} = \{(h, x) \in \Omega | h \leq 0\}$,

$$\psi(h, x) \approx \frac{Q_0^2}{4\alpha} \left(\frac{2\gamma(h + x)}{q_{2,0}} \right)^{\dfrac{2\alpha}{\gamma}} + \frac{\gamma(h + x)^2}{(\gamma - \alpha)^2} + \frac{Q_0 q_{2,0}}{\gamma^2 - \alpha^2} \left(\frac{2\gamma(h + x)}{q_{2,0}} \right)^{\dfrac{\alpha + \gamma}{\gamma}}, \tag{3.23}$$

where

$$\begin{aligned} Q_0 &= q_{1,0} + \frac{q_{2,0}}{\gamma - \alpha} \\ H_0 &= h_0 - \frac{Q_0}{2\alpha} + \frac{q_{2,0}}{\gamma^2 - \alpha^2} \\ X_0 &= x_0 - \frac{H_0}{\gamma - \alpha} - \frac{Q_0}{2\alpha(\gamma + \alpha)} + \frac{q_{2,0}}{2\gamma(\gamma^2 - \alpha^2)} \end{aligned} \tag{3.24}$$

and the initial conditions are $h(0) = h_0, x(0) = x_0, q_1(0) = q_{1,0}$ *and* $q_2(0) = q_{2,0} > 0$.

Proof: We prove theorem 3.1 and proposition 3.1 together:

Steady state Fokker-Planck equation for system (3.5)

In this subsection, we study the probability density function (pdf) of the system (3.5) for trajectories that stay inside the basin of attraction of A. We first generated 300s simulations for three values of the noise amplitude $\sigma = 0.03$ (pink), 0.09 (blue) and 0.12 green (fig. 3.3A) showing that the pseudo-distributions for points that do not escape the basin of attraction are peaked at A_σ shifted to the right from A. We now compute this pdf using WKB approximation [123]. The steady-state pdf p satisfies the stationary Fokker-Planck Equation (FPE)

$$\frac{\sigma}{2}\frac{\partial^2 p}{\partial h^2} - (\nabla \cdot \boldsymbol{B})p - \boldsymbol{B} \cdot \nabla p = -\delta_A, \tag{3.25}$$

where δ_A is the δ-Dirac function at point A. Due to the discontinuity of the field at $h = 0$ we compute $\nabla \cdot \boldsymbol{B}$ on the two half spaces ($h \geq 0$) and ($h \leq 0$) separately. In the small noise limit $\sigma \to 0$, the WKB solution has the form

$$p(\boldsymbol{s}) = K_\sigma(\boldsymbol{s}) e^{-\dfrac{\psi(\boldsymbol{s})}{\sigma}}, \tag{3.26}$$

where K_σ is a regular function that admits an expansion

$$K_\sigma(\boldsymbol{s}) = \sum_{i=0}^{\infty} K_i(\boldsymbol{s})\sigma^i. \tag{3.27}$$

The eikonal equation is obtained by injecting (3.26) in (3.25) and by keeping only the higher order terms in σ (ie σ^{-1})

$$\boldsymbol{B} \cdot \nabla\psi + \frac{1}{2}\left(\frac{\partial \psi}{\partial h}\right)^2 = 0 \tag{3.28}$$

and the transport equation is obtained using the order 1 terms:

$$\boldsymbol{B} \cdot \nabla K_0 + \frac{\partial \psi}{\partial h}\frac{\partial K_0}{\partial h} = -\left(\nabla \cdot \boldsymbol{B} + \frac{1}{2}\frac{\partial^2 \psi}{\partial h^2}\right) K_0. \tag{3.29}$$

To solve (3.28), we use the method of characteristics with notation $q = (q_1, q_2) = \nabla\psi$. Then eq. (3.28) becomes

$$F(\boldsymbol{s}, q, \psi) = \boldsymbol{B} \cdot q + \frac{1}{2}q_1^2 = 0 \tag{3.30}$$

and the characteristics are given by

$$\begin{aligned}
\frac{dh}{dt} &= b_1(\boldsymbol{s}) + q_1\\
\frac{dx}{dt} &= b_2(\boldsymbol{s})\\
\frac{dq_1}{dt} &= -F_h = -\frac{\partial b_1}{\partial h}q_1 - \frac{\partial b_2}{\partial h}q_2\\
\frac{dq_2}{dt} &= -F_x = -\frac{\partial b_1}{\partial x}q_1 - \frac{\partial b_2}{\partial x}q_2\\
\frac{d\psi}{dt} &= \frac{1}{2}q_1^2.
\end{aligned} \tag{3.31}$$

To define the initial condition, we can choose a neighborhood V_A of A (positioned at the origin), where ψ has a quadratic approximation

$$\psi(\boldsymbol{s}) \approx \frac{1}{2}\boldsymbol{s}^T R\boldsymbol{s} + o(|s|^2)) \text{ for } \boldsymbol{s} \in V_A, \tag{3.32}$$

and R is a symmetric positive definite matrix defined by a degenerated matrix equation at A

$$(J_A\boldsymbol{s})^T \cdot \nabla\psi + \frac{1}{2}q_1^2 = 0, \tag{3.33}$$

where J_A is the Jacobian matrix at point A defined by relation (3.9). We obtain

$$\psi(\boldsymbol{s}) \approx \frac{1}{2}\boldsymbol{s}^T \begin{pmatrix} 2\alpha & 2\gamma \\ 2\gamma & 2\gamma \end{pmatrix} \boldsymbol{s}. \tag{3.34}$$

The ψ contours are the ellipsoids given by

$$\alpha h^2 + 2\gamma xh + \gamma x^2 = \epsilon, \tag{3.35}$$

for small $\epsilon > 0$. To conclude, we choose for the initial conditions one of the small ellipsoids given by (3.35) by fixing later on the value of ϵ.

Solution in the subspace $\boldsymbol{h \leq 0}$

A direct integration of system (3.31) gives for $t \geq 0$

$$\begin{aligned}
h(t) &= \left(h_0 - \frac{x_0^2}{\alpha - 2\gamma} - \frac{q_{1,0}}{2\alpha}\right) e^{-\alpha t} + \frac{x_0^2}{\alpha - 2\gamma} e^{-2\gamma t} + \frac{q_{1,0}}{2\alpha} e^{\alpha t} \\
x(t) &= x_0 e^{-\gamma t} \\
q_1(t) &= q_{1,0} e^{\alpha t} \\
q_2(t) &= \left(q_{2,0} - \frac{2x_0 q_{1,0}}{\alpha - 2\gamma}\right) e^{\gamma t} - \frac{2x_0 q_{1,0}}{\alpha - 2\gamma} e^{(-\gamma + \alpha)t} \\
\psi(t) &= \frac{q_{1,0}^2}{4\alpha} e^{2\alpha t},
\end{aligned} \tag{3.36}$$

where the initial conditions are $h(0) = h_0, x(0) = x_0, q_1(0) = q_{1,0}$ and $q_2(0) = q_{2,0}$. Substituting the expression of x and q_1 in h, we obtain

$$\psi(h, x) = \alpha \left(h - \left(h_0 - \frac{x_0^2}{\alpha - 2\gamma} - \frac{q_{1,0}}{2\alpha}\right) \left(\frac{x}{x_0}\right)^{\frac{\alpha}{\gamma}} - \frac{x^2}{\alpha - 2\gamma} \right)^2. \tag{3.37}$$

We solve the transport equation (3.29) along the characteristics (3.36). Using (3.5) and (3.37), we obtain

$$\frac{dK_0(\boldsymbol{s}(t))}{dt} = \gamma K_0(\boldsymbol{s}(t)), \tag{3.38}$$

yielding

$$K_0(s(t)) = Ce^{\gamma t}. \tag{3.39}$$

For $\alpha > \gamma$, and choosing $\boldsymbol{s}(t) \in V_A$,

$$\tilde{\boldsymbol{s}}(t) \approx \int_0^t x_0 e^{-\gamma u} du \approx -x_0 \frac{e^{-\gamma t} - 1}{\gamma}. \tag{3.40}$$

Thus

$$K_0 \sim \frac{x_0}{x_0 + \gamma \boldsymbol{s} \cdot e_2} = \frac{x_0}{x_0 + \gamma x}, \tag{3.41}$$

where $e_2 = (0,1)^T$ is the eigenvector associated to the eigenvalue $\lambda_2 {=} {-}\gamma$. Finally,

$$p(\boldsymbol{s}) \sim \frac{x_0}{x_0 + \gamma x} e^{-\frac{\psi(\boldsymbol{s})}{\sigma}}. \tag{3.42}$$

Solution in the subspace $h \geq 0$

In this case, we cannot integrate system (3.31) analytically. In the neighborhood of A, $x \ll 1$ and since ψ is a smooth function, we can neglect the quadratic terms in system (3.31) yielding

$$\begin{aligned}
\frac{dh}{dt} &\approx -\alpha h + q_1 \\
\frac{dx}{dt} &= -\gamma x + h \\
\frac{dq_1}{dt} &= \alpha q_1 - q_2 \\
\frac{dq_2}{dt} &\approx -F_x = \gamma q_2 \\
\frac{d\psi}{dt} &= \frac{1}{2} q_1^2.
\end{aligned} \tag{3.43}$$

Integration of system (3.43) gives, for $t \geq 0$

$$\begin{aligned}
h(t) &= H_0 e^{-\alpha t} + \frac{Q_0}{2\alpha} e^{\alpha t} - \frac{q_{2,0}}{\gamma^2 - \alpha^2} e^{\gamma t} \\
x(t) &= X_0 e^{-\gamma t} + \frac{H_0}{\gamma - \alpha} e^{-\alpha t} + \frac{Q_0}{2\alpha(\gamma + \alpha)} e^{\alpha t} - \frac{q_{2,0}}{2\gamma(\gamma^2 - \alpha^2)} e^{\gamma t} \\
q_1(t) &= Q_0 e^{\alpha t} - \frac{q_{2,0}}{\gamma - \alpha} e^{\gamma t} \qquad (3.44) \\
q_2(t) &= q_{2,0} e^{\gamma t} \\
\psi(t) &= \frac{Q_0^2}{4\alpha} e^{2\alpha t} + \frac{q_{2,0}^2}{4\gamma(\gamma - \alpha)^2} e^{2\gamma t} - \frac{Q_0 q_{2,0}}{\gamma^2 - \alpha^2} e^{(\gamma + \alpha)t},
\end{aligned}$$

where

$$\begin{aligned}
Q_0 &= q_{1,0} + \frac{q_{2,0}}{\gamma - \alpha} \\
H_0 &= h_0 - \frac{Q_0}{2\alpha} + \frac{q_{2,0}}{\gamma^2 - \alpha^2} \qquad (3.45) \\
X_0 &= x_0 - \frac{H_0}{\gamma - \alpha} - \frac{Q_0}{2\alpha(\gamma + \alpha)} + \frac{q_{2,0}}{2\gamma(\gamma^2 - \alpha^2)}
\end{aligned}$$

and the initial conditions are $h(0) = h_0, x(0) = x_0, q_1(0) = q_{1,0}$ and $q_2(0) = q_{2,0}$.
To derive the eikonal solution, we eliminate the time and start with the relation

$$q_2 \approx 2\gamma(h + x), \qquad (3.46)$$

which is obtained from (3.34). Substituting (3.46) in h, we obtain near the attractor A

$$\psi(h, x) \approx \frac{Q_0^2}{4\alpha} \left(\frac{2\gamma(h + x)}{q_{2,0}} \right)^{\frac{2\alpha}{\gamma}} + \frac{\gamma(h + x)^2}{(\gamma - \alpha)^2} + \frac{Q_0 q_{2,0}}{\gamma^2 - \alpha^2} \left(\frac{2\gamma(h + x)}{q_{2,0}} \right)^{\frac{\alpha + \gamma}{\gamma}}. \qquad (3.47)$$

Furthermore, we solve the transport equation (3.29) along the characteristics (3.44). We differentiate twice (3.47) with respect to h, we obtain $\dfrac{\partial^2 \psi}{\partial h^2} \approx \dfrac{\gamma}{(\alpha - \gamma)^2}$, which leads to

$$\frac{dK_0(\boldsymbol{s}(t))}{dt} \approx \left(\alpha + \gamma - \frac{\gamma}{(\gamma - \alpha)^2} \right) K_0(\boldsymbol{s}(t)). \qquad (3.48)$$

Using (3.40) we obtain

$$K_0 \sim \left(\frac{x_0}{x_0 + \gamma x} \right)^{\frac{\alpha + \gamma}{\gamma} - \frac{1}{(\alpha - \gamma)^2}}. \qquad (3.49)$$

Finally, for $\boldsymbol{s} \in V_A$

$$p(\boldsymbol{s}) \sim K_0(\boldsymbol{s}) e^{-\dfrac{\psi(\boldsymbol{s})}{\sigma}}, \tag{3.50}$$

where K_0 and ψ are defined by relations (3.49) and (3.47), respectively. When $\alpha \neq \gamma$ and $\alpha \neq 2\gamma$, the exponent in (3.49) is positive when

$$\frac{\alpha+\gamma}{\gamma} - \frac{1}{(\gamma-\alpha)^2} > 0 \iff 1 - \left(\frac{\gamma}{\alpha}\right) - \left(\frac{\gamma}{\alpha}\right)^2 + \left(\frac{\gamma}{\alpha}\right)^3 - \frac{\gamma}{\alpha^3} > 0, \tag{3.51}$$

that is for $\dfrac{\gamma}{\alpha} > 0.45$. For the range of parameters $0.45\alpha < \gamma < \alpha$ and $\alpha \neq 2\gamma$, the pdf has a maximum located on the $h = 0^+$ axis shifted towards the right of A (fig. 3.3B, for three values of the noise amplitude $\sigma = 0.03$ (pink), 0.09 (blue) and 0.12 green and for $\gamma = 0.6$). This maximum gives the position of the shifted attractor A_σ, which depends on the noise amplitude. When $\dfrac{\gamma}{\alpha} \leq 0.45$, since the linearization approximation in (3.46) is not valid, formula (3.50) cannot be use to approximate the pdf. □

Computing the distance between A_σ and A

The distance between A and A_σ is defined by

Corollary 3.2 Position of the shifted stochastic attractor *The pdf p of stochastic trajectories solution of equation* (3.5) *that did not escape the basin of attraction Ω peaks at a shifted position compared to the attractor A, and the shift depends on the noise amplitude σ. The maximum of the pdf p is located on the line $h = 0^+$ and is given by the implicit equation*

$$-\frac{A1}{1+\dfrac{\gamma}{x_0}x} - \frac{1}{\sigma}\left(A_2 x^{\dfrac{2\alpha}{\gamma}-1} + A_3 x^{\dfrac{\alpha}{\gamma}} + A_4 x\right) = 0, \tag{3.52}$$

where

$$A_1 = \left(\frac{\alpha+\gamma}{\gamma} - \frac{1}{(\alpha-\gamma)^2}\right)\frac{\gamma}{x_0}, A_2 = \frac{Q_0^2}{q_{2,0}}\left(\frac{2\gamma}{q_{2,0}}\right)^{\dfrac{2\alpha}{\gamma}-1}, A_3 = \frac{2Q_0}{\gamma-\alpha}\left(\frac{2\gamma}{q_{2,0}}\right)^{\dfrac{\alpha}{\gamma}}, A_4 = \frac{2\gamma}{(\alpha-\gamma)^2}. \tag{3.53}$$

Proof: To study how the distance between A and A_σ depends on the noise amplitude σ, we use that the maximum of the pdf (3.50) is given by

$$\nabla p = 0. \tag{3.54}$$

However, the partial derivative along h is discontinuous, and the analytical expression for pdf p (3.42, 3.50) is decreasing with $|h|$ on both halves of the phase-space. Thus based on the numerical motivation

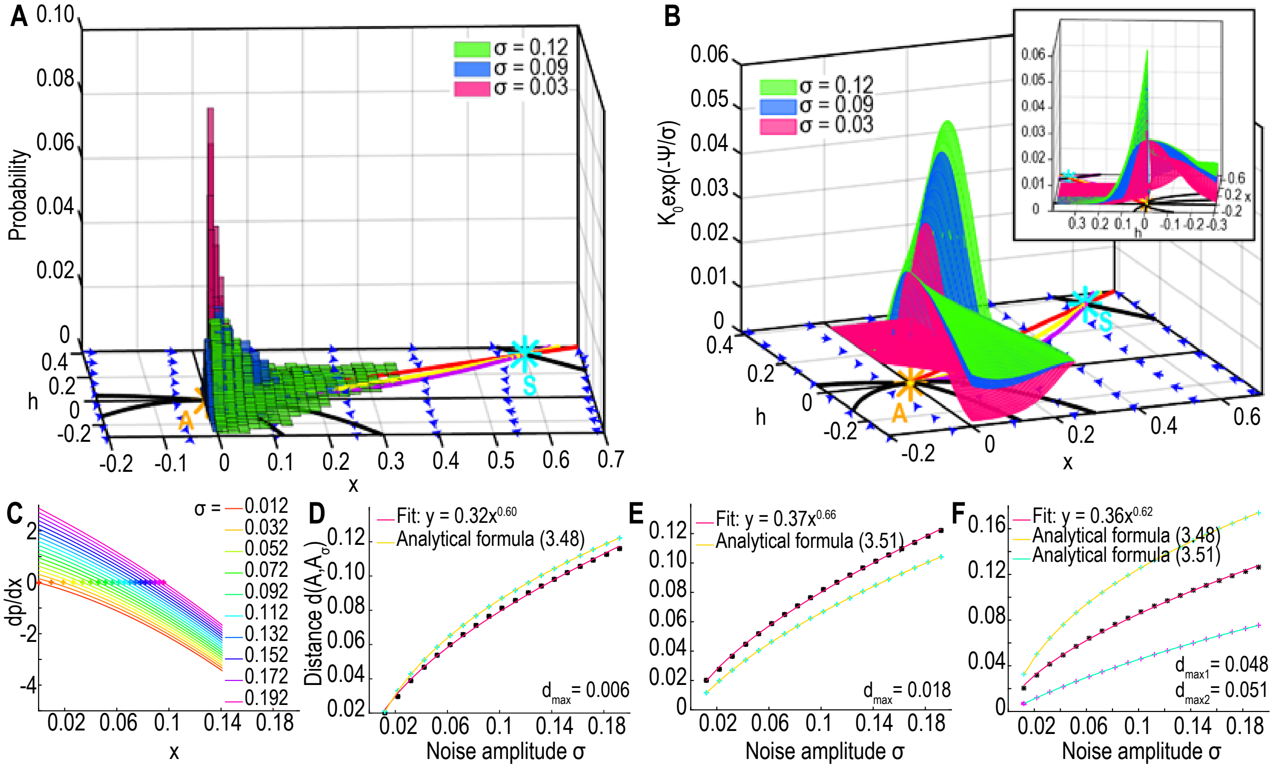

Figure 3.3: **Position of the shifted attractor A_σ A.** Simulated pdf of the trajectories for three noise levels $\sigma = 0.03$ (pink), $\sigma = 0.09$ (blue) and $\sigma = 0.12$ (green) for $\gamma = 0.6$ and $\alpha = 1$. **B.** Analytical distributions for the three noise levels. Inset: same distributions with a different perspective. **C.** $\frac{\partial p}{\partial x}_{|h=0^+}(x)$ for $\sigma \in [0.01, 0.2]$ (the crosses indicate the zeros). **D-E.** Distance $d(A, A_\sigma)$ as a function of σ. Numerical solution (black stars with numerical fit in pink) and analytical relation 3.58 (resp. 3.61, cyan crosses with yellow curve) for $\gamma = 0.6$ (resp. 0.9) and $\alpha = 1$. **F.** Distance $d(A, A_\sigma)$ as a function of σ. Numerical solution (black stars with numerical fit in pink) compared with the analytical expressions (3.58) and (3.61) (cyan crosses with yellow curve and magenta crosses with blue curve) in the case $\gamma = 0.75$ and $\alpha = 1$ for which neither polynomial approximation is valid.

that the maximum of the pdf A_σ is shifted along the x axis, we are left with solving $\frac{\partial p}{\partial x}_{|h=0^+} = 0$. Using relation (3.50), for $h \geq 0$ we obtain

$$-\frac{\left(\frac{\alpha+\gamma}{\gamma}-\frac{1}{(\alpha-\gamma)^2}\right)\gamma}{x_0+\gamma x}+\frac{1}{\sigma}\left(-\frac{Q_0^2}{q_{2,0}}\left(\frac{2\gamma}{q_{2,0}}\right)^{\frac{2\alpha}{\gamma}-1} x^{\frac{2\alpha}{\gamma}-1} -\frac{2Q_0}{\gamma-\alpha}\left(\frac{2\gamma}{q_{2,0}}\right)^{\frac{\alpha}{\gamma}} x^{\frac{\alpha}{\gamma}} - \frac{2\gamma x}{(\alpha-\gamma)^2}\right)=0, \tag{3.55}$$

We rewrite (3.55) as

$$-\frac{A1}{1+\frac{\gamma}{x_0}x}-\frac{1}{\sigma}\left(A_2 x^{\frac{2\alpha}{\gamma}-1}+A_3 x^{\frac{\alpha}{\gamma}}+A_4 x\right)=0, \tag{3.56}$$

where

$$A_1=\left(\frac{\alpha+\gamma}{\gamma}-\frac{1}{(\alpha-\gamma)^2}\right)\frac{\gamma}{x_0}, A_2=\frac{Q_0^2}{q_{2,0}}\left(\frac{2\gamma}{q_{2,0}}\right)^{\frac{2\alpha}{\gamma}-1}, A_3=\frac{2Q_0}{\gamma-\alpha}\left(\frac{2\gamma}{q_{2,0}}\right)^{\frac{\alpha}{\gamma}}, A_4=\frac{2\gamma}{(\alpha-\gamma)^2}. \tag{3.57}$$

The algebraic equation (3.56) describes the shift, compared to the attractor, of the pdf peak along the x axis. This equation cannot be solved analytically in general and we solved it numerically for various values of σ (fig. 3.3C). □

However, we shall describe two cases for which (3.56) can be approximated by a polynomial equation. We computed the absolute difference $d(\sigma) = |x_{M,num}(\sigma) - x_M(\sigma)|$ between the numerical result $x_{M,num}(\sigma)$ and the solution $x_M(\sigma)$ of the approximated polynomial equation (3.60) (respectively 3.62) that we define below, for $\sigma \in [0, 0.2]$, and using the criteria $d_{max} = \max_{\sigma\in[0,0.2]}(d(\sigma)) < 0.02$ (fig. 3.3D-F) we obtained the approximation validity range $0.5 < \frac{\gamma}{\alpha} \leq 0.645$ (respectively $0.885 \leq \frac{\gamma}{\alpha} < 1$).

Corollary 3.3 Approximated expression for the distance $|A_\sigma - A|$ in the parameter range $0.5 < \frac{\gamma}{\alpha} < 0.645$: *the solution of equation* (32) *is*

$$x_M(\sigma) = |A_\sigma - A| = \left(\frac{-q(\sigma)-\sqrt{\Delta(\sigma)}}{2}\right)^{1/3}+\left(\frac{-q(\sigma)+\sqrt{\Delta(\sigma)}}{2}\right)^{1/3}-\frac{c_2}{3c_1}, \tag{3.58}$$

where

$$\begin{aligned}
c_1 &= A_2 + A_3 + \frac{A_4\gamma}{x_0} \approx 397,2 \\
c_2 &= A_2 + A_3 \approx 117.5 \\
A_4 &= 7.5 \\
A_1 &\approx -17.7 \\
q(\sigma) &= \frac{2c_2^3 - 9c_1c_2A_4}{27c_1^3} + \frac{A_1}{c_1}\sigma \approx 5,5.10^{-5} - 0.04\sigma \\
\Delta(\sigma) &= q(\sigma)^2 + \frac{4}{27}\left(\frac{3c_1A_4 - c_2^2}{3c_1^2}\right)^3 \approx q(\sigma)^2 - 1,6.10^{-7}
\end{aligned} \tag{3.59}$$

(expression (3.58) *is valid as long as* $\Delta(\sigma) \geq 0$*, that is* $\sigma > 0.0114$*).*

The numerical applications are given for the parameter values $\alpha = 1, \gamma = 0.6$, $h_0 = 0.001$, $x_0 = 0.12$.
Proof: We approximate $\frac{2\alpha}{\gamma} - 1 \approx 2$ and $\frac{\alpha}{\gamma} \approx 2$ and (3.56) becomes the third order polynomial equation

$$A_1\sigma + A_4 x + \left(A_2 + A_3 + \frac{A_4\gamma}{x_0}\right)x^2 + (A_2 + A_3)\frac{\gamma}{x_0}x^3 = 0. \tag{3.60}$$

□

Corollary 3.4 Expression of distance $A_\sigma - A$ in the range $0.885 \leq \frac{\gamma}{\alpha} < 1$: *in this range the solution is*

$$x_M(\sigma) = \frac{-1 + \sqrt{1 - \frac{4\gamma}{x_0}\frac{A_1\sigma}{A_2 + A_3 + A_4}}}{2\gamma}x_0 \approx -0.56 + \frac{\sqrt{1 + 38.45\sigma}}{1.8}, \tag{3.61}$$

The numerical application is given for the parameter values $\alpha = 1$, $\gamma = 0.9$ and $\sigma \geq 0$ (fig. 3.3E cyan crosses and yellow curve).
Proof: Here we can approximate (3.56) by the second order polynomial equation

$$\frac{\gamma}{x_0}x^2 + x + \frac{A_1\sigma}{A_2 + A_3 + A_4} = 0, \tag{3.62}$$

□

To verify the range of validity of our approximations for the position of A_σ, we also ran simulations for $\sigma \in [0.03, 0.12]$ (fig. 3.4A $\sigma = 0.12$, green, 0.09, blue and 0.03, pink). We compared the distance $d(A, A_\sigma)$ obtained from numerical simulations (3.4B-C black stars) and the analytical formula (3.58) (resp. 3.61) (fig. 3.4B (resp. C) yellow curve) for $\alpha = 1$ and $\gamma = 0.6$ (resp. $\gamma = 0.9$). In the case $\gamma = 0.6$, we added an offset in formula (3.58) to minimize the absolute value of the difference between the analytical formula and the simulations:

$$\hat{c} = \min_{c \in [0,0.1]} \sum_{\sigma \in [0.03,0.12]} |x_M(\sigma) - c - x_{M,sim}(\sigma)|, \tag{3.63}$$

where $x_M(\sigma)$ is defined by (3.58) and $x_{M,sim}(\sigma)$ is the value obtained from the numerical simulations. Using a finite number of values, we found $\hat{c} = 0.032$. This offset is probably due to the approximations we made for the derivation of formula (3.58).
To conclude we have found here analytical expressions (3.58 and 3.61) for the position of A_σ and showed that these expressions approximate well the numerical simulations.

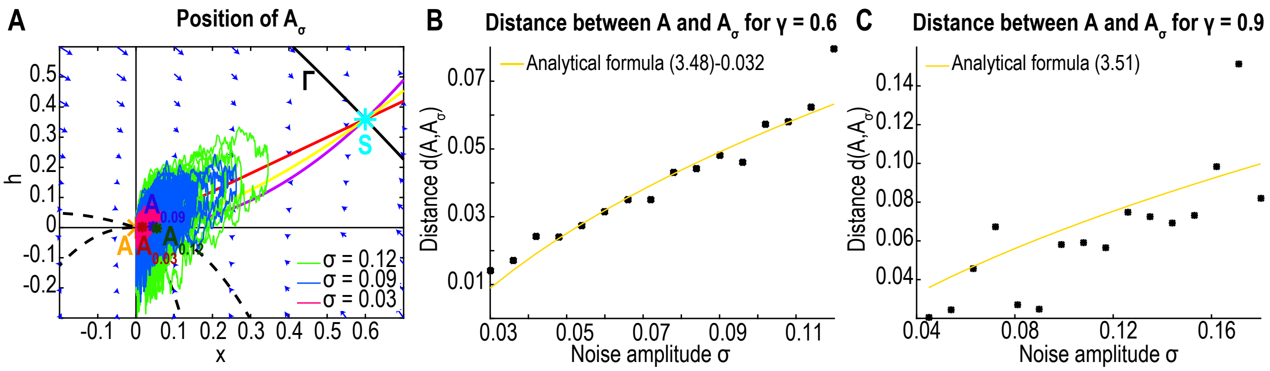

Figure 3.4: **Influence of the noise amplitude on the peak distribution A_σ. A.** Stochastic trajectories simulated for $T = 500s$ with three noise levels $\sigma = 0.03$ (pink), 0.09 (blue) and 0.12 (green) and the shifted peaks A_σ. **B.** Distance $d(A, A_\sigma)$ vs σ. Numerical simulations are obtained with a stopping time $T = 800$ s per noise value (black stars), compared to the analytical formula 3.58 (yellow) minus a corrective offset $\hat{c} = 0.032$. **C.** Distance $d(A, A_\sigma)$ vs σ. Numerical simulations are generated with a stopping time $T = 800$ s per noise value (black stars), compared to the analytical formula 3.61 (yellow).

3.4 Multiple re-entries and distributions of escape times and points

In this section, we report a novel mechanism of stochastic escape from an attractor, based on multiple re-entries.

3.4.1 The different steps of escape

The escape from the basin of attraction of A can be divided into three steps.

1. Step 1: starting from the attractor A, trajectories fall into the basin of attraction of the shifted equilibrium A_σ. The duration of this step is almost immediate and can be neglected compared with the durations of the next steps 2 and 3.

2. Step 2: trajectories fluctuate around the shifted equilibrium A_σ until they reach the separatrix Γ for the first time.

3. Step 3: trajectories cross Γ, exiting and reentering the basin of attraction several times before eventually escaping far away (fig. 3.5A-C).

We will quantify the excursions occurring in step 3 by counting the number of round-trips (RT) across Γ. We first study these three steps numerically by simulating 5000 trajectories starting from A and lasting $T = 300s$ for $\sigma = 0.78$. To obtain the distribution of exit times and points on the separatrix Γ at each RT, we decided to replace Γ by its tangent T_Γ at S (fig. 3.5A-C pink line). Indeed, the distribution of exit points peaks at a distance $O(\sqrt{\sigma})$ from S [134] and thus the difference between the separatrix and its tangent is of order 2. This approximation will allow us to use the analytical expression of the tangent T_Γ.

We then decompose the escape time in the first time to reach the separatrix Γ plus the time spent doing successive excursions outside and inside the basin of attraction (fig. 3.5D, the color gradient indicates the contribution of the trajectories doing a specific number of RT to the total distribution of escape times). This decomposition can be used to estimate the proportion of trajectories that escape at each RT and to evaluate the escape probability after crossing the separatrix as we will see below.

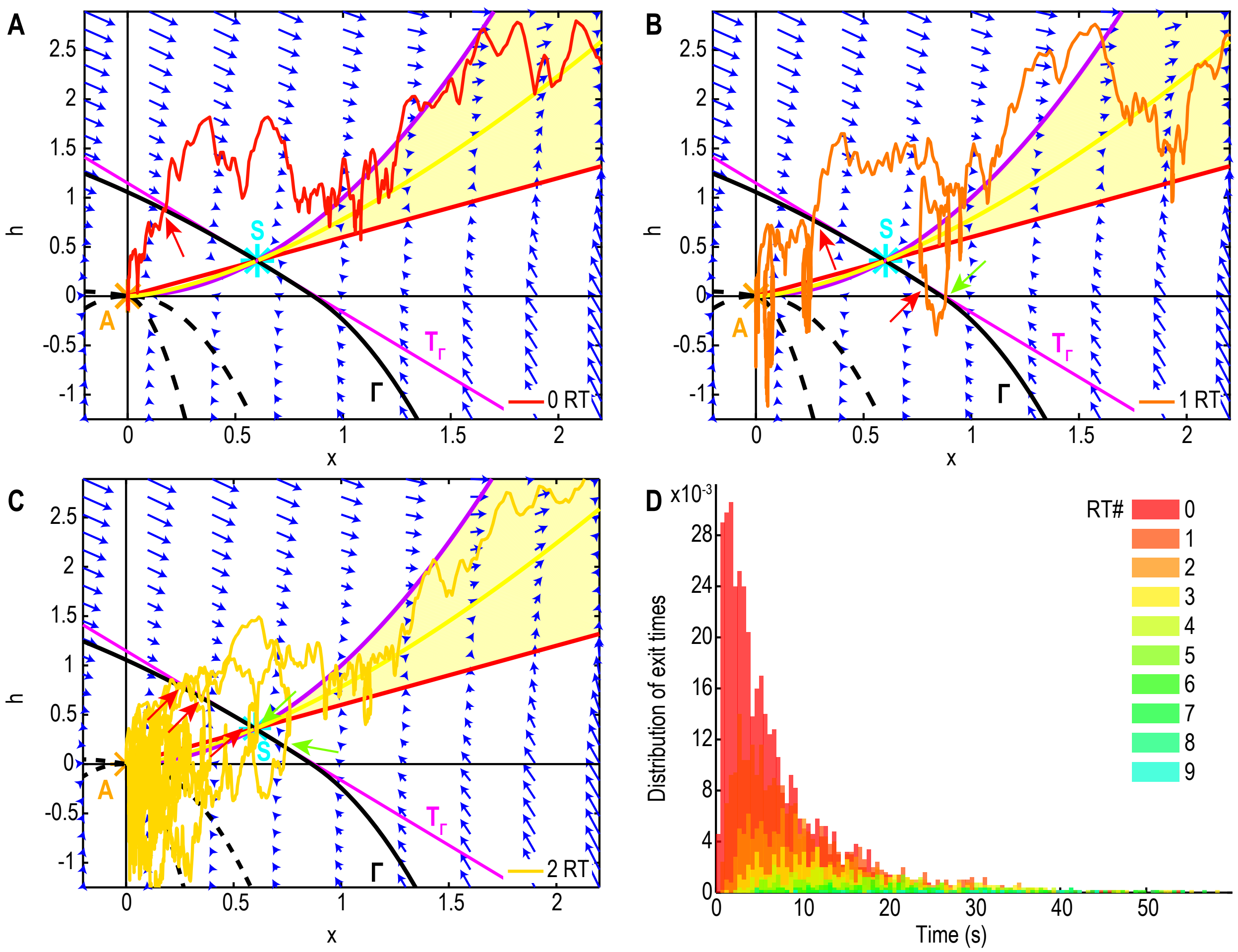

Figure 3.5: **Recurrent exit pattern and contribution to the escape time. A-C.** Trajectory doing zero (resp. one, two) RT before escape (red, resp. orange, yellow) the red (resp. green) arrows indicate exit (resp. reentry) points. **D.** Distribution of escape times from 5000 trajectories lasting $T = 300$ s ($\gamma = 0.6$, $\alpha = 1$ and $\sigma = 0.78$) with the contribution of trajectories doing for each number of RT around Γ before escaping (color gradient).

3.4.2 First exit time and exit points distributions on the separatrix Γ

We study here the influence of the noise on the distributions of first exit times and exit points: we simulate $N = 2500$ trajectories starting at A and lasting $T = 300$ s for $\sigma \in [0.21, 1.05]$. The first exit time can be very long for small values of σ (fig. 3.6A, orange distribution for $\sigma = 0.21$, and light green for $\sigma = 0.33$) but becomes shorter with peaked distributions when σ increases (dark green to red). The distribution of the first exit points is peaked and located on the left of the saddle-point S (fig. A.3.1A purple for $\sigma = 0.78$). We found here that the distance $d(P_E, S)$ between the peak P_E of this distribution and the saddle-point S for $\sigma \in [0.15, 1.05]$ is of order $O(\sqrt{\sigma})$ (fig. 3.6B) in agreement with the classical theory [134]. We further observed from numerical simulations that the density of exit points of the first trajectories that reenter the basin of attraction at least once follows a similar distribution as the one of first exit points for all trajectories (fig. A.3.1A green) indicating that there are no correlations between the position of the escape points and the phenomenon of reentry in the basin of attraction. Finally, the distribution of the first reentry points also peaks on the left of the saddle-point but spreads on both sides of S (fig. A.3.1A red).

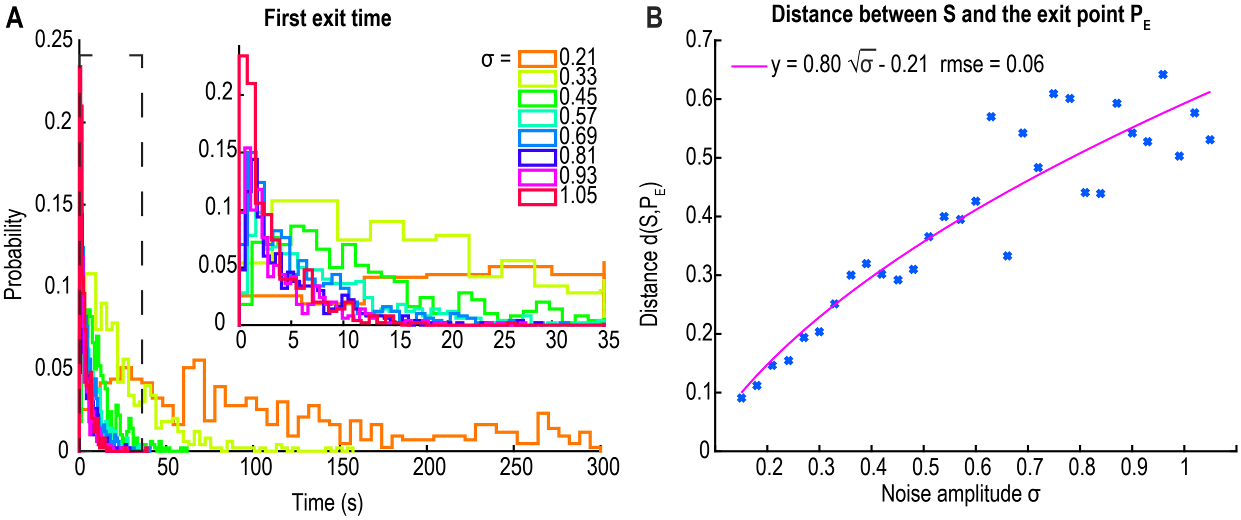

Figure 3.6: **Influence of the noise amplitude on the first exit times and points. A.** Distribution of the first exit times with respect to the noise amplitude σ with an inset on short times. **B.** Distance between the peak P_E of the distribution of first exit points on the separatrix and the saddle-point S with respect to the noise amplitude σ for $\gamma = 0.6$ and $\alpha = 1$ with a square-root fit (pink).

3.4.3 Characterization of the mean escape time

The mean escape time is given by the following lemma:

Lemma 3.1 *We consider a phase-space composed of a single bounded basin of attraction. Outside the basin of attraction the trajectories converge to infinity. Then, the mean escape time to infinity from the basin of attraction is given by the sum*

$$\langle \tau_{esc} \rangle = \langle \tau_0 \rangle + \frac{\langle \tau_{ext} \rangle + \langle \tau_{int} \rangle}{\tilde{p}}, \tag{3.64}$$

where $\tilde{p}$ *is the probability that a trajectory crossing the separatrix* Γ *does not return inside the basin of attraction,* $\langle \tau_0 \rangle$ *is the mean time to reach the separatrix for the first time and* $\langle \tau_{ext} \rangle$ *(resp.* $\langle \tau_{int} \rangle$*) is the mean time spent outside (resp. inside) the basin of attraction during one RT.*

Proof: To obtain a general expression for the mean escape time, we use Baye's law and condition by the RT numbers so that

$$\langle \tau_{esc} \rangle = \sum_{k=0}^{\infty} \langle \tau | k \rangle P_{RT}(k), \tag{3.65}$$

where $\langle \tau | k \rangle$ (resp. $P_{RT}(k)$) is the mean time (resp. probability) to return $k-$times inside the basin of attraction. Because, due to the strong Markov properties, the RT are independent events, the probability $\tilde{p}$ that a trajectory crossing the separatrix Γ escapes does not depend on k, yielding

$$P_{RT}(k) = \tilde{p}(1-\tilde{p})^{k-1}, \tag{3.66}$$

thus

$$\langle \tau_{esc} \rangle = \langle \tau_0 \rangle + (\langle \tau_{ext} \rangle + \langle \tau_{int} \rangle)\tilde{p} \sum_{k=1}^{\infty} k(1-\tilde{p})^{k-1} = \langle \tau_0 \rangle + \frac{\langle \tau_{ext} \rangle + \langle \tau_{int} \rangle}{\tilde{p}}, \tag{3.67}$$

where $\langle \tau_{ext} \rangle$ (resp. $\langle \tau_{int} \rangle$) is the mean time spent outside (resp. inside) the basin of attraction during one RT. □

To avoid counting small Brownian fluctuations as RT inherent to the discretization (fig. 3.7A black arrows), we added a second line $\tilde{\Gamma}$ at distance $\delta = 0.25$ parallel to the separatrix (fig. 3.7B blue line) and thus a trajectory is considered to have fully exited the basin of attraction once it has crossed both the tangent T_Γ and $\tilde{\Gamma}$.

Using this procedure we estimated the probability $\tilde{p}(k)$ to escape after k RT by counting the proportion of trajectories that reenter the basin of attraction at least once and we found using numerical simulations $\tilde{p}(1) \approx 0.40$. We iterated this process for each RT until all trajectories had escaped to infinity and found that the probability $\tilde{p}(k)$ for $k \geq 1$ does not depend on k (fig. A.3.1B), thus $\tau_{esc} \approx \tau_0 + 2.5(\tau_{ext} + \tau_{int})$. Finally, with the parameters $\alpha = 1$, $\gamma = 0.6$ and $\sigma = 0.78$, numerical simulations show that $\langle \tau_0 \rangle \approx 5s$ and $\langle \tau_{ext} \rangle + \langle \tau_{int} \rangle \approx 2.6s$ (fig. 3.7C).

To conclude, the process of entering and exiting multiple times increases the mean escape time by a factor of 2.3. In addition we found, based on simulations for $\sigma \in [0.54, 0.90]$, that the noise amplitude does not influence the number of RT before escape (fig. 3.7D) and that trajectories perform 2.5 RT on average.

3.4.4 Characterization of escape times distributions

The escape time distribution is given by the following lemma

Lemma 3.2 *Under the assumptions of lemma 3.1, the distribution of escape times is*

$$P(\tau_{esc} < t) = \sum_{k=0}^{\infty} f_0(t) * f_1(t)^{*k} \tilde{p}(1-\tilde{p})^k. \tag{3.68}$$

where $f(t)^{*k} = f(t) * f(t) * ... * f(t)$*,* k *times,* f_0 *is the distribution of escape times for trajectories escaping without any RT and* f_1 *of a single RT.*

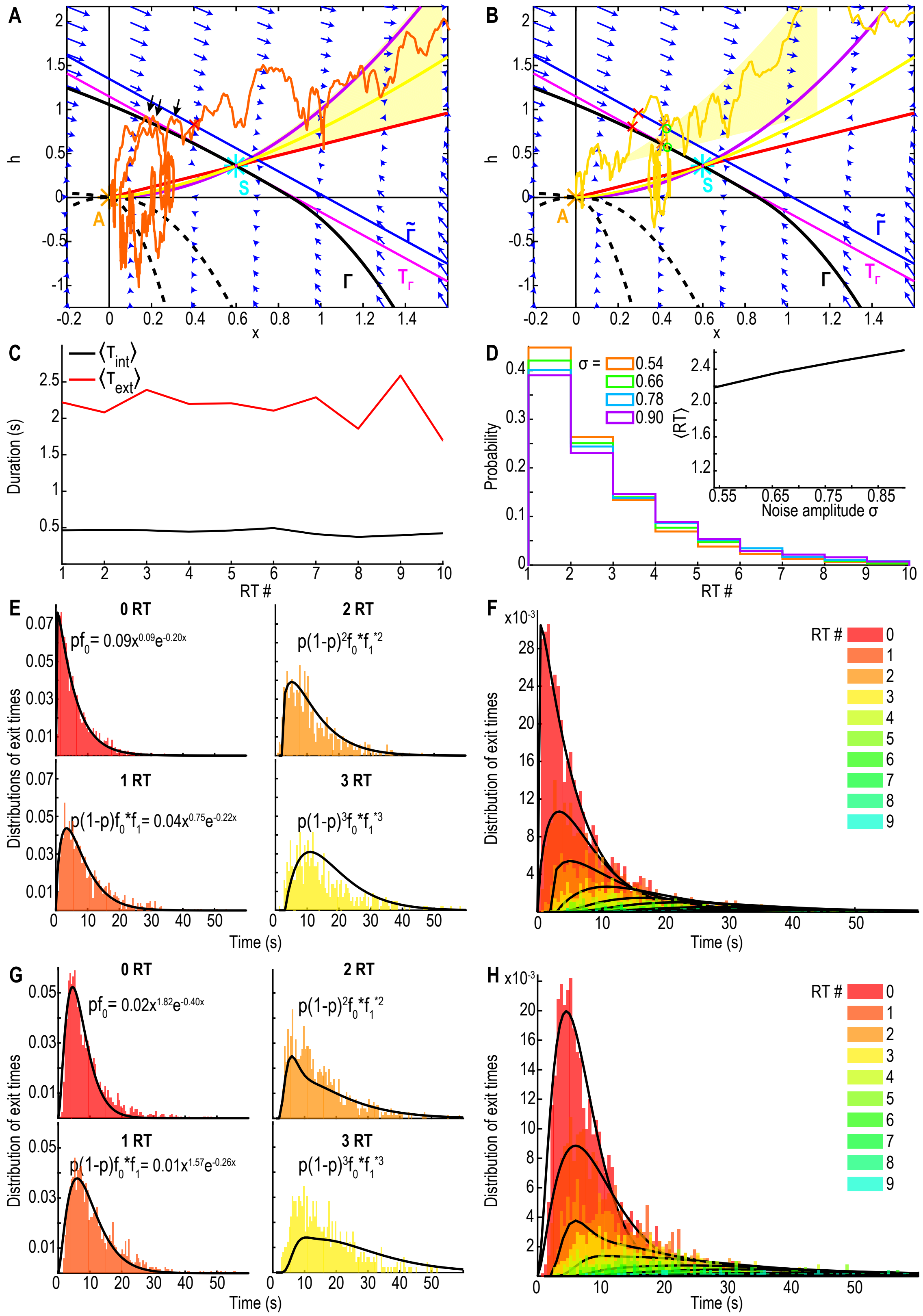

Figure 3.7: **Characterization of escape times. A.** Trajectory escaping (red cross) after small brownian fluctuations at the separatrix (black arrows). **B.** Trajectory exiting (red crosses) after crossing T_Γ (pink) and $\tilde{\Gamma}$ (blue), reentering (green circles) and reexiting (orange crosses) the basin of attraction before escaping. **C.** Mean time $\langle \tau_{ext} \rangle$ (resp. $\langle \tau_{int} \rangle$) spent outside (resp. inside) the basin of attraction at each RT. **D.** Distributions of the RT number before trajectories escape to infinity for $\sigma \in [0.54, 0.90]$. Inset: mean RT number $\langle RT \rangle$ with respect to the noise amplitude. **E.** Distribution of exit times for trajectories doing 0 (upper left, resp. 1 (lower left), 2 (upper right), 3 (lower right)) RT before escape. **F.** Distribution of exit times with the contribution of each RT number (color gradient) and analytical distribution (37) (black) **G-H.** Application to model (3.3)

	Parameters	Values
τ	Time constant for h	0.05s
J	Synaptic connectivity	4.21
K	Facilitation rate	0.037Hz
X	Facilitation resting value	0.08825
L	Depression rate	0.028Hz
τ_r	Depression time rate	2.9s
τ_f	Facilitation time rate	0.9s
T	Depolarization parameter	0

Table 3.1: Parameters of model (3.1)

Proof: To determine the distribution of escape times, we condition the escape on the number of RT, so that

$$P(\tau_{esc} < t) = \sum_{k=0}^{\infty} P(\tau^k < t|k) P_{RT}(k), \tag{3.69}$$

where $P(\tau^k < t|k)$ is the probability distribution of escape times after k RT. This probability is obtained by the k-th convolution of the distribution f_1 of times for trajectories exiting after a single RT with the distribution f_0 of escape times with 0 RT

$$P(\tau^k < t|k) = f_0(t) * f_1(t)^{*k}, \tag{3.70}$$

where $f(t)^{*k} = f(t) * f(t) * ... * f(t)$, k times. Thus (3.69) becomes

$$P(\tau_{esc} < t) = \sum_{k=0}^{\infty} f_0(t) * f_1(t)^{*k} \tilde{p}(1-\tilde{p})^k. \tag{3.71}$$

□

To compare this formula with our numerical results, we decided to fit the distributions with

$$f_i(t) = c_i t^{a_i} e^{-\lambda_i t}, \text{ for } i = 0, 1, a_i \geq 0 \text{ and } \lambda_i \geq 0 \tag{3.72}$$

Using the Matlab fit function (fig. 3.7C), we obtained for the distribution escape without any RT

$$\tilde{p} f_0(t) = 0.09 t^{0.09} e^{-0.20t} \tag{3.73}$$

and for the trajectories doing exactly one RT before escape

$$F_1(t) = \tilde{p}(1-\tilde{p}) f_0 * f_1(t) = 0.04 t^{0.75} e^{-0.22t}. \tag{3.74}$$

To recover the distribution f_1 (3.74), we deconvolved numerically F_1 from f_0 (3.73) (fig. 3.7E lower left). This procedure allows us to validate our approach by computing the distributions of 2 and 3 RT and comparing them with the empirical distributions (3.70) (fig. 3.7E upper and lower right). Finally, we decomposed the entire escape times distribution using (3.71) to evaluate the contribution of each term (fig. 3.7E-F).

3.5 Further application and concluding remarks

3.5.1 Distribution of interburst durations

The phase-space of system (3.3), restricted to the region $\{x \leq 0.5 \text{ and } h \leq 30\}$ is topologically equivalent to the phase-space of system (3.5). It contains one attractor and one saddle-point and the stable manifold of the saddle-point defines the boundary of the basin of attraction (fig. 3.1A). Following the result of system (3.5), trajectories fall into a basin of attraction centered around a shifted attractor towards the saddle-point S, as shown in fig. 3.1B, red (resp. blue, green) star for $\sigma = 1$ (resp. 1.5, 2.5)). The shifted attractor position depends on the noise amplitude σ (fig. 3.1C) and the escaping trajectories can return several times inside the basin of attraction before escaping far away (fig. 3.1D, one RT). We used formula (37) to fit the distribution of exit times (fig. 3.1E-F) and obtained, for $\sigma = 6$ the distribution of exit with no return

$$f_0(t) = 0.02t^{1.82}e^{-0.40t} \tag{3.75}$$

and the distribution of one RT is

$$f_1(t) = 0.01t^{1.57}e^{-0.26t}. \tag{3.76}$$

Finally, using numerical simulations, we estimated the escape probability $\tilde{p} \approx 0.37$ by generating trajectories starting from the attractor A and counting the fraction that fully escaped far away vs those that did return inside the basin of attraction (fig. A.3.2A). The mean escape time is given by formula (3.64):

$$\langle \tau_{esc} \rangle \approx \langle \tau_0 \rangle + 2.7(\langle \tau_{ext} \rangle + \langle \tau_{int} \rangle). \tag{3.77}$$

Using parameters of table 3.1, we obtain $\langle \tau_0 \rangle \approx 4.35$ s and $\langle \tau_{ext} \rangle + \langle \tau_{int} \rangle \approx 2.6$ s (fig. A.3.2B). We conclude that returns to the attractor increases the mean escape time from 4.35 s to 11.37 s leading to an increase by a factor 2.6. Moreover, the number of RT before escape does not depend on the noise amplitude (section 3.4.3 and fig. A.3.2C) and trajectories generate in average 2.7 RT before escape (fig. A.3.2C, inset). Finally, this escape mechanism could explain long interburst durations occurring in excitatory neuronal networks without the need of adding any other refractory mechanisms. Indeed, the present computations can be used to study the neuronal interburst dynamics modeled in the mean-field approximation by depression-facilitation equations [102, 109]. We also provided a possible explanation for the long interburst durations observed in neuronal networks reported in [52].

To conclude this article, motivated by finding a possible mechanism that generates long interburst intervals, we examined a family of stochastic dynamical systems perturbed by a small Gaussian noise. The dynamics exhibits specific properties such as peaks of the pdf inside the basin of attraction shifted compared to the attractor. In addition, escaping the basin is characterized by multiple reentries inside the attractor. We computed the position of this shifted attractor using WKB approximation and we derived algebraic formulas to link the position to the noise amplitude σ (formulas 3.58 and 3.61). We also computed the escape time, decomposed into the time to reach the boundary of the basin of attraction plus the time spent going back and forth through the separatrix (formulas 3.67 and 3.71). Finally, we emphasize the generic conditions associated with this escape dynamics into the following conjecture:

Conjecture 3.1 Recurrent exit mechanism
For stochastic dynamical systems of dimension ≥ 2 *perturbed by a small Gaussian noise, if the following conditions are satisfied:*

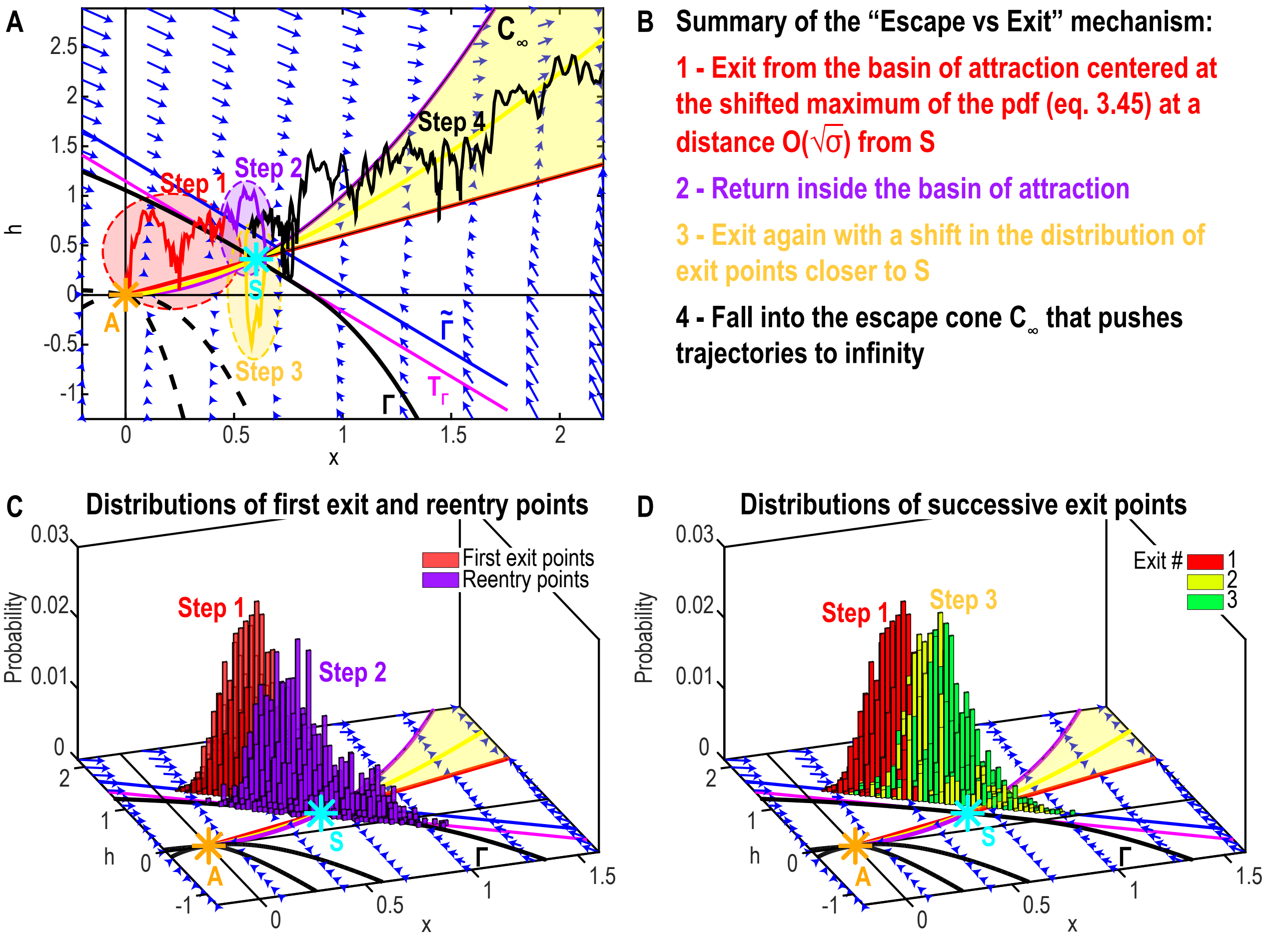

Summary of the "Escape vs Exit" mechanism:

1 - Exit from the basin of attraction centered at the shifted maximum of the pdf (eq. 3.45) at a distance $O(\sqrt{\sigma})$ from S

2 - Return inside the basin of attraction

3 - Exit again with a shift in the distribution of exit points closer to S

4 - Fall into the escape cone C_∞ that pushes trajectories to infinity

Figure 3.8: **Recurrent exit mechanism.** **A.** Trajectories exiting the basin of attraction (red), re entering (purple) and exiting again (yellow) before eventually escaping to infinity (black) after reaching the cone C_∞ (yellow surface). **B.** Schematic of escape process divided in four steps. **C.** Distribution of the first exit (resp. reentry) points (red, resp. purple) on the separatrix $\tilde{\Gamma}$. **D.** Distributions of successive exit points (first exit, red, second yellow, third green) on $\tilde{\Gamma}$.

1. *The distribution of exit points peaks at a distance* $O(\sqrt{\sigma})$ *from the saddle-point (generically satisfied [134]).*
2. *The shallow field near the separatrix allows the trajectories to reenter the basin of attraction with high probability.*
3. *The peaks of the successive exit points distributions converge to the saddle-point* S *(fig. 3.8C).*
4. *When trajectories enter the cone* C_∞ *(yellow surface in fig. 3.8A-B) where the field increases, they eventually escape to infinity,*

Then the trajectories present multiple reentries into the basin of attraction and the escape time τ_{esc} *is not given by the classical Kramer's exit theory and can be much higher due to the additive term in equation* (3.64).

Acknowledgements L. Zonca has received support from French Research Ministry (ED386 Ecole doctorale de Sciences Mathématiques Paris centre) and FRM (FDT202012010690). This project has received funding from the European Research Council (ERC) under the European Union's Horizon 2020 research and innovation program (grant agreement No 882673).

Appendix Figures

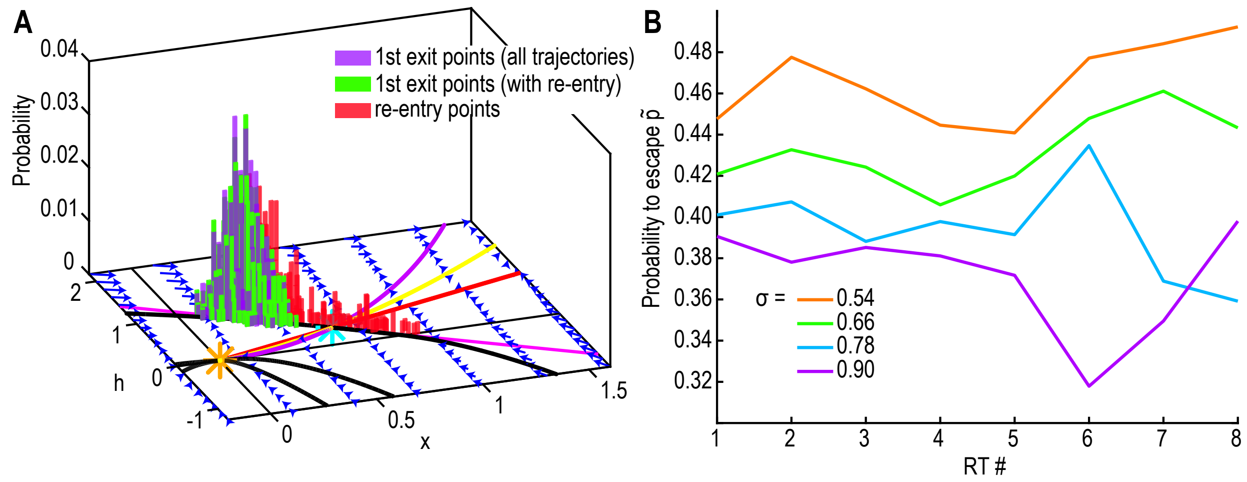

Figure A.3.1: **Distributions of the first exit points located on the separatrix Γ A.** for all trajectories (purple) and first exit for re-entering trajectories (green, 60% of trajectories), reentry points (red) for $\sigma = 0.78$. **B.** Probability to escape after exiting the basin of attraction for the k-th time, $\tilde{p}(k)$ estimated by the proportion of trajectories that reenter the basin of attraction after k RT for noise amplitudes $\sigma \in [0.54, 0.90]$.

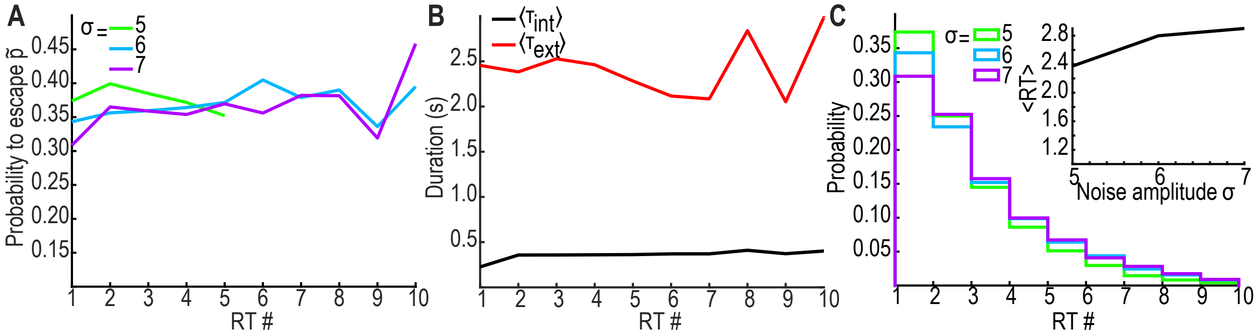

Figure A.3.2: **Probability $\tilde{p}$ to escape after exiting the basin of attraction A.** Probability $\tilde{p}$ vs the RT number for $\sigma \in [4, 7]$, with a linear fit. **B.** Mean times $\langle \tau_{ext} \rangle$ (red) and $\langle \tau_{int} \rangle$ (black) vs the RT number. **C.** Distributions of RT numbers before escape for $\sigma \in [4, 7]$. Inset: mean RT number with respect to σ

Part II

Applications to data analysis and computational neuroscience

Chapter 4

Astroglial gap junctions strengthen hippocampal network activity by sustaining afterhyperpolarization via KCNQ channels

submitted as DOSSI E., ZONCA L.*, PIVONKOVA H., VARGOVA L., CHEVER O., HOLCMAN D.$^+$ & ROUACH N.$^+$, "Astroglial gap junctions strengthen hippocampal network activity by sustaining afterhyperpolarization via KCNQ channels" *,$^+$contributed equally*

Abstract

Astrocytic networks mediated by gap-junction channels promote population activity by modulating neuronal excitability and network synchronization. Yet the underlying mechanisms remain unclear. Here using astroglial connexin-deficient mice, we found that astrocyte networks regulate neuronal bursting patterns via dynamic regulation of extracellular potassium levels. We then examined the physiological and molecular targets underlying the astroglial-mediated potassium regulation of neuronal patterns by an interdisciplinary approach combining electrophysiology and modeling. Using a novel facilitation-depression model, we identified neuronal afterhyperpolarization as the key parameter underlying bursting patterns regulation by extracellular potassium in mice with disconnected astrocytes. We confirmed experimentally this prediction, and revealed that astroglial network-control of extracellular potassium sustains neuronal afterhyperpolarization via activation of KCNQ voltage-gated K^+ channels. Altogether, these data identify the molecular mechanism by which astroglial gap-junctions strengthen neuronal population bursts, thus pointing to selective astroglial gap-junction modulators as alternative therapeutic targets to control aberrant activity in neurological diseases.

Introduction

Astrocytes are elements of the tripartite synapse playing a key role in brain information processing. At the single cell level, they can integrate neuronal activity via activation of their channels, receptors and transporters. In turn, they can modulate neuronal excitability, synaptic transmission and plasticity via several mechanisms including ions and neurotransmitters uptake, gliotransmitters release or physical coverage of synapses [45,46]. Astrocytes are also organized in intercellular networks via their extensive direct communication through gap junction (GJ) channels. These channels are formed by two main connexin (Cx) subunits, Cx43, which is present from embryonic to adult stages, and Cx30, whose expression starts later during development [47]. GJ allow intercellular trafficking and long-range exchange of various ions, metabolites and neuromodulators up to 1.5 kDa, important for the redistribution of energy metabolites to neurons, as well as for extracellular ion, neurotransmitter and volume homeostasis [48, 49]. Thereby, GJ-connected astrocytic networks control basal synaptic transmission and plasticity [163, 164]. Mice deficient for astroglial Cx43 and Cx30 have indeed increased hippocampal synaptic transmission and reduced long-term synaptic plasticity, due to impaired astroglial glutamate and potassium clearance and regulation of extracellular space volume during synaptic activity [164]. Astrocytic networks also control population activity by promoting sustained coordinated neuronal bursts [52–54]. We indeed found that astrocytic disconnection in Cx-deficient mice resulted in shorter, but more frequent population bursts, which translate in vivo into a reduced severity of evoked seizures and associated convulsive behavior [52], indicating that GJ-mediated astroglial networks can exacerbate pathological network activity. Yet, the cellular and molecular mechanisms underlying the alteration of bursting patterns remain unknown. Electrophysiological dissection of neuronal alterations in mice with disconnected astrocytes however revealed that the altered bursting pattern was associated with increased synaptic noise, leading to depolarization of neuronal resting membrane potential, as well as with decreased neuronal release probability and impaired synchronization [52]. In addition, increased neuronal excitability and decreased refractory period after bursting were also found. Thus, numerous alterations of neuronal membrane and synaptic properties were identified in Cx-deficient mice, questioning their relative contribution to the altered bursting pattern. Here we investigated the mechanisms by which astrocytic networks modulate neuronal network bursts dynamics. By combining experimental and modeling approaches, we found that astroglial networks regulate bursting patterns by controlling neuronal afterhyperpolarization (AHP) via extracellular potassium modulation of KCNQ channels activity.

Organisation of the chapter: In section 4.1, we present the experimental results showing that alteration of the bursting pattern in Cx-deficient mice results from the impairment of extracellular potassium regulation. Then we use modeling and numerical simulations (section 4.2) to decipher the respective influence of AHP, membrane depolarization, synaptic noise and depression, which are all affected by the imbalance of the extracellular potassium level. We also verify experimentally the model's predictions. Finally, we describe the experimental setup (subsections 4.4.1-4.4.4) and the model's equations (subsection 4.4.5) and we detail the data processing and segmentation procedure in the supplementary information (section 4.5).

4.1 Experimental results

4.1.1 Astroglial gap junctions regulate extracellular potassium levels during bursting

Astroglial GJ regulate neuronal bursting patterns and this is associated to changes in excitability and synaptic activity [52]. Yet, the underlying physiological and molecular mechanisms are unknown. GJ contribute to extracellular homeostasis of various ions, neurotransmitters and metabolites such as potassium ions (K^+), glutamate and glucose [49, 165], but their physiological relevance is unclear. We thus here first investigated whether astroglial GJ contribute to alterations in extracellular K^+ levels ($[K^+]_e$) during bursting activity. The astroglial membrane potential reflects the presence of high resting conductances for K^+ [46] and is thus highly sensitive, with a quasi-nernstian relationship, to alterations in $[K^+]_e$ [166,167]. We thus first assessed alterations in $[K^+]_e$ by recording astrocyte membrane potential using whole-cell patch clamp recordings. We observed that disconnected astrocytes in Cx-deficient mice (-/-) displayed a depolarized resting membrane potential compared to wild type (+/+) astrocytes (+/+: -82.98 ± 0.37 mV, -/-: -79.67 ± 0.69 mV, $p = 0.0001$; $n = 17$ and $n = 13$ cells from 4 +/+ and 5 -/- mice, respectively; fig. 4.1A-B) and more frequent, but smaller and shorter membrane potential depolarizations during bursting activity (membrane potential depolarization frequency (per min): +/+: 3.16 ± 0.40, -/-: 5.81 ± 0.62, $p = 0.0008$; ΔV_m during membrane potential depolarizations: +/+: 5.07 ± 0.86 mV, -/-: 2.68 ± 0.35 mV, $p = 0.0207$; membrane potential depolarization duration: +/+: 9.41 ± 0.49 s, -/-: 6.17 ± 0.91 s, $p = 0.0029$; $n = 17$ and $n = 13$ cells from 4 +/+ and 5 -/- mice, respectively; fig. 4.1A-B). We also found that astroglial membrane potential depolarization evoked-synaptically by Schaffer collateral stimulation with increasing strength (0.1 and 0.5 ms pulse width) was reduced in -/- astrocytes for both stimulation paradigms (membrane potential depolarization area ($mV \times s$): 0.1 ms, +/+: 20.76 ± 4.13, -/-: 7.79 ± 1.41, $p = 0.0072$; 0.5 ms, +/+: 24.25 ± 4.24, -/-: 10.65 ± 1.92, $p = 0.0077$; membrane potential depolarization amplitude (mV): 0.1 ms, +/+: 4.89 ± 0.82, -/-: 2.57 ± 0.31, $p = 0.0359$; 0.5 ms, +/+: 6.48 ± 0.83, -/-: 4.01 ± 0.46, $p = 0.0406$; $n = 17$ and $n = 11$ cells from 4 +/+ and 5 -/- mice, respectively; fig. 4.1C-D).

Further, to directly assess alterations in $[K^+]_e$ during resting and bursting activity, we performed simultaneous recordings of $[K^+]_e$ and field potentials using K^+-sensitive microelectrodes and electrophysiology in +/+ and -/- hippocampal slices (fig. 4.1E). We found that -/- slices presented higher basal $[K^+]_e$ between bursts (+/+: 2.96 ± 0.11 mM, -/-: 3.65 ± 0.25 mM, $p = 0.02$; $n = 16$ and $n = 17$ slices from 9 +/+ and 6 -/- mice, respectively; fig. 4.1F) as well as burst-associated $[K^+]_e$ transients with reduced amplitude, half-width, rise time and decay time, which reflected decreased burst strength (fig. 4.1E), compared to +/+ slices ($\Delta[K^+]_e$ during bursts: +/+: 2.07 ± 0.40 mM, -/-: 0.73 ± 0.11 mM, $p = 0.0009$; half-width: +/+: 10.34 ± 1.23 s, -/-: 5.09 ± 0.33 s, $p < 0.0001$; rise time: +/+: 2.28 ± 0.42 s, -/-: 0.99 ± 0.11 s, $p = 0.0019$; decay time: +/+: 21.63 ± 3.66 s, -/-: 8.78 ± 0.43 s, $p = 0.0003$; $n = 13$ and $n = 18$ slices from 8 +/+ and 9 -/- mice, respectively; fig. 4.1G). Altogether, these results indicate that disconnected astrocytes deficient for astroglial Cx impair extracellular K^+ homeostasis, which results in increased basal $[K^+]_e$ and decreased $[K^+]_e$ rise during bursting activity.

4.1.2 Switch between wild type and knockout bursting patterns by altering extracellular potassium levels

Since Cx-deficient astrocytes do not properly regulate $[K^+]_e$, we investigated whether the resulting $[K^+]_e$ changes induce an alteration of bursting activity in -/- mice. To do so, we first tested in +/+ mice the impact of $[K^+]_e$ increase on bursting pattern. To this end, we determined the $[K^+]_e$ that would reflect the increase in $[K^+]_e$ found in -/- mice. As reported above, we found that basal $[K^+]_e$ was increased by ≈ 0.7 mM in -/- slices, as measured by K^+-sensitive microelectrodes in the tissue (fig. 4.1F). However, this increase in basal $[K^+]_e$ is most likely a relative value, since these electrodes have limited access to the actual local $[K^+]_e$ in tissue nanocompartments. In addition, extrapolation of the exogenous $[K^+]_e$ that would be needed to mimic the actual local $[K^+]_e$ increase in -/- slices is challenging, as penetration and diffusion of exogenous K^+ is also limited in slices. Resting membrane potential of neurons is sensitive to $[K^+]_e$ and was previously reported to be depolarized by ≈ 5 mV in mice with disconnected astrocytes [52]. We thus searched the exogenous $[K^+]_e$ needed to mimic this depolarization, and found that increasing $[K^+]_e$ by 3.5 mM in +/+ slices depolarized pyramidal cells by ≈ 5 mV (before: -62.7 ± 0.6 mV; during K^+ application: -57.6 ± 1.5 mV, $n = 5$; $p < 0.001$). Remark-

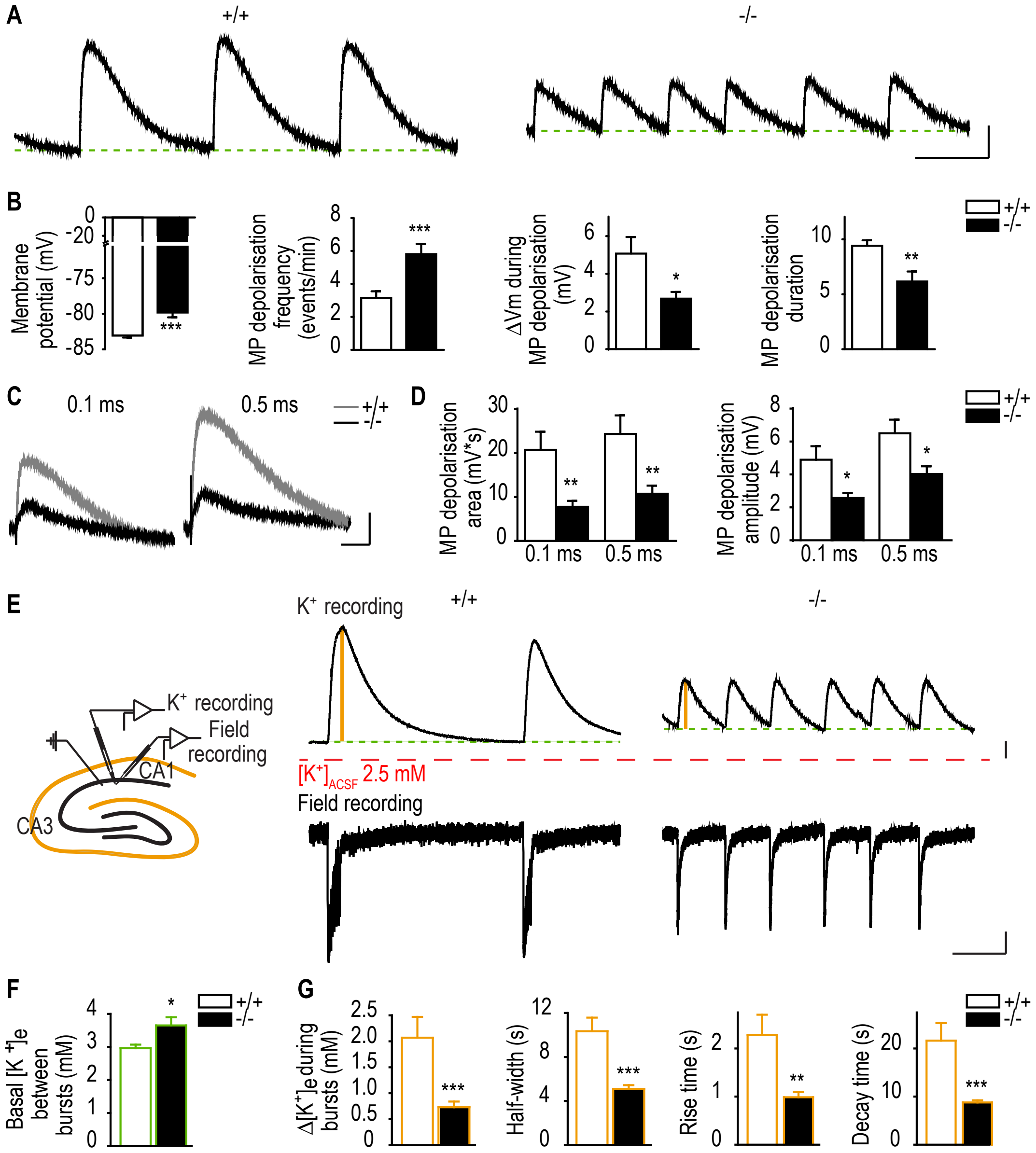

Figure 4.1: **Gap junction-mediated astroglial networks modulate extracellular potassium levels during bursting. A.** Representative traces of spontaneous astrocyte membrane depolarizations in +/+ (left) and -/- (right) slices bathed in 0 Mg^{2+}, picrotoxin ACSF and generating bursts. The green dashed lines indicate the resting membrane potential. Scale bars: 10 s, 2 mV. **B.** Quantification of CA1 stratum radiatum astrocyte resting membrane potential (MP), and spontaneous MP frequency, amplitude and duration in +/+ and -/- slices (+/+: $n = 17$ cells form 4 mice; -/-: $n = 13$ cells from 5 mice; unpaired t-test). **C.** Representative traces of evoked astrocyte response in +/+ (grey) and -/- (black) slices after 0.1 ms (left) and 0.5 ms (right) Schaffer collateral stimulation. Scale bars: 2 s, 2 mV. **D.** Quantification of MP depolarization area and amplitude in +/+ and -/- astrocytes after 0.1 and 0.5 ms Schaffer collateral stimulation (+/+: $n = 17$ cells form 4 mice; -/-: $n = 13$ cells from 5 mice; unpaired t-test). **E.** Left, schematics illustrating simultaneous recordings of extracellular K^+ and fEPSPs in the CA1 area of hippocampal slices. Right, representative traces from simultaneous recordings of K^+ transients (top) and field potentials (bottom) in CA1 stratum radiatum of +/+ and -/- mice. The red and green dashed lines indicate K^+ concentration in ACSF ($[K^+]_e = 2.5$ mM) and basal extracellular K^+ concentration measured between consecutive bursts, respectively. The orange bar indicates K^+ changes ($\Delta[K^+]_e$) recorded during bursts. Scale bars: 10 s, 0.2 mV (bottom)/0.5 mM (top). **F.** Quantification of basal $[K^+]_e$ between bursts, indicated by the green dashed line in panel **E** (+/+: $n = 16$ slices from 9 mice; -/-: $n = 17$ slices from 6 mice; $p < 0.05$, unpaired t-test). **G.** Quantification of $\Delta[K^+]_e$ during bursts (indicated by the orange line in panel **E**), half-width, rise time and decay time (+/+: $n = 13$ slices from 8 mice; -/-: $n = 18$ slices from 9 mice; unpaired t-test). Asterisks indicate statistical significance (*, $p < 0.05$; **, $p < 0.01$; ***, $p < 0.001$).

ably, the same increase in $[K^+]_e$ in +/+ slices strongly augmented burst frequency (before: 2.28 ± 0.26 bursts/min; during K^+ application: 6.47 ± 0.43 bursts/min, $n = 9$ slices from 4 mice; $p < 0.0001$), and decreased burst duration (before: 2.18 ± 0.22 s; during K^+ application: 1.52 ± 0.07 s, $n = 9$ slices from 4 mice; $p = 0.0065$; fig. 4.2A-B), thus mimicking alterations induced by disconnection of astrocytes in -/- mice. Conversely, we then tested in -/- mice the impact of $[K^+]_e$ decrease on bursting pattern. We found that decreasing $[K^+]_e$ by 1 mM in -/- slices reduced burst frequency (before: 5.67 ± 0.55 bursts/min; during K^+ application: 3.7 ± 0.32 bursts/min, $n = 6$ slices from 4 mice; $p = 0.0018$), as well as increased burst duration (before: 1.23 ± 0.06 s; during K^+ application: 1.76 ± 0.17 s, $n = 6$ slices from 4 mice; $p = 0.0115$; fig. 4.2C-D), thus rescuing wild type bursting pattern.

We previously reported that the altered bursting pattern in -/- mice is associated with a decreased neuronal release probability, a hallmark of synaptic depression [168]. Such release probability is correlated to the size of the vesicle readily releasable pool [169], determining in turn the recruitment of neurons during bursting activity [11, 170], which we also found to be reduced in -/- mice [52]. To further test the implication of $[K^+]_e$ alterations in the change of bursting pattern in -/- mice, we here tested whether they also contribute to the synaptic depression. To do so, we performed repetitive stimulation of Schaffer collaterals (10 Hz, 30 s), which induces a rapid synaptic facilitation followed by a depression, resulting from presynaptic glutamate depletion (fig. 4.2E). We found that responses to prolonged repetitive stimulation initially facilitated less and depressed faster in -/- compared to +/+ slices ($p < 0.0001$ and $p = 0.0436$, $n = 9$ and 7 slices for +/+ and -/-, respectively; fig. 4.2F-G). Remarkably, increasing $[K^+]_e$ by 3.5 mM in +/+ slices significantly reduced the initial facilitation ($p < 0.0001$) to -/- levels ($p = 0.1630$) and accelerated synaptic depression ($p < 0.001$; $n = 9$ slices; fig. 4.2F, orange). Conversely, decreasing extracellular K^+ by 1 mM in -/- slices increased the 10 Hz-induced initial facilitation and slowed down the subsequent depression ($p < 0.0001$ and $p = 0.0428$, $n = 7$ slices; fig. 4.2G, green) to +/+ level ($p = 0.9374$). Altogether, our data show that relevant changes in basal $[K^+]_e$ can fully switch wild type and knockout bursting patterns, pointing to their contribution to alteration of bursting activity in -/- mice.

4.1.3 Impairing extracellular glutamate homeostasis or metabolic support does not mimick the alteration of bursting pattern in astroglial Cx-deficient mice

Astroglial networks also play a key role in restraining basal synaptic activity through modulation of extracellular glutamate clearance rate. Astroglial Cx-deficient mice indeed show increased excitatory synaptic activity due to an impairment of synaptic glutamate uptake, which makes glutamate persist longer at the synapse and prolong its activation of AMPA and NMDA receptors currents [164]. To test if a persistent activation of glutamatergic receptors is responsible for the altered bursting pattern in Cx-deficient mice, we first prolonged in +/+ slices glutamate receptor activation by blocking AMPA receptor (AMPAR) desensitization with cyclothiazide (100 μM) (fig. S4.1A). We found that cyclothiazide causes a decrease in burst frequency (bursts/min, Control: 2.78 ± 0.25, cyclothiazide: 1.72 ± 0.27, $p = 0.0022$; $n = 10$ slices from 4 mice) with no effect on burst duration (Control: 1.85 ± 0.13 s, cyclothiazide: 1.82 ± 0.11 s, $p = 0.8816$; $n = 10$ slices from 4 mice). Furthermore, seizure-like events, which were never observed in control conditions, appeared after ≈ 20 min of cyclothiazide application with an average frequency of 0.37 ± 0.12 events/min ($p = 0.0199$; $n = 10$ slices from 4 mice) and duration of 12.39 ± 3.22 s (fig. S4.1A-B). Thus prolonging glutamate activation of AMPARs via inhibition of their desensitization did not reproduce the bursting pattern observed in slices from -/- mice. Conversely, decreasing glutamate activation of AMPARs in -/- slices via their partial inhibition with

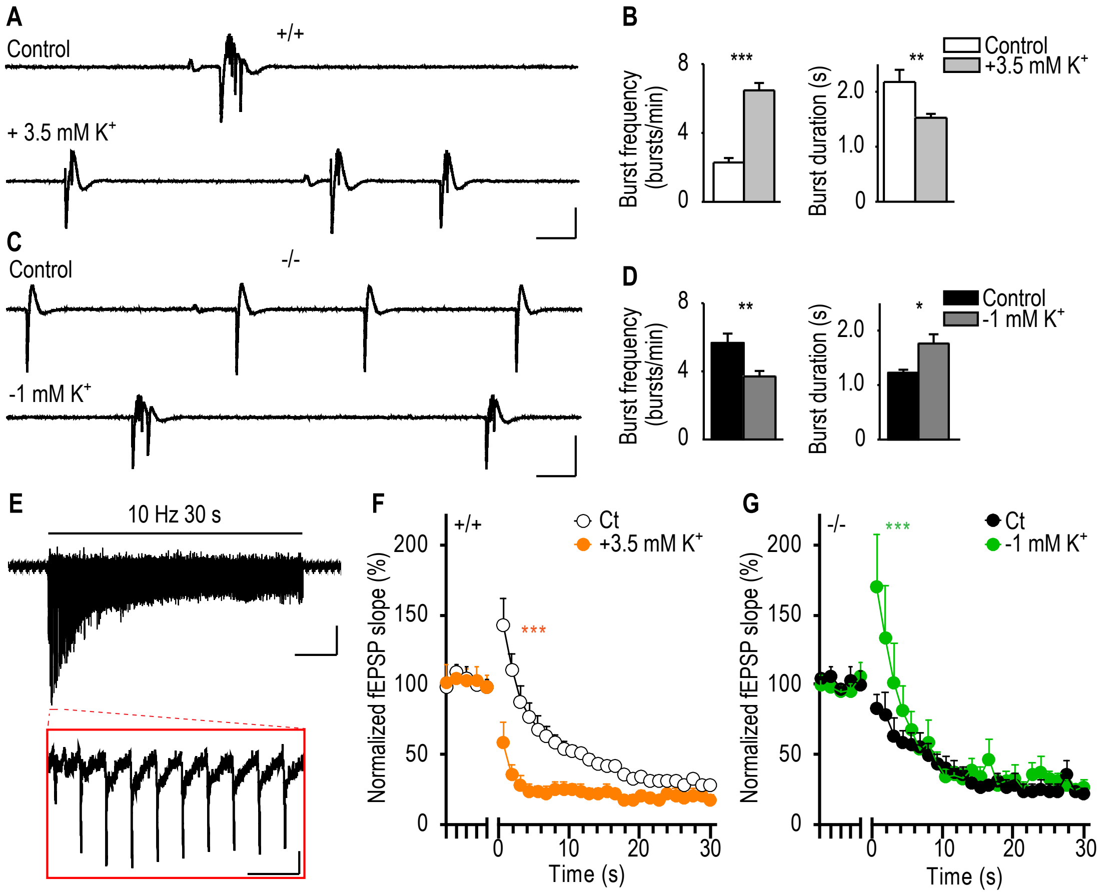

Figure 4.2: **Switch of bursting patterns between wild type and astroglial Cx-deficient mice via alterations of extracellular potassium levels. A.** Representative traces of hippocampal CA1 bursts recorded extracellularly in +/+ mice in control ACSF (top) and ACSF supplemented with 3.5 mM KCl (+ 3.5 mM K^+, bottom). Scale bars: 2 s, 400 μV. **B.** Quantification of burst frequency and duration ($n = 9$ slices from 4 mice; paired t-test). **C.** Representative traces of hippocampal CA1 bursts in -/- mice in control ACSF (top) and in ACSF depleted by 1 mM KCl (-1 mM K^+, bottom). Scale bars: 2 s, 400 μV. **D.** Quantification of burst frequency and duration ($n = 6$ slices from 4 mice; paired t-test). **E.** Top, Representative trace of fEPSPs evoked by repetitive stimulation (10 Hz, 30 s) of CA1 Schaffer collaterals. Scale bars: 5 s, 0.2 mV. Bottom, enlarged view of fEPSPs evoked by the first 10 stimuli. Scale bars: 200 ms, 0.2 mV. **F-G.** Quantification of relative changes in fEPSP slope induced by the 10 Hz stimulation over baseline responses measured before the onset of stimulation, in +/+ mice (**F**) in control ACSF (white) and ACSF supplemented with 3.5 mM KCl (orange; $n = 9$ slices; repeated measures two-way ANOVA), and in -/- mice (**G**) in control ACSF (black) and in ACSF depleted by 1 mM KCl (green; $n = 7$ slices; repeated measures two-way ANOVA). Asterisks indicate statistical significance (*, $p < 0.05$; **, $p < 0.01$; ***, $p < 0.0001$).

low NBQX concentration (0.5 μM) only decreased burst frequency (bursts/min, Control: 5.99 ± 0.29, NBQX: 3.43 ± 0.38, $p < 0.0001$; $n = 11$ slices from 6 mice), without affecting burst duration (Control: 0.94 ± 0.04 s, NBQX, 1.00 ± 0.04 s, $p = 0.2882$; $n = 11$ slices from 6 mice; fig. S4.1C-D). Altogether, these results indicate that the sole alteration in extracellular glutamate levels is unlikely to mediate the impaired bursting pattern observed in -/- mice. Another key feature of astroglial networks is to provide energy metabolites to neurons via GJ-mediated intercellular pathway, thereby sustaining synaptic transmission and neuronal population bursts [163]. To test whether an altered astroglial metabolic supply contributes to the alteration of the bursting pattern observed in Cx-deficient mice, we mimicked a decreased metabolite support by depriving +/+ slices from glucose. We found that this treatment only inhibited bursting activity, with halved burst frequency after 20 min and an almost complete block after 30 min (bursts/min, Control: 2.25 ± 0.31, 20 min: 1.24 ± 0.30, 30 min: 0.27 ± 0.07, $p = 0.05$ and $p < 0.0001$ for 20 and 30 min compared to Control; $n = 11$ slices; fig. S4.2). To ensure that this manipulation did not affect slice viability, we subsequently supplied to +/+ slices exogenous glucose (11 mM, 20 min), which fully restored bursting activity (2.45 ± 0.40 bursts/min, $p = 0.9290$ compared to control; $n = 11$ slices; fig. S4.2). Altogether, these data do not point to a role of impaired astroglial glucose supply in mediating the aberrant bursting pattern observed in -/- slices.

4.2 Modeling results

In this section, we present the results obtained from numerical simulations of the facilitation-depression model with AHP (see methods section 4.4.5 equations 4.1). First, we explain the model calibration and show that it can reproduce the distributions of burst and AHP durations in the +/+ and -/- cases (section 4.2.1). Then we detail the numerical procedure we used to decipher the respective influence of membrane depolarization, AHP, synaptic noise and depression on the modulation of burst and IBI (section 4.2.2). Finally, we show the experimental validation of the model's predictions (section 4.2.3).

4.2.1 Modeling neuronal bursting with astroglial networks

Our experimental data point to a role for astroglial networks in controlling bursting patterns via regulation of $[K^+]_e$. Extracellular K^+ has multiple physiological targets, such as membrane potential and AHP, as well as synaptic noise and depression. Remarkably, we found that all these membrane and synaptic properties are altered in mice with disconnected astrocytes [52] (se also fig. 4.2). This thus raises the question of their relative contribution to the changes in bursting pattern. To identify the properties underlying the astroglial network K^+-mediated burst regulation, we used here a modeling approach to study the burst generation, as there is no experimental tool to selectively target each of these properties. To do so, we developed a mean-field model based on experimental data consisting in neuronal patch-clamp recordings of hippocampal pyramidal cells from wild type and Cx-deficient mice, and which accounts for synaptic facilitation and depression and membrane properties, where we introduced an AHP component (fig. S4.3, see also Methods section 4.4.5). Analysis of these electrophysiological data was performed using voltage time-series segmentation into three phases: bursting, AHP and quiescent phase (QP) (fig. S4.3A, S4.4A and Supplementary Methods section 4.5.2) to generate the associated duration histograms (fig. S4.3B). We found that the distributions of burst durations and interburst intervals (IBI, which includes the AHP and QP) were shifted to lower values in Cx-deficient mice (burst durations: +/+, 3.06 ± 0.09 s, $n = 284$ bursts from 10 cells; -/-, 1.55 ± 0.02 s, $n = 250$ bursts from 6 cells; $p < 0.0001$; IBI: +/+, 18.02 ± 0.61 s, $n = 284$ bursts from 10 cells; -/-,

14.66 ± 0.31 s, $n = 250$ bursts from 6 cells; $p = 0.0033$; fig. S4.3B), and were also more peaked, reflecting reduction in variance (burst duration; $s_{+/+} = 1.52$ s, $s_{-/-} = 0.37$ s; IBI: $s_{+/+} = 10.27$ s, $s_{-/-} = 4.95$ s). The duration of the AHP was also decreased in -/- mice (+/+: 12.52 ± 0.56 s, -/-: 8.03 ± 0.19 s, $p < 0.0001$, fig. S4.3B), while the QP duration was only slightly changed (+/+, 5.50 ± 0.34 s; -/-, 6.63 ± 0.32 s, $p = 0.017$; fig. S4.3B). Further, we found an increase in the synaptic noise amplitude (+/+: $\tilde{\sigma}^2 = 1.97$, -/-: $\tilde{\sigma}^2 = 3.80$, fig. S4.3C) by computing the power spectral densities (PSD) of the QP using a Lorentzian fit on the low-pass filtered PSD at 30 Hz, as well as a depolarization of the membrane potential in Cx-deficient mice (+/+, -61.84 ± 1.43 mV, $n = 12$ cells; -/-, -57.04 ± 0.56 mV, $n = 10$ cells; $p = 0.0075$; fig. S4.3D). To explore the conditions under which numerical simulations can reproduce the experimental data, the model accounts for four phases (fig. 4.3A): 1) burst initiation (blue), that ends when the depression variable y reaches its minimum; 2) recovery from the bursting phase (red, mid-burst), until the membrane hyperpolarization reaches its maximum; 3) recovery of the membrane voltage to the resting potential (pink, burst refractory period); 4) membrane voltage fluctuations around the resting potential until the next burst starts (green, QP). Using this model, we simulated the mean membrane potential, the facilitation and the depression variables and obtained time-series showing spontaneous bursts followed by AHP periods (fig. 4.3B). To determine the values of the unknown parameters in our model, we compared the statistics of the simulated time-series to those of the experimental data. More specifically, we generated numerical simulations of system (4.1) that we segmented using a thresholding method (fig. S4.4B and Supplementary Methods section 4.5.2). We then obtained the statistics of bursting and AHP durations, which we fitted to generate distributions comparable to the ones extracted from segmenting the patch-clamp recordings (fig. S4.3; see also fig. S4.4A for more details). To determine the optimal values of the parameters (Table 4.1), we first calibrated the model for the wild type case (fig. 4.3C, upper). We then modified the AHP duration, noise amplitude and depolarization by changing the medium τ_{mAHP} and slow τ_{sAHP} time constants, the AHP depth T_{AHP}, the noise amplitude σ and the membrane depolarization T, in order to match the experimental distributions of the Cx-deficient case (fig. 4.3C, lower). Using this approach, we obtained a good fit for the AHP and burst durations in +/+ and -/- conditions. Further, since the experimental data indicated the presence of synaptic depression in Cx-deficient mice (fig. 4.2E-G), we investigated the depression level using the calibrated model. For that purpose, in the simulations, we reported the synaptic depression level y_i at the initiation of each detected burst (fig. 4.3D, inset). Interestingly, we found that neurons in conditions of astrocyte disconnection are more depressed compared to the control condition as the distribution of depression values is shifted to the left ($p < 0.0001$; fig. 4.3D), which is in agreement with the experimental data. Altogether, our calibrated mean-field model accounts for the bursts properties observed experimentally in +/+ and -/- conditions.

4.2.2 Modeling predicts that astroglial gap junctions-mediated regulation of AHP sets bursting pattern

We then determined the relative contribution of the changes in either AHP, basal membrane depolarization, synaptic noise or depression to the alteration of bursting pattern found in Cx-deficient mice. To do so, we ran simulations of the model with the parameters obtained in the fit of the +/+ distributions, except for the tested factor (AHP, noise amplitude or depolarization threshold), for which we used the data from the fit of the -/- condition (fig. 4.4, red). These simulations were then compared to the ones computed using all parameters from the fit of +/+ distributions (fig. 4.4, purple).

Using this approach, we first tested the selective effect of decreasing the AHP (medium τ_{mAHP} and slow τ_{sAHP} timescales and AHP depth T_{AHP}) and found a shift in the durations of bursts and IBI towards

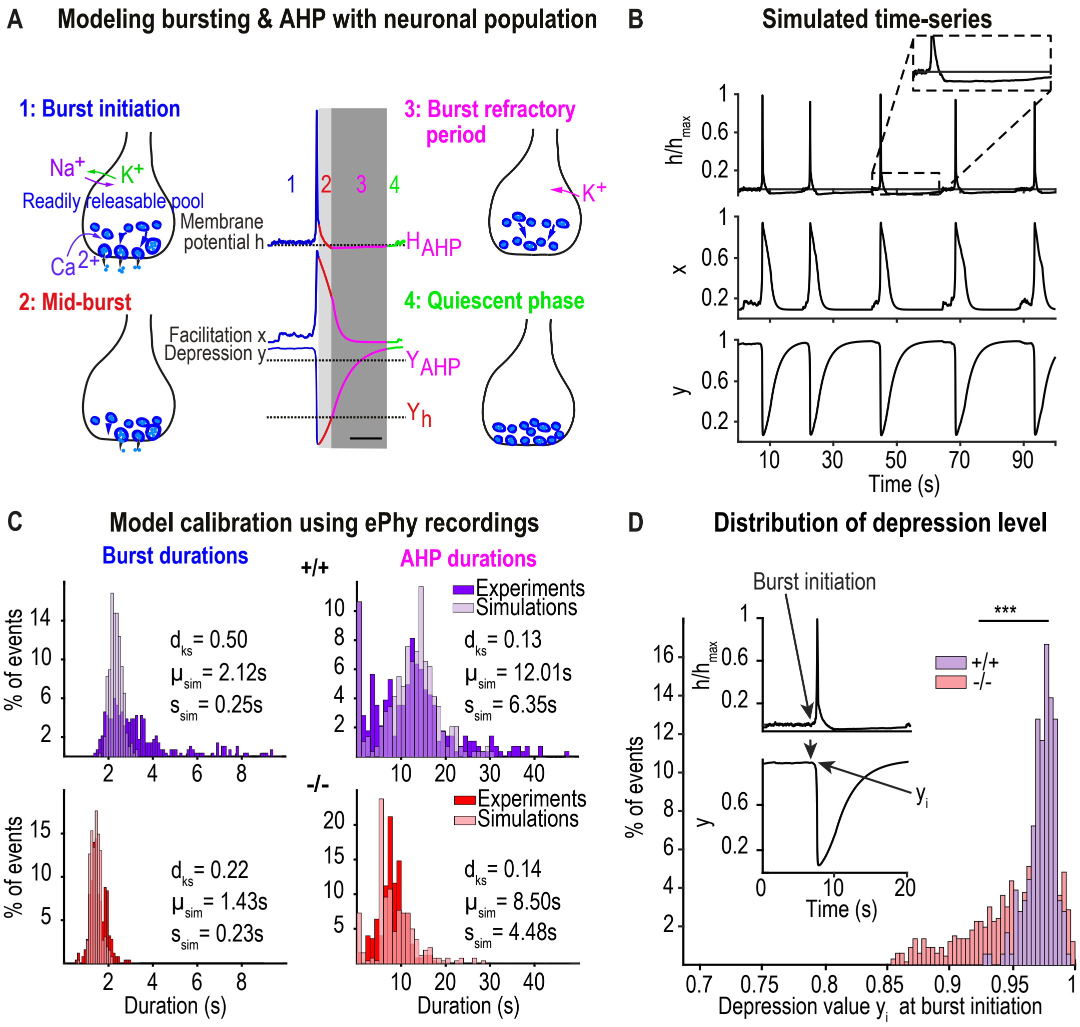

Figure 4.3: **Modeling neuronal network bursting using depression-facilitation and AHP dynamics.** **A.** Schematic decomposition of a burst, followed by AHP, into four steps: 1) burst initiation mediated by facilitation and synaptic depression; 2) recovery of synaptic depression until the maximum amplitude of hyperpolarization; 3) burst refractory period; 4) quiescent phase characterized by the lack of bursting activity. Scale bar: 5 s. **B.** Simulated time-series of normalized voltage (upper), facilitation x (center) and synaptic depression y (lower) over 100 s. **C.** Model calibration based on fitting simultaneously the experimental distributions of burst and AHP durations extracted from electrophysiological recordings segmentation (fig. S4.3A) of pyramidal neurons in +/+ (purple) and -/- (red) mice overlaid with the simulated distributions (light purple and red). **D.** Distribution of depression level y_i at burst initiation (arrow in the inset) obtained from 10^4 s simulations for +/+ (purple) and -/- (red). Asterisks indicate statistical significance in two-sample Kolmogorov-Smirnov test (***, $p < 0.0001$). Parameters are summarized in Table 4.1

reduced values ($p < 0.0001$; fig. 4.4A), mimicking for burst duration the value obtained experimentally in the -/- condition ($p = 0.23$; fig. 4.4A). We then investigated the selective impact of the membrane depolarization ($\Delta V = 5$ mV), and found no shift in the distribution histograms for bursts and IBI durations ($p = 0.78$ and $p = 0.60$, respectively, fig. 4.4B), thus resulting in a different pattern compared to the -/- condition ($p < 0.0001$, fig. 4.4B). We also tested the specific effect of increasing the synaptic noise (σ, noise amplitude), and found that this only caused a shift in burst durations with no effect on IBI durations ($p < 0.0001$ and $p = 0.23$ for bursts and IBI, respectively; fig. 4.4C).
Synaptic depression is an output of the model, and depends on AHP, membrane depolarization and synaptic noise (fig. S4.5A-C). Thus to investigate the effect of depression on burst and IBI durations, we reproduced the depression level at burst initiation that we observed in the +/+ case (fig. S4.5D, purple). To do so, we ran numerical simulations with short AHP (-/- parameters, Table 4.1) combined with a reduced depression recovery timescale (from $\tau_r = 2.9$ s to 1.9 s; fig. S4.5D, yellow). We found that with short AHP and low depression (yellow, fig. S4.5E) the bursts are longer than the ones in the -/- condition (red, short AHP and high depression; $p < 0.0001$), but still much shorter than in the +/+ case (purple, long AHP and low depression) (Supplementary fig. S4.5E). This result indicates that the depression level plays a role in the bursting pattern, but its change in the -/- condition is not sufficient to fully account for the bursting alteration. Furthermore, AHP durations in presence of low depression are even shorter compared to -/- ($p < 0.0001$; fig. S4.5F), since a low depression in a neuronal network triggers more bursts [11, 170]. These results indicate that only decreasing depression in the -/- condition is not sufficient to recover the WT phenotype. Altogether, these results indicate that only the reduction in AHP, but not the increase in membrane depolarization, synaptic noise or depression, results in the bursting pattern of the -/- condition.

4.2.3 Experimental validation of the role of AHP in switching between wild type and knockout bursting patterns

We then verified experimentally whether changes in AHP are responsible for the altered bursting in -/- slices, as predicted by the model. To do so, we first tested in +/+ mice the impact of inhibiting AHP using XE-991, inhibiting voltage-gated KCNQ channels, which mediate the AHP M-current. We found that XE-991 (10 μM) significantly increased burst frequency (Control, 1.78 ± 0.31 bursts/min; XE-991, 2.98 ± 0.420 bursts/min, $p = 0.0399$, $n = 5$ slices from 3 mice) and reduced burst duration (Control, 1.68 ± 0.27 s; XE-991, 1.12 ± 0.13 s; $p = 0.0340$, $n = 5$ slices from 3 mice; fig. 4.5A-B) in +/+ slices, thus mimicking alterations induced by astrocyte network disruption in -/- mice. Conversely, we found that increasing AHP in -/- slices with retigabine (40 μM), which activates KCNQ-type K^+ channels, decreased burst frequency (Control, 4.75 ± 0.33 bursts/min; retigabine, 1.15 ± 0.33 bursts/min, $p < 0.0001$, $n = 7$ slices from 3 mice) and increased burst duration (Control, 1.55 ± 0.1 s; retigabine, 1.98 ± 0.17 s, $p = 0.0481$, $n = 7$ slices from 3 mice; fig. 4.5C-D), thus rescuing +/+ bursting pattern in -/- mice. In all, these results confirm the model prediction that the reduction in AHP fully accounts for the altered bursting pattern observed with astrocyte disconnection. Further, they reveal that astrocyte GJ regulation of $[K^+]_e$ during bursting controls the activation of KCNQ voltage-gated K^+ channels.

4.3 Discussion

Here we combined molecular, physiological and modeling approaches to investigate the specific role of astroglial networks in the regulation of hippocampal bursting patterns. We found that astroglial GJ

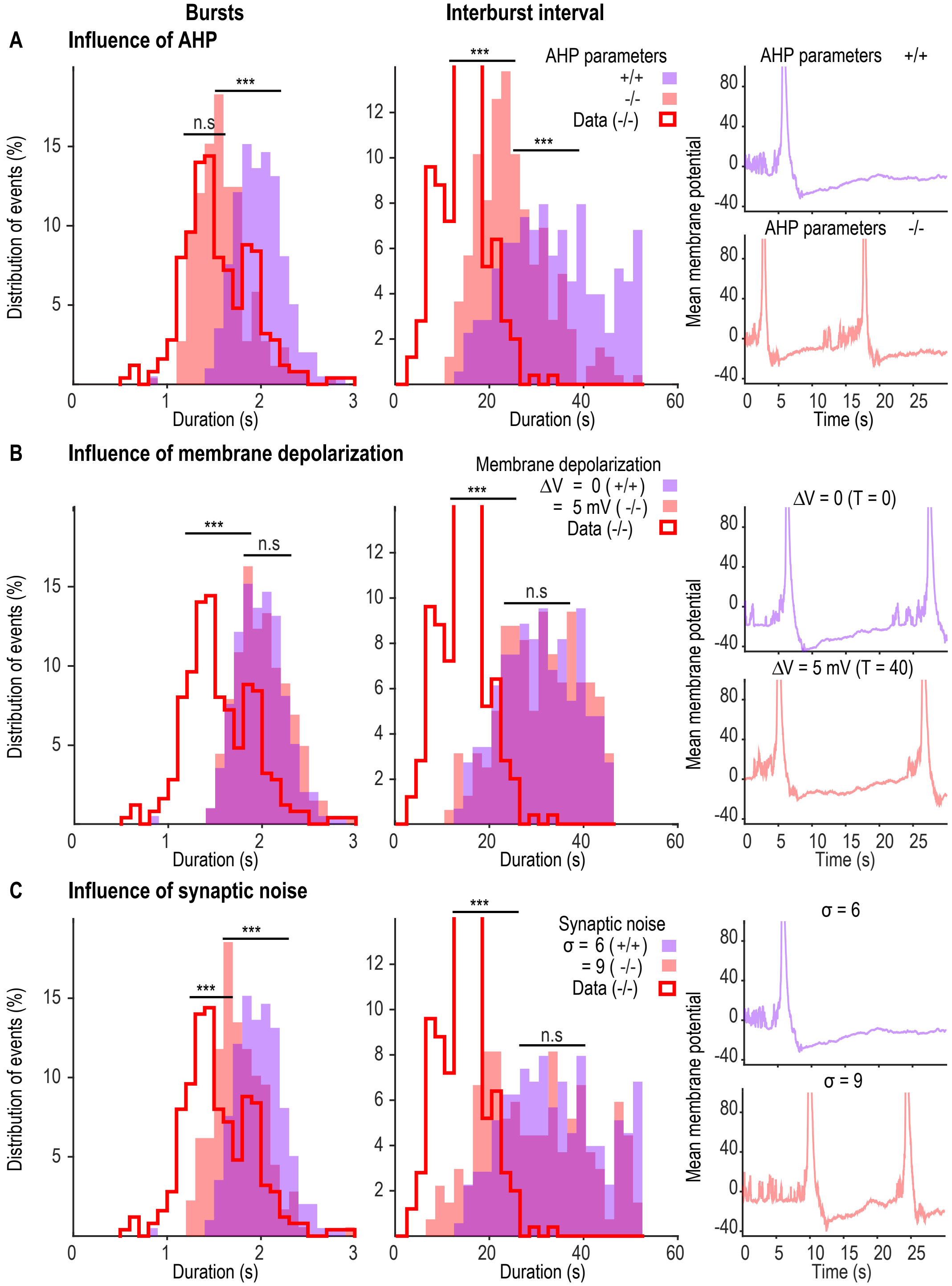

Figure 4.4: **Relative contribution of AHP, membrane potential depolarization and synaptic noise on bursting dynamics. A.** Left: distribution of burst (left) and IBI (right) durations for $\tau_{sAHP} = 10.5$ s, $\tau_{mAHP} = 0.35$ s and $T_{AHP} = -30$ (+/+, light purple), and for $\tau_{sAHP} = 5$ s, $\tau_{mAHP} = 0.15$ s and $T_{AHP} = -23$ (-/-, light red). $\sigma = 6$ and $T = 0$ for both +/+ and -/- (5000 s simulations; $p < 0.0001$ for burst and IBI, two-sample t-test). The red curves represent the burst and IBI duration distributions obtained in the experimental data from -/- mice. Right: simulated mean voltage time series with AHP parameters of +/+ (top) and -/- (bottom) conditions. **B.** Same plots as panel **A** with $\tau_{sAHP} = 10.5$ s, $\tau_{mAHP} = 0.35$ s, $T_{AHP} = -30$, $\sigma = 6$ and $T = 0$ (+/+, light purple) or $T = 40$ (-/-, light red) ($p = 0.88$ for burst and $p = 0.38$ for IBI, two-sample t-test). **C.** Same plots as panel **A** with $\tau_{sAHP} = 10.5$ s, $\tau_{mAHP} = 0.35$ s, $T_{AHP} = -30$, $T = 0$ and $\sigma = 6$ (+/+, light purple) or $\sigma = 9$ (-/-, light red) ($p < 0.0001$ for bursts and $p = 0.04$ for IBI, two-sample t-test). Asterisks indicate statistical significance (*, $p < 0.05$; ***, $p < 0.0001$).

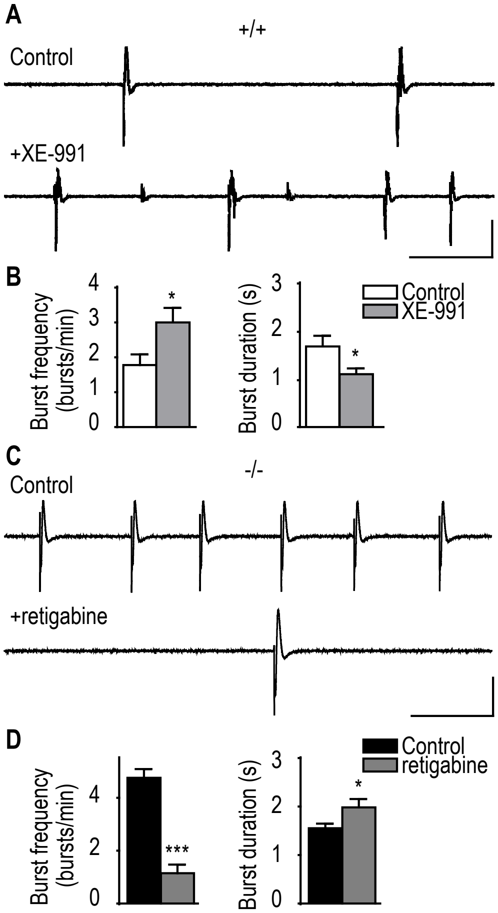

Figure 4.5: **Switch between wild type and astroglial Cx-deficient bursting patterns via alterations in AHP. A.** Representative traces of hippocampal bursts in +/+ mice in control condition (top) and in the presence of XE-991 (10 μM), an inhibitor of KCNQ channels. Scale bars: 10 s, 400 μV. **B.** Quantification of burst frequency and duration ($n = 5$ slices from 3 mice; paired t-test). **C.** Representative traces of hippocampal bursts in -/- mice in control condition (top) and in presence of retigabine (40 μM), an activator of KCNQ channels. Scale bars: 10 s, 200 μV. d) Quantification of burst frequency and duration ($n = 7$ slices from 3 mice; paired t-test). Asterisks indicate statistical significance (*, $p < 0.05$; ***, $p < 0.0001$).

strengthen hippocampal population bursts via extracellular K^+ regulation of KCNQ channels mediating AHP. Astroglial Cx deficiency indeed alters extracellular K^+ regulation, resulting in higher basal K^+ levels and smaller K^+ transients during bursting activity. Furthermore, changing basal $[K^+]_e$ levels allows switching between wild type and knockout bursting patterns. Finally, AHP was reduced in astroglial Cx-deficient mice and restoring it pharmacologically by activating KCNQ-type voltage-gated K^+ channels rescued normal bursting patterns. These data identify for the first time in the central nervous system a neuronal ion channel that is a target of astroglial GJ and underlies changes in network activity.

Extracellular glutamate homeostasis, metabolic support and astroglial networks regulation of bursting pattern In basal conditions, Cx-deficient astrocytes inadequately remove glutamate released from synapses [164]. The decreased glutamate clearance causes an accumulation of glutamate, which prolongs neuronal excitatory activity through enhanced AMPAR and NMDAR activation and glutamate spillover [164]. Here, we investigated whether an impaired glutamate clearance was involved in the altered bursting pattern found in Cx-deficient slices during sustained population activity. Reducing glutamate AMPAR activation in -/- slices by partially inhibiting them with low dose of NBQX only mildly decreased burst frequency, without increasing burst duration. In addition, prolonging AMPAR activation by inhibiting their desensitization with cyclothiazide neither increased burst frequency nor decreased burst duration in +/+ mice. Instead, this treatment induced seizure-like activity, which was never observed spontaneously in -/- mice (fig. S4.1). These results thus indicate that the impaired bursting in astroglial Cx-deficient mice is not due to an altered glutamate clearance leading to glutamate accumulation at the synapse. In the absence of functional astroglial networks, decreased presynaptic release probability was observed during spontaneous bursting activity [52]. Remarkably, a decreased release probability was also reported during active states of physiological slow oscillations [171]. Consistent with these data, it was previously shown that bursts are initiated when action potential-induced synchronous synaptic release of glutamate occurs and are sustained till exhaustion of vesicle pools [11, 170]. Accordingly, we here found in Cx-deficient mice that the readily releasable pool of synaptic vesicles during bursting was decreased, as shown by the impaired responses to prolonged 10 Hz stimulation (fig. 4.2E-G). The enhanced synaptic bombardment causing neuronal depolarization and spontaneous firing between bursts previously reported [52] likely decrease the readily releasable pool of synaptic vesicles during bursting, thus reducing synaptic efficacy, neuronal synchronization and burst strength.

GJ-mediated astroglial networks provide metabolic substrates to neurons. This intercellular pathway for glucose delivery from blood vessels to distal active neurons is activity-dependent and sustain glutamatergic activity [163]. Since burst duration and neuronal synchronization are reduced in -/- mice, an impaired energy supply to neurons could contribute to the altered bursting. However, recordings were performed in 11 mM glucose-containing ACSF, thereby bypassing a possible reduction in glucose supply. In addition, we tested in +/+ mice the effect of extracellular glucose deprivation. We found that it halved burst frequency after 20 min and almost fully blocked activity after 30 min, an effect which does not reproduce the knockout bursting pattern (fig. S4.2). These results thus indicate that the altered bursting pattern in astroglial Cx-deficient mice does not result from impaired energy supply.

Gap junction-mediated astroglial networks modulate extracellular potassium during bursting $[K^+]_e$ is tightly regulated in the brain and kept close to 3 mM in basal conditions, while local changes occur in presence of neuronal activity. Limited K^+ efflux from neurons may actually induce significant changes in $[K^+]_e$, due to the small volume of extracellular space and the low baseline $[K^+]_e$.

Physiological neuronal activity leads to $[K^+]_e$ increases of less than 1 mM, while pathological activity, such as seizures, can build $[K^+]_e$ up to 10-12 mM [172]. Changes in $[K^+]_e$ can strongly impact several neuronal processes, such as the activity of voltage-gated ion channels, synaptic transmission, neurotransmitter transport, the maintenance of membrane potential and excitability. Rapid changes in $[K^+]_e$ are thus tightly controlled by passive diffusion and cellular mechanisms of K^+ clearance [173]. Effective removal of extracellular K^+ is indeed vital for maintaining brain homeostasis and limiting neuronal network hyperexcitability during physiological brain processes. Early on, GJ-connected retinal glial cells have been shown to play a role in controlling $[K^+]_e$ through spatial buffering [174]. Local excess of K^+ is indeed dispersed through interconnected glial cells in which K^+ currents can traverse relatively long distances and transfer K^+ ions from sites of elevated $[K^+]_e$ to those with lower $[K^+]_e$. Astroglial GJ have been assumed to play a similar role. However, studies using knockout mice for astroglial Cxs suggested that astroglial GJ only partially account for K^+ spatial buffering in the hippocampus. GJ-mediated currents indeed represent $\approx 30\%$ of the astrocyte whole-cell currents [53], and although they contribute to extracellular K^+ homeostasis at both physiological (single and paired-pulse stimulation) [53,164] and pathological levels (trains of stimulations) [53], Cx-deficient astrocytes still display large K^+ clearance capacity. Further, the contribution of astrocytic GJs to extracellular K^+ buffering has recently been questioned. Recent work indeed reports that acute pharmacological inhibition of GJs does not alter synaptically-evoked extracellular K^+ transients in hippocampal slices, but only increases large and localized K^+ variations exceeding ≈ 10 mM [175]. However, in this work inhibition of astroglial GJ was performed using carbenoxolone, which is not a specific blocker of astroglial GJ. Carbenoxolone, which blocks GJ from all cell types, is indeed a mineralocorticoid agonist, which has several other off-target effects, as it inhibits numerous ion channels and pumps such as Na/K ATPases [176], chloride channels [177], voltage-gated Ca^{2+} channels [178], pannexin1 channels [179] as well as neurotransmitter receptors such as AMPARs [180] and GABAARs [181]. Carbenoxolone thus alters intrinsic neuronal membrane properties [182] and synaptic transmission [178], besides having some neurotoxic effects [182]. These multiple actions of carbenoxolone, independent of GJ inhibition, thus preclude its use to assess the impact of astroglial GJ on $[K^+]_e$. As up to now, there is no specific pharmacological inhibitor of astroglial GJ communication and the effects of $[K^+]_e$ are pleiotropic, here we combined molecular and modeling approaches to study the impact of astroglial GJ on $[K^+]_e$ and network activity. We hypothesized that the increased bursting activity in mice with disconnected astrocytes results from K^+ accumulation in the extracellular space, as it has been shown that an increment of $[K^+]_e$ from 5 to 10 mM can cause a 5-fold increase in the frequency of hippocampal interictal events [183, 184]. Further, since disconnected astrocytes display increased volume associated with decreased extracellular space [164], K^+ clearance by extracellular diffusion is also likely to be impaired, and thus contribute to extracellular K^+ build-up. Accordingly, we here found that resting $[K^+]_e$ between bursts is increased compared to +/+ mice (fig. 4.1A-B) [52]. This is in agreement with the steady-state depolarization of CA1 pyramidal cells [52] and astrocyte membrane potentials (fig. 4.1D-E) in a regime of bursting activity in mice with disconnected astrocytes. It is noteworthy that this effect is specific for the bursting regime of activity, as it was not observed in basal conditions [164]. In agreement with these observations, we found that K^+ transients during bursts are smaller and shorter in mice with disconnected astrocytes compared to +/+ mice, as well as burst-associated or synaptically-evoked astrocytic membrane depolarizations, which represent a sensitive measure of extracellular K^+ levels during activity (fig. 4.1). Astrocytic disconnection indeed prevents optimal coordination of neuronal populations and impairs synchronization [52]. Astrocytes, as part of the tripartite synapse, modulate neuronal synchronization and network activity, by preventing excessive accumulation of K^+ [172]. Furthermore, alterations in $[K^+]_e$ due to astrocyte disconnection may also alter local electric fields and synaptic current waveforms, thereby impacting on the whole network signal integration [185] and mediating transitions between tonic and phasic neuronal oscillations [186]. Remarkably, we also found that changing resting K^+ levels allows switching between +/+ and -/- bursting patterns, which points to the contribution of impaired extracellular K^+ homeostasis in the altered network activity of mice with disconnected astrocytes. Thus, the control of $[K^+]_e$ by GJ-connected astrocytes not only modulates neuronal excitability at the cellular level, but also regulates the global activity of neuronal networks.

KCNQ channels are a target of astroglial gap junctions Our experimental data point to a contribution of GJ-mediated astroglial networks in setting bursting patterns via $[K^+]_e$ modulation. Deciphering experimentally the physiological target of extracellular K^+ involved in the astroglial control of bursts is however challenging, as K^+ acts on multiple membrane (membrane potential and AHP) and synaptic properties (noise and depression), that are all altered in mice with disconnected astrocytes [52] (see also fig. 4.2). To investigate their relative contribution to the changes in bursting pattern, we thus here developed a novel neuronal network model based on experimental data and underlying burst generation. In this model, which accounts for synaptic facilitation/depression [102, 105, 109], we added the consequences of membrane properties and $[K^+]_e$ dynamics, by introducing an AHP component, without making the distinction between the variety of K^+ channels. To calibrate the model, we found the parameters by minimizing the difference between the distribution of bursts and IBI durations from simulations and the experimental ones. This modeling approach predicted that the astroglial network regulation of extracellular K^+ sets bursting pattern by controlling AHP. This suggested that impaired membrane depolarization and repolarizations of neurons in mice with disconnected astrocytes altered the proper temporally and spatially-restricted functioning of voltage-gated ion channels during bursting. Our electrophysiological recordings confirmed the role of AHP in the astroglial network regulation of bursting pattern, and identified that this GJ-control of AHP results from modulation of KCNQ voltage-gated K^+ channels activation. Interestingly, loss of Cx43 GJ channels in the heart causes a decrease in action potential duration in myocytes by increasing sustained repolarizing and inward rectifier K^+ currents [187]. Furthermore, Cx43 deletion in adult ventricular and fetal atrial myocytes also decreases the amplitude of the Nav1.5-mediated sodium current [188, 189], thereby indicating that Cx43 channels are necessary for proper sodium current function. Remarkably, it has also been shown in pancreatic β-cells that GJ channels formed by Cx36 coordinate KATP channel activity to promote synchronized and oscillatory insulin secretion under stimulatory levels of glucose or global β-cell inhibition at basal level of glucose [190]. Consistent with these data, we here report in the central nervous system that astroglial GJ modulate neuronal excitability via extracellular K^+ regulation of AHP mediated by KCNQ channels. By identifying KCNQ channels as downstream/molecular targets of astroglial GJ, our data uncover the molecular mechanism underlying astroglial network regulation of bursting pattern.

4.4 Methods

Experiments were carried out according to the guidelines of the European Community Council Directives of January 1st 2013 (2010/63/EU) and all efforts were made to minimize the number of used animals and their suffering. Experiments were performed in the hippocampus of wild-type mice (+/+) and Cx30-/-Cx43fl/fl hGFAP-Cre mice (-/-), provided by Pr. K. Willecke (University of Bonn, Germany), with conditional deletion of Cx43 in astrocytes and additional total deletion of Cx30. For all analyses, mice of both genders and littermates were used and ex vivo slice electrophysiology was performed on P16-P25 mice as previously described [163].

4.4.1 In vitro slice electrophysiology

Acute transverse hippocampal slices (400 μm) were prepared as previously described [163] from 16 to 25 days old +/+ and -/- mice. Slices were maintained in a storage chamber containing a standard artificial cerebrospinal fluid (ACSF; 119 mM NaCl, 2.5 mM KCl, 2.5 mM CaCl2, 1.3 mM MgSO4, 1 mM NaH2PO4, 26.2 mM NaHCO3, and 11 mM glucose, saturated with 95% O2 and 5% CO2) for 30 minutes, then stored in a magnesium-free ACSF in the presence of picrotoxin (100 μM) for at least 1 h before recording so that the slices can spontaneously generate population bursts. Slices were transferred in a submerged recording chamber mounted on an Olympus BX51WI microscope equipped for infrared-differential interference (IR-DIC) microscopy and were perfused with 0 Mg^{2+}-picrotoxin ACSF at a rate of 2 ml/min. Extracellular field and whole-cell patch-clamp recordings of astrocytes were performed. Field excitatory bursts were recorded with glass pipettes (2–5 MΩ) filled with ACSF and placed in stratum radiatum. Prolonged repetitive stimulation was performed at 10 Hz for 30 s. Whole-cell recordings were obtained from visually identified CA1 stratum radiatum astrocytes using 5-10 MΩ glass pipettes filled with 105 mM K-gluconate, 30 mM KCl, 10 mM HEPES, 10 mM phosphocreatine, 4 mM ATP-Mg, 0.3 mM GTP-Tris, and 0.3 mM EGTA (pH 7.4, 280 mOsm). The stimulations consisted of 0.1 and 0.5 ms electrical pulses (15 μA) applied through a glass pipette located in the stratum radiatum. CA1 astrocytes resting membrane potential, membrane and series resistance as well as membrane capacitance were monitored throughout the recordings. Measurements of membrane resistance and capacitance were performed on astrocytes clamped at -80 mV. Responses (neuronal fEPSP slope) to repetitive stimulation (10 Hz, 30 s) were binned (bin size 1.2 s) and normalized to mean baseline responses measured at 0.1 Hz before repetitive stimulation. Field potentials and patch-clamp recordings were acquired with Axopatch-1D amplifiers (Molecular Devices, USA), digitized at 10 kHz, filtered at 2 kHz, stored and analyzed on computer using pCLAMP9 and Clampfit10 software (Molecular Devices, USA).

For multi-electrode array (MEA) recordings, hippocampal slices were transferred on planar MEA petri dishes (200-30 ITO electrodes, organized in an 12x12 matrix, with internal reference, 30 μm diameter and 200 μm inter-electrode distance; Multichannel Systems, Germany). They were kept in place by using a small platinum anchor. The slices on MEAs were continuously perfused at a rate of 2 ml/min with a magnesium-free ACSF containing picrotoxin (100 μM), as previously described [52]. Pictures of hippocampal slices on MEAs were used to identify the location of the electrodes through the different hippocampal regions and to select the electrodes of interest. Data were sampled at 10 kHz and network spontaneous activity was recorded at room temperature by a MEA2100-60 system (bandwidth 1-3000 Hz, gain 2x, Multichannel Systems, Germany) through the MC Rack 4.5.1 software (Multichannel Systems, Germany).

4.4.2 Preparation of K^+-sensitive microelectrodes and measurement of extracellular K^+ concentration

Single-barreled K^+-selective microelectrodes were prepared using thin-walled borosilicate capillaries (GC150T-7.5, Harvard Apparatus, USA). The interior walls of the capillaries were silanized with silan vapors (N,N-Dimethyltrimethylsilylamine, Sigma Aldrich, France) for 15 min and dried at 200°C for 100 min. The tip of K^+-selective microelectrodes was filled with Potassium ionophore I (Cocktail A, Sigma Aldrich, France) and the rest of the electrode was backfilled with 200 mM KCl in ACSF background. The reference electrode was made of standard patch-clamp glass (GC150F-10, Harvard Apparatus, USA) and filled with ACSF containing (in mM): 119 NaCl, 2.5 KCl, 1 NaH2PO4, 26.2

NaHCO3, 2.5 CaCl2, 1.3 MgSO4 and 11 glucose. The K^+-selective microelectrodes were calibrated using solutions containing 0.5, 1, 2, 3, 4, 5, 6, 8, 10, 12, 20 and 40 mM KCl. The extracellular K^+ concentration was recorded in +/+ and -/- mouse hippocampal slices in a recording chamber mounted on an Olympus BX51WI microscope equipped for infrared differential interference microscopy and with 40x objective; slices were perfused with standard ACSF or magnesium-free ACSF containing picrotoxin (100 μM) at a rate of 2 ml/min. Both the K^+-selective and reference electrodes were placed in CA1 stratum radiatum, so that their tips were within 10 μm distance from each other. Data were acquired using Axopatch 200B amplifier, sampled at 20 kHz, low pass filtered (2 kHz), digitized (Digidata 1440), and stored and analyzed on computer using pCLAMP 9 and Clampfit 10 software (all from Molecular Devices, USA). The signal from the reference electrode was offline subtracted from the signal of the K^+-selective electrode to obtain a signal proportional to actual K^+ concentration. The relationship between the measured voltage and the actual K^+ concentration was derived from the log-linear fit function.

4.4.3 Burst Analysis

Raw data were analyzed with MC Rack (Multi-Channel System, Reutlingen, Germany). Detection of bursts was performed using the “Spike Sorter” algorithm, which sets a threshold based on multiples of standard deviation of the noise (5-fold) calculated over the first 500 ms of recording free of electrical activity. A 5-fold standard deviation threshold was used to automatically detect each event, which could be modified in real-time by the operator on visual check if needed. Analysis of burst duration was performed using Neuroexplorer (version 4.109, Nex Technologies, USA).

4.4.4 Drugs

NBQX and cyclothiazide were from Tocris (UK); all the other products were obtained from Sigma-Aldrich (France).

4.4.5 Generalized depression-facilitation model accounting for potassium dynamics

The facilitation-depression model [102, 105, 109] is a mean-field type representation of a sufficiently connected neuronal network. It consists of three equations for the mean voltage h, the mean depression y, and the mean synaptic facilitation x. However, this neuronal-network model does not account for long hyperpolarization periods, due to K^+ channel activation [38], leading to a refractory period. To account for these periods, we modified this initial model by introducing two new features:

1. A hyperpolarized equilibrium state, in addition to the resting state. This new state is defined by a negative value for the voltage h, with a new threshold ($T_{AHP} = -30$, see Table 4.1).
2. A medium and slow recovery of the voltage during AHP to the resting potential, modeled by two time constants τ_{mAHP} and τ_{sAHP}.

The general system becomes

$$\begin{aligned}
\tau_0 \dot{h} &= -(h - T_0) + Jxy(h - T_0)^+ + \sqrt{\tau_0}\sigma\dot{\omega} \\
\dot{x} &= \frac{X - x}{\tau_f} + K(1 - x)(h - T_0)^+ \\
\dot{y} &= \frac{1 - y}{\tau_r} - Lxy(h - T_0)^+,
\end{aligned} \tag{4.1}$$

where

$$\tau_0 = \begin{cases} \tau_{mAHP} & \text{if } (\dot{y} > 0) \text{ and } (y < Y_h) \\ \tau_{sAHP} & \text{if } (Y_h \leq y \leq Y_{AHP}) \text{ and } (h < H_{AHP}) \\ \tau & \text{otherwise} \end{cases} \tag{4.2}$$

and

$$T_0 = \begin{cases} T_{AHP} & \text{if } (\dot{y} > 0) \text{ and } (y < Y_h) \\ 0 & \text{otherwise.} \end{cases} \tag{4.3}$$

The threshold linear function $h^+ = max(h, 0)$ represents the firing rate and $\dot{\omega}$ is a Gaussian white noise centered at 0 and of variance 1. The noise amplitude is σ. The parameters J, K, L represent the synaptic connectivity, the facilitation increase rate during bursts and the rate of vesicular release probability (i.e. the depression) which decays during bursts [105, 110]. The time constants τ_f (facilitation) and τ_r (depression recovery) are defined in Table 4.1.

A burst can be initiated by a Dirac impulse at time t_0 ($T_0 = 0$ and $\tau_0 = \tau$) or just by the addition of a Gaussian white noise of low amplitude. It ends when the depression variable y starts to increase (fig. 4.3A, Step 1, blue). After y reaches the threshold value Y_h, then $\tau_0 = \tau_{mAHP}$ and the resting value $T_0 = T_{AHP}$. In practice this phase is defined for $y < Y_h$ and ($\dot{y} > 0$), Step 2 (red). These changes force the voltage to hyperpolarize and lasts until $y > y_{AHP}$ or $h > H_{AHP}$. During the last phase, we change the time constant $\tau_0 = \tau_{sAHP}$ and the resting value $T_0 = 0$ (Step 3, purple). For $y > Y_{AHP}$ and $h \geq H_{AHP}$, we are back to and $\tau_0 = \tau$ and $T_0 = 0$ (fig. 4.3A, Step 4). The role of the noise is to generate spontaneous bursts (fig. 4.3B). The parameters K, L and J are adapted from [105, 109] to fit the patch-clamp recordings data (see Table 4.1). The fine-tuning of all parameters is obtained by best fitting the burst and AHP time distributions, as described in the Results section 4.2.1. The AHP parameters are determined using the order of magnitudes observed in CA1 hippocampal pyramidal neurons [38].

4.4.6 Numerical Simulations

We ran numerical simulations of equations (4.1) in MATLAB using a Runge-Kutta 4 scheme with $\delta_t = 10$ ms (we also used $\delta_t = 1$ ms to confirm the robustness of the numerical scheme).

	Parameters	Values
σ	Noise amplitude	6
τ	Fast time constant for h	0.05s
τ_{mAHP}	Medium time constants for h	0.35s (+/+) / 0.15s (-/-)
τ_{sAHP}	Slow time constants for h	10.5s (+/+) / 5s (-/-)
J	Synaptic connectivity	4.21 (*modified: 3-5 in* [145])
K	Facilitation rate	0.037Hz (*modified: 0.04Hz in* [109])
X	Facilitation resting value	0.08825 (*modified: 0.5-0.1 in* [145])
L	Depression rate	0.028Hz (*modified: 0.037Hz in* [109])
τ_r	Depression time rate	2.9s (*modified: 2-20s in* [109])
τ_f	Facilitation time rate	0.9s (*modified: 1.3s in* [109])
T	Depolarization parameter	0
σ	Noise amplitude	3
T_{AHP}	Undershoot threshold	-30 (+/+) / -23 (-/-)

Table 4.1: Model parameters

4.4.7 Time series segmentation

To detect the bursts and IBI, we developed a segmentation procedure based on various time series: MEA recordings of hippocampal slices from +/+ and -/- mice, patch-clamp recordings of hippocampal pyramidal cells from +/+ and -/- mice and numerical simulations. The method is detailed in the Supplementary Information section 4.5.2, but we briefly summarize here the principles used for the experimental data: we first filtered the individual action potentials using a sliding window of length $T_w = 1s$ to compute the local average $s_m(t) = \frac{1}{T}\int_{t-T/2}^{t+T/2} s(t)dt$. A burst is detected when $s_m(t)$ exceeds a threshold T_{e1} and the end of the burst is determined when $s_m(t)$ reaches its equilibrium value T_{e2}. This segmentation is used to extract the burst and IBI durations in both MEA and patch-clamp recordings (see supplementary information section 4.5.2 for details). The threshold T_{e2} is estimated by fitting a horizontal line to the epochs preceding the burst, and we define the burst detection threshold as $T_{e1} = \frac{max_{[0,T_f]} s_m(t) + T_{e2}}{2}$.

4.4.8 Statistical analysis

Data are expressed as mean ± SEM, unless otherwise stated. Statistical significance for between groups comparisons was determined by paired and unpaired two tailed t-tests. One-way ANOVA with Dunnett post hoc test was performed for 0 glucose experiment. Repeated measures two-way ANOVA was performed for repetitive stimulation (10 Hz, 30 s). Two-sample Kolmogorov-Smirnov test was used for distribution comparison. Differences were considered significant at $p < 0.05$. Statistical analysis was performed using GraphPad Prism 5 software and figures were prepared using Adobe Illustrator CS3. Exact p values are given unless $p < 0.0001$ or $p > 0.9999$.

Data availability

The data that support the findings of this study are available from the corresponding author upon reasonable request.

Acknowledgements

This work was supported by grants from the European Research Council (Consolidator grant #683154), European Union's Horizon 2020 research and innovation program (Marie Sklodowska-Curie Innovative Training Networks, grant #722053, EU-GliaPhD) to N.R., Ligue Francaise contre l'Epilepsie and Aviesan to E.D., Grant Agency of the Czech Republic (GACR: 19-02046S) to L.V. and H.P., French government's scholarship program to H.P., Fondation pour la Recherche Medicale to O.C. and French Research Ministry (ED386, Ecole Doctorale de Sciences Mathématiques Paris centre) and Fondation pour la Recherche Medicale (FRM FDT202012010690) to L.Z.

Author contributions

E.D. performed and analyzed patch-clamp and MEA experiments, interpreted the data and wrote the manuscript. L.Z. analyzed the data, developed the mathematical model and wrote the manuscript. L.V. introduced and validated of the method for measurement of the extracellular K^+ concentration with K^+-sensitive microelectrodes. H.P. performed and analyzed the recordings with K^+-sensitive microelectrodes. O.C. performed and analyzed patch-clamp experiments. D.H. developed the mathematical model and wrote the manuscript. N.R. designed the study, analyzed and interpreted the data and wrote the manuscript.

Ethical approval

All applicable international, national, and/or institutional guidelines for the care and use of animals were followed.

supplementary information for DOSSI E., ZONCA L.*, PIVONKOVA H., VARGOVA L., CHEVER O., HOLCMAN D.$^+$ & ROUACH N.$^+$, "Astroglial gap junctions strengthen hippocampal network activity by sustaining afterhyperpolarization via KCNQ channels" *,$^+$contributed equally*

4.5 Supplementary methods: signal processing

4.5.1 Noise analysis

To quantify the level of the noise in the voltage of the wild type and Cx-deficient datasets we selected the time periods outside bursting and AHP (quiescent phase) in the patch recording experiments. To obtain a significant time period we concatenated these phases for different cells that were rarely spiking. We computed the power spectra $P_{+/+}$ and $P_{-/-}$ for the wild type and Cx-deficient voltage time series (1000s for the wild type and 600s for the Cx-deficient), and filtered them using a low pass filter (Butterworth of order 3) with a cutoff frequency at 100Hz. To extract from these power spectra further information we used model (4.1) around its equilibrium point in the presence of a continuous Brownian noise. Under the condition of neither burst nor AHP, the voltage equation can be approximated by

$$\tau \dot{h} = -(1 - J\langle x\rangle\langle y\rangle)h + \sqrt{\tau}\sigma\dot{\omega}, \tag{S4.4}$$

where we use the approximation that the facilitation and depression are constant equal to $\langle x\rangle$ and $\langle y\rangle$ respectively. Equation (S4.4) is an Ornstein-Uhlenbeck process and the associated power spectrum is a Lorentzian:

$$P(\omega) = \frac{1}{\omega^2 + \dfrac{\gamma^2}{\tau^2}}\frac{\sigma^2}{\tau}, \tag{S4.5}$$

where $\gamma = 1 - J\langle x\rangle\langle y\rangle$. We fitted equation (S4.5) to the filtered power spectra $P_{+/+}$ and $P_{-/-}$ as shown in fig. S4.3C. The amplitude of the noise for the wild type case is $\dfrac{\sigma^2}{\tau} = 1.967$ and for the Cx-deficient case $\dfrac{\sigma^2}{\tau} = 3.801$. We conclude that the amplitude of the noise is doubled in the Cx-deficient compared to the wild type. Interestingly, the cutoff frequency γ is similar $\dfrac{\gamma}{\tau} = 1.84$ in the wild type and $\dfrac{\gamma}{\tau} = 1.90$ in the Cx-deficient.

4.5.2 Time-series segmentation

We describe here the segmentation methods we developed to differentiate bursting and hyperpolarization from resting phases, in the case of patch clamp, MEA recordings and numerical simulations.

- For the patch-clamp data, we first apply a low-pass filter to the input membrane potential $s(t)$ using a sliding time window of length $T_w = 1s$ resulting in the output signal $s_m(t)$ (fig. S4.4A1). We detect burst initiation when the filtered signal reaches a threshold such as $s_m(\tau^i) = T_{e1}$, where $T_{e1} = \dfrac{T_{e2} + max(s_m)}{2}$mV is the average between the maximum value of the filtered signal and the resting membrane potential T_{e2} (fig. S4.4A2, yellow line). We note that although burst initiation

occurred before τ^i when the signal s_m was at resting state, we neglected this delay of the order of few ms. We determine the time of burst termination when the signal decreases to its resting state defined by $s_m(\tau^e) = T_{e2}$ (fig. S4.4A2, red line).
The end of the burst τ^e is the beginning of the AHP phase that lasts until the signal s_m has increased back to its resting value T_{e2} at time τ^a (fig. S4.4A3, magenta trace).
Finally, we define the QP as the time period between the end of AHP until the initiation of the next burst (fig. SS4.4A3, green trace).
In summary, we segmented the n^{th} burst duration $BD = \tau^e_n - \tau^i_n$ (fig. S4.44, blue line), hyperpolarization duration $AHPD = \tau^a_n - \tau^e_n$, (magenta line), and quiescent phases $QP = \tau^i_{n+1} - \tau^a_n$ (green line).

- For MEA recordings, we apply a low-pass filter to the input field recordings using a sliding time window of length $T_w = 0.4s$. We detect bursts and interburst intervals on the absolute value of the filtered signal $|s_{m,MEA}|$.
  Specifically we detect the burst initiation time τ^i when the signal reaches one third of its maximum value such as $|s_{m,MEA}|(\tau^i) = \dfrac{max(|s_{m,MEA}|)}{3}$ and the end time τ^e of the burst when $|s_{m,MEA}|(\tau^e) = \dfrac{max(|s_{m,MEA}|)}{15}$.
  Because it is not possible to vizualize the hyperpolarization in MEA recordings, this segmentation only provides the statistics of burst durations and interburst intervals.

- In numerical simulations, the burst initiation is detected when the mean voltage $h(\tau) = T_1$ (fig. S4.4B1). Here we cannot neglect the time delay between the burst initiation and the time detection τ. We set the time τ^i of burst initiation as the last time previous to τ where the mean voltage h was equal to its resting value: $h(\tau^i) = T$ (fig. S4.4B2). Similarly, we detect burst termination by finding the time τ such as the mean voltage passes a second threshold $T_2 < T$ leading to $h(\tau) = T_2$. To account for a possible delay, we consider as the burst termination the last time τ^e before τ where h is equal to its resting value $h(\tau^e) = T$ (fig. S4.4B2).
  We detect the AHP and QP phases similarly as for the patch recordings.

The distributions obtained from this segmentation are given in fig. S4.3A-B.

4.6 Supplementary figures

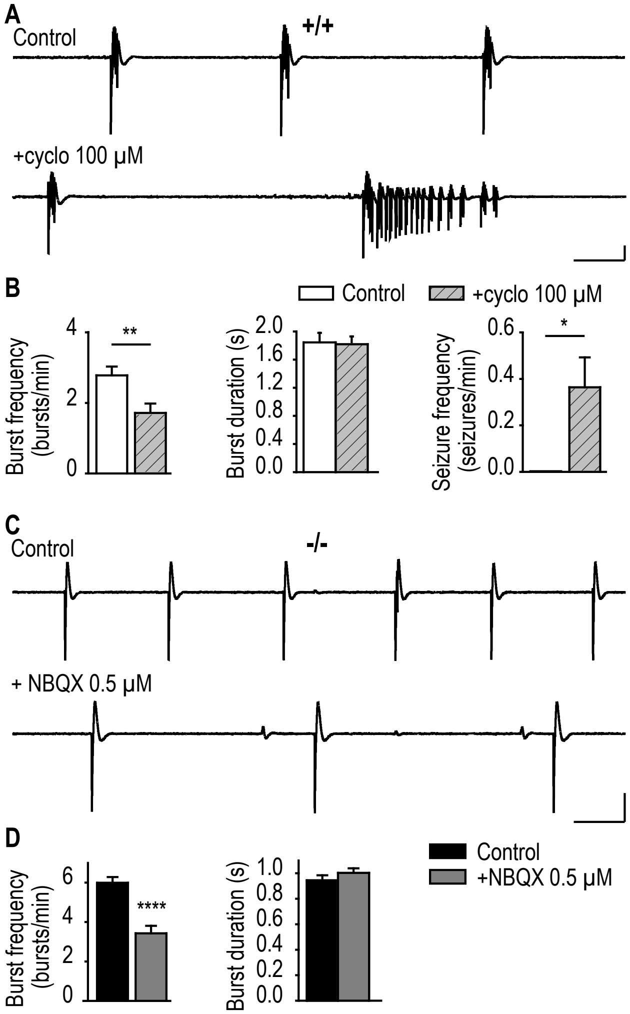

Figure S4.1: **Impaired bursting in astroglial Cx-deficient mice is not due to altered extracellular glutamate homeostasis. A.** Representative traces of hippocampal bursts in +/+ mice in control condition (top) and in presence of cyclothiazide (100 μM; bottom). Scale bars: 5 s, 200 μV. **B.** Quantification of burst frequency and duration and of seizure frequency ($n = 10$ slices from 4 mice; paired t-test). **C.** Representative traces of hippocampal bursts in −/− mice in control (top) and in presence of NBQX (0.5 μM; bottom). Scale bars: 5 s, 200 μV. **D.** Quantification of burst frequency and duration ($n = 11$ slices from 6 mice; paired t-test). Asterisks indicate statistical significance (*, $p < 0.05$; **, $p < 0.01$; ***, $p < 0.0001$).

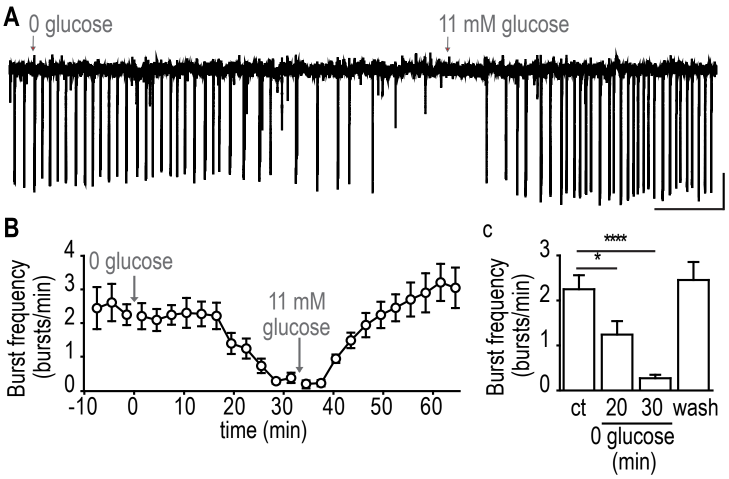

Figure S4.2: **Impaired bursting in astroglial Cx-deficient mice is not due to altered metabolic support.** **A.** Representative field potentials recording of hippocampal bursting activity in +/+ mice during application of glucose-free ACSF (0 glucose) and washout in normal ACSF (11 mM glucose). Scale bars: 5 min, 0.2 mV. **B.** Temporal profile of burst frequency changes during perfusion of 0 glucose-ACSF (30 min) and washout in 11 mM glucose-containing ACSF (30 min) ($n = 11$ slices). **C.** Quantification of burst frequency in control, after 20 and 30 min in 0 glucose-ACSF and after 20 min of washout in normal ACSF ($n = 11$ slices; one-way ANOVA). Asterisks indicate statistical significance (*, $p < 0.05$; ***, $p < 0.0001$).

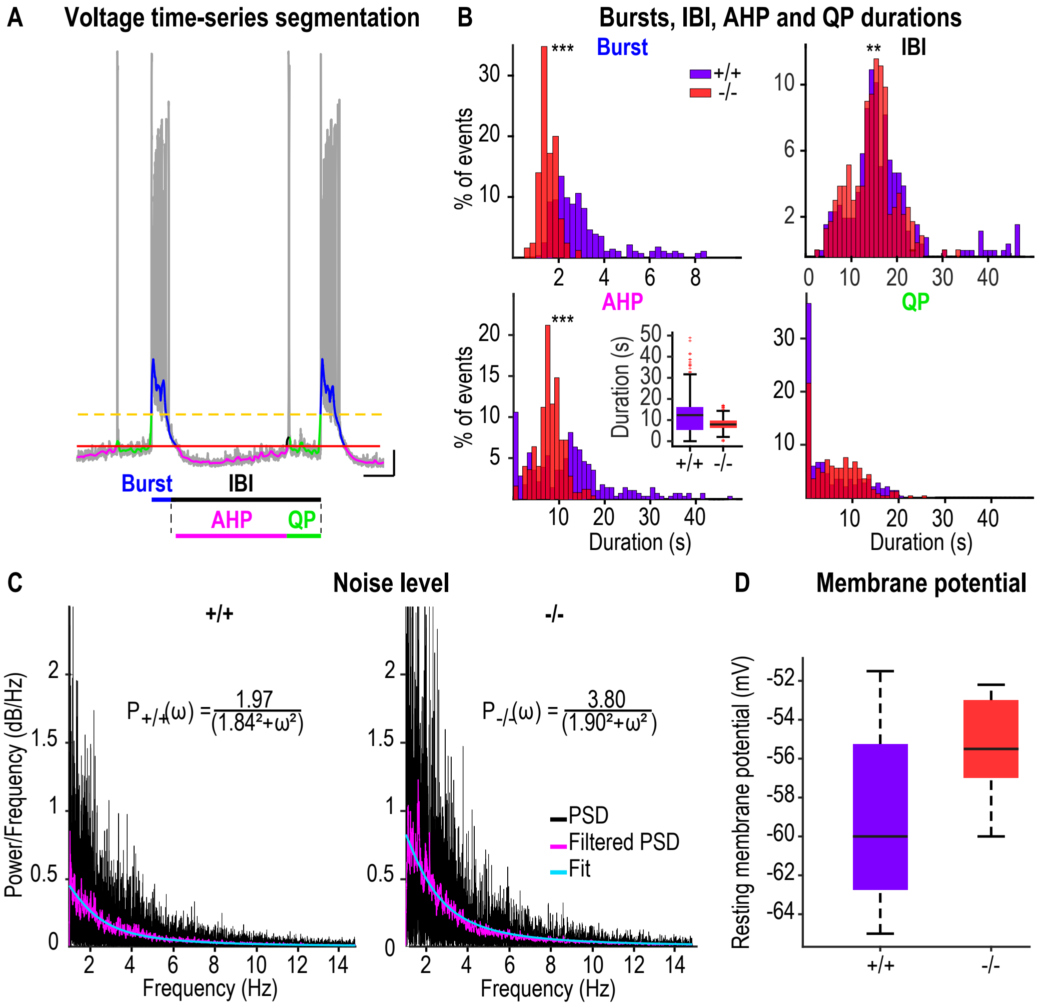

Figure S4.3: **Statistics of burst dynamics from electrophysiological time-series in neurons from +/+ and Cx-deficient mice.** **A.** Segmentation of patch-clamp recordings in hippocampal neurons in 3 phases: burst (blue), AHP (pink), and QP (green) using two thresholds T_1 and T_2 (red and yellow dotted lines). AHP and QP form IBI (black). Scale bar: 10 s, 10 mV. **B.** Distributions of bursts (upper left), IBI (upper right), AHP (lower left, inset boxplots) and QP (lower right) durations from neurons in +/+ (purple) and −/− (red) mice ($n = 10$ neurons for +/+ and $n = 6$ neurons for −/−; two sample t-test). **C.** Power spectrum (black) of the QPs and power spectrum P_F for the filtered signal at $f_c = 30$ Hz (low-pass filter, pink trace). The fit of a Lorentzian $P(\omega) = \dfrac{1}{\omega^2 + \dfrac{\gamma^2}{\tau^2}}$ to P_F for the +/+ (left) and −/− (right) is shown in blue. The extracted noise amplitude $\tilde{\sigma}^2$ is 1.97 and 3.80 for +/+ and −/−, respectively. **D.** Resting membrane potentials in neurons from +/+ ($n = 12$ cells, purple) and −/− mice ($n = 10$ cells, red; $p = 0.0075$, unpaired t-test). Asterisks indicate statistical significance (**, $p < 0.01$; ***, $p < 0.0001$).

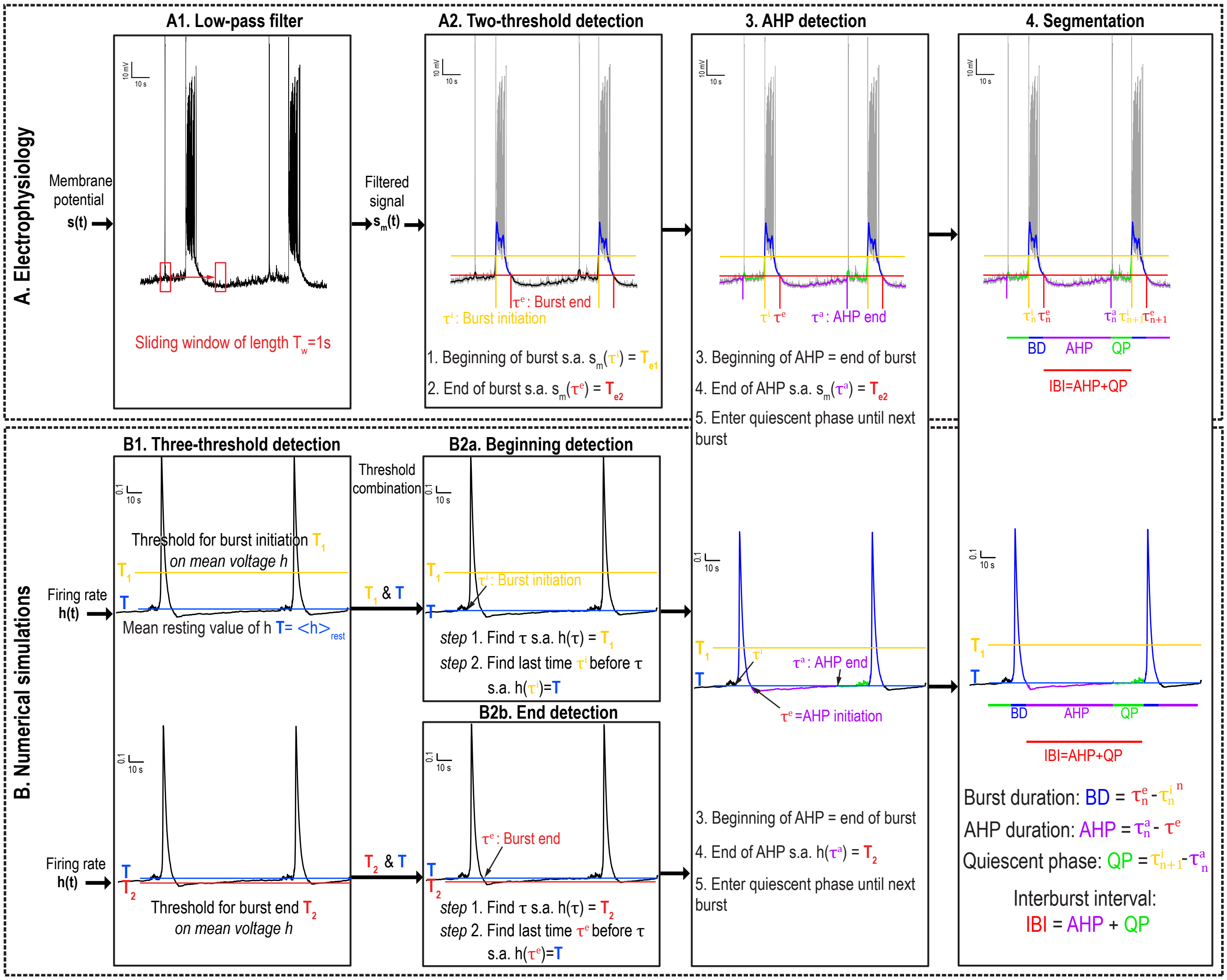

Figure S4.4: **Burst detection algorithms. Upper: Burst detection for patch clamp electrophysiological traces: A1.** The membrane potential signal is low-pass filtered using a sliding window of length $T_w = 1s$. **A2.** Threshold detection is applied to the filtered signal s_m. **3.** AHP begins at the end of the burst and lasts until s_m is back above resting membrane potential where the QP begins until the next burst. **4.** Extraction of burst durations, (BD,blue), AHP duration (magenta) and quiescent phases (QP, green). IBI are composed of AHP and QP. **Lower: Detection algorithm for simulated traces. B1-B2.** Burst initiation is detected combining two thresholds, T_1 (yellow) and T (blue) on the mean voltage h, and burst end is detected with the thresholds T_2 (red) and T (blue) on h. **3-4.** AHP and QP are detected similarly as in the experimental traces, yielding a three period segmentation.

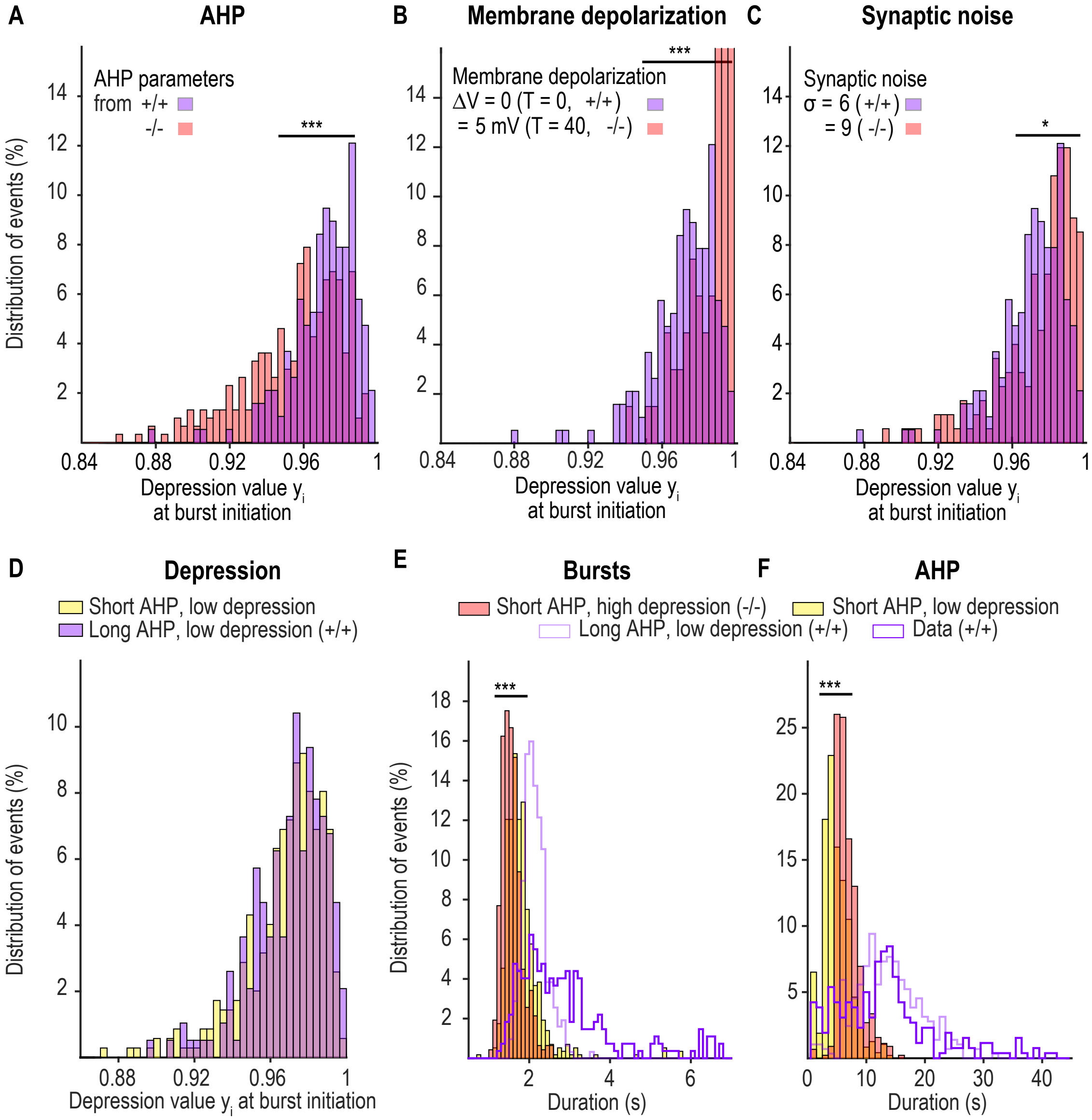

Figure S4.5: **Synaptic depression: dependence on AHP, depolarization and noise; and influence on burst dynamics. A.** Distribution of depression level at burst initiation from 5000 s simulations with $\tau_{sAHP} = 10.5$ s, $\tau_{mAHP} = 0.35$ s, $T_{AHP} = -30$ (+/+, light purple), and for $\tau_{sAHP} = 7.5$ s, $\tau_{mAHP} = 0.15$ s, $T_{AHP} = -23$ ($-/-$, light red). $\sigma = 6$ and $T = 0$ for both conditions ($p < 0.001$, two-sample Kolmogorov-Smirnov test). **B.** Distribution of depression level at burst initiation from 5000 s simulations with $\tau_{sAHP} = 10.5$ s, $\tau_{sAHP} = 0.35$ s, $T_{AHP} = -30$, $\sigma = 6$ and $T = 0$ (+/+, light purple) or $T = 40$ ($-/-$, light red) ($p < 0.001$, two-sample Kolmogorov-Smirnov test). **C.** Distribution of depression level at burst initiation from 5000 s simulations with $\tau_{sAHP} = 10.5$ s, $\tau_{mAHP} = 0.35$ s, $T_{AHP} = -30$, $T = 0$ and $\sigma = 6$ (+/+, light purple) or $\sigma = 9$ ($-/-$, light red) ($p = 0.0013$, two-sample Kolmogorov-Smirnov test). **D.** Distribution of depression level at burst initiation from 5000 s simulations with $\tau_{sAHP} = 10.5$ s, $\tau_{mAHP} = 0.35$ s, $T_{AHP} = -30$, $\sigma = 6$, $T = 0$ and with $\tau_r = 2.9$ s (light purple) and for $\tau_{sAHP} = 5$ s, $\tau_{mAHP} = 0.15$ s, $T_{AHP} = -23$, $\sigma = 6$, $T = 0$ and with $\tau_r = 1.9$ s (light yellow; $p = 0.614$, two-sample Kolmogorov-Smirnov test). **E.** Distribution of burst durations for $\tau_{sAHP} = 5$ s, $\tau_{mAHP} = 0.15$ s, $T_{AHP} = -23$, $\sigma = 6$ and $T = 0$ (light red, $-/-$) and reduced depression (light yellow; $p < 0.0001$, two-sample Kolmogorov-Smirnov test). The distribution of burst durations for +/+ parameters is indicated by the light purple line. **F.** Distribution of AHP, with the same parameters as in (**E**). The purple curves represent the distribution of burst **E** and AHP **F** durations obtained from experimental data in +/+ mice. Asterisks indicate statistical significance (***, $p < 0.0001$; **, $p < 0.001$).

Chapter 5

Up and Down states occurring in neuronal networks regulate the emergence and fragmentation of the α-band

under review in PLoS Computational Biology: ZONCA L. & HOLCMAN D., "Up and Down states occurring in neuronal networks regulate the emergence and fragmentation of the alpha-band"

Abstract

Rhythmic neuronal network activity underlies brain oscillation. At the neuronal level, these rhythms are driven by the fraction of Up and Down states in cortical or hippocampus regions. To investigate how connected neuronal networks contribute to the emergence of the α-band in parallel with the regulation of Up and Down states, we introduce a computational model based on synaptic short-term depression-facilitation with afterhyperpolarization (AHP). We found that the α-band is generated by the network behavior near the attractor of the Up-state. To better characterize the emergence and stability of thalamocortical oscillations containing α and δ rhythms during anesthesia, we model the stochastic interactions of two excitatory with one inhibitory networks, showing that this minimal network topology leads to a persistent α-band in the neuronal voltage characterized by dominant Up over Down states. Finally, we show here that the emergence of the α-band appears when external inputs are stopped, while the fragmentation occurs at small synaptic noise or with increasing inhibition inputs. Interaction between excitatory neuronal networks with and without AHP seems to be a general principle underlying network oscillations that could apply to generate other rhythms.

Introduction

Electroencephalogram (EEG) is used to monitor the brain activity in various conditions such as sleep [34, 191], coma [192] or meditation [193] and to reveal and quantify the presence of multiple frequency oscillations [142] over time [143]. This analysis can be used to asses the level of consciousness or depth of unconsciousness of the brain. For example, during general anesthesia under propofol, a dominant oscillation is the α-band (8-12Hz) [30, 31]. However, the precise mechanisms underlying the emergence or disappearance of this α-band remain unknown. Interestingly, when the level of sedation becomes too high, the EEG shows that the α-band can get fragmented and even disappear replaced by a different transient motif called burst-suppression, which consists in alternation of periods of high frequency activity followed by iso-electric suppression periods where the EEG is almost flat [31]. In general, large doses of hypnotic in prolonged anesthesia in rodents alters brain synaptic architecture [194], confirming the need to avoid over sedation. Burst-suppression is a motif associated with a too deep anesthesia and its presence could indicate possible post anesthetic complications, although it has been attributed to ATP depletion [195]. Recently, it was shown that the loss of the α-band announces the appearance of burst-suppressions [144], however, this causality between α-band suppression and burst-suppressions remains unexplained.

The α-band revealed by the EEG signal reflects the local neuronal circuitry activity associated with the Up and Down states [196–198], which corresponds to a depolarized and hyperpolarized membrane voltage of a neuron respectively [28]. The alternation between Up and Down states generates slow wave oscillations present in NREM sleep, as reported in slices electrophysiology [199] as well as using modeling approaches [200, 201]. Similarly, the emergence of the α-band during anesthesia could result from network interactions, as proposed by models based on the Hodgkin-Huxley formalism [71–73].

Since Up and Down states reflect the neuronal activity at the population level [27, 28], we propose here to investigate the emergence and fragmentation of the α-band using a modeling approach based on synaptic short-term plasticity [102, 105], which is often used to obtain estimations for burst or interburst durations [109, 147, 202]. These models based on facilitation and depression have recently been used to evaluate the working memory capacity to remember a sequence of words [203].

Here, we use a mean-field neuronal model that accounts for both synaptic short-term dynamics and afterhyperpolarization (AHP) [158] resulting in a refractory period during which neurons stop firing after a burst. As a result, at a population level, AHP can modify the type of oscillations [70], from waxing and waning spindle oscillations to slow waves.

We first study a single, two and then three interacting neuronal networks, a minimal configuration revealing the coexistence of α-oscillations and switching between Up and Down states. As we shall see, only the neuronal population with AHP can trigger spontaneous switching between Up and Down states while the other one, without AHP is at the origin of the α-oscillations in the Up state. We also investigate the role of synaptic noise and model the effect of propofol as an excitatory current for inhibitory neurons.

5.1 Results

5.1.1 EEG reveals the dynamics of the α-band during general anesthesia

General anesthesia can be monitored using EEG (fig. 5.1A) that often reveals a stable α-band which persists in time (fig. 5.1B). The origin of the α-band is not fully understood but it was found to result from the dynamics of neuronal populations involving the reciprocal connexions between the thalamus and the cortex. During anesthesia involving the propofol agent, the inhibitory neurons are activated resulting in the emergence and stability of the α-band. Increase of the anesthetic agent can lead to a deeper anesthesia characterized by a transient disapearance of the α-band (fig. 5.1C) so that the spectrum is carried by the δ-band. This disappearance can be quantified by two values, defining a fragmentation level which would account for the persistence in the α-power compared to a threshold value over a specific period of time in duration (P_α) and number of disruptions in the power band (D_α) (see Methods section 5.2.1). The exact mechanisms leading to the stability and the peak of the α-band frequency remains unclear. In the remaining part of this manuscript we propose to develop mean-field models based on synaptic properties to address this question.

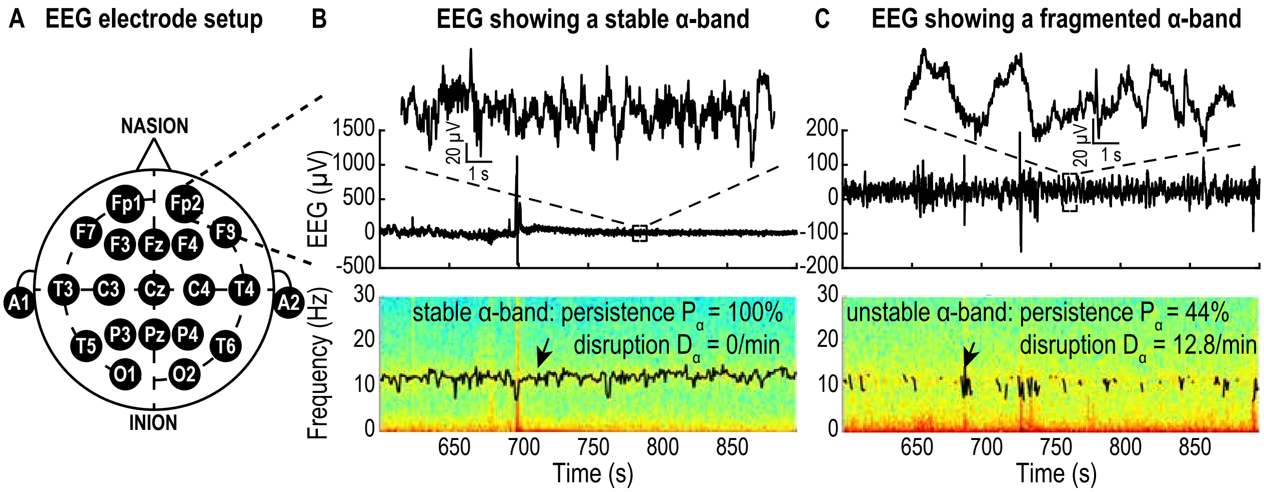

Figure 5.1: **EEG recorded during general anesthesia A.** Schematic of EEG electrode setup on a patient's head. **B.** Upper: Time recordings showing the EEG (inset: 5 s). The EEG signal is composed of multiple bands as shown in the spectrogram (lower panel) composed of two major bands: the δ-band (0-4Hz) and the α-band (8-12Hz) tracked by its maximum (black curve) revealing the persistence of the α-band during anesthesia. **C.** Same as A for a case of fragmented α-band. Data from the database VitalDB [204].

5.1.2 A single neuronal population can exhibit α-oscillations or slow waves through switching between Up and Down states

The synaptic depression-facilitation model generates locked α-oscillations

To analyze the change between a persistent α-band and a δ-band we develop a mean-field model of neuronal networks based on short term synaptic plasticity (fig. 5.2A). The first model consists of one well connected population of excitatory neurons described by three variables: the mean voltage h, the synaptic facilitation x and the depression y, resulting in a stochastic dynamical system (see Methods, section 5.2.2, equations 4) showing bi-stability: one attractor corresponds to the Down state (hyperpolarized, low frequency oscillations) and the second one to the Up state (depolarized, high frequency oscillations). One fundamental parameter is the level of connectivity J that we shall vary (fig. 5.2B). We found that such a system can generate a dominant oscillatory band where the peak value is an increasing function of the connectivity J (fig. 5.2C). In the present scenario the network dynamics is locked into an Up state and the dominant oscillations are generated by the imaginary part of the eigenvalues at the Up state attractor. This result shows that the persistent oscillations are the consequence of the noise and of the synaptic properties as well as the biophysical parameters (Table 1, SI), indeed, changing the synaptic properties can lead to the fragmentation and disappearance of the band where most of the energy is now located in the δ-band as quantified by the spectral edge frequency at 95% (SEF95, fig. S1). In addition, varying the noise amplitude allows to either fragment the band (fig. 5.2D, $\sigma = 7$) or to increase the power and the persistence of the band (fig. 5.2D, $\sigma = 15$) but it does not affect the value of the peak of the dominant oscillation (fig. 5.2E). Indeed, similarly as for the EEG data presented in section 5.1.1 we quantified the fragmentation level (Methods section

5.2.1) for different noise amplitudes and found it varies from $(P_\alpha, D_\alpha) = (52\%, 34/min)$ for $\sigma = 5$ to $(P_\alpha, D_\alpha) = (86\%, 16/min)$ for $\sigma = 7$ and to $(P_\alpha, D_\alpha) = (100\%, 0/min)$ for $\sigma = 15$ which is coherent with the fragmentation levels observed in the human EEG data. This fragmentation of the α-band results only from the changes in the noise amplitude and can occur even though the population is locked into the Up state, suggesting that the loss the α-band is independent from the switch between Up and Down states. However, the present model does not allow a dynamic switch between Up and Down states, thus we decided to add AHP to our model to explore a larger range of dynamics (see Methods).

The synaptic depression-facilitation model with AHP generates Up and Down states but no α-oscillations

The synaptic depression-facilitation model with AHP is constructed by adding the AHP components to the mean-field equations (5.2) presented above (see Methods). The dynamics exhibit a bi-stability characterized by Up and Down states (fig. 5.3A-B). Contrary to the system without AHP, in the Up state the dynamics do not exhibit a dominant oscillation band other than δ (fig. S5.2) due to the non imaginary eigenvalues at the Up state attractor. Interestingly, by increasing the network connectivity J we can modulate the fraction of time spent in the Up state: for J small ($J = 5.6$) the dynamics spends 37% of the time in the Up state, while for $J = 7.6$ it represents 79% (fig. 5.3C-D and see also fig. S5.2A-B). Finally, increasing the noise leads to more frequent switches between Up and Down states (fig. S5.2C-D). To conclude, this model recapitulates the switch between Up and Down states but does not generate a stable α-band.

Adding a stimulation during the Up states cannot change the oscillation rhythm between Up and Down states in the stable AHP model

Adding an additive input current on the mean voltage h during the Up states simulates a situation where the observed network projects an excitatory input on a second network that would send a positive feedback when activated. The second network would only get activated by such stimuli when the first (observed) network is in the Up state. In previous studies with a 2D model (modeling only the firing rate and depression) we showed that such stimulus stabilizes the Up state [105]. Here we ran simulations for the cases with and without AHP where we added a constant input current only when the system was in the Up state (fig. S5.3). In the case without AHP, the dynamics stays locked in the Up state (fig. S5.3A), even in the case of a negative feedback current (upper) and the amplitude of the current I_{Up} does not affect the peak value of the oscillatory band (fig. S3B). In the case with AHP the dynamics is not changed either: the dynamics switches between Up and Down states (fig. S5.3C) and the proportion of time spent in either Up or Down state is not affected by the value of the current I_{Up} (fig. S5.3D).

5.1.3 Modelling the effect of inhibition on the excitatory short term synaptic model with and without AHP

To explore the range of oscillatory behaviors, we connected an inhibitory neuronal network to the excitatory one that could have or not the AHP (see Methods, section 5.2.3, equations 5.4). We also added a constant stimulating current I_i on the inhibitory population (fig. 5.4A).

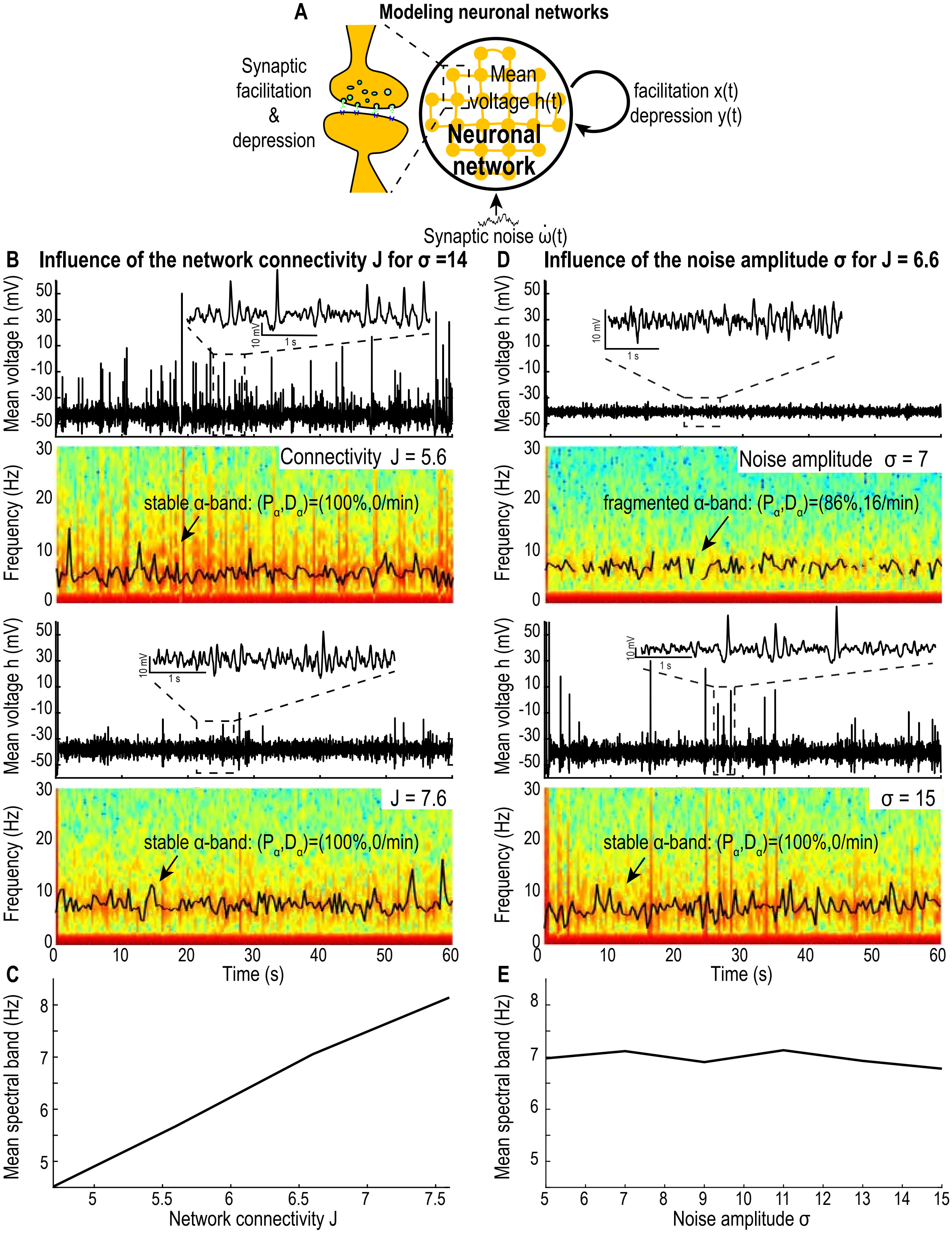

Figure 5.2: **Effect of network connectivity J and noise amplitude σ on model** (5.2) **without AHP. A.** Schematic of the facilitation-depression model (5.2). **B.** Time-series and spectrograms of h (60s simulations) with peak value of the dominant oscillatory band (black curve) for $J = 5.6$ (upper) and 7.6 (lower). **C.** Mean value of the dominant oscillatory frequency for $J \in [4.8, 7.8]$. **D.** Time-series and spectrograms of h (60s simulations) peak value of the dominant oscillatory band (black curve) for $\sigma = 7$ (upper) and 15 (lower). **E.** Mean value of the dominant oscillatory frequency for $\sigma \in [5, 15]$. Synaptic plasticity timescales: $\tau = 0.01$s, $\tau_r = 0.2$s and $\tau_f = 0.12s$.

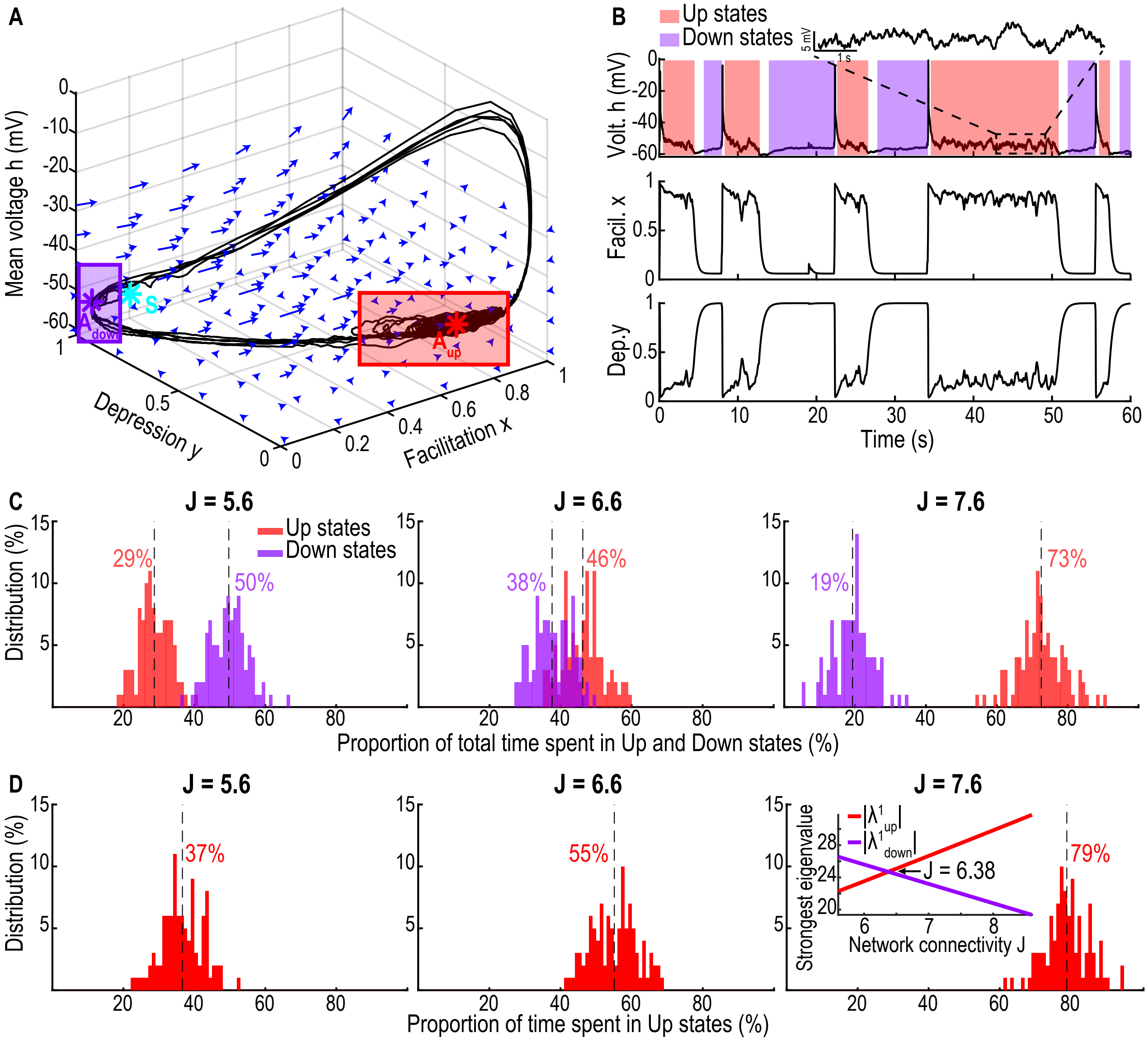

Figure 5.3: **Single population exhibiting Up and Down states A.** 3D phase space of system (5.2) with the two attractors A_{Down} (purple) and A_{Up} (red) and the saddle-point S (cyan). The purple (resp. red) rectangle shows the subspace of Down (resp. Up) states. **B.** Time series of the mean voltage h (upper) showing Down (purple, resp. Up, red) states and an inset during the Up state (magnification: ×4), facilitation x (center) and depression y (lower, synaptic plasticity timescales: $\tau = 0.025$s, $\tau_r = 0.5$s and $\tau_f = 0.3$s). **C.** Distributions of the fraction of time spent in Down t_{Down} (purple, resp. Up t_{Up}, red) states for network connectivity $J = 5.6$ (left), 6.6 (center) and 7.6 (right) for 1000 minutes simulations. Vertical dotted lines indicate mean values. **D.** Distribution of the fraction of the total time spent in Up state $\dfrac{t_{Up}}{t_{Up} + t_{Down}}$ for the three values of J. Inset: strongest attractive eigenvalue of the Down state $|\lambda^1_{A_{Down}}|$ (purple, resp. Up state, $|\lambda^1_{A_{Up}}|$, red) with respect to the network connectivity J.

In the case where the excitatory network has AHP the dynamics exhibit switching between Up and Down states (fig. 5.4B). Interestingly, by increasing the current I_i we modulate the fraction of time spent in Up state by the excitatory system (fig. 5.4C-D). However, independently of the value of I_i the Up state does not show any persistent α-oscillations (fig. 5.4E). Finally, modulating the current I_i is not sufficient in a dynamics that exhibits the α-band to switch between band frequency dominance (fig. 5.4F).

5.1.4 Two excitatory connected to an inhibitory networks leads to the coexistence of Up and Down states and α-oscillations

To define the conditions for which the Up and Down states can coexist with an α-band, we explore a model that contains two coupled excitatory components with one inhibitory component (see Methods, section 5.2.4, equations 5.5). This investigation is driven by the α-oscillation that can be generated by the thalamo-cortical loop (fig. 5.5A). The thalamo-cortical excitatory subsystem is decomposed into two components α and U/D connected by reciprocal connections and receives an inhibitory input from the inhibitory subsystem NR. The NR component sends reciprocal connections to the U/D component and can also be activated by an external stimulation I_i. We focus on the sum of the three voltage components because it is the one recorded by EEG. During general anesthesia with propofol, increasing the dose leads to a fragmentation and transient disappearance of the α-band. To assess under which conditions this phenomenon could be generated, we followed the same protocol by first investigating the effect of switching off all external stimuli, followed by increasing an injected current to the inhibitory neuronal component to simulate an increase of the propofol concentration.

Suppressing external stimuli into two excitatory coupled to an inhibitory network leads to the spontaneous emergence of α-oscillations

External stimuli are switch off during the loss of consciousness at the start of a general anesthesia. We modeled here this transition by first adding stimuli modeled as excitatory input current $I_{ext} = 300 + 20\xi$ (resp. $I_{ext,2} = 100 + 20\xi$) where ξ is a Gaussian white noise of mean 0 and variance 1. We applied I_{ext} and $I_{ext,2}$ to the three components of the model (fig. 5.5A, blue and green) for the first 40 seconds of the simulation. To model the beginning of anesthesia, we set the external stimuli I_{ext} and $I_{ext,2}$ to zero for the rest of the simulation (fig. 5.5B). We found that during the wakefulness period, during which $I_{ext} > 0$ from 0 to 40s, there is no dominant oscillatory band in the spectrogram, but after the suppression of the external inputs $I_{ext} = 0$ from 40 to 120s, the network stabilizes in the Up state and a dominant stable α-band appears (fig. 5.5B).

Constant low input on inhibition modulates the switching between Up and Down states

We first studied the effect of increasing the inhibitory input current I_i (fig. 5.6A) on the fraction of time the system spends in Up and Down states. For $I_i = 0$, we found that the dynamics is characterized by a large proportion of time spent in the Up state (99%) showing persistent α-oscillations (fig. 5.6B). The transition from Up to Down is characterized by a disappearance of the α-band, however, the transition from Down to Up is associated with a burst which can either lead to the emergence of an α-band or a return to the Down state. By increasing I_i from 0 to 50 and 150 we found that the fraction of time spent in Up states decreases from 99% to 89% and to 4.5% (fig. 5.6C-E). Each network has a

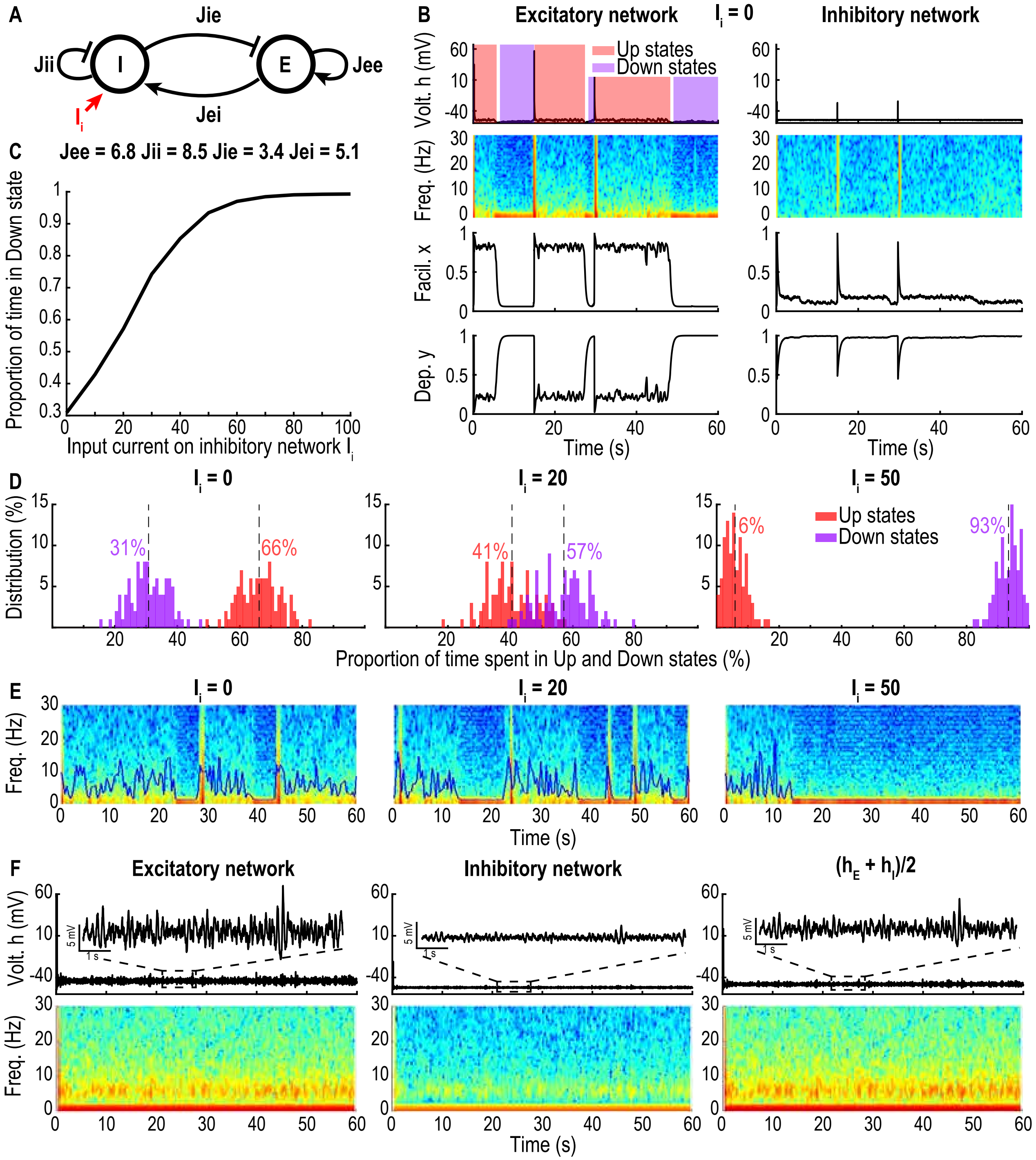

Figure 5.4: **Excitatory-inhibitory network.** **A.** Schematic of connectivity between the excitatory (E) and inhibitory (I) networks. **B.** Time series of the excitatory with AHP (left) and inhibitory (right) networks with the spectrograms of h for $J_{EE} = 6.8, J_{II} = 8.5, J_{IE} = 3.4, J_{EI} = 5.1$, $\tau = 0.025$s, $\tau_r = 0.5$s, $\tau_f = 0.3$s and $I_i = 0$. **C.** Fraction of time spent in the Down state by the excitatory network with respect to $I_i \in [0, 100]$. **D.** Distributions of the fraction of time spent in the Down (purple, resp. Up, red) state by the excitatory network for $I_i = 0$ (left), 20 (center) and 50 (right). **E.** Spectrograms (60s simulations) of h_E for for $I_i = 0$ (left), 20 (center) and 50 (right) with SEF 95 (blue line). **F.** Time series of the mean voltage h (upper) and spectrograms (lower) for the case where the excitatory network does not have AHP and with the timescales $\tau = 0.01$s, $\tau_r = 0.2$s, $\tau_f = 0.12$s, showing an α-band.

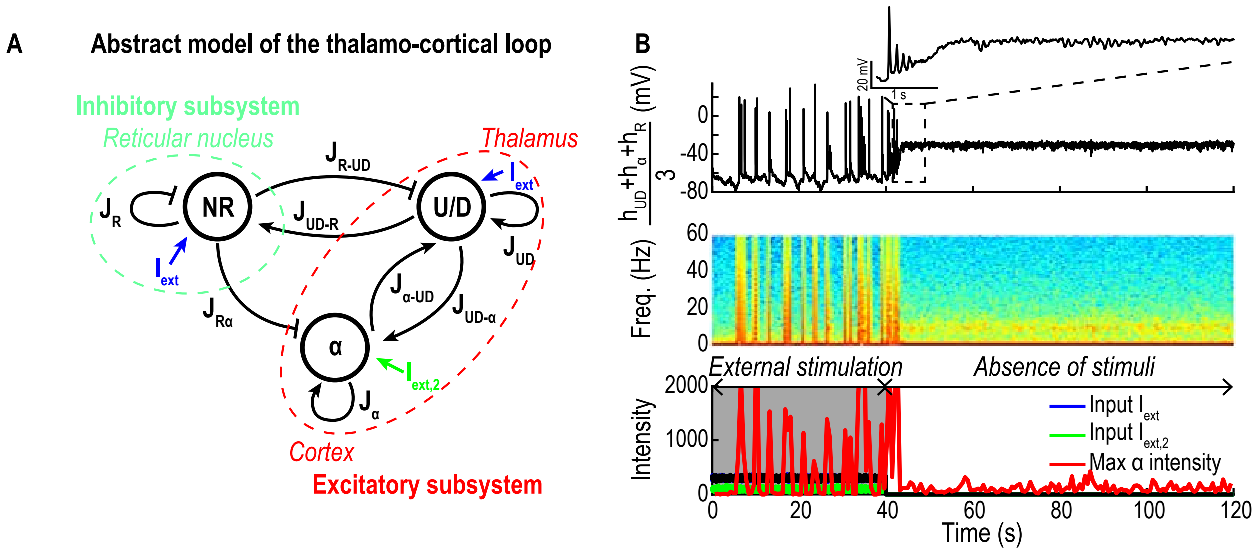

Figure 5.5: **Emergence of the α-band following external stimuli suppression. A.** Connectivity matrix between the two excitatory α, U/D and inhibitory (NR) network, with the external inputs I_{ext} (blue) and $I_{ext,2}$ (green). **B**. Time-series for the sum of the three populations voltage $h_\alpha + h_{UD} + h_R$ (upper), spectrograms (center) and maximum value of α intensity (red) and inputs I_{ext} (blue and green, lower). The timescale parameters for U/D are $\tau = 0.025$s, $\tau_r = 0.5$s, $\tau_f = 0.3$s; for NR and α: $\tau = 0.07$s, $\tau_r = 0.14$s, $\tau_f = 0.086$s, $\sigma_{UD} = \sigma_R = 6.25$ and $\sigma_\alpha = 1.5$.

different contribution to the EEG. The U/D component (with AHP) shows a fragmented and weak α-band while the inhibitory network does not exhibit any particular oscillatory band. Finally, the α component (without AHP) exhibits a very strong dominant α-band (fig. S5.4A-B).

To study the impact of the network connectivity on the emergence of a dominant band, we varied together the intrinsic connectivities $J_{UD} = J_\alpha$ of both excitatory networks (fig. 5.6F-H). We found that a small connectivity $J_{UD} = J_\alpha = 5$ is associated with a large number of Down states (88%) and transient bursts rarely lead to a stable α-band (fig. 5.6F). By increasing $J_{UD} = J_\alpha$ to 5.6 and 6.5 the fraction of Up states increases to 43% and 99% respectively (fig. 5.6I) leading to stable Up states associated with a persistent α-band.

Transient responses of the thalamo-cortical model to step and stairs inputs

To study the possible responses of the thalamo-cortical model to propofol bolus and constant increasing we consider a step input (protocol 1) and a stairs (protocol 2) as shown in fig. 5.7A.

To analyze the response to a step input (protocol 1), we ran simulations for $N = 2500$ iterations lasting $T = 2$min where we simulated a strong injection by a positive input current $I_i = 1000$ on the inhibitory network (NR) lasting $t_i = 20$s (fig. 5.7B-C). To quantify the response we collected the statistics of two durations: 1) the duration t_C after which the α-band disappears after the step function begins. 2) the duration t_U after which the α-band reappears after the end of the step function. Interestingly, for some realizations the α-band does not disappear (fig. 5.7C), we thus characterized this effect by the collapse probability p_C. We found that $p_C = 53\%$, $t_C = 9.42 \pm 5.36$s and $t_U = 4.39 \pm 2.58$s (fig. 5.7D). The histogram for t_C is characterized by an abrupt decay at 20s confirming that the suppression of the α-band can only occur during the stimulation period. However, the time t_U is dominated by an exponential decay, a classical feature of dynamical systems driven by noise over a separatrix.

Each network has a different contribution to the EEG. The U/D excitatory network with AHP shows

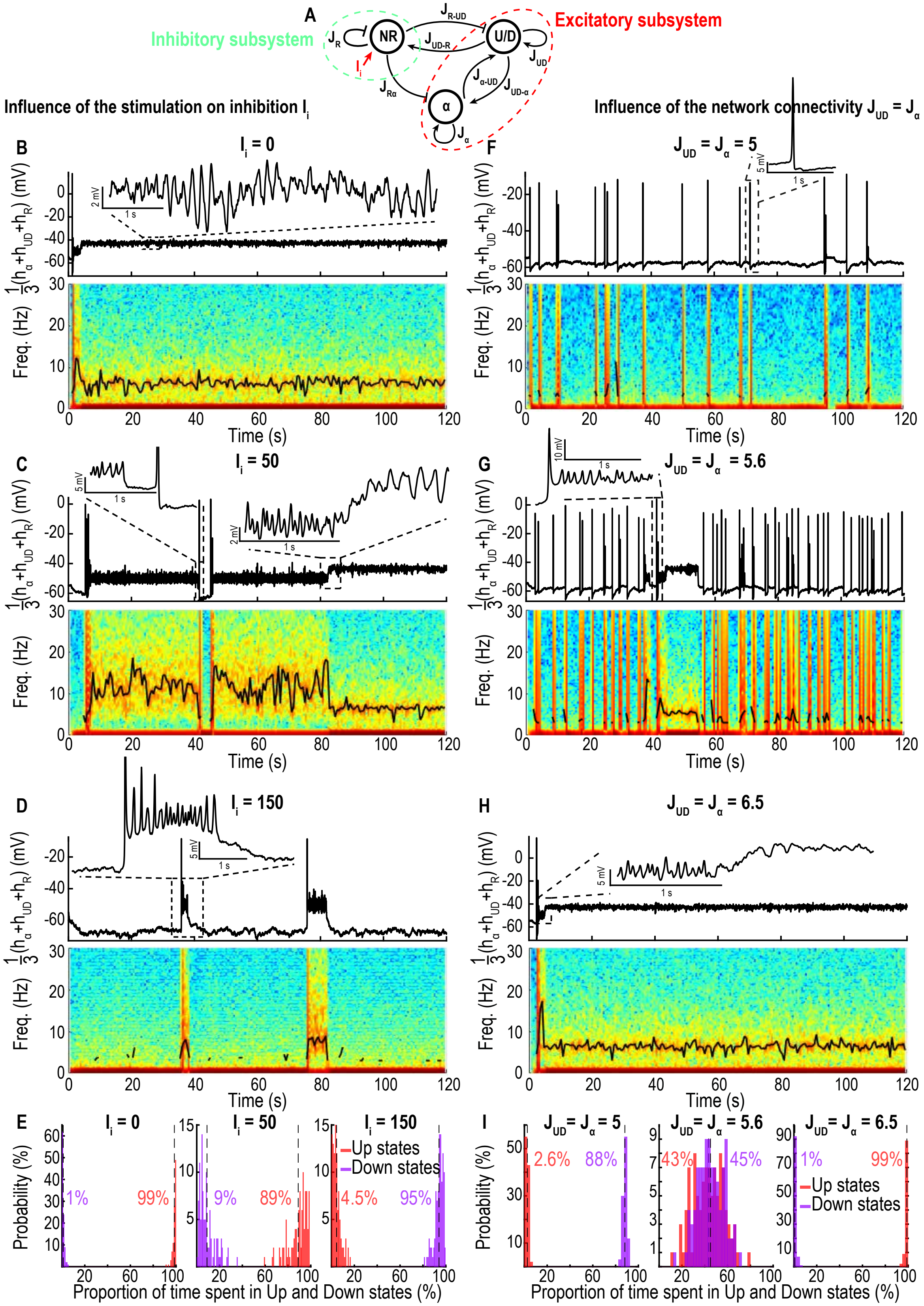

Figure 5.6: **Three compartment model exhibiting Up-Down states and α-band in the Up state.** **A.** Schematic of connectivity between the two excitatory (α, U/D) and inhibitory (NR) components. **B-D**. Time-series of the sum of the three populations voltage $h_\alpha + h_{UD} + h_R$ (upper) and spectrograms (lower) with position of maximum of the oscillatory band (black) for $J_{UD} = J_\alpha = 6.5$ and $I_i = \{0, 50, 150\}$. **E.** Fraction of time spent in the Up and Down states for the three values of I_i. **F-H** Time-series of $h_\alpha + h_{UD} + h_R$ (Upper) and spectrograms (lower) for $I_i = 0$ and $J_\alpha = J_{UD} = \{5, 5.6, 6.5\}$. **I.** Fraction of time spent in the Up and Down states for the three values of $J_{UD} = J_\alpha$. Timescales for U/D: $\tau = 0.025$s, $\tau_r = 0.5$s, $\tau_f = 0.3$s; for NR and α: $\tau = 0.005$s, $\tau_r = 0.2$s, $\tau_f = 0.12$s

a weak α-band while the inhibitory network NR only exhibits weak power in the slow δ-wave region ($\leq 1Hz$). Finally, the α excitatory component without AHP exhibits a very strong dominant α-band (fig. S5.5A-B).

To analyze the effect of a slower increase of the input (stairs function, protocol 2) we ran simulations for $N = 2500$ iterations lasting $T = 2$min where we simulated a stairs increase from $I_i = 0$ to 1000 on the inhibitory network (NR) lasting $t_i = 60$s (fig. 5.7E-F). We collected the statistics of the durations t_C (disappearance of the α-band) and t_U (reemergence of the α-band) as well as the probability to collapse p_C. We found that the probability to collapse is slightly lower in this case $p_C = 40\%$, $t_C = 53.39 \pm 4.44$s and $t_U = 4.20 \pm 2.43$s (fig. 5.7G). Similarly, the histogram of t_C is characterized by an abrupt decay at 60s confirming that the suppression of the α-band can only occur during the stimulation period, while the histogram of t_U is dominated by an exponential decay.

Discussion

We presented here minimal computational principles based on coarse-grained neuronal network models necessary to generate α-oscillations. A single neuronal population driven by synaptic short-term plasticity can illicit oscillations at a defined frequency, which directly depends on the value of the network connectivity: a higher connectivity generates faster oscillations (fig. 5.2B-C). Interestingly, we show here that the α-oscillations results from the combination of network connectivity, synaptic and biophysical properties, leading to a focus attractor, around which the stochastic mean population voltage oscillates in the phase-space (fig. S5.7A-B). Moreover, we showed that spontaneous switching between Up and Down states in a single neuronal population is modulated by AHP and also that the network connectivity controls the proportion Up vs Down states: a higher connectivity J results in a dominant percentage of time spent in Up states (fig. 5.3C-D). The stability of the oscillations during Up states for a population without AHP could result from the intrinsic network regulation: indeed, interactions between hundreds of inhibitory interneurons and hippocampal pyramidal excitatory neurons can redistribute the firing load to maintain the oscillation frequency even when up to 25% of the synapses are deactivated [205].

When we added an excitatory input current on the inhibitory coupled to excitatory population, the proportion of time spent in Up states decreased and, after reaching a threshold value ($I_i = 60$), the network became completely silenced, characterized by Down states only (fig. 5.4C-D). When coupling two excitatory and one inhibitory neuronal population (fig. 5.5A), α-oscillations, generated by the excitatory component without AHP, co-existed with spontaneous switching between Up and Down states induced by the excitatory population with AHP, as summarized in fig. 5.8. Stimulating the inhibitory population induces the fragmentation of the α-band by modulating directly the proportion of Up vs Down states (fig. 5.6B-E).

Finally, we suggest that synaptic noise has two main roles on the network properties: 1) increasing the noise intensity stabilizes the α-band (fig. 5.2D) and 2) when an external stimulation is applied to the inhibitory system in a step or stairs input, the network can react with opposite behavior: either the network activity collapses, leading to a suppression of all oscillatory bands in the EEG or a stable persistent α-band emerges during the entire stimulation (fig. 5.7). Finally, we propose that three connected neuronal populations are sufficient to generate an α-oscillation that could be fragmented by increasing the inhibitory pathway, as suggested during general anesthesia [31]. The present model could be generalized to study the emergence and disappearance of other oscillations such as the θ-oscillations occurring during REM sleep [32–34].

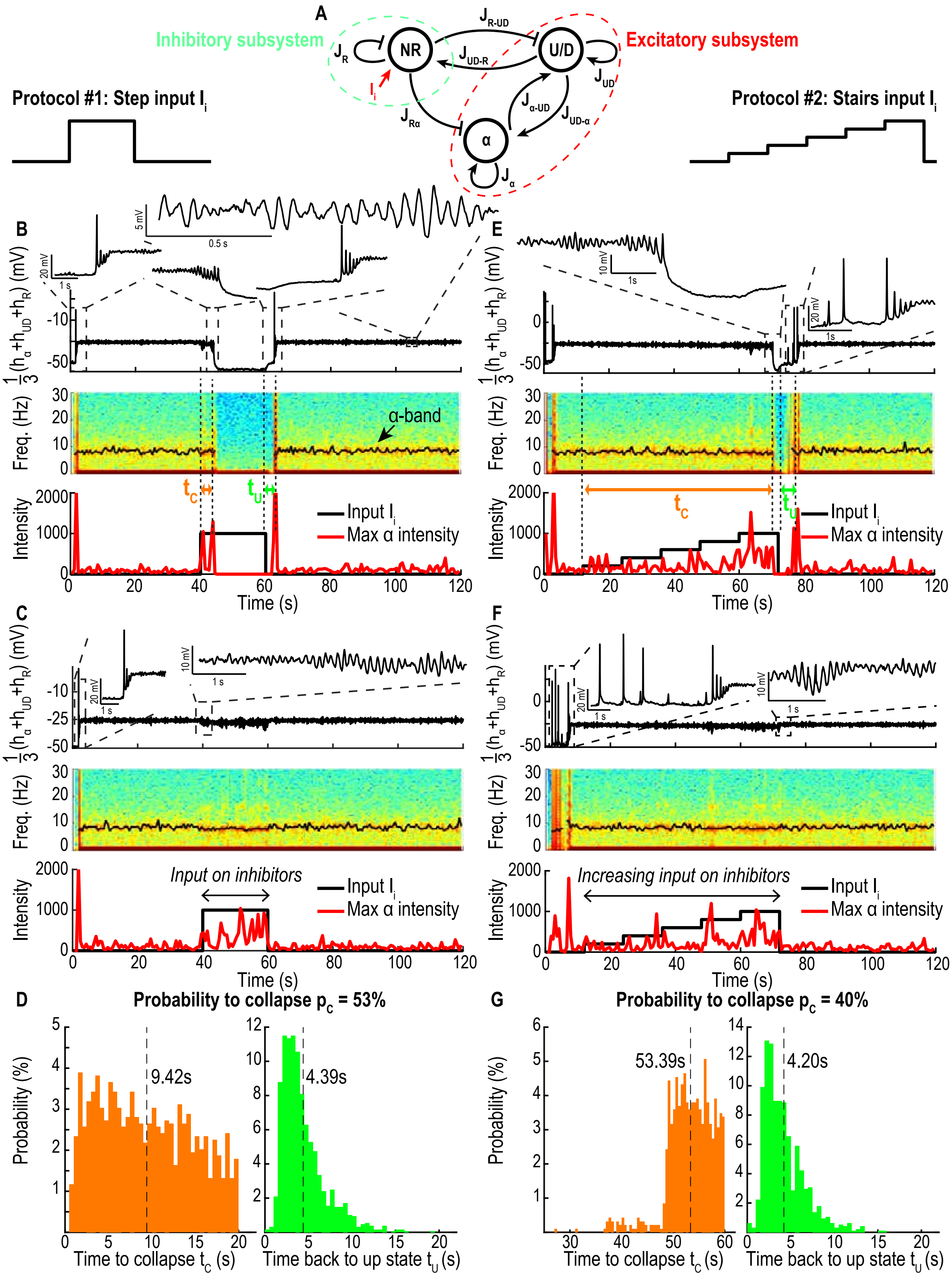

Figure 5.7: **Cases of collapse of the α-band. A.** Schematic of connectivity between the two excitatory (α and U/D) and inhibitory (NR) networks. **B-C**. Time-series of the sum of the three populations voltage $h_\alpha + h_{UD} + h_R$ (upper), spectrogram (center) with position of maximum of the α-band (black, collapsing (B) and persistent (C)), maximum value of α intensity (red) and input I_i (black, lower) for a step input. **D.** Distributions of the delay t_C between the beginning of stimulation and the collapse (orange) and delay between the end of the stimulation and the moment the reapparition of the α-band (green). **E-G.** Same as B-D for a stairs input. Timescales for U/D, α and NR: $\tau = 0.005$s, $\tau_r = 0.1$s, $\tau_f = 0.06$s

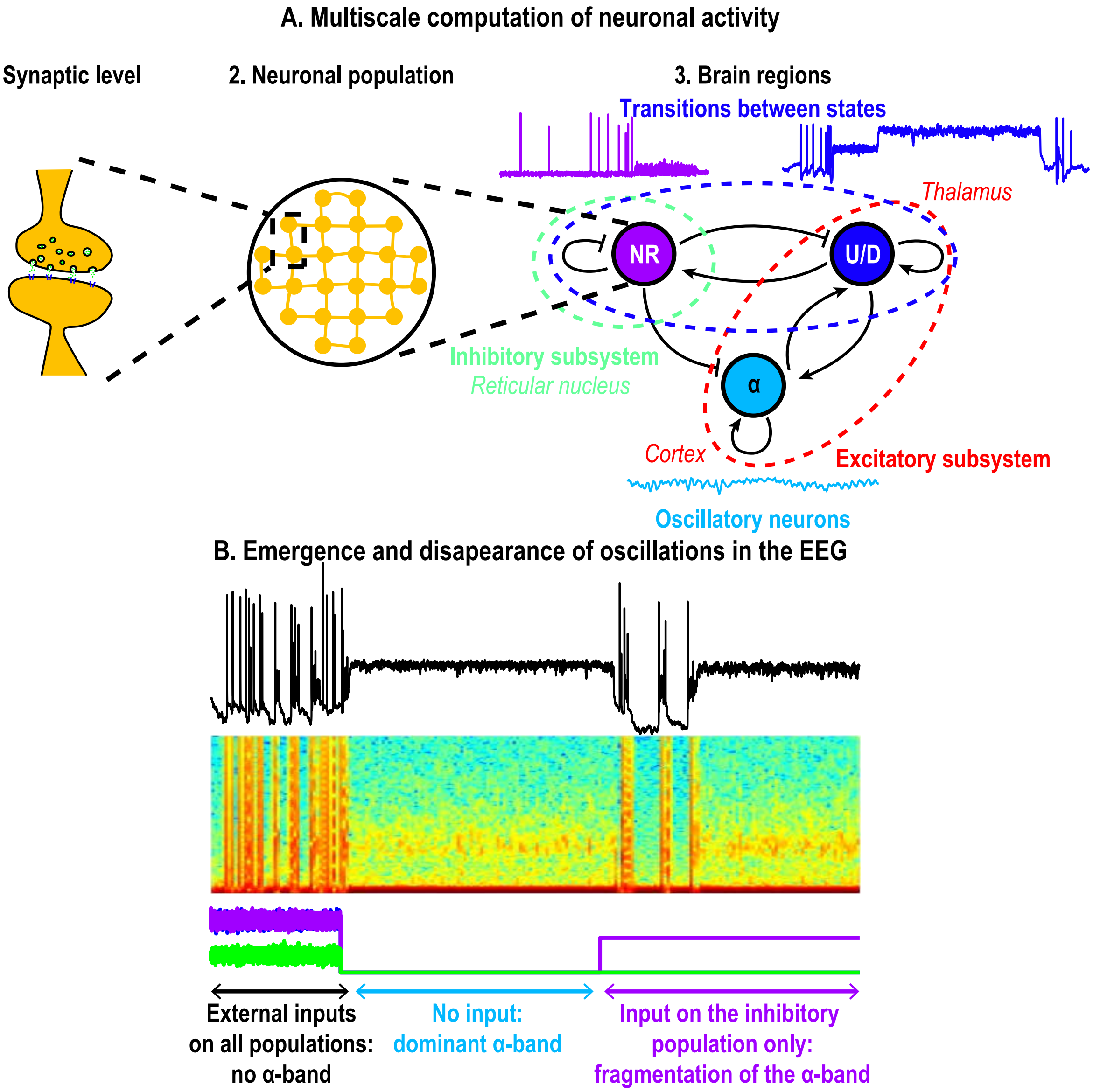

Figure 5.8: **Computational principle underlying the α-band dynamics.** **A.** Multiscale models 1. synaptic level: short-term facilitation and depression mechanisms, 2. neuronal population: mean voltage fluctuations and 3. interactions between different brain regions (thalamus and cortex, models 5.4 and 5.5) resulting in the different activity patterns observed in EEG at a global scale. **B.** α-band emerges in the Up-state due to noise but can be altered by external inputs.

Modeling the dynamics of the α-band

The origin of the α-band [198] remains unclear. Early modeling efforts using the Hodgkin-Huxley framework [70] suggested a key role of ionic currents such as sodium, potassium currents, low threshold calcium, AHP and synaptic currents (GABAs, AMPA) that could reproduce various patterns of oscillations such as waxing and waning spindle oscillations [71] as well as initiation, propagation and termination of spindle oscillations (see also [206]). By varying the GABA conductances similar models could reproduce the dominant α-oscillation observed in propofol anesthesia [72, 73]. Indeed the GABA conductance regulates the firing frequencies and the synchronization of pyramidal neurons [207]. In contrast, in the present model, based on synaptic dynamics driven by noise, the α-band is generated only when the mean voltage is in the Up state, suggesting that the ionic mechanisms are not necessary to generate the α-band, but contribute to the termination of the Up states and thus control the α-band fragmentation. Furthermore, adding an input current to the inhibitory population allows to generate transitions between spindles (fig. 5.4C-D and 5.6B-E). In addition, we found that the α-band can be stabilized by increasing the noise amplitude, while the peak frequency of the α-band was unchanged (fig. 5.2D-E). Thus, we propose that the synaptic noise could be responsible for the stabilization of the α-band. Interestingly, the α-band is persistent in young subjects and becomes sparser with age [208]. Possibly, a higher neuronal activity (in younger subjects) leads to higher extracellular potassium which, in turn, increases the synaptic noise [52]. Another possible mechanism for fragmenting the α-band could involve the metabolism pathway, when the ATP concentration coupled to the sodium concentration is decreased: during a burst, a high sodium concentration depletes ATP that deregulates the K^+ repolarization current and thus leads to a phase of suppression [195].

Relation between Up and Down states and the α-band

Neuronal networks exhibit collective transitions from Up to Down states [27, 28, 199]. We reported here that the α-oscillations are only generated when the neuronal ensemble is in the Up state. Interestingly, we could not generate, in a single neuronal population, at the same time this α-oscillation and the Up-Down states transitions. Rather we needed a minimum of two coupled excitatory neuronal populations. We reported here that the fraction of time spent in Up and Down states depends on the level of synaptic connectivity (fig. 5.3C-D and 5.6F-I). However, by adding an inhibitory network, we were able to modulate the proportion of time spent in Up vs Down states by changing the input stimulation current (fig. 5.4C-D and 5.6B-E) on this inhibitory population without varying the connectivity. The mechanism is feasible because the inhibitory input on both excitatory populations allows to destabilize the Up state and thus increase the transitions to Down state modulating the overall fraction of time spent in the Up states. To conclude, in the extreme case where the Down states are dominant, the overall voltage dynamics resemble iso-electric suppressions without the need to account for a metabolic stress [209, 210].

Predictions and limitations of the model to interpret the α-band during general anesthesia

The physiological mechanisms leading to the emergence of the α-band shortly after propofol injection during general anesthesia remains unclear [30, 31]. Possibly, during wakefulness, the amount of external stimuli suppresses the emergence of α-oscillations [34]. When the external stimuli ceases with propofol injection, the α-oscillation could become dominant (fig. 5.5B). The present model suggests that the initial state represents an already anesthetized brain where the neuronal networks do not receive any external stimuli, leading to the spontaneous emergence of the α-band.

General anesthesia needs to be sustained over the whole course of a surgery and thus controlling optimally the anesthetic injection to prevent cortical awareness or a too deep anesthesia remains a difficult problem [208]. Population models such as the one presented here could be used to test different activation pathways of anesthetic drugs. The present model accounts for the appearance an iso-electric suppression [211] in the EEG of the order of a few seconds (fig. 5.7B,E) induced by increasing transiently the hypnotic. We predicted here that the fragmentation of the α-band results from a shift between Up and Down states dominance that could be tested with in vivo experiments. It would be interesting to further account for longer term consequences of an anesthetic input (several minutes). Indeed, the causality between α-suppressions and burst-suppressions [144] remains unexplained, suggesting that this relation could involve other mechanisms than the ones we modeled here based on synaptic plasticity, AHP and network connectivity.

5.2 Methods

5.2.1 Definition of the fragmentation level of an oscillatory band

The emergence of the α-rhythm is characterized by a continuous band in the range [8-12]Hz in the spectrogram of the EEG, yet there are no universal criteria to define its persistence in time and frequency. In this section, we define a fragmentation measure of the $\alpha-$band. We start by detecting the peak spectral value $S_\alpha(t)$ in each bin of the spectrogram by finding the highest power value in the extended range $\alpha_{min} = 4 - \alpha_{max} = 16$ Hz. If $S_\alpha(t) > T_\alpha$, we consider that the band is present and attribute $x_{pr}(t) = 1$, otherwise $x_{pr}(t) = 0$. For a signal divided into N bins at times t_k, we can define the fraction of total presence of the α band as the persistence level:

$$P_\alpha = \frac{1}{N} \sum_{k=1}^{N} x_{pr}(t_k), \tag{5.1}$$

Another measure of the fragmentation level is the disruption number D_α that we count as the number of time per minute where the peak spectral value $S_\alpha(t)$ goes under the threshold T_α. We call the fragmentation level the pair $F_\alpha = (P_\alpha, D_\alpha)$ (fig S5.6). For the human EEG data from VitalDB (fig. 5.1), we used a window size $w = 0.5s$ (which is the same as the window size used to compute the spectrogram) and a threshold value $T_\alpha = 1.5$, for the simulated data we had stronger power in every frequency range in the spectrogram and thus we used $T_\alpha = 10$.

5.2.2 Modeling a single neuronal population based on synaptic depression-facilitation dynamics

For a sufficiently well connected ensemble of neurons, we use a mean-field system of equations to study bursting dynamics, AHP and the emergence of Up and Down states. This stochastic dynamical system consists of three equations [102, 109, 158] for the mean voltage h, the depression y, and the synaptic facilitation x:

$$\begin{aligned} \tau_0 \dot{h} &= -(h - T_0) + Jxy(h - T_0)^+ + \sqrt{\tau_0}\sigma\dot{\omega} \\ \dot{x} &= \frac{X - x}{\tau_f} + K(1 - x)(h - T_0)^+ \\ \dot{y} &= \frac{1 - y}{\tau_r} - Lxy(h - T_0)^+, \end{aligned} \tag{5.2}$$

where $h^+ = max(h, 0)$ is the population mean firing rate [105]. The term Jxy reflects the combined synaptic short-term dynamics with the network activity. The second equation describes facilitation, and the third one depression. The parameter J accounts for the mean number of synaptic connections per neuron [102, 110]. We previously distinguished [109] the parameters K and L which describe how the firing rate is transformed into synaptic events that are changing the duration and probability of vesicular release respectively. The time scales τ_f and τ_r define the recovery of a synapse from the network activity. We account for AHP with two features: 1) a new equilibrium state representing hyperpolarization after the peak response of the burst 2) two timescales for the medium and slow recovery to the resting membrane potential to describe the slow transient to the steady state. Finally, $\dot{\omega}$ is an additive Gaussian noise and σ its amplitude, representing fluctuations in the firing rate.

In the case of a neuronal network that does not exhibit AHP the resting membrane potential is constant $T_0 = 0$ and $\tau_0 = cst \in [0.005, 0.025]$s. However, for a population showing AHP after the bursts, the resting membrane potential T_0 and the recovery time constant τ_0 of the voltage h are defined piece-wise as follows:

- $\tau_0 = \tau$ and $T_0 = 0$ in the subspace $\Omega_{fast} = \{y > Y_{AHP}$ and $h \geq H_{AHP}\}$, which represents the fluctuations around the resting membrane potential during the down state and the burst dynamics.
- $\tau_0 = \tau_{mAHP}$ and $T_0 = T_{AHP} < 0$ in the subspace $\Omega_{mAHP} = \{y < \frac{1}{1 + Lx(h - T_0)} (\iff \dot{y} > 0)$ and $y < Y_h$ or $\dot{y} < 0\}$. This part of the phase-space defines the moment when the hyperpolarizing currents at the end of the burst become dominant and force the voltage to hyperpolarize.
- $\tau_0 = \tau_{sAHP}$ and $T_0 = 0$ in the subspace $\Omega_{sAHP} = \{y < \frac{1}{1 + Lx(h - T_0)}$ and $(Y_{AHP} < y$ or $h < H_{AHP})\}$, which represents the slow recovery to resting membrane potential.

The threshold parameters defining the three phases are $Y_h = 0.5$, $Y_{AHP} = 0.85$ and $H_{AHP} = -7.5$. In this study, we varied the network connectivity parameter $J \in [5.6, 8.6]$ and all other parameters are described in Table 1, SI.

To convert the mean-field variable h into a mean voltage $\tilde{h}$ in mV, we use the following normalization

$$\tilde{h} = \frac{h - h_{min}}{h_{max} - h_{min}} A_{max} + V_{rest}, \tag{5.3}$$

where $V_{rest} = -70$ mV and we identified $h_{min} = -100$ and $h_{min} = 1200$ based on numerical simulations and chose $A_{max} = 200mV$ according to the classical amplitude of local field potential recordings.

5.2.3 Two-populations model of the thalamo-cortical loop

To model the interactions between one excitatory E and inhibitory I neuronal network, we coupled two systems of equations (5.2)) as follows:

$$
\begin{aligned}
\tau_0 \dot{h_E} &= -(h_E - T_0) + J_{EE} x_E y_E (h_E - T_0)^+ - J_{IE} \frac{\tau_0}{\tau} x_I y_I (h_I - T)^+ + \sqrt{\tau_0}\sigma_E \dot{\omega}_E \\
\dot{x_E} &= \frac{X - x_E}{\tau_f} + K(1 - x_E)(h_E - T_0)^+ \\
\dot{y_E} &= \frac{1 - y_E}{\tau_r} - L x_E y_E (h_E - T_0)^+, \\
\tau \dot{h_I} &= -(h_I - T) - J_{II} x_I y_I (h_I - T)^+ + J_{EI} \frac{\tau}{\tau_0} x_E y_E (h_E - T_0)^+ + \sqrt{\tau}\sigma_I \dot{\omega}_I + I_i \\
\dot{x_I} &= \frac{X - x_I}{\tau_f} + K(1 - x_I)(h_I - T)^+ \\
\dot{y_I} &= \frac{1 - y_I}{\tau_r} - L x_I y_I (h_I - T)^+,
\end{aligned}
\tag{5.4}
$$

where τ_0 and T_0 for the excitatory population can either be constant, in the absence of AHP or defined piece-wise when it is present, as already discussed in subsection 5.2.2. The inhibitory population is always modeled without AHP and thus τ is constant and $T = 0$. All other parameters are described in the central columns called “2 populations” of Table 5.1.

5.2.4 Three connected neuronal populations to model the thalamo-cortical loop

To model the thalamo-cortical loop, we connected three neuronal networks. One excitatory network driven by AHP generates the Up-Down state dynamics (referred to as U/D in figs. 5.5, 5.6 and 5.7). The second excitatory network is not driven by AHP and is referred as α in figs. 5.5, 5.6 and 5.7. Both networks are coupled with an inhibitory one (called NR), which does not exhibit any AHP. The equations extend the case of two neuronal networks presented in subsection 5.2.3 and the connectivity matrix with 9 elements is presented in Table 5.1. The overall system of equations is

$$\begin{aligned}
\tau_0 \dot{h_{UD}} &= -(h_{UD} - T_0) + J_{UD} x_{UD} y_{UD} (h_{UD} - T_0)^+ + J_{\alpha-UD} \frac{\tau_0}{\tau} x_\alpha y_\alpha (h_\alpha - T)^+ \\
&\quad - J_{R-UD} \frac{\tau_0}{\tau} x_R y_R (h_R - T)^+ + \sqrt{\tau_0} \sigma_{UD} \dot{\omega}_{UD} \\
\dot{x_{UD}} &= \frac{X - x_{UD}}{\tau_f} + K(1 - x_{UD})(h_{UD} - T_0)^+ \\
\dot{y_{UD}} &= \frac{1 - y_{UD}}{\tau_r} - L x_{UD} y_{UD} (h_{UD} - T_0)^+, \\
\tau \dot{h_\alpha} &= -(h_\alpha - T) + J_\alpha x_\alpha y_\alpha (h_\alpha - T)^+ + J_{UD-\alpha} \frac{\tau}{\tau_0} x_{UD} y_{UD} (h_{UD} - T_0)^+ \\
&\quad - J_{R-\alpha} x_R y_R (h_R - T)^+ + \sqrt{\tau} \sigma_\alpha \dot{\omega}_\alpha \\
\dot{x_\alpha} &= \frac{X - x_\alpha}{\tau_f} + K(1 - x_\alpha)(h_\alpha - T)^+ \\
\dot{y_\alpha} &= \frac{1 - y_\alpha}{\tau_r} - L x_\alpha y_\alpha (h_\alpha - T)^+, \\
\tau \dot{h_R} &= -(h_R - T) - J_R x_R y_R (h_R - T)^+ + J_{UD-R} \frac{\tau}{\tau_0} x_{UD} y_{UD} (h_{UD} - T_0)^+ \\
&\quad + J_{\alpha-R} x_\alpha y_\alpha (h_\alpha - T)^+ + \sqrt{\tau} \sigma_R \dot{\omega}_R + I_i \\
\dot{x_R} &= \frac{X - x_R}{\tau_f} + K(1 - x_R)(h_R - T)^+ \\
\dot{y_R} &= \frac{1 - y_R}{\tau_r} - L x_R y_R (h_R - T)^+,
\end{aligned} \tag{5.5}$$

where τ_0 and T_0 for the first excitatory population U/D are defined piece-wise in part 5.2.2 and all other parameters are given in Table 5.1 (right columns: "3 populations").

5.2.5 Origin of oscillations in the Up state

We study here the origin of the oscillations observed in the spectrograms of h in relation with the Up and Down states.

Oscillations around the Up state attractor for a neuronal population without AHP

In the absence of AHP, the focus attractor A_{Up} has two complex conjugated eigenvalues. Thus the deterministic dynamics oscillates around the point A_{Up} at a frequency

$$2\pi\omega_{Up} = Im(\lambda_2^{A_{Up}}) \iff \omega_{Up} \in [5.85, 8.26] Hz \text{ for } J \in [5.6, 8.6]. \tag{5.6}$$

which corresponds to the dominant spectral band observed in fig. 5.2. The oscillation eigenfrequency ω_{Up} depends on the network connectivity J (fig. 5.2A-B), but not on the noise amplitude (fig. 5.2C-D). Note that the noise allows to generate persistent oscillation compared to the case of the pure deterministic system. Finally, increasing the noise amplitude stabilizes the α-band (fig. 5.2C-D).

Note that if we take $\tau = 0.025s, \tau_r = 0.5s$ and $\tau_f = 0.3s$, then the eigenvalues of A_{Up} become $\lambda^1_{A_{Up}} \in [-22.28, -31.76]$ and the complex-conjugate eigenvalues

$$\lambda^{2,3}_{A_{Up}} \in [-2.46, -5.89] \pm i[14.71, 20.75]$$

leading to an eigenfrequency $\omega_{Up} \in [2.34, 3.30]$Hz (fig. S5.1) which explains the disappearance of the dominant α-band in this case (see also fig. S5.7C).
Finally, since $|\lambda^1_{A_{Up}}| \gg |Re(\lambda^2_{A_{Up}})|$ the dynamics is very anisotropic and the oscillations are confined in a 2D manifold (fig. S5.7A.1-A.3, light red trajectories).

The Up state stability is due to multiple re-entries in its basin of attraction

To explain the locking in the Up state, we recall that the stochastic trajectories starting inside the basin of attraction of the Up state can cross the separatrix Γ and fall into the Down state. However, because the deterministic vector field of system (5.2) is very shallow near Γ, the additive noise on the h variable can push the trajectories back into the Up state, where the field is stronger, and thus the trajectory is brought in a neighborhood of A_{Up} and continues oscillating, as shown in fig. S5.7B (see inset).
To explain the other frequencies (than the eigenfrequency ω_{Up}) observed in the spectrum of h (fig. S5.7C), we note that when a trajectory falls back in the Up state, it can produce a longer or shorter loop depending on its initial distance to the attractor A_{Up}. These oscillations between the two basins of attraction define stochastic oscillations that contribute to the spectrogram of h.

Oscillations between Up and Down state in a neuronal population containing an AHP component

For a neuronal network with an AHP component, the Up state has only real negative eigenvalues (fig. S5.8C), thus no oscillations are expected near the attractor. However, the presence of a slow AHP component (fig. S5.8A-B pink) can push the dynamics into the Down state, as opposed to the case without AHP. Finally, in the Down state, the trajectories fluctuate with the noise until they escape. Once trajectories cross the separatrix Γ, they follow an almost deterministic path close to that of the unstable manifold of S fig. S5.8A-B grey) showing a long excursion in the phase-space before falling back near the attractor A_{Up}. This dynamics explains the recurrent switches between Up and Down states.

Supplementary information for ZONCA L. & HOLCMAN D., "Up and Down states occurring in neuronal networks regulate the emergence and fragmentation of the alpha-band"

5.3 Supplementary results

Table 5.1 summarizes the parameters used for all the simulation results presented in the main text and in the following supplementary figures.

	1 population		2 populations		3 populations		
	no AHP	AHP	no AHP & I	AHP	same E	no AHP & I	AHP
τ	0.005 (α) - 0.01s (θ)	0.025s	0.005 (α) - 0.01s	0.025s	0.005s	0.005-0.07s	0.025s
τ_r	0.2 - 0.5s	0.5s	0.2 - 0.5s	0.5s	0.1s	0.1 -0.2s	0.5s
τ_f	0.12 - 0.3s	0.3s	0.12 - 0.3s	0.3s	0.06s	0.06 - 0.12s	0.3s
τ_{mAHP}		0.3s		0.12s	0.06s		0.12s
τ_{sAHP}		1s - 10.5s		1s	0.5s		1s
$J_{E_1E_1}$	5.6 - 8.6		6.8		5.6	6.5	
J_{E_1I}			5.1		5.6	6.5	
J_{IE_1}			3.4		4.48	16.25	
J_{II}			8.5		5.6	3.25	
$J_{E_1E_2}$					2.8	1.3	
$J_{E_2E_1}$					1.12	1.3	
J_{E_2I}					0	0	
J_{IE_2}					4.48	16.25	
$J_{E_2E_2}$					4.2	6.5	
σ	5 - 15		2.75 (σ_I) 5.5 (σ_E)		10 (σ_T) 3 ($\sigma_{C,R}$)	2.5 ($\sigma_{T,C,R}$)	
T_{AHP}		-30		-30	-30		-30
K	0.5 Hz						
L	0.3 Hz						
X	0.06						

Table 5.1: Models 5.2 (1 population), 5.4 (2 populations) and 5.5 (3 populations) parameters (see Main text, Methods). For model (5.4) and (5.5), the inhibitory population is always without AHP and the excitatory populations can be with or without AHP. For model (5.5) E_1 corresponds to the network with AHP (U/D), and E_2 to the network without AHP (α).

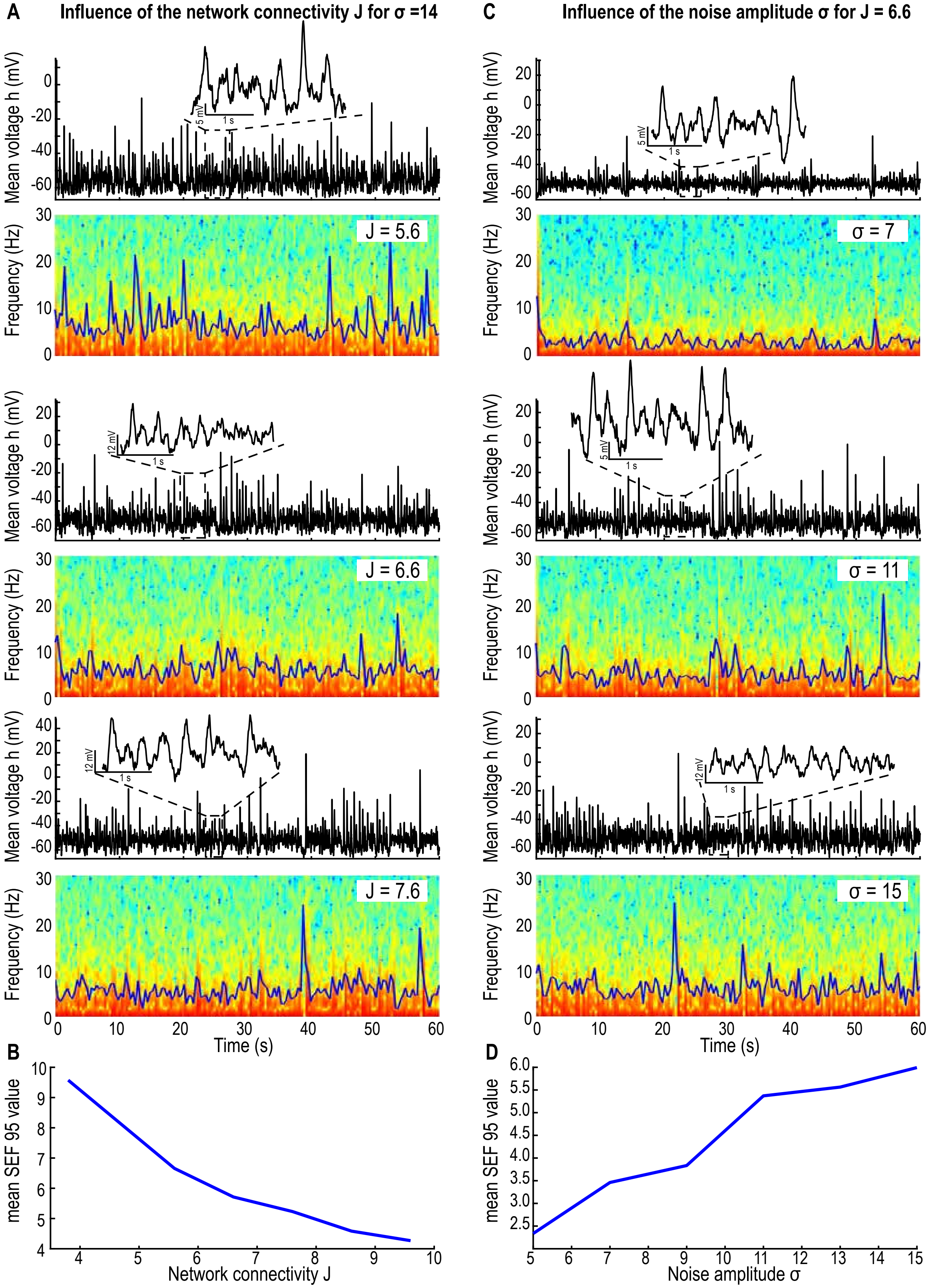

Figure S5.1: **Effect of network connectivity J and noise amplitude σ on model** (5.2) **without AHP. A.** Time-series and spectrograms of h (60s simulations) with SEF95 (blue curve) for $J = 5.6$ (upper), 6.6 (center) and 7.6 (lower). **B.** Mean value of the SEF95 for $J \in [3.8, 10]$. **C.** Time-series and spectrograms of h (60s simulations) with SEF95 (blue curve) for $\sigma = 7$ (upper), 11 (center) and 15 (lower). **D.** Mean value of the SEF95 for $\sigma \in [5, 15]$. Synaptic plasticity timescales: $\tau = 0.025$s,$\tau_r = 0.5$s and $\tau_f = 0.3$s.

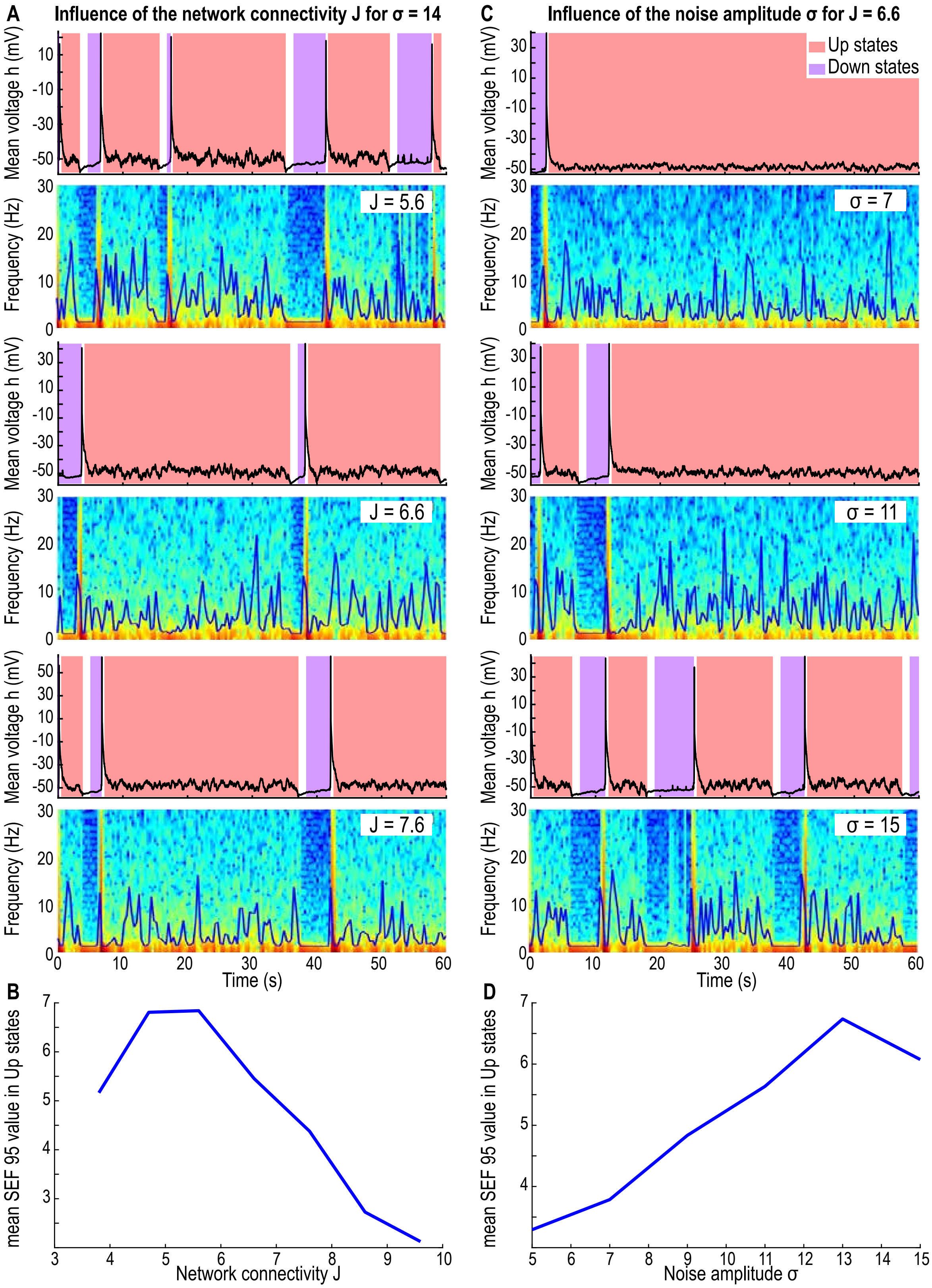

Figure S5.2: **Effect of network connectivity J and noise amplitude σ on model (5.2) with AHP.** **A.** Time-series and spectrograms of h (60s simulations) with SEF95 (blue curve) for $J = 5.6$ (upper), 6.6 (center) and 7.6 (lower). **B.** Mean value of the SEF95 in the upstates for $J \in [3.8, 10]$. **C.** Time-series and spectrograms of h (60s simulations) with SEF95 (blue curve) for $\sigma = 7$ (upper), 11 (center) and 15 (lower). **D.** Mean value of the SEF95 in the Up states for $\sigma \in [5, 15]$. Synaptic plasticity timescales: $\tau = 0.025$s,$\tau_r = 0.5$s and $\tau_f = 0.3$s.

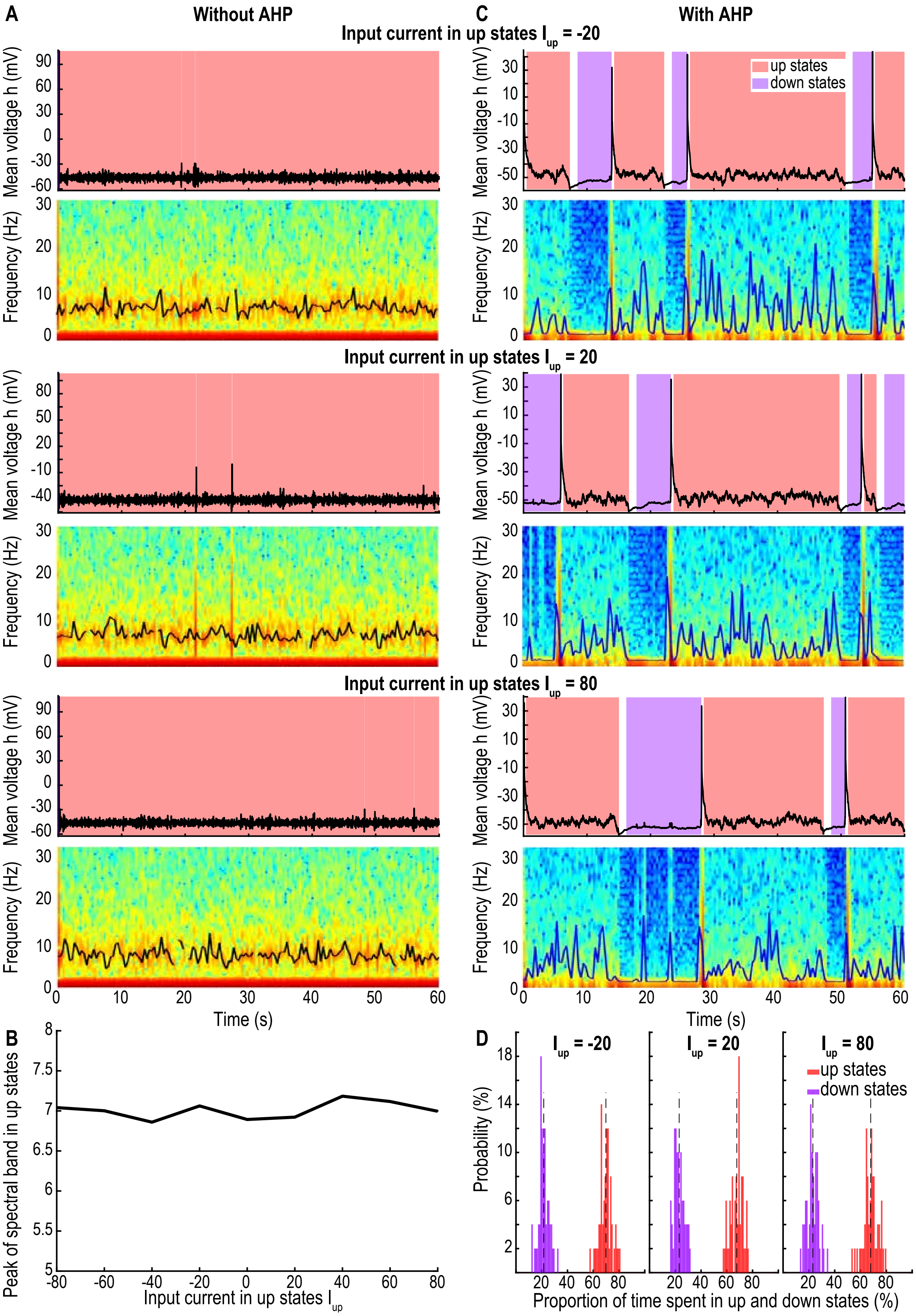

Figure S5.3: **Effect of an input current I_{up} during the up states in model** (5.2)**. A.** Time-series and spectrograms of h (60s simulations, model (1) without AHP with $J = 6.6$, $\sigma = 10$, $\tau = 0.01$s,$\tau_r = 0.2$s and $\tau_f = 0.12$s), with peak value of the oscillatory band, (black curve) for $I_{up} = -20$ (upper) 20 (center) and 80 (lower). **B.** Mean peak value of the oscillatory band for $I_{up} \in [-80, 80]$. **C.** Time-series and spectrograms of h (60s simulations, model (1) with AHP with $J = 6.6$, $\sigma = 14$, $\tau = 0.025$s,$\tau_r = 0.5$s and $\tau_f = 0.3s$). **D.** Proportion of time spent in up vs down states for $I_{up} = \{-20, 20, 80\}$ ($N = 50$ simulations of $T = 5$min, model (5.2) with AHP).

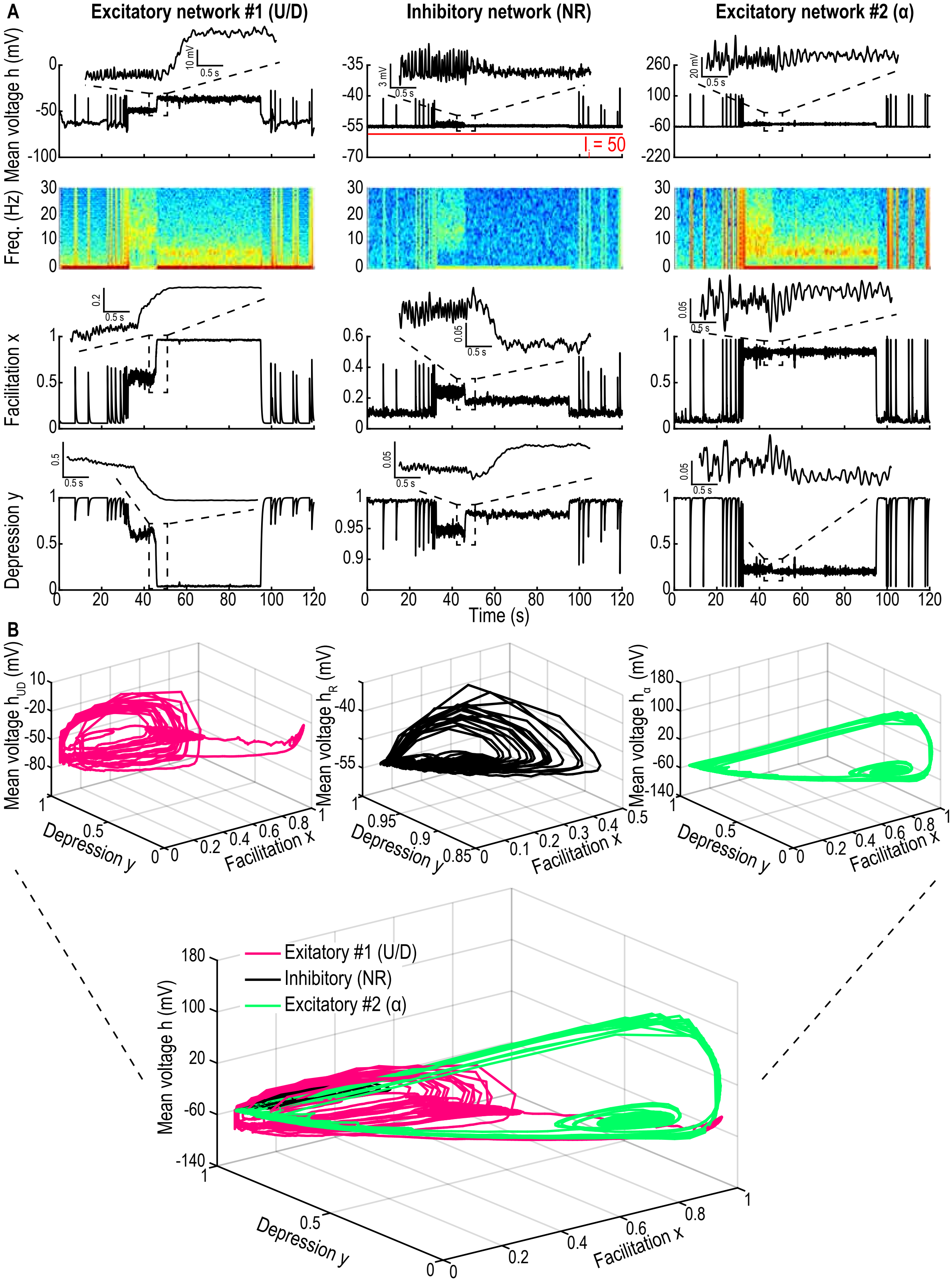

Figure S5.4: **Contribution of the three components of model** (5.5) **for a constant input. A.** Time-series of mean voltage h, spectrogram, facilitation x and depression y of system (5.5) (120s simulations) for the excitatory network with AHP (U/D, left: $\tau = 0.025$s, $\tau_f = 0.3$s,$\tau_r = 0.5$s), the inhibitory network (NR, center) and the excitatory network without AHP (α, right: $\tau = 0.005$s, $\tau_f = 0.12$s, $\tau_r = 0.2$s) with a constant input $I_i = 50$ on the inhibitory network (red line). **B.** Trajectories in the $h - x - y$ phase space of each component (U/D, pink, left, NR black, center and α, green, right).

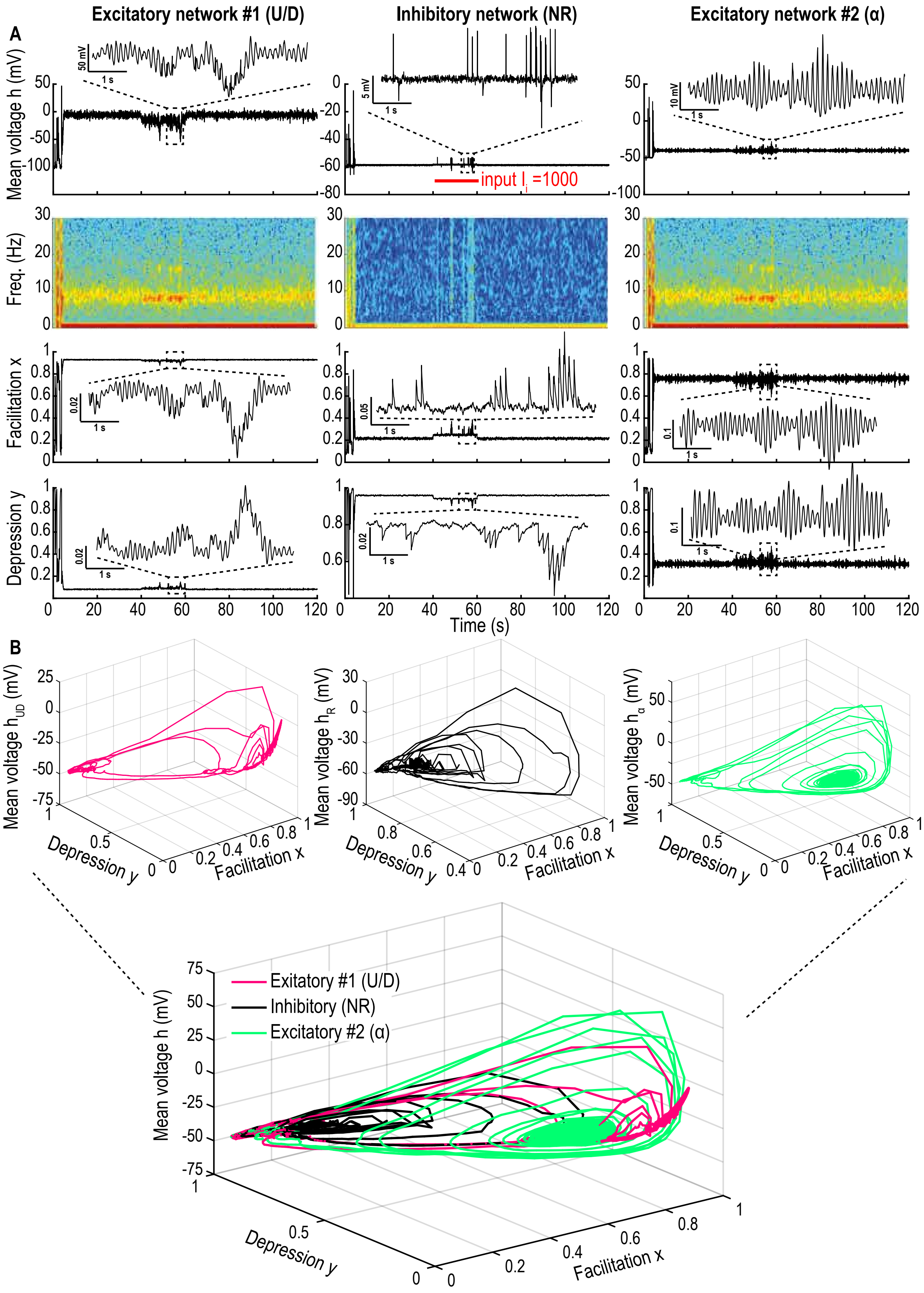

Figure S5.5: **Contribution of the three components of model** (5.5) **for a step input. A.** Time-series of mean voltage h, spectrogram, facilitation x and depression y of system (5.5) (120s simulations) for the excitatory network with AHP (U/D, left: $\tau = 0.005$s, $\tau_f = 0.06$s,$\tau_r = 0.12$s), the inhibitory network (NR, center) and the excitatory network without AHP (α, right: $\tau = 0.005$s, $\tau_f = 0.06$s,$\tau_r = 0.12$s) with a step input $I_i = 1000$ at 40-60s on the inhibitory network (red line). **B.** Trajectories in the $h - x - y$ phase space of each component (U/D, pink, left, NR black, center and α, green, right).

5.4 Supplementary methods

5.4.1 Fragmentation level of an oscillatory band

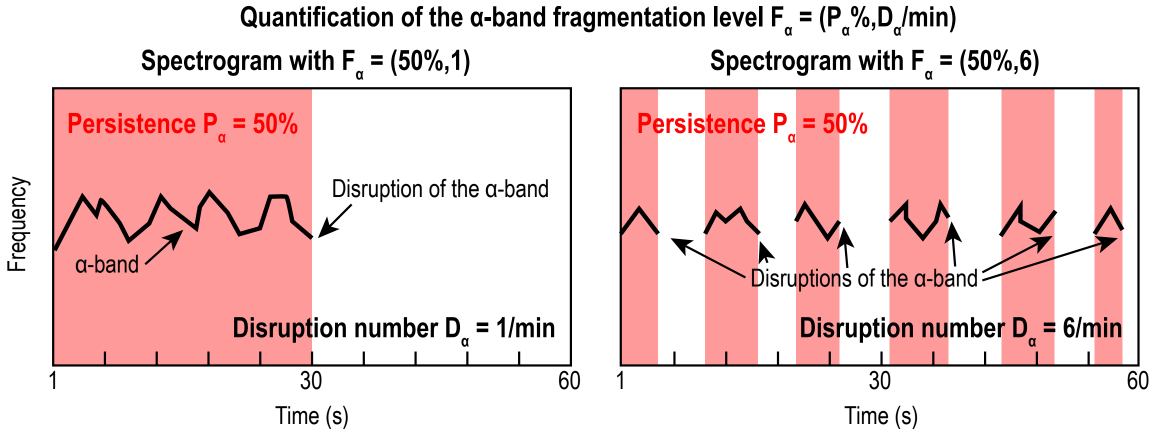

Figure S5.6: **Schematic showing the quantification of the fragmentation level in a spectrogram.**

5.4.2 Mathematical analysis of the phase-space associated with the mean-field depression-facilitation model

We shall now describe the phase-space of the dynamical system (5.2) with and without AHP. In a first subsection we describe the three critical points (two attractors and a saddle-point) and the linearized dynamics around each point and in a second subsection we describe the numerical method used to obtain the shape of the separatrix delimiting the basins of attraction of each attractor.

Description of the three critical points of the phase-space of network model (5.2)

The phase-space of the deterministic system (5.2) contains three critical points that we shall analyze now.

Down state attractor point A_{Down}

The basin of attraction of the critical point $A_{Down} = (0, X, 1)$ (fig. S5.7A and S5.8A, purple) defines the Down state region. The Jacobian at this point is

$$J_{A_{Down}} = \begin{pmatrix} \dfrac{-1 + JX}{\tau} & 0 & 0 \\ K(1-X) & -\dfrac{1}{\tau_f} & 0 \\ LX & 0 & -\dfrac{1}{\tau_r} \end{pmatrix}. \tag{S5.7}$$

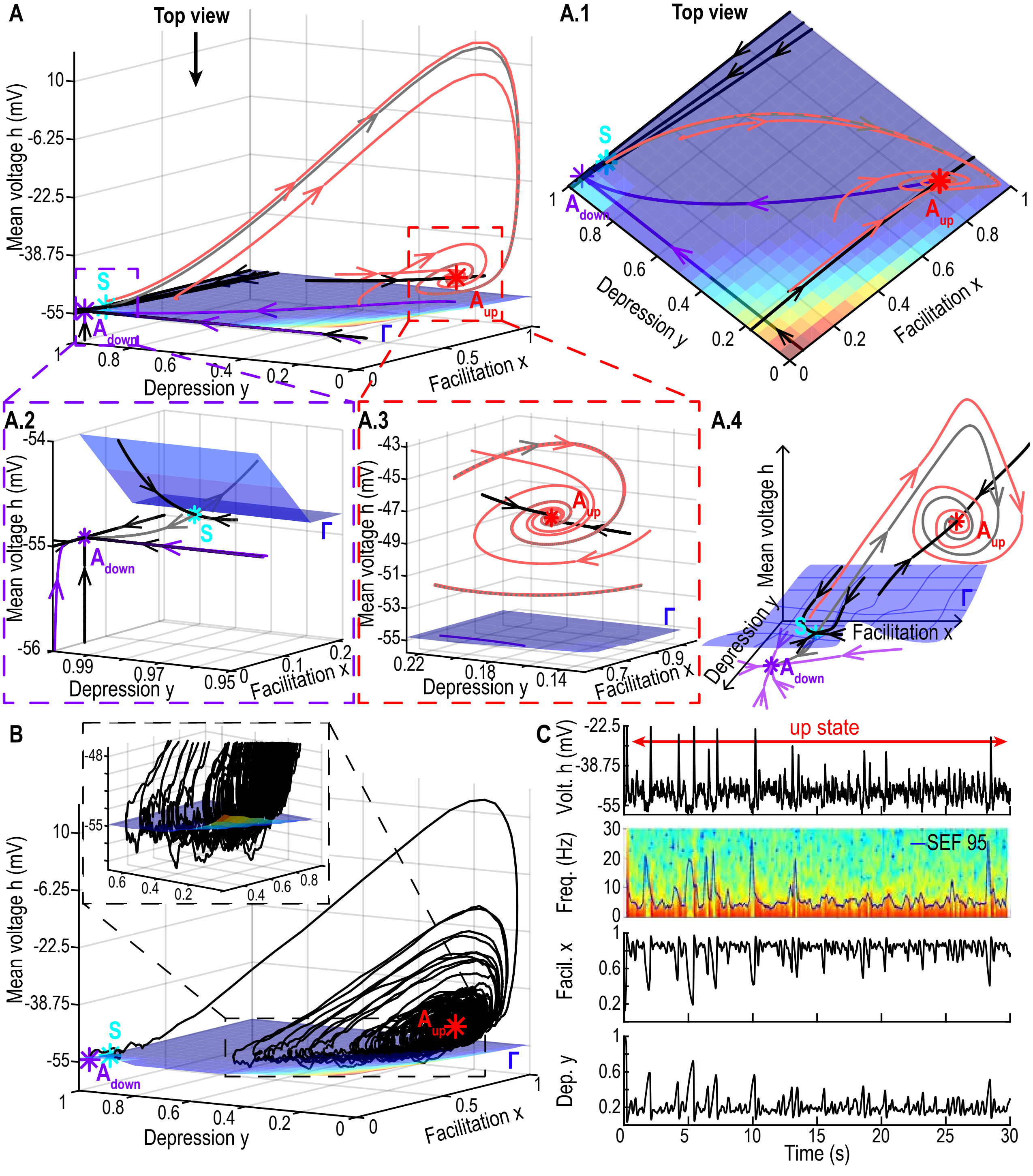

Figure S5.7: **Phase-space of system** (5.2) **without AHP. A.** 3D phase-space of the system with the two attractors A_{Down} (purple, resp. A_{Up}, red) and saddle-point S (cyan) with its 2-dimensional stable manifold Γ (blue surface) which defines the separatrix. Stable trajectories (black curves) and unstable manifold of S (grey) and deterministic trajectories starting below (purple, resp. above light red) Γ falling to A_{Down} (resp. A_{Up}). Top view (A.1), inset around A_{Down} and S (A.2), inset around A_{Up} where deterministic trajectories oscillate at their eigenfrequency ω_{Up} (light red, A.3), schematic summary of the entire phase-space (A.4). **B.** Stochastic trajectory lasting $T = 30s$ with $\sigma = 10$ starting at A_{Down} and oscillating around A_{Up}. **C.** (h, x, y)-time series of a stochastic trajectory, with the spectrogram of the mean voltage h and SEF95 (blue curve).

The eigenvalues are $\left(\lambda_1^{A_{Down}}, \lambda_2^{A_{Down}}, \lambda_3^{A_{Down}}\right) = \left(\frac{JX-1}{\tau}, -\frac{1}{\tau_f}, -\frac{1}{\tau_r}\right)$. When the connectivity J varies in the range $[5.6, 8.6]$, the attractor A_{Down} is a stable-node since the first eigenvalue is negative as long as $J \leq \frac{1}{X} \approx 16.67$. For $J \in [5.6, 8.6], \tau = 0.025s, \tau_f = 0.3s, \tau_r = 0.5s$ and the parameter values of Table 5.1, we obtain that $\lambda_1^{A_{Down}} \in [-19, -27]$, $\lambda_2^{A_{Down}} \approx -3.33$ and $\lambda_3^{A_{Down}} \approx -2$. The dynamics at this point is identical for the systems exhibiting AHP or not.

Up state attractor A_{Up}

The second critical point (fig. S5.7A and S5.8A, red) is obtained by solving

$$\begin{aligned} x_{Up} &= \frac{\tau_f K(J+1) + LX\tau_r + \sqrt{\Delta}}{2(J\tau_f K + L\tau_r)} \\ y_{Up} &= \frac{1}{Jx_{Up}} \\ h_{Up} &= T + T_0 + \frac{x_{Up} - X}{\tau_f K(1 - x_{Up})}, \end{aligned} \tag{S5.8}$$

where

$$\Delta = (\tau_f K(J+1) + LX\tau_r)^2 - 4(J\tau_f K + L\tau_r)\tau_f K. \tag{S5.9}$$

The dynamics around this point depends on whether the system exhibits AHP or not, we will now describe these two cases.

1. **Neuronal network without AHP:** For that system, the resting membrane potential T_0 and the recovery timescale τ_0 of the mean voltage h are constant in the entire phase-space. The numerical range of values for the position of the critical point A_{Up} for $J \in [5.6, 8.6], \tau = 0.01s, \tau_f = 0.2s, \tau_r = 0.12s$ and parameters values from Table 5.1 is $A_{Up} = (h_{A_{Up}} \in [73.15, 124.59]$, $x_{A_{Up}} \in [0.83, 0.89]$, $y_{A_{Up}} \in [0.22, 0.13])$. The Jacobian at this point is

$$J_{A_{Up}} = \begin{pmatrix} 0 & \frac{Jy_{Up}(h_{Up} - T - T_0)^+}{\tau_0} & \frac{Jx_{Up}(h_{Up} - T - T_0)^+}{\tau_0} \\ K(1 - x_{Up}) & -\frac{1}{\tau_f} - K(h_{Up} - T - T_0)^+ & 0 \\ -\frac{L}{J} & -Ly_{1,2}(h_{Up} - T - T_0)^+ & -\frac{1}{\tau_r} - Lx_{Up}(h_{Up} - T - T_0)^+. \end{pmatrix} \tag{S5.10}$$

   With the present parameters, $J_{A_{Up}}$ has one real negative and two complex conjugate eigenvalues with negative real part thus A_{Up} is a stable-focus: $\lambda_1^{A_{Up}} \in [-55.71, -79.40]$ for the real eigenvalue and the two complex conjugate eigenvalues are

$$\lambda_{2,3}^{A_{Up}} \in [-6.16, -14.73] \pm i[36.78, 51.87].$$

2. **Neuronal network exhibiting AHP:** the Up state attractor A_{Up} is situated in the subspace of medium dynamics with hyperpolarization Ω_{mAHP} (fig. S5.8A-B, orange) where $T_0 = T_{AHP} = -30$

and $\tau_0 = \tau_{m,AHP} \in [0.06, 0.3]$s. For $J \in [5.6, 8.6], \tau = 0.025s, \tau_f = 0.3s, \tau_r = 0.5s$ the position of A_{Up} is now $A_{Up} = \left(h_{A_{Up}} \in [-0.74, 19.84], x_{A_{Up}} \in [0.83, 0.89], y_{A_{Up}} \in [0.22, 0.13]\right)$. Here, the eigenvalues of $J_{A_{Up}}$ are real and negative, thus for the system with AHP A_{Up} is a stable-node. The numerical values are now $\lambda_1^{A_{Up}} \in [-34.01, -43.96]$, $\lambda_2^{A_{Up}} \in [-11.67, -18.94]$ and $\lambda_3^{A_{Up}} \in [-3.96, -3.65]$.

Saddle-point S

The third critical point S (fig. S5.7A and S5.8A, cyan) is solution of equations

$$\begin{aligned} x_S &= \frac{\tau_f K(J+1) + LX\tau_r - \sqrt{\Delta}}{2(J\tau_f K + L\tau_r)} \\ y_S &= \frac{1}{Jx_S} \\ h_S &= T + T_0 + \frac{x_S - X}{\tau_f K(1 - x_S)}, \end{aligned} \tag{S5.11}$$

for $J \in [5.6, 8.6], \tau = 0.01s, \tau_f = 0.2s, \tau_r = 0.12s$ and the parameters are presented in Table 5.1, we get $A_S = (h_S \in [2.52, 1.08], x_S \in [0.18, 0.12], y_S \in [0.97, 0.99])$. The Jacobian at S does not depend on whether the system exhibits AHP or not and it has one real positive and two real negative eigenvalues, it is thus a saddle-node with an unstable manifold of dimension one and a stable manifold of dimension two. With the present parameters, we obtain $\lambda_1^S \in [-28.80, -25.03]$, $\lambda_2^S \in [18.96, 16.08]$ and $\lambda_3^S \in [-4.89, -4.97]$. Finally, the stable two-dimensional manifold Γ defines the separatrix between the basins on attraction of Down A_{Down} and Up A_{Up} states.

Numerical construction of the separatrix

To represent the stable manifold Γ of the saddle-point S, we use the following algorithm based on numerical approximations (figs. S5.7A-B and S5.8A-B, blue surface). Since Γ defines the separatrix between the two basins of attraction for the attractors A_{Down} and A_{Up}, we ran simulations of the noiseless dynamics for $\sigma = 0$ of system (5.2) with the initial condition sampling the entire phase space. We used grid points $(h_i, x_i, y_i) \in [-35, 500] \times [0, 1], \times[0, 1])$ with $\delta_h = 1, \delta_x = \delta_y = 0.05$. Each initial point was then attributed to the basin of attraction of the attractor at which the corresponding trajectory ended. The separatrix Γ is defined as the border between the set of initial points falling into the basin of A_{Down} and those falling into the basin of A_{Up}.
This separatrix does not define a bounded domain for neither attractor but rather separates the entire phase-space in two subdomains, one above Γ leading to the Up state and the other one below Γ to the Down state.

5.4.3 Segmentation of the time-series to detect Up and Down states

To determine whether the neuronal population is in an Up or a Down state, we segmented the simulated time-series according to the following criteria:

- the Up states are defined in the subspace $\{x \geq x_{Up} = 0.5\&h \leq h_{Up} = 0.175h_{max}\}$,

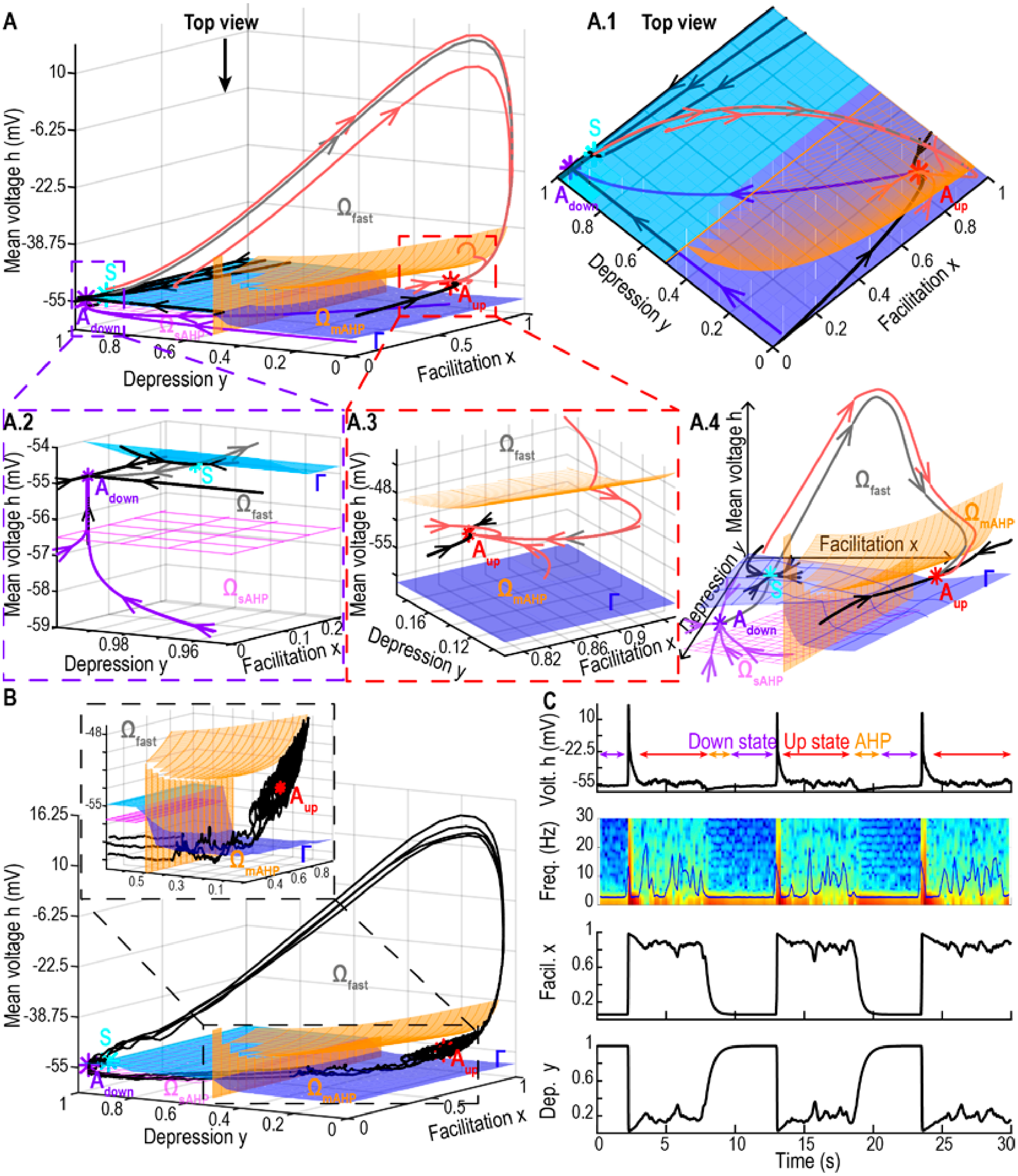

Figure S5.8: **Phase-space of system** (5.2) **with AHP. A.** 3D phase-space of system (5.2) with the two attractor points A_{Down} (purple), A_{Up} (red) and the saddle-point S (cyan) with its 2-dimensional stable manifold Γ (blue surface) which defines the separatrix. Stable trajectories (black curves) and unstable manifold of S (grey) and deterministic trajectories starting below (purple, resp. above light red) Γ falling to A_{Down} (resp. A_{Up}). The phase-space is separated into 3 subspaces defining the different dynamics: fast Ω_{fast} (above pink and orange meshes), medium Ω_{mAHP} (below the orange mesh) and slow Ω_{sAHP} (below the pink mesh). Top view (A.1), inset around A_{Down} and S (A.2), inset around A_{Up} (A.3), schematic summary of the entire phase-space (A.4). **B.** Stochastic trajectory lasting $T = 30s$ with $\sigma = 10$ starting at A_{Down} and oscillating between A_{Up} and A_{Down}. **C.** (h, x, y)-time series of a stochastic trajectory, with the spectrogram of the mean voltage h and SEF95 (blue curve).

- the Down states are defined when $\{y \geq y_{Down} = 0.95\}$

We added the threshold on h for the Up state detection because we do not want to count the bursts, defining the transition from Down to Up, as an Up state.
To determine the proportion of time spent in Up vs Down state for one neuronal population with AHP (fig. 3C-D, main text), we ran simulations of system (5.2) with AHP for $N = 100$ trajectories of duration $T = 600s$ with $J \in \{5.6, 6.6, 7.6\}$ and $\sigma = 14$.
Similarly, for the model (5.4) with two populations (fig. 4B-D, main text), we segmented the time-series of the excitatory population for $N = 100$ trajectories of duration $T = 600s$.
Finally for the three population network (5.5), we segmented the time-series of the excitatory network α without AHP ($N = 100$ trajectories of duration $T = 300s$).

5.4.4 Numerical methods

All simulations were run in Matlab, using Runge-Kutta 4 scheme with a time step $\Delta t = 0.005$s. We also tried $\Delta t = 0.001$s and obtained the same results, thus ensuring stability.

Discussion and perspectives

In this PhD, I have introduced and analyzed a new model of neuronal bursting which accounts for a refractory AHP period after the bursts. The mathematical analysis of the deterministic model allowed to find formulas for the burst and AHP durations (section 1.2) and the stochastic analysis of the model driven by a small noise term revealed several novel phenomena: 1) the peaked distribution of burst duration comes from the confined exit points on the separatrix (section 1.1.3), 2) the noise induces a shift in the attractor's position that I could characterize in a generic framework (section 3.3) and 3) in the case of a shallow field close to the peak of the exit point location, exiting the basin of attraction is not sufficient to escape, thus revealing a novel escape pattern composed of many round-trips in and out of the basin of attraction before a definitive escape (chapter 2 and section 3.4). Finally I have shown how simulations of this model, combined with statistical time-series analysis could help understand the mechanisms underlying neuron-glia interactions (chapter 4), and I proposed an oscillatory mechanism in the brain during general anesthesia (chapter 5). I will discuss below some remaining open questions and perspectives for my future work.

6.1 Computation of the stochastic separatrix associated to the recurrent exit pattern *(chapter 2 and section 3.4)*

Escape from an attractor usually ends when trajectories hit the boundary of the basin of attraction for the first time. However, as we have seen in chapter 2 there are exceptions where trajectories can re-enter multiple times in the basin before escaping to infinity. In this case, the first passage time through the deterministic separatrix Γ (fig. 6.1A-B cyan curve) delimiting the basin of attraction is not sufficient to characterize the full escape time. Instead, we propose to account for the recurrent entries by extending the basin of attraction through the addition of a bounded region where trajectories can re-enter with high probability (fig. 6.1A see also section 2.2 page 80). Numerical simulations suggest that the boundary C could be defined by the maximal distance of the stochastic reentering trajectories to the separatrix Γ (fig. 6.1A red curve). In this added region, the trajectories have a very low probability to escape, while on the other side they almost surely escape to infinity thus defining a stochastic separatrix that I propose to characterize.

The stochastic separatrix is defined as the external boundary of all possible exiting trajectories conditioned to a return inside the basin in a finite time. For the stochastic process X_t satisfying the stochastic differential equation $X_t = b(X_t)dt + \sigma dW_t$ where b is the deterministic drift, σ the noise amplitude and W_t a standard Wiener process, the trajectories starting at the separatrix Γ and conditioned to return inside the basin define a stochastic bridge process

$$\hat{X}_t := (X_t | X_0 \in \Gamma \text{ and } X_{T_{rt}} \in \Gamma), \tag{6.1}$$

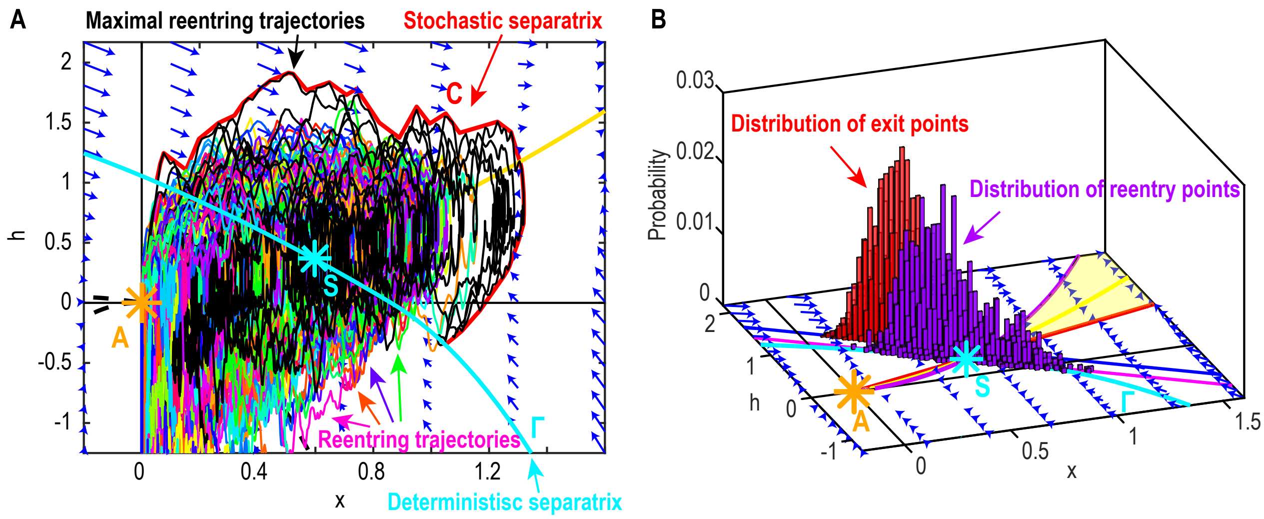

Figure 6.1: **A.** Trajectories reentering the basin of attraction of A (yellow) by crossing multiple times the deterministic separatrix Γ (cyan). The trajectories with the maximal distances to Γ (black) define the stochastic separatrix C (red). **B.** The distributions of the exit (resp. reentry) points on the deterministic separatrix Γ (red, resp. purple) are peaked close to the saddle-point S (cyan star).

where T_{rt} is the time to return to Γ. However, there are several difficulties compared to the classical study of Brownian or Ornstein-Uhlenbeck bridges [212–214] starting with the fact that here, the drift b is nonlinear. In addition, the recurrent exit pattern occurs in dimensions ≥ 2 and we do not condition the stochastic process X_t to start at (respectively, return to) a specific location but rather, at any point of the deterministic separatrix Γ. Thus, we will need to integrate over the whole distribution of exit (respectively, reentry) points (fig. 6.1B), that we can determine by solving the corresponding FPE. However, an option to overcome this difficulty could be to consider the stochastic process $D_t := d(X_t, \Gamma)$ of the distance between X_t and Γ conditioned to start at (respectively return to) 0:

$$\hat{D}_t := \left(D_t | D_0 = 0 \text{ and } D_{T_{rt}} = 0\right). \tag{6.2}$$

In either case, we will then need to integrate over all possible return times $T_{rt} \geq 0$. To do so, we first need to determine the distribution of return times and to show that it is peaked with a finite mean and fast enough decay to infinity. Then we will need to define the ensemble $C := max\left(\hat{D}_t\right)$ of the maximum distances to the separatrix from the ensemble of re-entering trajectories wich will define the stochastic separatrix. Finally, we will need to show that the MFPT for trajectories crossing C is equivalent to the mean escape time computed using Baye's law accounting for all RTs around the deterministic separatrix (sections 2.2 and 3.7).

To conclude, this open question suggests that the definition of the basin of attraction can differ in the stochastic case compared to the deterministic one in a similar fashion to the stochastic attractor, which is shifted compared to its deterministic position (section 3.3). Similarly, it would be interesting to understand the dependency of this difference with respect to the noise amplitude σ.

6.2 Image analysis, clustering and modeling to further investigate neuron-glia interactions *(chapter 4)*

6.2.1 Analysis and clustering of in vivo calcium imaging from astrocyte activity

In order to further understand how astrocytes regulate neuronal activation, I collaborate with the group of Neuroglial Interactions in Cerebral Physiopathology, under the direction of Prof. N. Rouach in Collège de France. We work on in vivo data of astrocyte activity from freely behaving mice. The data consists of long video recordings ($> 1h$) of fluorescent Ca^{2+} activity. This results in noisy and very heavy data which is difficult to process. I currently work on a data analysis pipeline to segment the images into ROIs and extract their time-series. The goal is to build a classification algorithm that will automatically detect the different types of Ca^{2+} events. There are two main difficulties: 1) the choice of features that need to separate the data well enough while being as concise as possible and 2) the choice of a good metric to assess for the distance between each point (i.e. each event) in the feature space. I propose to summarize the video event features in a single image to preserve the importance of the spatial information. Thus, I need to find a relevant distance to compare images. A good option could be the Earth mover's distance (also known as the Wasserstein metric) which is defined in the optimal transport theory [215,216]. It is a natural way to compare probability distributions [217] and it can be used for multi-dimensional histograms [218] which makes it very suitable for image comparison. Preliminary results indicate that these choices could lead to a good classification of the events.

Finally, the question of the biological interpretation of these clusters remains open. In order to examine this question, I will confront the clustering results to the electrophysiological activity of the neurons that was recorded simultaneously. I shall assess the neuronal activity through the spectral analysis of the electrophysiological time-series. Altogether this project aims at understanding the correlation and causality between neuronal and astrocytic activities.

6.2.2 Development of a detailed neuron-glia network model

To conclude this section about investigation of neuron-glia interactions, I propose to build a detailed model of a neuron-astrocyte network based on the extension of the tri-compartment model introduced in [50,51] which represents the regulation of extracellular K^+ by accounting for the neuronal, extracellular and astrocytic ionic concentrations. The goal here is to extend the equations into a two-dimensional network by connecting together many such tri-partite compartments (fig. 6.2). The neurons will be modeled using the Hodgkin-Huxley formalism to which we shall add equations to account for synaptic short term plasticity and they will be connected together through electrical synapses. Astrocytes uptake the extracellular K^+ released by the neurons through channels called $Kir4.1$ (fig. 6.2, dark green) and they regulate their intracellular ionic concentrations through gap junctions that we will model with the Goldman-Hodgkin-Katz equation. Finally the ionic diffusion through the extracellular space will be modeled using Fick's law.

The challenge in this project is to find the correct parameters values and connectivity matrices between the different compartments, which is difficult given the high dimensionality of the model. Another difficulty is the cost of computations, especially since we want to model large-scale networks to assess how astrocytes redistribute K^+ over long distances. Ultimately it would be very interesting to derive from this high dimensional model a mean field version, which would explicitly account for the astrocytes K^+ regulation but would be reduced in lower dimension and thus much easier to analyze and simulate.

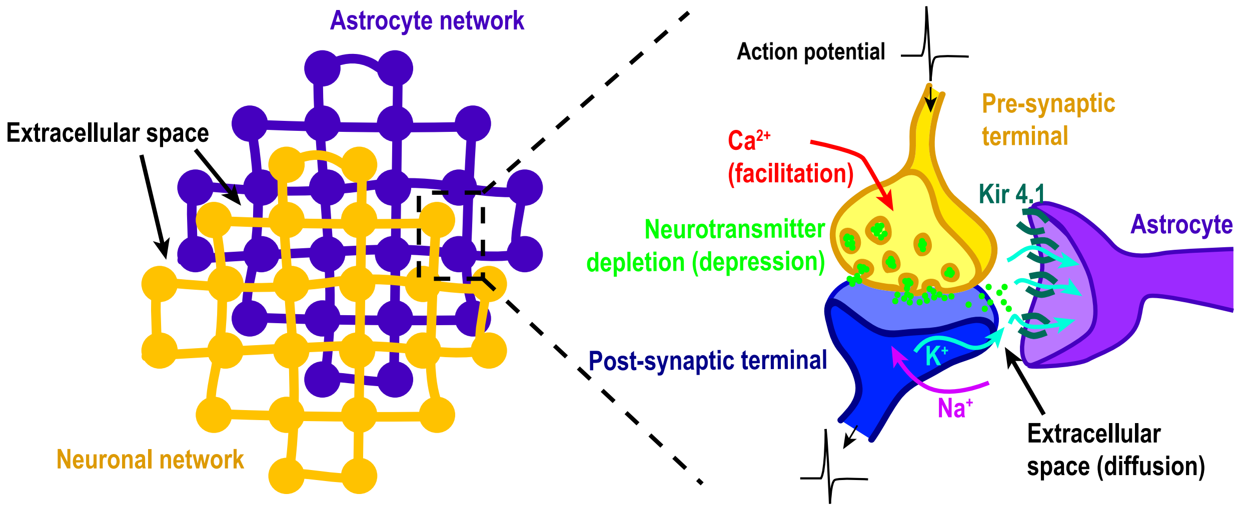

Figure 6.2: Schematic of the tri-compartment network model. Left: the neurons (yellow) are connected together through electrical synapses, astrocytes (purple) are connected through gap junctions and ions can diffuse in the extracellullar space (white). Right: inset on a tripartite synapse, astrocytes regulate the extracellular K^+ released by the neurons through Kir 4.1 channels (dark green).

6.3 Interdisciplinary study of the underlying mechanisms involved in the genesis and maintenance of brain rhythms *(chapter 5)*

I presented in chapter 5 a multi-scale model of the thalamo-cortical loop that could account for the emergence and fragmentation of the α-band associated to the proportion of time spent in Up vs Down states. Currently, we are working with a team of electrophysiologists to design experiments that would validate the model's predictions.

Following up on this new collaboration there are different paths I would like to explore. First, the question of causality remains unexplained: how is the suppression of the α-band connected with the burst-suppression that follows [144]? Understanding the mechanisms underlying this causality could help build tools to prevent unwanted effects such as burst-suppressions resulting from a too deep anesthesia. Furthermore, these results could find other applications such as predicting the occurrence of an epilepsy seizure or a stroke. To this end, we will need to extend the thalamo-cortical loop model which does not account for this causality so far.

Another path I want to explore is to adapt the model to the study other neuronal rhythms such as the θ-oscillation observed during REM sleep [32, 33] or the fast γ-oscillations [33, 34, 36] involved in memory encoding. Indeed, we found that the frequency of oscillations in the Up state is an increasing function of the network connectivity (fig. 5.2B-C) and that it also depends on the synaptic properties (fig. S5.1 and section 5.2.5). It would be interesting to verify experimentally these predictions and then to explore with numerical simulations of the thalamo-cortical loop model how these mechanisms affect the genesis and maintenance of the oscillations for each frequency range. More generally, it would be very interesting to investigate the physiological similarities or differences of the mechanisms underlying the genesis of the different oscillatory frequencies.

Acronyms

Ca^{2+} Calcium. 10, 12, 13, 17, 127, 175

K^+ Potassium. 13, 15, 17, 114, 123, 126–128, 154, 174, 175

Na^+ Sodium. 10, 175

aEIF Exponential adaptative integrate and fire. 15, 175

AHP Afterhyperpolarization. 6, 13, 21, 34, 43, 44, 46, 48, 50, 52, 54, 56, 58, 60, 62, 64, 66, 68, 70, 115, 120, 121, 123, 126, 128, 130, 131, 144, 155, 175

AMPA α-amino-3-hydroxy-5-methyl-4-isoxazolepropionic acid. 118, 154, 175

AMPAR AMPA receptor. 118, 126, 127, 175

ATP adénosine triphosphate. 154, 175

Cx Connexin. 15, 115, 116, 118, 121, 126, 128, 175

EEG Electroencephalogram. 13, 36, 141, 147, 155, 175

EMD Earth mover's distance. 175

fEPSP Field electrophysiological post-synaptic potential. 117, 119, 129, 175

FPE Fokker-Planck equation. 19, 21, 29, 50, 95, 175

GABA γ-aminobutyric acid. 15, 16, 154, 175

GABAAR GABA A receptor. 127, 175

GJ Gap junctions. 115, 120, 123, 126–128, 175

HH Hodgkin-Huxley. 15, 174, 175

IBI Interburst interval. 6, 10, 11, 13, 21, 34, 44, 68, 120, 121, 128, 132, 175

IF Integrate and fire. 15, 175

KCNQ Low-threshold voltage-gated K^+ channels (also known as M-channels). 114, 123, 126, 128, 175

KO Knockout. 35, 175

LIF Leaky integrate and fire. 15, 175

MEA Multi-electrode array. 11, 132, 175

MFPT Mean first passage time. 77, 173, 175

MMOs Mixed-mode oscillations. 17, 175

NBQX 2,3-dioxo-6-nitro-7-sulfamoyl-benzo[f]quinoxaline (AMPA receptor antagonist). 120, 126, 175

NMDA N-Methyl-D-aspartic acid. 118, 175

NMDAR NMDA receptor. 126, 175

NREM Non-rapid eye motion (also known as paradoxical sleep). 175

pdf Probability density function. 27, 29, 31, 50, 95, 99, 175

PSD Power spectral density. 121, 175

QP Quiescent phase. 21, 28, 35, 44, 68, 120, 175

REM Rapid eye motion (also know as paradoxical sleep). 13, 38, 175

ROI Region of interest. 174, 175

RRP Readily-releasable pool. 12, 175

RT Round trips. 33, 78, 106, 108, 173, 175

SDE Stochastic differential equation. 175

STP Short-term synaptic plasticity. 12, 18, 19, 175

WKB Wentzel-Kramers-Brillouin. 21, 29, 51, 95, 175

WT Wild type. 35, 123, 175

Bibliography

[1] K. D. Piatkevich, S. Bensussen, H.-A. Tseng, S. N. Shroff, V. G. Lopez-Huerta, D. Park, E. E. Jung, O. A. Shemesh, C. Straub, H. J. Gritton, *et al.*, “Population imaging of neural activity in awake behaving mice,” *Nature*, vol. 574, no. 7778, pp. 413–417, 2019.

[2] H. Jahnsen and R. Llinás, “Ionic basis for the electro-responsiveness and oscillatory properties of guinea-pig thalamic neurones in vitro,” *The Journal of physiology*, vol. 349, no. 1, pp. 227–247, 1984.

[3] J. E. Lisman, “Bursts as a unit of neural information: making unreliable synapses reliable,” *Trends in neurosciences*, vol. 20, no. 1, pp. 38–43, 1997.

[4] J. Smith, H. Ellenberger, K. Ballanyi, D. Richter, and J. Feldman, “Pre-bötzinger complex: a brainstem region that may generate respiratory rhythm in mammals,” *Science*, vol. 254, pp. 726–729, November 1991.

[5] Y. Cui, K. Kam, D. Sherman, W. A. Janczewski, Y. Zheng, and J. L. Feldman, “Defining pre-bötzinger complex rhythm- and pattern-generating neural microcircuits in vivo,” *Neuron*, vol. 91, pp. 602–614, August 2016.

[6] E. Marder, D. Bucher, D. J. Schulz, and A. L. Taylor, “Invertebrate central pattern generation moves along,” *Current Biology*, vol. 15, pp. R685–R699, September 2005.

[7] M. Avoli, M. D’Antuono, J. Louvel, R. Köhling, G. Biagini, R. Pumain, G. D’Arcangelo, and V. Tancredi, “Network and pharmacological mechanisms leading to epileptiform synchronization in the limbic system in vitro,” *Progress in neurobiology*, vol. 68, no. 3, pp. 167–207, 2002.

[8] J. Schiller, G. Major, H. J. Koester, and Y. Schiller, “Nmda spikes in basal dendrites of cortical pyramidal neurons,” *Nature*, vol. 404, no. 6775, pp. 285–289, 2000.

[9] F. Zeldenrust, W. J. Wadman, and B. Englitz, “Neural coding with bursts—current state and future perspectives,” *Frontiers in Computational Neuroscience*, vol. 12, p. 48, July 2018.

[10] E. M. Izhikevich, “Bursting (scholarpedia),” 2006.

[11] K. J. Staley, M. Longacher, J. S. Bains, and A. Yee, “Presynaptic modulation of ca3 network activity,” *Nature neuroscience*, vol. 1, no. 3, pp. 201–209, 1998.

[12] C. Verderio, A. Bacci, S. Coco, E. Pravettoni, G. Fumagalli, and M. Matteoli, “Astrocytes are required for the oscillatory activity in cultured hippocampal neurons,” *European Journal of Neuroscience*, vol. 11, pp. 2793–2800, April 1999.

[13] D. Cohen and M. Segal, "Homeostatic presynaptic suppression of neuronal network bursts," *Journal of Neurophysiology*, vol. 101, pp. 2077–2088, January 2009.

[14] D. F. de Sevilla, J. Garduño, E. Galván, and B. Washington, "Calcium-activated afterhyperpolarizations regulate synchronization and timing of epileptiform bursts in hippocampal ca3 pyramidal neurons," *Journal of Neurophysiology*, vol. 96, pp. 3028–3041, December 2006.

[15] C. F. Stevens and Y. Wang, "Facilitation and depression at single central synapses," *Neuron*, vol. 14, no. 4, pp. 795–802, 1995.

[16] H. Markram and M. Tsodyks, "Redistribution of synaptic efficacy between neocortical pyramidal neurons," *Nature*, vol. 382, no. 6594, pp. 807–810, 1996.

[17] G.-q. Bi and M.-m. Poo, "Synaptic modification by correlated activity: Hebb's postulate revisited," *Annual review of neuroscience*, vol. 24, no. 1, pp. 139–166, 2001.

[18] P. Finlayson and M. Cynader, "Synaptic depression in visual cortex tissue slices: an in vitro model for cortical neuron adaptation," *Experimental Brain Research*, vol. 106, no. 1, pp. 145–155, 1995.

[19] W. Betz, "Depression of transmitter release at the neuromuscular junction of the frog," *The Journal of physiology*, vol. 206, no. 3, pp. 629–644, 1970.

[20] D. Swandulla, M. Hans, K. Zipser, and G. J. Augustine, "Role of residual calcium in synaptic depression and posttetanic potentiation: fast and slow calcium signaling in nerve terminals," *Neuron*, vol. 7, no. 6, pp. 915–926, 1991.

[21] W. G. Regehr, K. R. Delaney, and D. W. Tank, "The role of presynaptic calcium in short-term enhancement at the hippocampal mossy fiber synapse," *Journal of Neuroscience*, vol. 14, no. 2, pp. 523–537, 1994.

[22] A. Ghanbari, A. Malyshev, M. Volgushev, and I. H. Stevenson, "Estimating short-term synaptic plasticity from pre-and postsynaptic spiking," *PLoS computational biology*, vol. 13, no. 9, p. e1005738, 2017.

[23] B. Pakkenberg, D. Pelvig, L. Marner, M. J. Bundgaard, H. J. G. Gundersen, J. R. Nyengaard, and L. Regeur, "Aging and the human neocortex," *Experimental gerontology*, vol. 38, no. 1-2, pp. 95–99, 2003.

[24] R. J. Butera, J. Rinzel, and C. Smith, Jeffrey, "Models of respiratory rhythm generation in the pre-bötzinger complex. i. bursting pacemaker neurons," *Journal of Neurophysiology*, vol. 82, pp. 382–397, July 1999.

[25] R. J. Butera, J. Rinzel, and C. Smith, Jeffrey, "Models of respiratory rhythm generation in the pre-bötzinger complex. ii. populations of coupled pacemaker neurons," *Journal of Neurophysiology*, vol. 82, pp. 398–415, July 1999.

[26] C. Del Negro, S. M. Johnson, R. J. Butera, and C. Smith, Jeffrey, "Models of respiratory rhythm generation in the pre-bötzinger complex. iii. experimental tests of model predictions," *Journal of Neurophysiology*, vol. 86, pp. 59–74, July 2001.

[27] O. Garaschuk, R.-I. Milos, C. Grienberger, N. Marandi, H. Adelsberger, and A. Konnerth, "Optical monitoring of brain function in vivo: from neurons to networks," *Pflügers Archiv*, vol. 453, no. 3, pp. 385–396, 2006.

[28] R. Cossart, D. Aronov, and R. Yuste, "Attractor dynamics of network up states in the neocortex," *Nature*, vol. 423, no. 6937, pp. 283–288, 2003.

[29] G. M. Shepherd, *The synaptic organization of the brain.* Oxford university press, 2004.

[30] P. L. Purdon, A. Sampson, K. J. Pavone, and E. N. Brown, "Clinical electroencephalography for anesthesiologists: part i: background and basic signatures," *Anesthesiology*, vol. 123, no. 4, pp. 937–960, 2015.

[31] E. N. Brown, R. Lydic, and N. D. Schiff, "General anesthesia, sleep, and coma," *New England Journal of Medicine*, vol. 363, no. 27, pp. 2638–2650, 2010.

[32] G. Buzsáki, "Theta oscillations in the hippocampus," *Neuron*, vol. 33, no. 3, pp. 325–340, 2002.

[33] S. M. Montgomery, A. Sirota, and G. Buzsáki, "Theta and gamma coordination of hippocampal networks during waking and rapid eye movement sleep," *Journal of Neuroscience*, vol. 28, no. 26, pp. 6731–6741, 2008.

[34] G. Buzsaki, *Rhythms of the Brain.* Oxford University Press, 2006.

[35] T. Akam and D. M. Kullmann, "Oscillatory multiplexing of population codes for selective communication in the mammalian brain," *Nature Reviews Neuroscience*, vol. 15, no. 2, pp. 111–122, 2014.

[36] D. Zakharov, M. Krupa, and B. Gutkin, "Modeling dopaminergic modulation of clustered gamma rhythms," *Communications in Nonlinear Science and Numerical Simulation*, vol. 82, p. 105086, 2020.

[37] M. Chalk, B. Gutkin, and S. Deneve, "Neural oscillations as a signature of efficient coding in the presence of synaptic delays," *Elife*, vol. 5, p. e13824, 2016.

[38] E. C. McKiernan and D. F. Marrone, "Ca1 pyramidal cells have diverse biophysical properties, affected by development, experience, and aging," *PeerJ*, vol. 5, p. e3638, September 2017.

[39] A. V. Tzingounis, M. Kobayashi, K. Takamatsu, and R. A. Nicoll, "Hippocalcin gates the calcium activation of the slow afterhyperpolarization in hippocampal pyramidal cells," *Neuron*, vol. 53, pp. 487–493, February 2007.

[40] A. V. Tzingounis and R. A. Nicoll, "Contribution of kcnq2 and kcnq3 to the medium and slow afterhyperpolarization currents," *Proceedings of the National Academy of Sciences*, vol. 105, pp. 19974–19979, December 2008.

[41] A. Verkhratsky and A. Butt, *Glial physiology and pathophysiology.* John Wiley & Sons, 2013.

[42] M. R. Freeman and D. H. Rowitch, "Evolving concepts of gliogenesis: a look way back and ahead to the next 25 years," *Neuron*, vol. 80, no. 3, pp. 613–623, 2013.

[43] B. A. Barres, "The mystery and magic of glia: a perspective on their roles in health and disease," *Neuron*, vol. 60, no. 3, pp. 430–440, 2008.

[44] N. J. Allen and B. A. Barres, “Glia—more than just brain glue,” *Nature*, vol. 457, no. 7230, pp. 675–677, 2009.

[45] G. Perea, M. Navarrete, and A. Araque, “Tripartite synapses: astrocytes process and control synaptic information,” *Trends in neurosciences*, vol. 32, no. 8, pp. 421–431, 2009.

[46] G. Dallérac, O. Chever, and N. Rouach, “How do astrocytes shape synaptic transmission? insights from electrophysiology,” *Frontiers in cellular neuroscience*, vol. 7, p. 159, 2013.

[47] C. Giaume, A. Koulakoff, L. Roux, D. Holcman, and N. Rouach, “Astroglial networks: a step further in neuroglial and gliovascular interactions,” *Nature Reviews Neuroscience*, vol. 11, no. 2, pp. 87–99, 2010.

[48] F. Amzica, M. Massimini, and A. Manfridi, “Spatial buffering during slow and paroxysmal sleep oscillations in cortical networks of glial cells in vivo,” *Journal of Neuroscience*, vol. 22, no. 3, pp. 1042–1053, 2002.

[49] U. Pannasch and N. Rouach, “Emerging role for astroglial networks in information processing: from synapse to behavior,” *Trends in neurosciences*, vol. 36, no. 7, pp. 405–417, 2013.

[50] J. Sibille, K. Dao Duc, D. Holcman, and N. Rouach, “The neuroglial potassium cycle during neurotransmission: Role of kir4.1 channels,” *PLoS Computational Biology*, vol. 11, March 2015.

[51] N. Rouach, K. D. Duc, J. Sibille, and D. Holcman, “Dynamics of ion fluxes between neurons, astrocytes and the extracellular space during neurotransmission,” *Opera Medica et Physiologica*, vol. 4, no. 1, 2018.

[52] O. Chever, E. Dossi, U. Pannasch, M. Derangeon, and N. Rouach, “Astroglial networks promote neuronal coordination,” *Science signaling*, vol. 9, January 2016.

[53] A. Wallraff, R. Köhling, U. Heinemann, M. Theis, K. Willecke, and C. Steinhäuser, “The impact of astrocytic gap junctional coupling on potassium buffering in the hippocampus,” *Journal of Neuroscience*, vol. 26, no. 20, pp. 5438–5447, 2006.

[54] U. Pannasch, M. Derangeon, O. Chever, and N. Rouach, “Astroglial gap junctions shape neuronal network activity,” *Communicative & integrative biology*, vol. 5, no. 3, pp. 248–254, 2012.

[55] L. Lapique, “Recherches quantitatives sur l’excitation electrique des nerfs traitee comme une polarization.,” *Journal of Physiology and Pathololgy*, vol. 9, pp. 620–635, 1907.

[56] A. N. Burkitt, “A review of the integrate-and-fire neuron model: I. homogeneous synaptic input,” *Biological cybernetics*, vol. 95, no. 1, pp. 1–19, 2006.

[57] A. N. Burkitt and G. M. Clark, “Analysis of integrate-and-fire neurons: synchronization of synaptic input and spike output,” *Neural computation*, vol. 11, no. 4, pp. 871–901, 1999.

[58] Y.-H. Liu and X.-J. Wang, “Spike-frequency adaptation of a generalized leaky integrate-and-fire model neuron,” *Journal of computational neuroscience*, vol. 10, no. 1, pp. 25–45, 2001.

[59] N. Brunel and V. Hakim, “Fast global oscillations in networks of integrate-and-fire neurons with low firing rates,” *Neural Computation*, vol. 11, pp. 1621–1671, November 1999.

[60] L. Neltner and D. Hansel, “On synchrony of weakly coupled neurons at low firing rate,” *Neural Computation*, vol. 13, pp. 765–774, April 2001.

[61] R. Brette and W. Gerstner, “Adaptive exponential integrate-and-fire model as an effective description of neuronal activity,” *Journal of neurophysiology*, vol. 94, no. 5, pp. 3637–3642, 2005.

[62] J. Touboul and R. Brette, “Dynamics and bifurcations of the adaptive exponential integrate-and-fire model,” *Biological cybernetics*, vol. 99, no. 4, pp. 319–334, 2008.

[63] A. Buchin, S. Rieubland, M. Häusser, B. S. Gutkin, and A. Roth, “Inverse stochastic resonance in cerebellar purkinje cells,” *PLoS computational biology*, vol. 12, no. 8, p. e1005000, 2016.

[64] E. M. Izhikevich, “Which model to use for cortical spiking neurons?,” *IEEE transactions on neural networks*, vol. 15, no. 5, pp. 1063–1070, 2004.

[65] F. Han, Z. Wang, Y. Du, X. Sun, and B. Zhang, “Robust synchronization of bursting hodgkin–huxley neuronal systems coupled by delayed chemical synapses,” *International Journal of Non-Linear Mechanics*, vol. 70, pp. 105–111, 2015.

[66] Y. Chen, J. Wang, X. Wei, B. Deng, H. Yu, F. Su, and G. Li, “Desynchronization of morris: Lecar network via robust adaptive artificial neural network,” in *Frontier and Future Development of Information Technology in Medicine and Education*, pp. 3531–3536, Springer, 2014.

[67] A. L. Hodgkin and A. F. Huxley, “A quantitative description of membrane current and its application to conduction and excitation in nerve,” *The Journal of physiology*, vol. 117, pp. 500–544, March 1952.

[68] A. Roxin, N. Brunel, and D. Hansel, “Role of delays in shaping spatiotemporal dynamics of neuronal activity in large networks,” *Physical Review Letters*, vol. 94, p. 238103, June 2005.

[69] A. Chizhov, F. Campillo, M. Desroches, A. Guillamon, and S. Rodrigues, “Conductance-based refractory density approach for a population of bursting neurons,” *Bulletin of Mathematical Biology*, vol. 81, pp. 4124–4143, October 2019.

[70] A. Destexhe, A. Babloyantz, and T. J. Sejnowski, “Ionic mechanisms for intrinsic slow oscillations in thalamic relay neurons,” *Biophysical journal*, vol. 65, no. 4, pp. 1538–1552, 1993.

[71] A. Destexhe, T. Bal, D. A. McCormick, and T. J. Sejnowski, “Ionic mechanisms underlying synchronized oscillations and propagating waves in a model of ferret thalamic slices,” *Journal of neurophysiology*, vol. 76, no. 3, pp. 2049–2070, 1996.

[72] S. Ching, A. Cimenser, P. L. Purdon, E. N. Brown, and N. J. Kopell, “Thalamocortical model for a propofol-induced α-rhythm associated with loss of consciousness,” *Proceedings of the National Academy of Sciences*, vol. 107, no. 52, pp. 22665–22670, 2010.

[73] A. E. Soplata, M. M. McCarthy, J. Sherfey, S. Lee, P. L. Purdon, E. N. Brown, and N. Kopell, “Thalamocortical control of propofol phase-amplitude coupling,” *PLoS computational biology*, vol. 13, no. 12, p. e1005879, 2017.

[74] R. FitzHugh, “Impulses and physiological states in theoretical models of nerve membrane,” *Biophysical journal*, vol. 1, no. 6, pp. 445–466, 1961.

[75] J. Nagumo, S. Arimoto, and S. Yoshizawa, "An active pulse transmission line simulating nerve axon," *Proceedings of the IRE*, vol. 50, no. 10, pp. 2061–2070, 1962.

[76] M. Krupa, A. Vidal, M. Desroches, and F. Clément, "Mixed-mode oscillations in a multiple time scale phantom bursting system," *SIAM Journal on Applied Dynamical Systems*, vol. 11, no. 4, pp. 1458–1498, 2012.

[77] A. Tonnelier and W. Gerstner, "Piecewise linear differential equations and integrate-and-fire neurons: Insights from two-dimensional membrane models," *Phys. Rev. E*, vol. 67, p. 021908, Feb 2003.

[78] C. Morris and H. Lecar, "Voltage oscillations in the barnacle giant muscle fiber," *Biophysical journal*, vol. 35, no. 1, pp. 193–213, 1981.

[79] B. Ermentrout and N. Kopell, "Parabolic bursting in an excitable system coupled with a slow oscillation," *SIAM Journal on Applied Mathematics*, vol. 46, pp. 233–253, April 1986.

[80] A. L. Shilnikov and N. F. Rulkov, "Origin of chaos in a two-dimensional map modeling spiking-bursting neural activity," *International Journal of Bifurcation and Chaos*, vol. 13, no. 11, pp. 3325–3340, 2003.

[81] X. Shi and Q. Lu, "Burst synchronization of electrically and chemically coupled map-based neurons," *Physica A*, vol. 388, pp. 2410–2419, June 2009.

[82] R. Lozi, M.-S. Abdelouahab, and G. Chen, "Mixed-mode oscillations based on complex canard explosion in a fractional-order fitzhugh-nagumo model.," *Applied Mathematics and Nonlinear Sciences*, vol. 5, no. 2, pp. 239–256, 2020.

[83] J. Hindmarsh and R. Rose, "A model of neuronal bursting using three coupled first order differential equations," *Proceedings of the Royal Society of London B*, vol. 221, pp. 87–102, March 1984.

[84] J. Rinzel, "Bursting oscillations in an excitable membrane model," in *Ordinary and Partial Differential Equations* (B. D. Sleeman and R. J. Jarvis, eds.), pp. 304–316, Springer Berlin Heidelberg, 1985.

[85] X. Liang, M. Tang, M. Dhamala, and Z. Liu, "Phase synchronization of inhibitory bursting neurons induced by distributed time delays in chemical coupling," *Physical Review E*, vol. 80, p. 066202, December 2009.

[86] K. Tsaneva-Atanasova, H. M. Osinga, T. Rieß, and A. Sherman, "Full system bifurcation analysis of endocrine bursting models," *Journal of theoretical biology*, vol. 264, no. 4, pp. 1133–1146, 2010.

[87] H. Osinga and K. Tsaneva-Atanasova, "Dynamics of plateau bursting depending on the location of its equilibrium," *Journal of neuroendocrinology*, vol. 22, no. 12, pp. 1301–1314, 2010.

[88] W. Teka, K. Tsaneva-Atanasova, R. Bertram, and J. Tabak, "From plateau to pseudo-plateau bursting: Making the transition," *Bulletin of mathematical biology*, vol. 73, no. 6, pp. 1292–1311, 2011.

[89] H. Baldemir, D. Avitabile, and K. Tsaneva-Atanasova, “Pseudo-plateau bursting and mixed-mode oscillations in a model of developing inner hair cells,” *Communications in Nonlinear Science and Numerical Simulation*, vol. 80, p. 104979, 2020.

[90] W. Teka, J. Tabak, and R. Bertram, “The relationship between two fast/slow analysis techniques for bursting oscillations,” *Chaos: An Interdisciplinary Journal of Nonlinear Science*, vol. 22, no. 4, p. 043117, 2012.

[91] J. L. Callot, F. Diener, M. M. Diener, *et al.*, “Chasse au canard (première partie),” *Collectanea Mathematica*, pp. 37–76, 1981.

[92] E. K. Ersöz, M. Desroches, and M. Krupa, “Synchronization of weakly coupled canard oscillators,” *Physica D: Nonlinear Phenomena*, vol. 349, pp. 46–61, 2017.

[93] E. K. Ersöz, M. Desroches, A. Guillamon, J. Rinzel, and J. Tabak, “Canard-induced complex oscillations in an excitatory network,” *Journal of mathematical biology*, vol. 80, no. 7, pp. 2075–2107, 2020.

[94] E. M. Izhikevich and F. Hoppensteadt, “Classification of bursting mappings,” *International Journal of Bifurcation and Chaos*, vol. 14, no. 11, pp. 3847–3854, 2004.

[95] E. M. Izhikevich, *Dynamical Systems in Neuroscience: the Geometry of Excitability and Bursting.* MIT Press, 2007.

[96] M. Golubitsky, K. Josic, and L. Shiau, “Bursting in coupled cell systems,” in *Bursting: The Genesis Of Rhythm In The Nervous System*, ch. 8, pp. 201–222, World Scientific, 2005.

[97] M. Golubitsky, K. Josic, T. Kaper, H. Broer, B. Krauskopf, and G. Vegter, “An unfolding theory approach to bursting in fast-slow systems, in “global analysis of dynamical systems”,” *J Physiol*, pp. 277–308, 2001.

[98] H. M. Osinga, A. Sherman, and K. Tsaneva-Atanasova, “Cross-currents between biology and mathematics: The codimension of pseudo-plateau bursting,” *Discrete and continuous dynamical systems. Series A*, vol. 32, no. 8, p. 2853, 2012.

[99] H. R. Wilson and J. D., “Excitatory and inhibitory interactions in localized populations of model neurons,” *Communications Biology*, vol. 1, pp. 1–24, January 1972.

[100] H. R. Wilson and J. D., “A mathematical theory of the functional dynamics of cortical and thalamic nervous tissue,” *Kybernetik*, vol. 13, pp. 55–80, September 1973.

[101] R. Ben-Yishai, R. L. Bar-Or, and H. Sompolinsky, “Theory of orientation tuning in visual cortex.,” *Proceedings of the National Academy of Sciences*, vol. 92, no. 9, pp. 3844–3848, 1995.

[102] M. V. Tsodyks and H. Markram, “The neural code between neocortical pyramidal neurons depends on neurotransmitter release probability,” *Proc. Natl. Acad. Sci. USA*, vol. 94, pp. 719–723, January 1997.

[103] M. Tsodyks, K. Pawelzik, and H. Markram, “Neural networks with dynamic synapses,” *Neural computation*, vol. 10, no. 4, pp. 821–835, 1998.

[104] J. A. Varela, K. Sen, J. Gibson, J. Fost, L. Abbott, and S. B. Nelson, "A quantitative description of short-term plasticity at excitatory synapses in layer 2/3 of rat primary visual cortex," *Journal of Neuroscience*, vol. 17, no. 20, pp. 7926–7940, 1997.

[105] D. Holcman and M. Tsodyks, "The emergence of up and down states in cortical networks," *PLoS Computational Biology*, vol. 2, pp. 174–181, March 2006.

[106] K. D. Duc, Z. Schuss, and D. Holcman, "Oscillatory decay of the survival probability of activated diffusion across a limit cycle," *Physical Review E*, vol. 89, no. 3, p. 030101, 2014.

[107] D. Holcman and Z. Schuss, "Oscillatory survival probability and eigenvalues of the non-self-adjoint fokker–planck operator," *Multiscale Modeling & Simulation*, vol. 12, no. 3, pp. 1294–1308, 2014.

[108] K. Dao Duc, Z. Schuss, and D. Holcman, "Oscillatory survival probability: Analytical and numerical study of a non-poissonian exit time," *Multiscale Modeling & Simulation*, vol. 14, no. 2, pp. 772–798, 2016.

[109] K. Dao Duc, C.-Y. Lee, P. Parutto, D. Cohen, M. Segal, N. Rouach, and D. Holcman, "Bursting reverberation as a multiscale neuronal network process driven by synaptic depression-facilitation," *PloS One*, vol. 10, no. 5, p. e0124694, 2015.

[110] E. Bart, S. Bao, and D. Holcman, "Modeling the spontaneous activity of the auditory cortex," *Journal of computational neuroscience*, vol. 19, no. 3, pp. 357–378, 2005.

[111] J. M. Cortes, M. Desroches, S. Rodrigues, R. Veltz, M. A. Muñoz, and T. J. Sejnowski, "Short-term synaptic plasticity in the deterministic tsodyks–markram model leads to unpredictable network dynamics," *Proceedings of the National Academy of Sciences*, vol. 110, no. 41, pp. 16610–16615, 2013.

[112] C. Guerrier, J. A. Hayes, G. Fortin, and D. Holcman, "Robust network oscillations during mammalian respiratory rhythm generation driven by synaptic dynamics," *Proceedings of the National Academy of Sciences*, vol. 112, no. 31, pp. 9728–9733, 2015.

[113] M. I. Dykman, M. M. Millonas, and V. N. Smelyanskiy, "Observable and hidden singular features of large fluctuations in nonequilibrium systems," *Physics Letters A*, vol. 195, no. 1, pp. 53–58, 1994.

[114] M. I. Dykman, E. Mori, J. Ross, and P. Hunt, "Large fluctuations and optimal paths in chemical kinetics," *The Journal of chemical physics*, vol. 100, no. 8, pp. 5735–5750, 1994.

[115] R. S. Maier and D. L. Stein, "Effect of focusing and caustics on exit phenomena in systems lacking detailed balance," *Phys. Rev. Lett.*, vol. 71, pp. 1783–1786, Sep 1993.

[116] B. Lindner, J. Garcıa-Ojalvo, A. Neiman, and L. Schimansky-Geier, "Effects of noise in excitable systems," *Physics reports*, vol. 392, no. 6, pp. 321–424, 2004.

[117] R. Kuske, "Multi-scale analysis of noise-sensitivity near a bifurcation," in *Nonlinear stochastic dynamics* (N. Namachchivaya and Y. Lin, eds.), pp. 147–156, Springer Science+Business Media Dordrecht, 2003.

[118] L. Schimansky-Geier, A. Tolstopjatenko, and W. Ebelin, "Noise induced transitions due to external additive noise," *Physics Letters A*, vol. 108, no. 7, pp. 329–332, 1985.

[119] L. Arnold, "A new example of an unstable system being stabilized by random parameter noise," *Inform. Comm. Math. Chem*, vol. 7, pp. 133–140, 1979.

[120] L. Arnold, "Stabilization by noise revisited," *ZAMM-Journal of Applied Mathematics and Mechanics/Zeitschrift für Angewandte Mathematik und Mechanik*, vol. 70, no. 7, pp. 235–246, 1990.

[121] V. Wihstutz, "On stabilizing the double oscillator by mean zero noise," in *Nonlinear stochastic dynamics* (N. Namachchivaya and Y. Lin, eds.), pp. 179–190, Springer Science+Business Media Dordrecht, 2003.

[122] H. A. Kramers, "Brownian motion in a field of force and the diffusion model of chemical reactions," *Physica*, vol. 7, no. 4, pp. 284–304, 1940.

[123] Z. Schuss, *Theory and Applications of Stochastic Differential Equations.* Wiley, 1980.

[124] C. Gardiner, *Handbook of Stochastic Methods for Physics, Chemistry, and the Natural Sciences.* Proceedings in Life Sciences, Springer-Verlag, 1985.

[125] Z. Schuss, *Theory and Applications of Stochastic Processes: An Analytical Approach.* Springer New York, 2010.

[126] C. Dellago, P. G. Bolhuis, and D. Chandler, "Efficient transition path sampling: Application to lennard-jones cluster rearrangements," *The Journal of chemical physics*, vol. 108, no. 22, pp. 9236–9245, 1998.

[127] A. Nitzan, *Chemical dynamics in condensed phases: relaxation, transfer and reactions in condensed molecular systems.* Oxford university press, 2006.

[128] Z. Schuss, *Nonlinear filtering and optimal phase tracking*, vol. 180. Springer Science & Business Media, 2011.

[129] J.-P. Fouque, G. Papanicolaou, and K. R. Sircar, *Derivatives in financial markets with stochastic volatility.* Cambridge University Press, 2000.

[130] A. T. Hawk, S. S. M. Konda, and D. E. Makarov, "Computation of transit times using the milestoning method with applications to polymer translocation," *The Journal of Chemical Physics*, vol. 139, no. 6, p. 08B611, 2013.

[131] A. Godec and R. Metzler, "Universal proximity effect in target search kinetics in the few-encounter limit," *Physical Review X*, vol. 6, no. 4, p. 041037, 2016.

[132] D. S. Grebenkov, R. Metzler, and G. Oshanin, "Full distribution of first exit times in the narrow escape problem," *New Journal of Physics*, vol. 21, no. 12, p. 122001, 2019.

[133] M. I. Freidlin and A. D. Wentzell, "Random perturbations," in *Random perturbations of dynamical systems*, pp. 15–43, Springer, 1998.

[134] B. Bobrovsky and Z. Schuss, "A singular perturbation method for the computation of the mean first passage time in a nonlinear filter," *SIAM Journal on Applied Mathematics*, vol. 42, no. 1, pp. 174–187, 1982.

[135] R. S. Maier and D. L. Stein, "Oscillatory behavior of the rate of escape through an unstable limit cycle," *Phys. Rev. Lett.*, vol. 77, pp. 4860–4863, Dec 1996.

[136] T. Verechtchaguina, I. M. Sokolov, and L. Schimansky-Geier, "First passage time densities in resonate-and-fire models," *Physical Review E*, vol. 73, no. 3, p. 031108, 2006.

[137] T. Verechtchaguina, I. Sokolov, and L. Schimansky-Geier, "First passage time densities in non-markovian models with subthreshold oscillations," *EPL (Europhysics Letters)*, vol. 73, no. 5, p. 691, 2006.

[138] T. Verechtchaguina, I. Sokolov, and L. Schimansky-Geier, "Interspike interval densities of resonate and fire neurons," *Biosystems*, vol. 89, no. 1-3, pp. 63–68, 2007.

[139] Z. Schuss, *Diffusion and Stochastic Processes. An Analytical Approach.* Springer-Verlag, New York, NY, 2009.

[140] Y. Lanoiselée, N. Moutal, and D. S. Grebenkov, "Diffusion-limited reactions in dynamic heterogeneous media," *Nature communications*, vol. 9, no. 1, pp. 1–16, 2018.

[141] D. S. Grebenkov, "A unifying approach to first-passage time distributions in diffusing diffusivity and switching diffusion models," *Journal of Physics A: Mathematical and Theoretical*, vol. 52, no. 17, p. 174001, 2019.

[142] R. D. Traub and R. Miles, *Neuronal networks of the hippocampus*, vol. 777. Cambridge University Press, 1991.

[143] D. L. Schomer and F. L. Da Silva, *Niedermeyer's electroencephalography: basic principles, clinical applications, and related fields.* Lippincott Williams & Wilkins, 2012.

[144] J. Cartailler, P. Parutto, C. Touchard, F. Vallée, and D. Holcman, "Alpha rhythm collapse predicts iso-electric suppressions during anesthesia," *Communications Biology*, vol. 2, September 2019.

[145] O. Barak and M. Tsodyks, "Persistent activity in neural networks with dynamic synapses," *PLoS Comput Biol*, vol. 3, no. 2, p. e35, 2007.

[146] G. Mongillo, O. Barak, and M. Tsodyks, "Synaptic theory of working memory," *Science*, vol. 319, pp. 1543–1546, March 2008.

[147] K. Dao Duc, P. Parutto, X. Chen, J. Epsztein, A. Konnerth, and D. Holcman, "Synaptic dynamics and neuronal network connectivity are reflected in the distribution of times in up states," *Frontiers in Computational Neuroscience*, vol. 9, p. 96, July 2015.

[148] Z. Schuss and A. Spivak, "The exit distribution on the stochastic separatrix in kramers' exit problem," *SIAM Journal of Applied Mathematics*, May-June 2002.

[149] Z. Schuss and A. Spivak, "Where is the exit point?," *Chemical Physics*, vol. 235, p. 227–242, 1998.

[150] S. Coombes and P. C. Bressloff, *Bursting: The Genesis Of Rhythm In The Nervous System.* World Scientific, 2005.

[151] B. J. Matkowsky and Z. Schuss, “The exit problem for randomly perturbed dynamical systems,” *SIAM Journal on Applied Mathematics*, vol. 33, no. 2, pp. 365–382, 1977.

[152] V. Smelyanskiy, M. Dykman, and B. Golding, “Time oscillations of escape rates in periodically driven systems,” *Physical review letters*, vol. 82, no. 16, p. 3193, 1999.

[153] H. C. Tuckwell, J. Jost, and B. S. Gutkin, “Inhibition and modulation of rhythmic neuronal spiking by noise,” *Physical Review E*, vol. 80, no. 3, p. 031907, 2009.

[154] B. Matkowsky, Z. Schuss, and C. Tier, “Uniform expansion of the transition rate in kramers’ problem,” *Journal of statistical physics*, vol. 35, no. 3-4, pp. 443–456, 1984.

[155] N. Agudov and A. Malakhov, “Decay of unstable equilibrium and nonequilibrium states with inverse probability current taken into account,” *Physical Review E*, vol. 60, no. 6, p. 6333, 1999.

[156] B. Ermentrout, M. Pascal, and B. Gutkin, “The effects of spike frequency adaptation and negative feedback on the synchronization of neural oscillators,” *Neural computation*, vol. 13, no. 6, pp. 1285–1310, 2001.

[157] B. S. Gutkin and G. B. Ermentrout, “Dynamics of membrane excitability determine interspike interval variability: a link between spike generation mechanisms and cortical spike train statistics,” *Neural computation*, vol. 10, no. 5, pp. 1047–1065, 1998.

[158] L. Zonca and D. Holcman, “Modeling bursting in neuronal networks using facilitation-depression and afterhyperpolarization,” *Communications in Nonlinear Science and Numerical Simulation*, vol. 94, p. 105555, 2021.

[159] M. I. Dykman and D. Ryvkine, “Synchronization of noise-induced escape: how it starts and ends,” in *Noise in Complex Systems and Stochastic Dynamics III*, vol. 5845, pp. 228–237, International Society for Optics and Photonics, 2005.

[160] B. Hille, “Ionic channels in excitable membranes. current problems and biophysical approaches,” *Biophysical Journal*, vol. 22, no. 2, pp. 283–294, 1978.

[161] R. Yuste, *Dendritic spines*. MIT press, 2010.

[162] E. Niedermeyer and F. L. da Silva, *Electroencephalography: basic principles, clinical applications, and related fields*. Lippincott Williams & Wilkins, 2005.

[163] N. Rouach, A. Koulakoff, V. Abudara, K. Willecke, and C. Giaume, “Astroglial metabolic networks sustain hippocampal synaptic transmission,” *Science*, vol. 322, no. 5907, pp. 1551–1555, 2008.

[164] U. Pannasch, L. Vargová, J. Reingruber, P. Ezan, D. Holcman, C. Giaume, E. Syková, and N. Rouach, “Astroglial networks scale synaptic activity and plasticity,” *Proceedings of the national academy of sciences*, vol. 108, no. 20, pp. 8467–8472, 2011.

[165] G. Dallérac, J. Zapata, and N. Rouach, “Versatile control of synaptic circuits by astrocytes: where, when and how?,” *Nature Reviews Neuroscience*, vol. 19, no. 12, pp. 729–743, 2018.

[166] F. Amzica, “Physiology of sleep and wakefulness as it relates to the physiology of epilepsy,” *Journal of clinical neurophysiology*, vol. 19, no. 6, pp. 488–503, 2002.

[167] F. Amzica and M. Massimini, “Glial and neuronal interactions during slow wave and paroxysmal activities in the neocortex,” *Cerebral Cortex*, vol. 12, no. 10, pp. 1101–1113, 2002.

[168] R. S. Zucker and W. G. Regehr, “Short-term synaptic plasticity,” *Annual review of physiology*, vol. 64, no. 1, pp. 355–405, 2002.

[169] L. E. Dobrunz and C. F. Stevens, “Heterogeneity of release probability, facilitation, and depletion at central synapses,” *Neuron*, vol. 18, no. 6, pp. 995–1008, 1997.

[170] D. Cohen and M. Segal, “Network bursts in hippocampal microcultures are terminated by exhaustion of vesicle pools,” *Journal of Neurophysiology*, vol. 106, no. 5, pp. 2314–2321, 2011.

[171] S. Crochet, S. Chauvette, S. Boucetta, and I. Timofeev, “Modulation of synaptic transmission in neocortex by network activities,” *European Journal of Neuroscience*, vol. 21, no. 4, pp. 1030–1044, 2005.

[172] A. Bellot-Saez, O. Kékesi, J. W. Morley, and Y. Buskila, “Astrocytic modulation of neuronal excitability through k+ spatial buffering,” *Neuroscience & Biobehavioral Reviews*, vol. 77, pp. 87–97, 2017.

[173] W. Walz, “Role of astrocytes in the clearance of excess extracellular potassium,” *Neurochemistry international*, vol. 36, no. 4-5, pp. 291–300, 2000.

[174] C. J. Karwoski, H.-K. Lu, and E. A. Newman, “Spatial buffering of light-evoked potassium increases by retinal muller (glial) cells,” *Science*, vol. 244, no. 4904, pp. 578–580, 1989.

[175] B. Breithausen, S. Kautzmann, A. Boehlen, C. Steinhäuser, and C. Henneberger, “Limited contribution of astroglial gap junction coupling to buffering of extracellular k+ in ca1 stratum radiatum,” *Glia*, vol. 68, no. 5, pp. 918–931, 2020.

[176] Q. Zhou, Z. Zhang, T. Nagasawa, and S. Hiai, “The structure activity relationship of saikosaponins and glycyrrhizin derivatives for na+, k (+)-atpase inhibiting action,” *Yao xue xue bao = Acta pharmaceutica Sinica*, vol. 31, no. 7, pp. 496–501, 1996.

[177] C. Böhmer, U. Kirschner, and F. Wehner, “18-β-glycyrrhetinic acid (bga) as an electrical uncoupler for intracellular recordings in confluent monolayer cultures,” *Pflügers Archiv*, vol. 442, no. 5, pp. 688–692, 2001.

[178] J. P. Vessey, M. R. Lalonde, H. A. Mizan, N. C. Welch, M. E. Kelly, and S. Barnes, “Carbenoxolone inhibition of voltage-gated ca channels and synaptic transmission in the retina,” *Journal of neurophysiology*, vol. 92, no. 2, pp. 1252–1256, 2004.

[179] K. Michalski and T. Kawate, “Carbenoxolone inhibits pannexin1 channels through interactions in the first extracellular loop,” *Journal of General Physiology*, vol. 147, no. 2, pp. 165–174, 2016.

[180] K. R. Tovar, B. J. Maher, and G. L. Westbrook, “Direct actions of carbenoxolone on synaptic transmission and neuronal membrane properties,” *Journal of neurophysiology*, vol. 102, no. 2, pp. 974–978, 2009.

[181] C. B. Ransom, Z. Ye, W. J. Spain, and G. B. Richerson, “Modulation of tonic gaba currents by anion channel and connexin hemichannel antagonists,” *Neurochemical research*, vol. 42, no. 9, pp. 2551–2559, 2017.

[182] N. Rouach, M. Segal, A. Koulakoff, C. Giaume, and E. Avignone, “Carbenoxolone blockade of neuronal network activity in culture is not mediated by an action on gap junctions,” *The Journal of physiology*, vol. 553, no. 3, pp. 729–745, 2003.

[183] P. A. Rutecki, F. J. Lebeda, and D. Johnston, “Epileptiform activity induced by changes in extracellular potassium in hippocampus,” *Journal of neurophysiology*, vol. 54, no. 5, pp. 1363–1374, 1985.

[184] S. F. Traynelis and R. Dingledine, “Potassium-induced spontaneous electrographic seizures in the rat hippocampal slice,” *Journal of neurophysiology*, vol. 59, no. 1, pp. 259–276, 1988.

[185] M. Amiri, N. Hosseinmardi, F. Bahrami, and M. Janahmadi, “Astrocyte-neuron interaction as a mechanism responsible for generation of neural synchrony: a study based on modeling and experiments,” *Journal of computational neuroscience*, vol. 34, no. 3, pp. 489–504, 2013.

[186] F. Fröhlich, M. Bazhenov, I. Timofeev, M. Steriade, and T. J. Sejnowski, “Slow state transitions of sustained neural oscillations by activity-dependent modulation of intrinsic excitability,” *Journal of Neuroscience*, vol. 26, no. 23, pp. 6153–6162, 2006.

[187] S. B. Danik, G. Rosner, J. Lader, D. E. Gutstein, G. I. Fishman, and G. E. Morley, “Electrical remodeling contributes to complex tachyarrhythmias in connexin43-deficient mouse hearts,” *The FASEB Journal*, vol. 22, no. 4, pp. 1204–1212, 2008.

[188] J. A. Jansen, M. Noorman, H. Musa, M. Stein, S. de Jong, R. van der Nagel, T. J. Hund, P. J. Mohler, M. A. Vos, T. A. van Veen, *et al.*, “Reduced heterogeneous expression of cx43 results in decreased nav1. 5 expression and reduced sodium current that accounts for arrhythmia vulnerability in conditional cx43 knockout mice,” *Heart rhythm*, vol. 9, no. 4, pp. 600–607, 2012.

[189] T. Desplantez, M. L. McCain, P. Beauchamp, G. Rigoli, B. Rothen-Rutishauser, K. K. Parker, and A. G. Kleber, “Connexin43 ablation in foetal atrial myocytes decreases electrical coupling, partner connexins, and sodium current,” *Cardiovascular research*, vol. 94, no. 1, pp. 58–65, 2012.

[190] N. L. Farnsworth and R. K. Benninger, “New insights into the role of connexins in pancreatic islet function and diabetes,” *FEBS letters*, vol. 588, no. 8, pp. 1278–1287, 2014.

[191] A. Roebuck, V. Monasterio, E. Gederi, M. Osipov, J. Behar, A. Malhotra, T. Penzel, and G. Clifford, “A review of signals used in sleep analysis,” *Physiological measurement*, vol. 35, no. 1, p. R1, 2013.

[192] N. André-Obadia, J. Zyss, M. Gavaret, J.-P. Lefaucheur, E. Azabou, S. Boulogne, J.-M. Guérit, A. McGonigal, P. Merle, V. Mutschler, *et al.*, “Recommendations for the use of electroencephalography and evoked potentials in comatose patients,” *Neurophysiologie clinique*, vol. 48, no. 3, pp. 143–169, 2018.

[193] T. Lomas, I. Ivtzan, and C. H. Fu, “A systematic review of the neurophysiology of mindfulness on eeg oscillations,” *Neuroscience & Biobehavioral Reviews*, vol. 57, pp. 401–410, 2015.

[194] M. Wenzel, A. Leunig, S. Han, D. S. Peterka, and R. Yuste, “Prolonged anesthesia alters brain synaptic architecture,” *Proceedings of the National Academy of Sciences*, vol. 118, no. 7, 2021.

[195] S. Ching, P. L. Purdon, S. Vijayan, N. J. Kopell, and E. N. Brown, "A neurophysiological–metabolic model for burst suppression," *Proceedings of the National Academy of Sciences*, vol. 109, no. 8, pp. 3095–3100, 2012.

[196] M. Steriade, F. Amzica, and D. Contreras, "Cortical and thalamic cellular correlates of electroencephalographic burst-suppression," *Electroencephalography and clinical neurophysiology*, vol. 90, no. 1, pp. 1–16, 1994.

[197] M. Steriade, "Grouping of brain rhythms in corticothalamic systems," *Neuroscience*, vol. 137, no. 4, pp. 1087–1106, 2006.

[198] R. R. Llinás and M. Steriade, "Bursting of thalamic neurons and states of vigilance," *Journal of neurophysiology*, vol. 95, no. 6, pp. 3297–3308, 2006.

[199] M. V. Sanchez-Vives and D. A. McCormick, "Cellular and network mechanisms of rhythmic recurrent activity in neocortex," *Nature neuroscience*, vol. 3, no. 10, pp. 1027–1034, 2000.

[200] A. Compte, M. V. Sanchez-Vives, D. A. McCormick, and X.-J. Wang, "Cellular and network mechanisms of slow oscillatory activity (< 1 hz) and wave propagations in a cortical network model," *Journal of neurophysiology*, vol. 89, no. 5, pp. 2707–2725, 2003.

[201] D. Levenstein, G. Buzsáki, and J. Rinzel, "Nrem sleep in the rodent neocortex and hippocampus reflects excitable dynamics," *Nature communications*, vol. 10, no. 1, pp. 1–12, 2019.

[202] L. Zonca and D. Holcman, "Escape from an attractor generated by recurrent exit and application to interburst duration in neuronal network," *arXiv preprint arXiv:2009.06745*, 2021.

[203] Y. Mi, M. Katkov, and M. Tsodyks, "Synaptic correlates of working memory capacity," *Neuron*, vol. 93, no. 2, pp. 323–330, 2017.

[204] H.-C. Lee and C.-W. Jung, "Vital recorder—a free research tool for automatic recording of high-resolution time-synchronised physiological data from multiple anaesthesia devices," *Scientific reports*, vol. 8, no. 1, pp. 1–8, 2018.

[205] L. P. Savtchenko and D. A. Rusakov, "Regulation of rhythm genesis by volume-limited, astroglia-like signals in neural networks," *Philosophical Transactions of the Royal Society B: Biological Sciences*, vol. 369, no. 1654, p. 20130614, 2014.

[206] J. S. Goldman, N. Tort-Colet, M. Di Volo, E. Susin, J. Bouté, M. Dali, M. Carlu, T.-A. Nghiem, T. Górski, and A. Destexhe, "Bridging single neuron dynamics to global brain states," *Frontiers in systems neuroscience*, vol. 13, p. 75, 2019.

[207] I. Pavlov, L. P. Savtchenko, I. Song, J. Koo, A. Pimashkin, D. A. Rusakov, and A. Semyanov, "Tonic gabaa conductance bidirectionally controls interneuron firing pattern and synchronization in the ca3 hippocampal network," *Proceedings of the National Academy of Sciences*, vol. 111, no. 1, pp. 504–509, 2014.

[208] E. N. Brown and P. L. Purdon, "The aging brain and anesthesia," *Current Opinion in Anesthesiology*, vol. 26, no. 4, pp. 414–419, 2013.

[209] J. J. Harris, R. Jolivet, and D. Attwell, "Synaptic energy use and supply," *Neuron*, vol. 75, no. 5, pp. 762–777, 2012.

[210] J. J. Harris, E. Engl, D. Attwell, and R. B. Jolivet, “Energy-efficient information transfer at thalamocortical synapses,” *PLoS computational biology*, vol. 15, no. 8, p. e1007226, 2019.

[211] T. Altwegg-Boussac, A. E. Schramm, J. Ballestero, F. Grosselin, M. Chavez, S. Lecas, M. Baulac, L. Naccache, S. Demeret, V. Navarro, *et al.*, “Cortical neurons and networks are dormant but fully responsive during isoelectric brain state,” *Brain*, vol. 140, no. 9, pp. 2381–2398, 2017.

[212] F. Balabdaoui, J. Pitman, *et al.*, “The distribution of the maximal difference between a brownian bridge and its concave majorant,” *Bernoulli*, vol. 17, no. 1, pp. 466–483, 2011.

[213] M. Barczy, P. Kern, *et al.*, “Sample path deviations of the wiener and the ornstein–uhlenbeck process from its bridges,” *Brazilian Journal of Probability and Statistics*, vol. 27, no. 4, pp. 437–466, 2013.

[214] A. Mazzolo, “Constraint ornstein-uhlenbeck bridges,” *Journal of Mathematical Physics*, vol. 58, no. 9, p. 093302, 2017.

[215] Y. Ollivier, H. Pajot, and C. Villani, *Optimal Transport: Theory and Applications*, vol. 413. Cambridge University Press, 2014.

[216] C. Villani, *Optimal transport: old and new*, vol. 338. Springer Science & Business Media, 2008.

[217] M. Arjovsky, S. Chintala, and L. Bottou, “Wasserstein generative adversarial networks,” in *International conference on machine learning*, pp. 214–223, PMLR, 2017.

[218] F. Serratosa and G. Sanroma, “A fast approximation of the earth-movers distance between multi-dimensional histograms,” *International Journal of Pattern Recognition and Artificial Intelligence*, vol. 22, no. 08, pp. 1539–1558, 2008.